Chapter 2
Propagation Modeling

The design of spectrally efficient wireless communication systems requires a thorough understanding of the radio propagation channel. The characteristics of the radio channel will vary greatly with the operating frequency, and the propagation environment, e.g., line-of-sight (LoS) versus non-line-of-sight (NLoS), stationary versus mobile transmitters and receivers, and other factors. This chapter emphasizes land mobile radio channels, including those found in cellular land mobile radio systems and other types of vehicular radio systems. However, many of the concepts are of a fundamental nature and will apply to other types of radio channels as well.

A typical cellular land mobile radio system consists of a collection of fixed base stations (BSs) that define radio coverage areas known as cells. The height and placement of the BS antennas affects the proximity of local scatterers at the BSs. In a macrocellular environment where the cell radii are large, the BS antennas are well elevated above the local terrain and are free of local scatterers. Mobile stations (MSs), on the other hand, tend to be surrounded by local scatterers due to their low elevation antennas. Sometimes a line-of-sight (LoS) condition will exist between a BS and a MS, for example in a rural (or open) environment. However, in an urban environment, a non-line-of-sight (NLoS) condition typically exists between the BSs and MSs. As a consequence, the radio waves must propagate between the BSs and MSs via reflections, diffraction, and scattering. Due to the typically large distance between the BSs and MSs in macrocellular systems, radio propagation is often assumed to occur in a two-dimensional (2-D) plane. As shown in Fig. 2.1, multiple plane waves will arrive at the MS (or BS) receiver antenna(s) from different directions, with each having a distinct polarization, amplitude, phase, and delay. This phenomenon is called multipath propagation. The multiple plane waves combine vectorially at each MS (or BS) receiver antenna to produce a composite received signal.

Commercial cellular land mobile radio systems operate at UHF frequencies in bands located at 700/800/900 MHz and 1800/1900 MHz. At these frequencies, the carrier wavelength, λ_c, is approximately 15 cm and 30 cm, respectively, using the relationship $c = f_c\lambda_c$, where f_c is the carrier frequency and c is the speed of light. Therefore, small changes in the propagation delays of the individual multipath components due to MS mobility on the order of a few centimeters will cause a large change in the relative phases of the plane wave components arriving at the MS (or BS) receiver antennas. Hence, when the arriving plane waves combine vectorially at the receiver antenna(s), they will experience constructive and destructive addition depending on the physical location of the MS. If the MS is moving or there are changes in the location of the scatterers, then these spatial variations will manifest themselves as time variations in the amplitude and phase of the composite signal received at each MS (or BS) antenna, a phenomenon known as envelope fading. If the propagation environment is such that no individual multipath component is dominant, such as when NLoS conditions exist between the BS and MS, then the composite receive envelope under narrowband propagation conditions is often modeled as being Rayleigh distributed at any time. Such a channel is said to exhibit Rayleigh fading. However, if a dominant multipath component exists, such as when a LoS or specular condition exists between the BS and MS, then the envelope is often modeled as being Ricean distributed at any time. Such a channel is said to exhibit Ricean fading.

Radio channels are reciprocal in the sense that if a propagation path exists it carries energy equally well in both directions. However, the spatial distribution of arriving plane waves may be significantly different in each direction. A MS in a typical NLoS macrocellular environment is usually surrounded by local scatterers, so that the plane waves will arrive at the MS antenna from many different directions, as shown in Fig. 2.1. Two-dimensional (2-D) isotropic scattering, where the plane waves arrive from all azimuth directions with equal probability and with equal strength, is a very commonly used reference model to describe the signals received at a MS in this case. The BSs, on the other hand, are relatively free from local scatterers. Hence, plane waves tend to arrive at a BS with a small azimuth angle of arrival (AoA) spread as shown in Fig. 2.1. It will be shown later in this chapter that these differences in the scattering environment for the forward and reverse links

G.L. Stüber, *Principles of Mobile Communication*, DOI 10.1007/978-3-319-55615-4_2

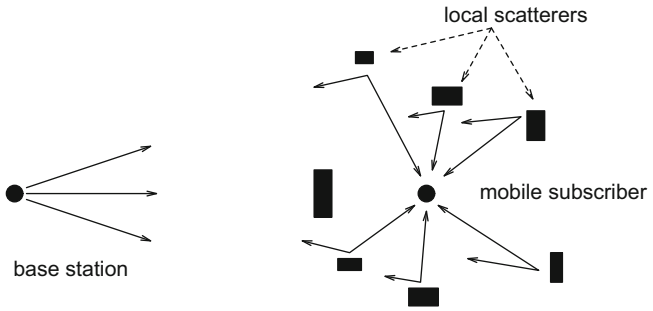

Fig. 2.1 Typical macrocellular radio propagation environment

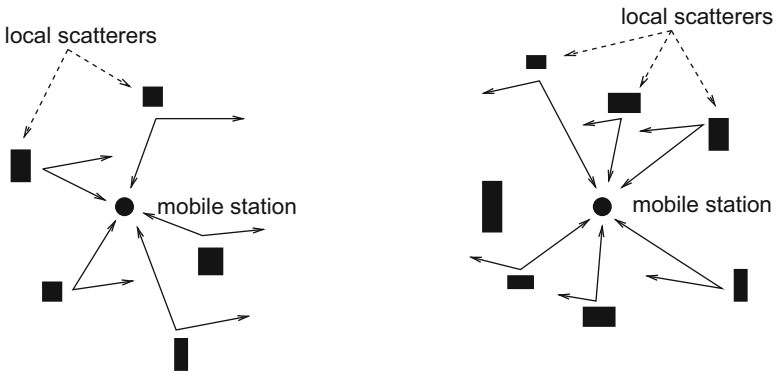

Fig. 2.2 Typical mobile-to-mobile radio propagation environment

will cause significant and important differences in the spatial correlation properties of the respective faded envelopes at the MSs and BSs.

Some types of land mobile radio systems, such as mobile ad hoc networks, consist of vehicle-to-vehicle (or mobile-to-mobile) and vehicle-to-infrastructure links. In this book vehicle-to-vehicle links are referred to as mobile-to-mobile links, because the user terminals are not necessarily vehicular mounted. A typical mobile-to-mobile radio propagation environment is depicted in Fig. 2.2. Such mobile-to-mobile communication systems differ from conventional cellular radio systems where one end of the link (the BS) is stationary and free of scattering, and only the MS is moving. Though the received signal envelope of mobile-to-mobile links is still Rayleigh faded under NLoS narrowband propagation conditions, the mobility of both the transmitters and receivers, and scattering at both ends of the links, causes these links to exhibit much different statistical properties than cellular land mobile radio channels.

If the received envelope or squared-envelope is averaged over a spatial distance of 20–30 wavelengths, an estimated of the mean envelope or mean squared-envelope can be obtained. Sometimes, this quantity is called the local mean because it corresponds to a particular locality. The local mean will experience slow variations over distances of several tens of wavelengths due to the presence of large terrain features such as buildings, hills, and valleys. This phenomenon is known as shadow fading or shadowing. Experimental observations have confirmed that the local mean signal strength follows a log-normal distribution. This log-normal distribution applies to both macrocellular [171, 194] and microcellular environments [149, 226, 228].

If the local mean is averaged over a sufficiently large spatial distance (to average over the shadows), the area mean is obtained. The area mean is the average signal strength that is received to/from a MS over locations that lie at the same distance from the BS. The area mean is inversely proportional to the path loss, which describes how the area mean decreases with the distance between the BS and MS. Early studies by Okumura [250] and Hata [161] yielded an empirical path loss model for macrocellular radio systems operating in urban, suburban, and rural areas. The Okumura–Hata model is accurate to within 1 dB for distances ranging from 1 to 20 km and carrier frequencies between 150 and 1000 MHz, and was adopted in the COST207 study [78]. The Okumura–Hata model is only valid for carrier frequencies less than 1000 MHz. Consequently, when additional spectrum were made available in the 1990s for cellular systems operating in the 1800/1900 MHz band, new path loss models were needed. The COST231 study [81] resulted in the COST231-Hata model that extended the Okumura–Hata model to the 1800/1900 MHz band, and provided the Walfish–Ikegami model for path loss prediction in LoS and NLoS urban microcells. More recent models include the 3GPP models [1] and their extension to mm-wave frequencies [158].

The remainder of this chapter presents the fundamentals of radio propagation modeling, analysis and simulation. Section 2.1 considers conventional narrow-band fixed-to-mobile channels, and various properties of the faded envelope are considered. Section 2.2 considers mobile-to-mobile channels. Section 2.3 treats the statistical characterization of wide-band multipath-fading channels. Simulation models for fading channels are covered in Sect. 2.5. Shadowing models and simulation techniques are discussed in Sect. 2.6. Finally, Sect. 2.7 treats theoretical and empirical models for path loss in macrocellular and microcellular systems.

2.1 Fixed-to-Mobile Channels

For land mobile radio applications, the signals from the BSs are usually transmitted with vertical polarization, meaning that the electric field is perpendicular to the Earth's surface. At VHF frequencies, vertical polarization produces a higher field strength close to the ground than horizontal polarization. Likewise, the MS antennas are also vertically polarized, although tilting of the MS antenna will result in a polarization mismatch. Even if the signals are transmitted with vertical polarization, reflections and diffractions from objects will cause the signals to undergo depolarization. This effect can be exploited by using polarization diverse antennas. For example, cross-polarized antennas, where two antennas having $+45°$, and $-45°$ polarizations from vertical are sometimes used at the BSs.

In cellular land mobile radio systems, the radio signals will propagate in three dimensions. However, if the distance between the BS and MS is sufficiently large, the radio propagation environment is often modeled as occurring in a two-dimensional (2-D) plane. Figure 2.3 depicts a horizontal $x-y$ plane, where a MS is moving in the direction of the positive x-axis with velocity v. The BS is assumed stationary. With vertical polarization, the electric field vector is aligned with the z-axis. The nth plane wave arrives at the MS antenna with an angle of incidence θ_n. The MS movement introduces a Doppler shift, or frequency shift, into the incident plane wave. The Doppler shift is given by

$$f_{D,n} = f_m \cos(\theta_n) \ \text{Hz} \tag{2.1}$$

where $f_m = v/\lambda_c$ and λ_c is the wavelength of the arriving plane wave, and f_m is the maximum Doppler frequency occurring when $\theta_n = 0$. Plane waves arriving from the right half plane will experience a positive Doppler shift, while those arriving from the left half plane will experience a negative Doppler shift.

Consider the transmission of the bandpass signal

$$s(t) = \text{Re}\left\{\tilde{s}(t)e^{j2\pi f_c t}\right\}. \tag{2.2}$$

where $\tilde{s}(t)$ is the complex envelope of the bandpass signal, f_c is the carrier frequency, and $\text{Re}\{z\}$ denotes the real part of z. If the channel is comprised of N propagation paths, then the noiseless received bandpass waveform is

$$r(t) = \text{Re}\left\{\sum_{n=1}^{N} C_n e^{j\phi_n - j2\pi c\tau_n/\lambda_c + j2\pi(f_c+f_{D,n})t}\tilde{s}(t-\tau_n)\right\}, \tag{2.3}$$

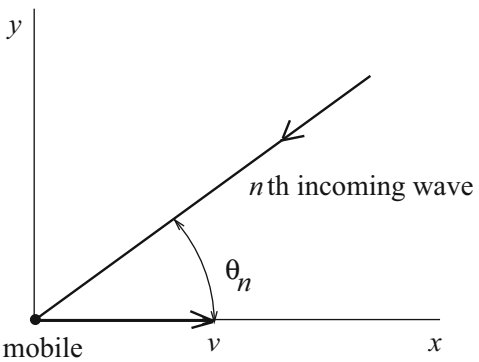

Fig. 2.3 A typical plane wave incident on a MS receiver

where C_n, ϕ_n, $f_{D,n}$, and τ_n are the amplitude, phase, Doppler shift, and time delay, respectively, associated with the nth propagation path, and $c = f_c\lambda_c$ is the speed of light. The magnitude C_n depends on the cross sectional area of the nth reflecting surface or the length of the nth diffracting edge. The phase ϕ_n is randomly introduced by the nth scatterer and can be assumed to be uniformly distributed on $[-\pi, \pi)$. The delay $\tau_n = d_n/c$ is the propagation delay associated with the nth propagation path, where d_n is the length of the path. The set of path lengths, $\{d_n\}$, will depend on the physical scattering geometry which has not been specified at this point. The Doppler shift $f_{D,n}$ of the nth propagation path is as discussed previously.

Similar to (2.2), the received bandpass signal $r(t)$ has the representation

$$r(t) = \mathrm{Re}\left\{\tilde{r}(t)e^{j2\pi f_c t}\right\}, \tag{2.4}$$

where the received complex envelope is

$$\tilde{r}(t) = \sum_{n=1}^{N} C_n e^{j\phi_n(t)}\tilde{s}(t-\tau_n) \tag{2.5}$$

and

$$\phi_n(t) = \phi_n - 2\pi c\tau_n/\lambda_c + 2\pi f_{D,n}t \tag{2.6}$$

is the time-variant phase associated with the nth path. The complex envelope at the input of the channel, $\tilde{s}(t)$, and the complex envelope at the output of the channel, $\tilde{r}(t)$, are related through the convolution integral

$$\tilde{r}(t) = \int_0^t g(t,\tau)\tilde{s}(t-\tau)\mathrm{d}\tau \tag{2.7}$$

where $g(t, \tau)$ is the time-variant complex impulse response of the channel. From (2.5), it follows that

$$g(t,\tau) = \sum_{n=1}^{N} C_n e^{j\phi_n(t)}\delta(\tau-\tau_n), \tag{2.8}$$

where $\delta(\cdot)$ is the Dirac delta function or unit impulse function.

From (2.5) and (2.6), several interesting observations can be made. Since the carrier wavelength λ_c is small (approximately 30 cm at 1 GHz), even small changes in the path delays $d_n = c\tau_n$ will cause large changes in the phases $\phi_n(t)$, due to the term $2\pi c\tau_n/\lambda_c$. For a straight line trajectory $2\pi c\tau_n/\lambda_c = 2\pi d_n/\lambda_c$. Also, due to the Doppler frequency $f_{D,n}$, the phases $\phi_n(t)$ vary with time. Hence, at any given point in space-time, the phases $\phi_n(t)$ will result in the constructive or destructive addition of the N multipath components, a phenomenon known as fading.

If the differential path delays $\tau_i - \tau_j$ for all i, j are very small compared to the modulation symbol period, T, then the τ_n that appear in the argument of Dirac delta function in (2.8) can be approximated by their average value $\bar{\tau}$, i.e., $\tau_n \approx \bar{\tau}$. In this case, the complex channel impulse response has the form

$$g(t,\tau) = g(t)\delta(\tau-\hat{\tau}), \tag{2.9}$$

where

$$g(t) = \sum_{n=1}^{N} C_n e^{j\phi_n(t)}. \tag{2.10}$$

Note that $\phi_n(t)$ remains as defined with the τ_n in (2.6), since the approximation $f_c\tau_n \approx f_c\bar{\tau}$ *cannot* be made when f_c is large. Therefore, the received complex envelope is

$$\tilde{r}(t) = g(t)\tilde{s}(t-\hat{\tau}) \tag{2.11}$$

which experiences fading due to the time-varying complex channel gain $g(t)$. In the frequency domain, the received complex envelope is

$$\tilde{R}(f) = G(f) * \left(\tilde{S}(f)\mathrm{e}^{-j2\pi f\hat{\tau}}\right). \tag{2.12}$$

Since the channel changes with time, $G(f)$ has a finite non-zero width in the frequency domain. Due to the convolution operation, the output spectrum $\tilde{R}(f)$ will be larger than the input spectrum $\tilde{S}(f)$. This broadening of the transmitted signal spectrum is caused by the channel time variations and is called frequency spreading or Doppler spreading.

The time-variant channel transfer function can be obtained by taking the Fourier transform of (2.9) with respect to the τ variable, giving

$$T(f,t) = \mathscr{F}\{g(t,\tau)\} = g(t)\mathrm{e}^{-j2\pi f\hat{\tau}}. \tag{2.13}$$

The time-variant channel magnitude response is $|T(f,t)| = |g(t)|$. Note that all frequency components in the received signal are scaled by the same time-variant magnitude $|g(t)|$. In this case the received signal is said to exhibit frequency flat fading, because the magnitude of the time-variant channel transfer function is constant (or flat) with respect to frequency variable f.

If the differential path delays $\tau_i - \tau_j$ for some i, j are sufficiently large compared to the modulation symbol period T, then the magnitude response $|T(f,t)|$ is no longer flat and the channel exhibits frequency-selective fading. Sometimes frequency-selective fading channels are called wide-band channels. A simplified concentric-ellipses model for frequency-selective fading channels is depicted in Fig. 2.4, where the transmitter and receiver are located at the foci of the ellipses. Considering only single bounce reflections between the transmitter and receiver, all paths that are associated with scatterers on the nth elliptical contour will have the same propagation delay τ_n. Frequency-selective channels have strong scatterers that are located on several ellipses such that the corresponding differential path delays $\tau_i - \tau_j$ for some i, j, are significant compared to the modulation symbol period T.

2.1.1 Envelope Correlation

A flat fading channel can be characterized by assuming the transmission of a continuous wave sinusoid at frequency f_c, because the channel magnitude response is flat. For convenience, the transmitted sinusoid is assumed to have complex envelope $\tilde{s}(t) = 1$ in (2.5). From (2.4) and (2.5), the corresponding received bandpass signal can be expressed in the quadrature form

$$r(t) = g_I(t)\cos(2\pi f_c t) - g_Q(t)\sin(2\pi f_c t), \tag{2.14}$$

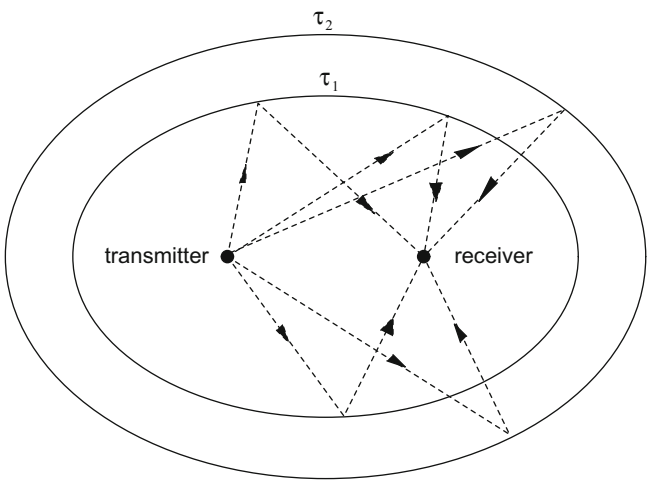

Fig. 2.4 Concentric-ellipses model for frequency-selective fading channels

where

$$g_I(t) = \sum_{n=1}^{N} C_n \cos(\phi_n(t)) \tag{2.15}$$

$$g_Q(t) = \sum_{n=1}^{N} C_n \sin(\phi_n(t)) \tag{2.16}$$

are the in-phase and quadrature components of the received bandpass signal. Assuming that the bandpass random process $r(t)$ is wide-sense stationary, the autocorrelation function of $r(t)$ is

$$\begin{aligned}\phi_{rr}(\tau) &= \mathrm{E}[r(t)r(t+\tau)] \\ &= \phi_{g_I g_I}(\tau)\cos(2\pi f_c \tau) - \phi_{g_I g_Q}(\tau)\sin(2\pi f_c \tau),\end{aligned} \tag{2.17}$$

where $\mathrm{E}[\ \cdot\ ]$ is the ensemble average operator, and

$$\phi_{g_I g_I}(\tau) \triangleq \mathrm{E}[g_I(t)g_I(t+\tau)] \tag{2.18}$$

$$\phi_{g_I g_Q}(\tau) \triangleq \mathrm{E}[g_I(t)g_Q(t+\tau)]. \tag{2.19}$$

Problem 2.1 shows that the wide-sense stationarity of the bandpass random process $r(t)$ imposes the condition

$$\phi_{g_I g_I}(\tau) = \phi_{g_Q g_Q}(\tau) \tag{2.20}$$

$$\phi_{g_I g_Q}(\tau) = -\phi_{g_Q g_I}(\tau). \tag{2.21}$$

The expectations in (2.18) and (2.19) are now calculated.

It is safe to assume that the phases $\phi_n(t)$ are statistically independent random variables at any time t, since the path delays τ_n are all independent due to the random placement of scatterers and the phases ϕ_n are also independent. Furthermore, the phases $\phi_n(t)$ at any time t can be treated as being uniformly distributed over the interval $[-\pi, \pi)$. The azimuth angles of arrival, θ_n are all independent due to the random placement of scatterers. In the limit as $N \to \infty$, the central limit theorem can be invoked and $g_I(t)$ and $g_Q(t)$ can be treated as Gaussian random processes. Also, in the limit as $N \to \infty$, the discrete azimuth angles of arrival θ_n can be replaced by a continuous random variable θ having the probability density function $p(\theta)$. By using these statistical properties, the autocorrelation function $\phi_{g_I g_I}(\tau)$ can be obtained from (2.15), (2.6), and (2.1) as follows:

$$\begin{aligned}\phi_{g_I g_I}(\tau) &= \lim_{N\to\infty} \mathrm{E}_{\boldsymbol{\tau},\boldsymbol{\theta},\boldsymbol{\phi}}[g_I(t)g_I(t+\tau)] \\ &= \frac{\Omega_p}{2}\mathrm{E}_\theta[\cos(2\pi f_m \tau\cos(\theta))]\end{aligned} \tag{2.22}$$

where

$$\boldsymbol{\tau} = (\tau_1, \tau_2, \ldots, \tau_N) \tag{2.23}$$

$$\boldsymbol{\theta} = (\theta_1, \theta_2, \ldots, \theta_N) \tag{2.24}$$

$$\boldsymbol{\phi} = (\phi_1, \phi_2, \ldots, \phi_N) \tag{2.25}$$

$$\Omega_p = \mathrm{E}[|g(t)|^2] = \mathrm{E}[g_I^2(t)] + \mathrm{E}[g_Q^2(t)] = \sum_{n=1}^{N} C_n^2 \tag{2.26}$$

and Ω_p can be interpreted as the received envelope power, while $\Omega_p/2$ is the power received in the corresponding bandpass waveform in (2.14) as given by $\phi_{rr}(0)$ in (2.17).

Likewise, the cross-correlation function $\phi_{g_I g_Q}(\tau)$ can be derived as

$$\begin{aligned}\phi_{g_I g_Q}(\tau) &= \lim_{N\to\infty} \mathrm{E}_{\boldsymbol{\tau},\boldsymbol{\theta},\boldsymbol{\phi}}[g_I(t)g_Q(t+\tau)] \\ &= \frac{\Omega_p}{2}\mathrm{E}_\theta[\sin(2\pi f_m \tau\cos(\theta))]. \end{aligned} \tag{2.27}$$

Evaluation of the expectations in (2.22) and (2.27) requires the fraction of arriving power $p(\theta)$, and the antenna azimuth gain pattern $G(\theta)$, as a function of the azimuth angle θ. Here, the overall power angle distribution $p(\theta)G(\theta)$ is a probability density function that integrates to unity over all arrival angles, such that the total received envelope power is given by

$$\int_{-\pi}^{\pi} G(\theta)p(\theta)\mathrm{d}\theta = 1. \tag{2.28}$$

One simple and commonly used model assumes that the plane waves arrive at the receiver antenna from all azimuth directions with equal probability, i.e., $p(\theta) = 1/(2\pi), \theta \in [-\pi, \pi)$, and an isotropic antenna is used such that the antenna gain is uniform for all azimuth arrival angles, i.e., $G(\theta) = 1, \theta \in [-\pi, \pi)$. This model was first suggested by Clarke [74], and is commonly referred to as Clarke's 2-D isotropic scattering model. The expectation in (2.22) becomes

$$\begin{aligned}\phi_{g_I g_I}(\tau) &= \frac{\Omega_p}{2}\int_{-\pi}^{\pi} \cos\left(2\pi f_m \tau\cos(\theta)\right) p(\theta)G(\theta)\mathrm{d}\theta \\ &= \frac{\Omega_p}{2}\frac{1}{\pi}\int_{0}^{\pi} \cos\left(2\pi f_m \tau\cos(\theta)\right) \mathrm{d}\theta \\ &= \frac{\Omega_p}{2}J_0(2\pi f_m\tau), \end{aligned} \tag{2.29}$$

where

$$J_0(x) = \frac{1}{\pi}\int_{0}^{\pi} \cos\left(x\cos(\theta)\right) \mathrm{d}\theta \tag{2.30}$$

is the zero-order Bessel function of the first kind. The normalized autocorrelation function $\phi_{g_I g_I}(\tau)/(\Omega_p/2)$ in (2.29) is plotted against the normalized time delay $f_m\tau$ in Fig. 2.5.

Likewise, for 2-D isotropic scattering and an isotropic receiver antenna, the cross-correlation function in (2.27) becomes

$$\phi_{g_I g_Q}(\tau) = \frac{\Omega_p}{4\pi}\int_{-\pi}^{\pi} \sin\left(2\pi f_m \tau\cos(\theta)\right) \mathrm{d}\theta = 0. \tag{2.31}$$

A cross-correlation of zero means that $g_I(t)$ and $g_Q(t)$ are uncorrelated and, since they are Gaussian, independent random processes. The fact that $g_I(t)$ and $g_Q(t)$ are independent is a consequence of the symmetry of the 2-D isotropic scattering environment and the isotropic receiver antenna. In general, $g_I(t)$ and $g_Q(t)$ are correlated random processes for non-isotropic scattering environments and/or a non-isotropic receiver antenna.

2.1.2 *Doppler Spectrum*

The autocorrelation of the channel complex envelope $g(t) = g_I(t) + jg_Q(t)$ is

$$\begin{aligned}\phi_{gg}(\tau) &= \frac{1}{2}\mathrm{E}[g^*(t)g(t+\tau)] \\ &= \phi_{g_I g_I}(\tau) + j\phi_{g_I g_Q}(\tau), \end{aligned} \tag{2.32}$$

as derived in greater detail at the beginning of Sect. 4.9. The Doppler spectrum and autocorrelation function of the channel complex envelope are Fourier transform pairs, that is,

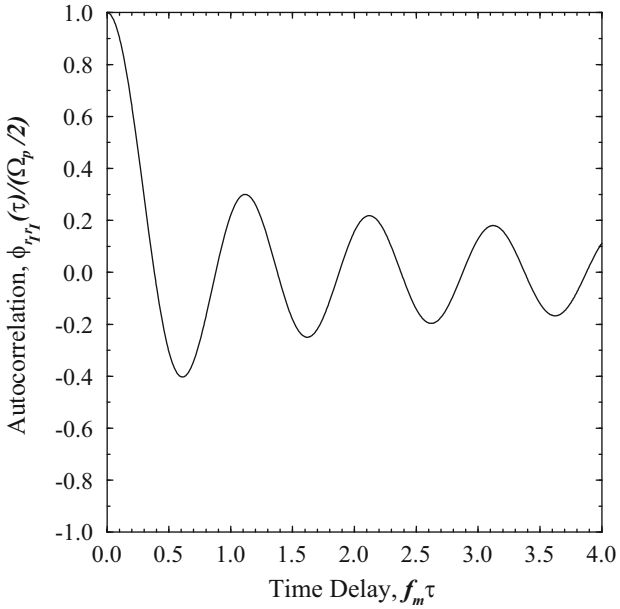

Fig. 2.5 Normalized autocorrelation function of the quadrature components of the received complex envelope with 2-D isotropic scattering and an isotropic receiver antenna

$$S_{gg}(f) = \int_{-\infty}^{\infty} \phi_{gg}(\tau) \mathrm{e}^{-j2\pi f\tau} \mathrm{d}\tau$$
$$\phi_{gg}(\tau) = \int_{-\infty}^{\infty} S_{gg}(\tau) \mathrm{e}^{j2\pi f\tau} \mathrm{d}\tau,$$

where

$$S_{gg}(f) = S_{g_I g_I}(f) + jS_{g_I g_Q}(f), \tag{2.33}$$

is the Doppler spectrum. From (2.33), it may appear that the Doppler spectrum is complex valued. However, the autocorrelation function $\phi_{g_I g_I}(\tau)$, as with any autocorrelation function, is an even valued function such that $\phi_{g_I g_I}(\tau) = \phi_{g_I g_I}(-\tau)$. Hence, its Fourier transform $S_{g_I g_I}(f)$ is real valued. Moreover, the cross-correlation function $\phi_{g_Q g_I}(\tau)$ in (2.32), as with any cross-correlation function, satisfies the property

$$\phi_{g_I g_Q}(\tau) = \phi_{g_Q g_I}(-\tau). \tag{2.34}$$

Combining (2.34) with (2.21) yields the property

$$\phi_{g_I g_Q}(\tau) = -\phi_{g_I g_Q}(-\tau). \tag{2.35}$$

This means that the cross-correlation function $\phi_{g_I g_Q}(\tau)$ is an odd function of τ and, hence, its Fourier transform $S_{g_I g_Q}(f)$ is purely imaginary-valued. Therefore, the Doppler spectrum in (2.33) is always real valued.

For the autocorrelation function in (2.29), the corresponding psd is [147, 6.671.7]

$$\begin{aligned} S_{g_I g_I}(f) &= \mathscr{F}[\phi_{g_I g_I}(\tau)] \\ &= \begin{cases} \frac{\Omega_p}{2\pi f_m} \frac{1}{\sqrt{1-(f/f_m)^2}} & |f| \le f_m \\ 0 & \text{otherwise} \end{cases}. \end{aligned} \tag{2.36}$$

For the case of 2-D isotropic scattering and an isotropic receiver antenna $S_{g_Q g_I}(f) = 0$ so that $S_{gg}(f) = S_{g_I g_I}(f)$.

The power spectrum of the channel complex envelope $g(t)$ can also be related to that of the received bandpass process $r(t)$ in (2.14). From (2.17),

$$\phi_{rr}(\tau) = \mathrm{Re}\left\{\phi_{gg}(\tau)\mathrm{e}^{j2\pi f_c\tau}\right\}. \tag{2.37}$$

As shown in Sect. 4.9, by using the identity

$$\mathrm{Re}\{z\} = \frac{z+z^*}{2} \tag{2.38}$$

and the property $\phi_{gg}(\tau) = \phi^*_{gg}(-\tau)$, the bandpass Doppler spectrum is

$$S_{rr}(f) = \frac{1}{2}\Big(S_{gg}(f-f_c) + S_{gg}(-f-f_c)\Big). \tag{2.39}$$

The Doppler spectrum $S_{gg}(f)$ is always a real-valued function of frequency, but not necessarily even. The corresponding bandpass Doppler spectrum $S_{rr}(f)$ is always real-valued and even.

2.1.2.1 Doppler Spectrum Alternate Approach

The Doppler spectrum can be derived by using a different approach that is sometimes useful because it can avoid the need to evaluate integrals. As mentioned earlier, the incident power on the receiver antenna is a function of the azimuth angle θ, such that the fraction of the total received power arriving between angles θ and $\theta + \mathrm{d}\theta$ is $p(\theta)\mathrm{d}\theta$. If the antenna has an azimuth gain of $G(\theta)$, then the fraction of the total power received between angles θ and $\theta + \mathrm{d}\theta$ is $G(\theta)p(\theta)\mathrm{d}\theta$. From (2.1), the Doppler frequency $f = f_m\cos(\theta)$ is an even function of the arrival angle θ. Therefore, the Doppler spectrum can be expressed as [171]

$$S_{gg}(f)|\mathrm{d}f| = \frac{\Omega_p}{2}\Big(G(\theta)p(\theta) \;+\; G(-\theta)p(-\theta)\Big)|\mathrm{d}\theta|. \tag{2.40}$$

From (2.1),

$$|\mathrm{d}f| = f_m|-\sin(\theta)\mathrm{d}\theta| = \sqrt{f_m^2 - f^2}\;|\mathrm{d}\theta|. \tag{2.41}$$

Therefore,

$$S_{gg}(f) = \frac{\Omega_p}{2\sqrt{f_m^2-f^2}}\Big(G(\theta)p(\theta) \;+\; G(-\theta)p(-\theta)\Big), \tag{2.42}$$

where

$$\theta = \cos^{-1}\left(f/f_m\right). \tag{2.43}$$

Hence, if $p(\theta)$ and $G(\theta)$ are known, the Doppler spectrum can be easily calculated. Once again, for 2-D isotropic scattering and an isotropic antenna $G(\theta)p(\theta) = 1/(2\pi)$, so that

$$S_{gg}(f) = \begin{cases} \frac{\Omega_p}{2\pi f_m}\frac{1}{\sqrt{1-(f/f_m)^2}} & |f| \le f_m \\ 0 & \text{otherwise} \end{cases}. \tag{2.44}$$

The same result was obtained from the autocorrelation function in (2.29), but it required the evaluation of a Fourier transform integral.

The normalized Doppler spectrum $S_{gg}(f)/(\Omega_p/2\pi f_m)$ in (2.44) is plotted against the normalized Doppler frequency f/f_m in Fig. 2.6. Notice that $S_{gg}(f)$ is limited to the range of frequencies $0 \le |f| \le f_m$ and $S_{gg}(f) = \infty$ at $f = \pm f_m$. In reality, the Doppler spectrum is bounded, and the singular behavior at $f = \pm f_m$ is due to the assumption of 2-D plane wave propagation.

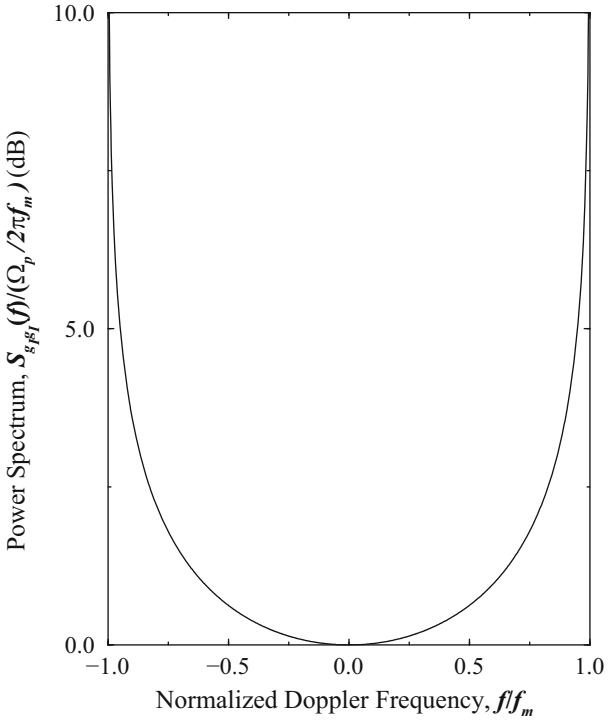

Fig. 2.6 Normalized psd of the quadrature components of the received complex envelope with 2-D isotropic scattering channel and an isotropic receiver antenna

Aulin [22] modified Clarke's 2-D model to yield a 3-D model that accounts for both azimuth and elevation angles-of-arrival. The resulting Doppler spectrum has the general same U-shape as Fig. 2.6, but does not have singularities at frequencies $f = \pm f_m$.

In some cases, it is appropriate to model the received signal as consisting of a strong specular or LoS component plus a scatter component. In this case, the azimuth distribution $p(\theta)$ might have the form

$$p(\theta) = \frac{1}{K+1}\hat{p}(\theta) + \frac{K}{K+1}\delta(\theta - \theta_0), \tag{2.45}$$

where $\hat{p}(\theta)$ is the continuous distribution of the *scatter* component, θ_0 is the angle-of-arrival (AoA) of the specular or LoS component, and K is the ratio of the received specular to scattered power. Figure 2.7 shows a plot of $p(\theta)$ for one such scattering environment, where the scatter component is characterized by 2-D isotropic scattering, i.e., $\hat{p}(\theta) = 1/(2\pi), \theta \in [-\pi, \pi)$. The correlation functions $\phi_{g_I g_I}(\tau)$ and $\phi_{g_I g_Q}(\tau)$ corresponding to (2.45) can be readily obtained from (2.22) and (2.27) as

$$\phi_{g_I g_I}(\tau) = \frac{1}{K+1}\frac{\Omega_p}{2}J_0(2\pi f_m \tau) + \frac{K}{K+1}\frac{\Omega_p}{2}\cos(2\pi f_m \tau \cos(\theta_0)) \tag{2.46}$$

$$\phi_{g_I g_Q}(\tau) = \frac{K}{K+1}\frac{\Omega_p}{2}\sin(2\pi f_m \tau \cos(\theta_0)). \tag{2.47}$$

The azimuth distribution in (2.45) yields a complex envelope having a Doppler spectrum of the form

$$S_{gg}(f) = \frac{1}{K+1}S^c_{gg}(f) + \frac{K}{K+1}S^d_{gg}(f) \tag{2.48}$$

where $S^d_{gg}(f)$ is the discrete portion of the Doppler spectrum due to the specular component and $S^c_{gg}(f)$ is the continuous portion of the Doppler spectrum due to the scatter component. For the case when $\hat{p}(\theta) = 1/(2\pi), \theta \in [-\pi, \pi]$, the correlation functions in (2.46) and (2.47) are obtained and the corresponding Doppler spectrum can be obtained, by using the cross-correlation property in (2.34) along with (2.33), as

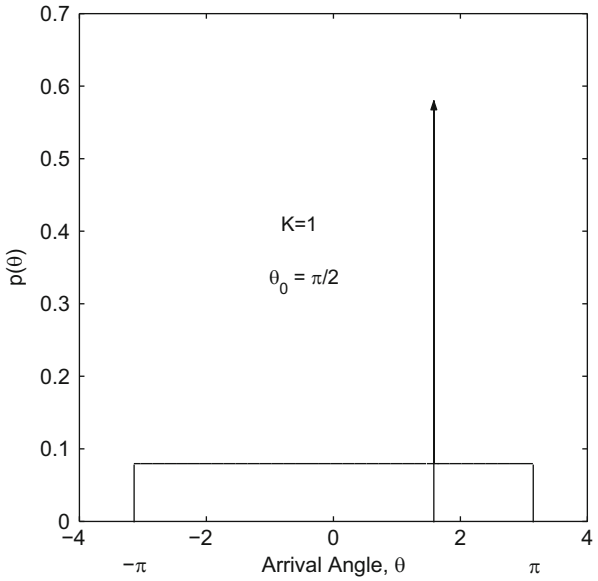

Fig. 2.7 Plot of $p(\theta)$ vs. θ with 2-D isotropic scattering plus a LoS or specular component arriving at angle $\theta_0 = \pi/2$

$$S_{gg}(f) = \begin{cases} \frac{1}{K+1} \cdot \frac{\Omega_p}{2\pi f_m} \frac{1}{\sqrt{1-(f/f_m)^2}} + \frac{K}{K+1} \frac{\Omega_p}{2} \delta(f - f_m \cos(\theta_0)) & 0 \le |f| \le f_m \\ 0 & \text{otherwise} \end{cases}. \tag{2.49}$$

Note that the Doppler spectrum in (2.49) has the same shape as Fig. 2.6, except for the discrete spectral tone at frequency $f = f_m \cos(\theta_0)$.

Sometimes the azimuth distribution $p(\theta)$ may not be uniform, a condition commonly called non-isotropic scattering. Several distributions have been suggested to model non-isotropic scattering. One possibility is the Gaussian distribution

$$p(\theta) = \frac{1}{\sqrt{2\pi}\sigma_S} \exp\left\{-\frac{(\theta-\mu)^2}{2\sigma_S^2}\right\}, \tag{2.50}$$

where μ is the mean AoA, and σ_S is the root mean square (rms) AoA spread. Another possibility is the von Mises distribution

$$p(\theta) = \frac{1}{2\pi I_0(k)} \exp\{k\cos(\theta-\mu)\}, \tag{2.51}$$

where $\theta \in [-\pi, \pi)$, $I_0(\cdot)$ is the zeroth-order modified Bessel function of the first kind, $\mu \in [-\pi, \pi)$ is the mean AoA, and k controls the spread of scatterers around the mean. When $k = 0$, the von Mises distribution reduces to $p(\theta) = 1/(2\pi)$, yielding 2-D isotropic scattering. As k increases, the scatterers become more clustered around the mean AoA μ and the scattering becomes increasingly non-isotropic as shown in Fig. 2.8. Still another possibility is the cosine distribution

$$p(\theta) = \begin{cases} \frac{\pi}{4\theta_{\max}} \cos\left(\frac{\pi}{2}\frac{\theta}{\theta_{\max}}\right) & , \ |\theta| \le \theta_{\max} \le \frac{\pi}{2} \\ 0 & , \ \text{elsewhere} \end{cases}. \tag{2.52}$$

The parameter $\theta_{\max}$ controls the AoA spread of the incoming waves. Figure 2.9 shows a plot of $p(\theta)$ for $\theta_{\max} = 30°$, 60°, and 90°. Note that the distribution is symmetric about $\theta = 0$. Therefore, this azimuth distribution is less flexible than either the Gaussian or von Mises distributions. The density in (2.52) is sometimes used to model the *elevation* AoA distribution of scatterers in 3-D propagation models, where the mean elevation AoA is zero degrees [361].

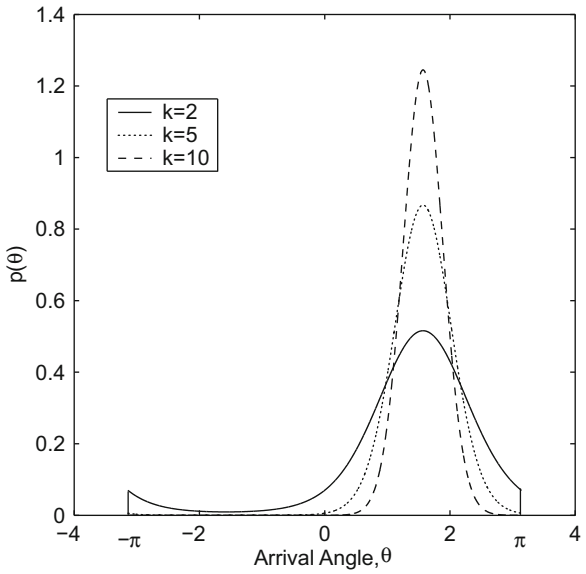

Fig. 2.8 Plot of $p(\theta)$ vs. θ for the von Mises distribution with a mean angle-to-arrival $\mu = \pi/2$

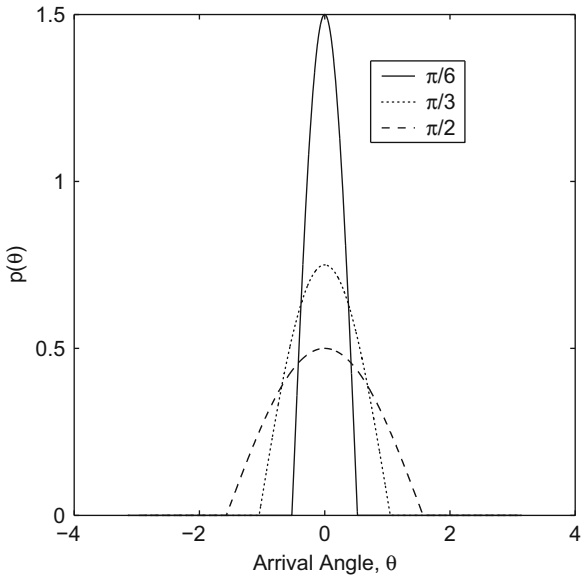

Fig. 2.9 Plot of $p(\theta)$ vs. θ for the angle-of-arrival pdf in (2.52) for various $\theta_{\max}$. The mean angle of arrival is $\theta = 0$

Once the azimuth distribution is specified, the correlation functions $\phi_{g_I g_I}(\tau)$ and $\phi_{g_I g_Q}(\tau)$ can be readily obtained by evaluating the expectations in (2.22) and (2.27), respectively, using, for example, the densities in (2.50), (2.51), or (2.52). The Doppler spectrum, $S_{gg}(f)$, can be obtained by taking the Fourier transform of $\phi_{gg}(\tau)$ in (2.33) or, alternatively, by substituting the azimuth distribution $p(\theta)$ directly into (2.42).

2.1.3 Received Envelope and Phase Distribution

2.1.3.1 Rayleigh Fading

When the composite received signal consists of a large number of sinusoidal components, the received complex envelope $g(t) = g_I(t) + jg_Q(t)$ can be treated as a complex Gaussian random process. For some types of scattering environments, e.g., 2-D isotropic scattering, $g_I(t)$ and $g_Q(t)$ at any time t_1 are independent identically distributed Gaussian random variables with zero mean and variance $b_0 = \mathrm{E}[g_I^2(t_1)] = \mathrm{E}[g_Q^2(t_1)]$. Under these conditions the magnitude of the received complex envelope

$$\alpha \triangleq |g(t_1)| = \sqrt{g_I^2(t_1) + g_Q^2(t_1)} \tag{2.53}$$

has a Rayleigh distribution at any time t_1, as shown in (A.26), i.e.,

$$p_\alpha(x) = \frac{x}{b_0} \exp\left\{-\frac{x^2}{2b_0}\right\}, \qquad x \geq 0, \tag{2.54}$$

The received envelope power is equal to the second moment of α, $\Omega_p = \mathrm{E}[\alpha^2] = 2b_0$, so that

$$p_\alpha(x) = \frac{2x}{\Omega_p} \exp\left\{-\frac{x^2}{\Omega_p}\right\}, \qquad x \geq 0. \tag{2.55}$$

This type of fading is called Rayleigh fading. . The corresponding squared-envelope $\alpha^2 = |g(t_1)|^2$ is exponentially distributed at any time t_1 with density

$$p_{\alpha^2}(x) = \frac{1}{\Omega_p} \exp\left\{-\frac{x}{\Omega_p}\right\}, \qquad x \geq 0. \tag{2.56}$$

The squared-envelope is important for the performance analysis of digital communication systems because it is proportional to the received signal power and, hence, the received signal-to-noise ratio. The performance of digital communication links on flat fading channels will be discussed in more detail in Chap. 5.

2.1.3.2 Ricean Fading

As mentioned earlier, some types of scattering environments have a specular or LoS component. In this case, $g_I(t)$ and $g_Q(t)$ are Gaussian random processes with non-zero means $m_I(t)$ and $m_Q(t)$, respectively. If it is again assumed that $g_I(t)$ and $g_Q(t)$ are uncorrelated, and the random variables $g_I(t_1)$ and $g_Q(t_1)$ have the same variance b_0, then the magnitude of the received complex envelope $\alpha = |g(t_1)|$ at any time t_1 has a Ricean distribution as shown in (A.61), i.e.,

$$p_\alpha(x) = \frac{x}{b_0} \exp\left\{-\frac{x^2 + s^2}{2b_0}\right\} I_o\left(\frac{xs}{b_0}\right) \qquad x \geq 0, \tag{2.57}$$

where

$$s^2 = m_I^2(t) + m_Q^2(t) \tag{2.58}$$

is called the non-centrality parameter. This type of fading is called Ricean fading and is often used to describe fading in environments where a LoS or strong specular path exists between the transmitter and receiver.

A very simple Ricean fading model assumes that the means $m_I(t)$ and $m_Q(t)$ are constants, i.e., $m_I(t) = m_I$ and $m_Q(t) = m_Q$. Such an approach will certainly yield a Ricean distributed envelope, but it lacks any physical meaning. A better model has been suggested by Aulin [22], such that the azimuth distribution $p(\theta)$ is defined in (2.45) and shown in Fig. 2.7. In this case, the LoS or specular component determines the means $m_I(t)$ and $m_Q(t)$ of the in-phase and quadrature components, respectively, as follows:

$$m_I(t) = s \cdot \cos(2\pi f_m \cos(\theta_0)t + \phi_0) \tag{2.59}$$

$$m_Q(t) = s \cdot \sin(2\pi f_m \cos(\theta_0)t + \phi_0), \tag{2.60}$$

where $f_m \cos(\theta_0)$ and ϕ_0 are the Doppler shift and random phase associated with the LoS or specular component, respectively.

The Rice factor, K, is defined as the ratio of the LoS or specular power s^2 to scattered power $2b_0$, i.e., $K = s^2/2b_0$. When $K = 0$, there is no LoS or specular component and the envelope exhibits Rayleigh fading. When $K = \infty$, there is no scatter component and the channel does not exhibit any fading at all. The envelope distribution can be rewritten in terms of the Rice factor and the average envelope power $\Omega_p = \mathrm{E}[\alpha^2] = s^2 + 2b_0$ by first noting that

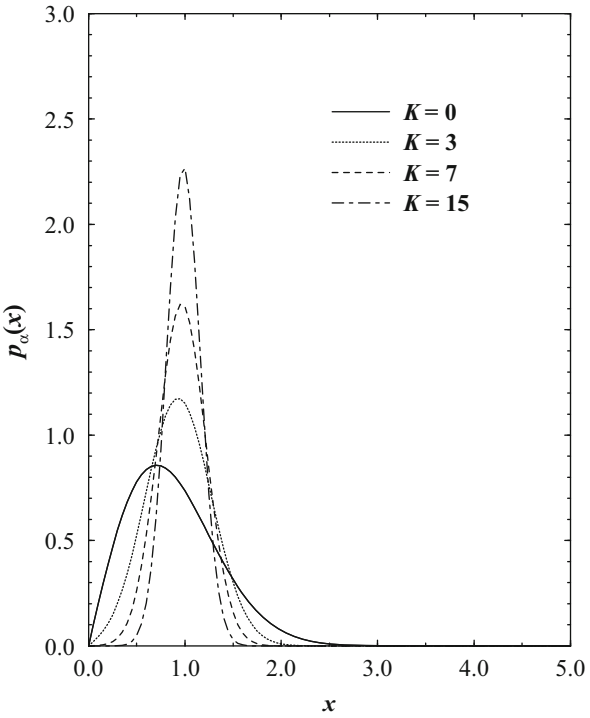

Fig. 2.10 The Rice pdf for several values of K with $\Omega_p = 1$

$$s^2 = \frac{K\Omega_p}{K+1}, \qquad b_0 = \frac{\Omega_p}{2(K+1)}. \tag{2.61}$$

Substituting s^2 and b_0 into (2.57) yields

$$p_\alpha(x) = \frac{2(K+1)x}{\Omega_p} \exp\left\{-K - \frac{(K+1)x^2}{\Omega_p}\right\} I_o\left(2x\sqrt{\frac{K(K+1)}{\Omega_p}}\right), \quad x \geq 0. \tag{2.62}$$

Figure 2.10 shows the Rice pdf for several values of K. The curve for $K = 0$ is the Rayleigh pdf.

The squared-envelope $\alpha^2 = |g(t_1)|^2$ at any time t_1 has the following non-central chi-square distribution with two degrees of freedom:

$$p_{\alpha^2}(x) = \frac{(K+1)}{\Omega_p} \exp\left\{-K - \frac{(K+1)x}{\Omega_p}\right\} I_o\left(2\sqrt{\frac{K(K+1)x}{\Omega_p}}\right), \quad x \geq 0. \tag{2.63}$$

2.1.3.3 Nakagami Fading

The Nakagami distribution was introduced by Nakagami in the early 1940s to characterize rapid fading in long distance HF channels [238]. The Nakagami distribution was selected to fit empirical data, and is known to provide a closer match to some measurement data than either the Rayleigh, Ricean, or log-normal distributions [57].

Nakagami fading describes the magnitude of the received complex envelope by the distribution

$$p_\alpha(x) = 2\left(\frac{m}{\Omega_p}\right)^m \frac{x^{2m-1}}{\Gamma(m)} \exp\left\{-\frac{mx^2}{\Omega_p}\right\} \qquad m \geq \frac{1}{2}, \tag{2.64}$$

where $\Omega_p = \mathrm{E}[\alpha^2]$. Figure 2.11 shows the Nakagami distribution for several values of the shape factor, m. Beyond its empirical justification, the Nakagami distribution is often used for the following reasons. First, the Nakagami distribution can model fading conditions that are either more or less severe than Rayleigh fading. When $m = 1$, the Nakagami distribution becomes the Rayleigh distribution, when $m = 1/2$ it becomes a one-sided Gaussian distribution, and when $m \to \infty$ the

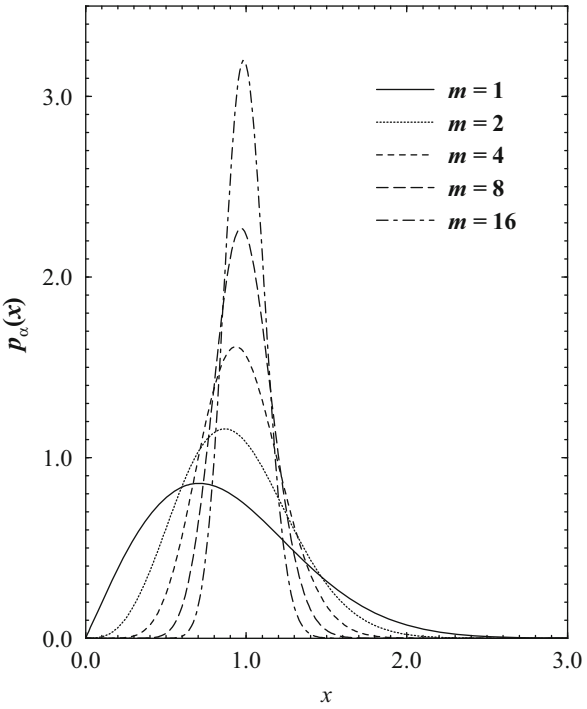

Fig. 2.11 The Nakagami pdf for several values of m with $\Omega_p = 1$

distribution approaches an impulse (no fading). Second, the Rice distribution can be closely approximated by using the following relation between the Rice factor K and the Nakagami shape factor m [238];

$$K \approx \sqrt{m^2 - m} + m - 1 \tag{2.65}$$

$$m \approx \frac{(K+1)^2}{(2K+1)}. \tag{2.66}$$

Finally, since the Rice distribution contains a Bessel function while the Nakagami distribution does not, the Nakagami distribution often leads to convenient closed form analytical expressions that may otherwise be intractable.

With Nakagami fading, the squared-envelope has the Gamma distribution

$$p_{\alpha^2}(x) = \left(\frac{m}{\Omega_p}\right)^m \frac{x^{m-1}}{\Gamma(m)} \exp\left\{-\frac{mx}{\Omega_p}\right\}. \tag{2.67}$$

By using the relationship between the K factor and the shape factor m in (2.65), the cumulative distribution function (cdf), $F_{\alpha^2}(x) = \mathrm{P}(\alpha^2 \leq x)$ of the squared-envelope with Nakagami and Ricean fading is plotted in Fig. 2.12. It is apparent from Fig. 2.12 that a Gamma distribution can approximate a non-central chi-square distribution to a reasonable degree of accuracy. However, the reader is cautioned that the tails of the pdf are often the most important. The reason being that the bit errors in a communication link tend occur during deep fades, which correspond to small values of x in the cdf. Figure 2.12 does not show how well the tails of a non-central chi-square pdf are approximated by a Gamma pdf.

2.1.3.4 Envelope Phase

The phase of the channel complex envelope $g(t) = g_I(t) + jg_Q(t)$ is

$$\phi(t) = \mathrm{Tan}^{-1}\left(\frac{g_Q(t)}{g_I(t)}\right). \tag{2.68}$$

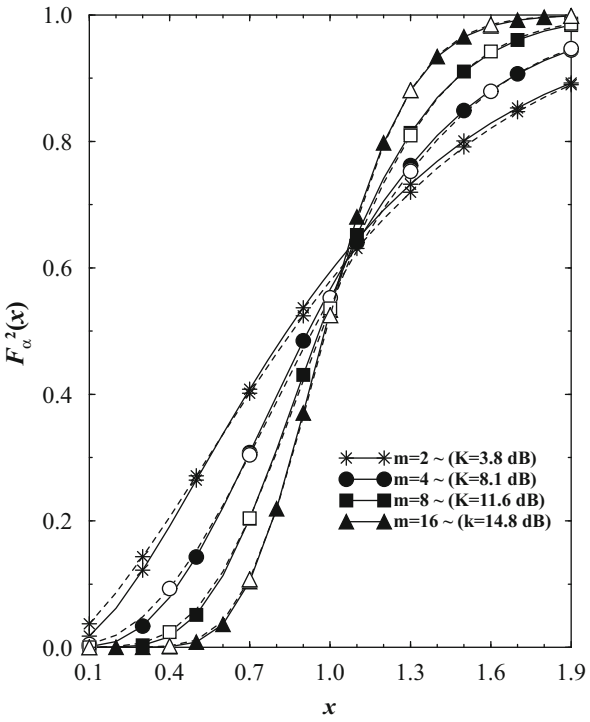

Fig. 2.12 Comparison of the cdf of the squared-envelope with Ricean and Nakagami fading

For Rayleigh fading, $g_I(t_1)$ and $g_Q(t_1)$ are independent identically distributed zero-mean Gaussian random variables at any time t_1. It follows (Appendix A.3.2.4) that the phase $\phi \equiv \phi(t_1)$ at any time t_1 is uniformly distributed over the interval $[-\pi, \pi)$, i.e.,

$$p_\phi(x) = \frac{1}{2\pi}, \quad -\pi \le x \le \pi. \tag{2.69}$$

For Ricean fading channels, the phase ϕ is not uniformly distributed and takes on a more complicated integral form, see Problem 2.9.

2.1.4 Envelope Correlation and Spectra

The autocorrelation of the envelope $\alpha(t) = |g(t)|$ of a complex Gaussian random process can be expressed in terms of the hypergeometric function $F(\cdot, \cdot; \cdot, \cdot)$ as [89]

$$\begin{aligned}\phi_{\alpha\alpha}(\tau) &= \mathrm{E}[\alpha(t)\,\alpha(t+\tau)] \\ &= \frac{\pi}{2}|\phi_{gg}(0)|F\left(-\frac{1}{2}, -\frac{1}{2}; 1, \frac{|\phi_{gg}(\tau)|^2}{|\phi_{gg}(0)|^2}\right),\end{aligned} \tag{2.70}$$

where

$$|\phi_{gg}(\tau)|^2 = \phi^2_{g_Ig_I}(\tau) + \phi^2_{g_Ig_Q}(\tau). \tag{2.71}$$

The above expression is analytically cumbersome, but fortunately a useful approximation can be obtained by expanding the hypergeometric function into the following infinite series:

$$F\left(-\frac{1}{2}, -\frac{1}{2}; 1, x\right) = 1 + \frac{1}{4}x + \frac{1}{64}x^2 + \cdots \tag{2.72}$$

Neglecting the terms beyond second order yields the approximation

$$\phi_{\alpha\alpha}(\tau) \doteq \frac{\pi}{2}|\phi_{gg}(0)|\left(1+\frac{1}{4}\frac{|\phi_{gg}(\tau)|^2}{|\phi_{gg}(0)|^2}\right). \tag{2.73}$$

At $\tau = 0$, the approximation gives $\phi_{\alpha\alpha}(0) = 5\pi\Omega_p/8$, whereas the true value is $\phi_{\alpha\alpha}(0) = \Omega_p$. Hence, the relative error in the signal power is only 1.86%, leading us to believe that the approximation is probably very good.

The psd of the received envelope can be obtained by taking the Fourier transform of $\phi_{\alpha\alpha}(\tau)$. The psd will include a discrete spectral component at $f = 0$, due to the dc component of the received envelope. Since we are primarily interested in the continuous portion of the psd, the autocovariance function $\lambda_{\alpha\alpha}(\tau)$ is of interest, where

$$\begin{aligned}\lambda_{\alpha\alpha}(\tau) &= \mathrm{E}[\alpha(t)\alpha(t+\tau)] - \mathrm{E}[\alpha(t)]\mathrm{E}[\alpha(t+\tau)] \\ &= \frac{\pi}{2}|\phi_{gg}(0)|\left(1+\frac{1}{4}\frac{|\phi_{gg}(\tau)|^2}{|\phi_{gg}(0)|^2}\right) - \frac{\pi}{2}|\phi_{gg}(0)| \\ &= \frac{\pi}{8|\phi_{gg}(0)|}|\phi_{gg}(\tau)|^2. \end{aligned} \tag{2.74}$$

For 2-D isotropic scattering and an isotropic receiver antenna $|\phi_{gg}(\tau)|^2 = \phi^2_{g_I g_I}(\tau)$ and, therefore,

$$\lambda_{\alpha\alpha}(\tau) = \frac{\pi\Omega_p}{16}J_0^2(2\pi f_m\tau). \tag{2.75}$$

Figure 2.13 plots the normalized envelope autocovariance $\lambda_{\alpha\alpha}(\tau)/(\pi\Omega_p/16)$ against the normalized time delay $f_m\tau$ for the case of 2-D isotropic scattering, $p(\theta) = 1/(2\pi), -\pi \le \theta \le \pi$ and an isotropic receiver antenna $G(\theta) = 1$.

The Fourier transform of $\lambda_{\alpha\alpha}(\tau)$ yields the continuous portion $S^c_{\alpha\alpha}(f)$ of the envelope psd $S_{\alpha\alpha}(f)$, and can be calculated by using the identities $|\phi_{gg}(\tau)|^2 = \phi_{gg}(\tau)\phi^*_{gg}(\tau)$ and $\phi_{gg}(\tau) = \phi^*_{gg}(-\tau)$ to write

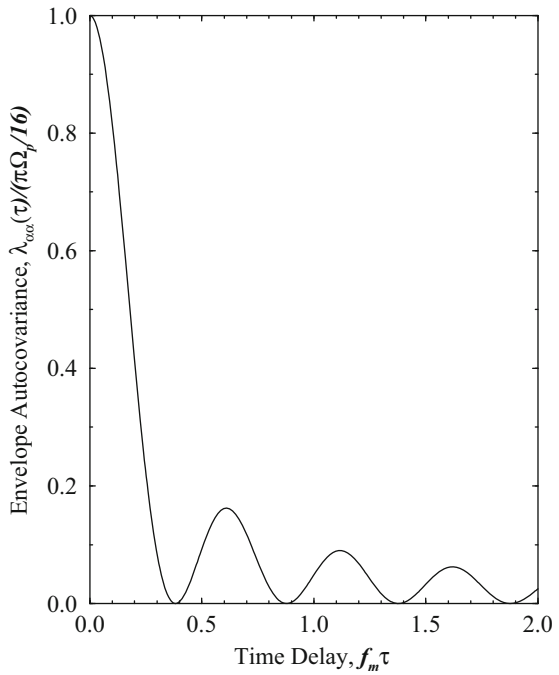

Fig. 2.13 Normalized envelope autocovariance against the normalized time delay $f_m\tau$ for a 2-D isotropic scattering with an isotropic receiver antenna

$$
\begin{aligned}
S^c_{\alpha\alpha}(f) &= \frac{\pi}{8|\phi_{gg}(0)|} S_{gg}(f) * S_{gg}(f) \\
&= \frac{\pi}{8|\phi_{gg}(0)|} \int_{-\infty}^{\infty} S_{gg}(x) S_{gg}(x-f)\mathrm{d}x \\
&= \frac{\pi}{8|\phi_{gg}(0)|} \int_{-f_m}^{f_m-|f|} S_{gg}(x) S_{gg}(x+|f|)\mathrm{d}x\,, \quad 0 \le |f| \le 2f_m.
\end{aligned}
\tag{2.76}
$$

Note that $S_{\alpha\alpha}(f)$ is always real, positive, and even. It is centered about $f = 0$ with a spectral width of $4f_m$, where f_m is the maximum Doppler frequency. To proceed further, $S_{gg}(f)$ needs to be specified. With 2-D isotropic scattering and an isotropic receiver antenna $S_{gg}(f) = S_{g_I g_I}(f)$, where $S_{g_I g_I}(f)$ is given by (2.36). The result from evaluating (2.76) is (see Problem 2.10)

$$
S^c_{\alpha\alpha}(f) = \frac{\Omega_p}{16\pi} \frac{1}{f_m} K\left(\sqrt{1 - \left(\frac{f}{2f_m}\right)^2} \right) \qquad 0 \le |f| \le 2f_m, \tag{2.77}
$$

where $K(\,\cdot\,)$ is the complete elliptic integral of the first kind, defined by

$$
K(\gamma) = \int_0^1 \frac{\mathrm{d}x}{\sqrt{(1-x^2)(1-\gamma^2 x^2)}}. \tag{2.78}
$$

The continuous portion of the normalized envelope psd $S_{\alpha\alpha}(f)/(\Omega_p/16\pi f_m)$ is plotted against the normalized frequency f/f_m in Fig. 2.14.

The psd of the received envelope $\alpha(t)$ for a non-isotropic scattering channel can be obtained using the above procedure. For example, consider the particular scattering environment shown in Fig. 2.7 with the associated Doppler spectrum in (2.49). To obtain the continuous portion of the psd of the envelope $\alpha(t)$, substitute (2.49) into (2.76) to obtain (see Problem 2.13)

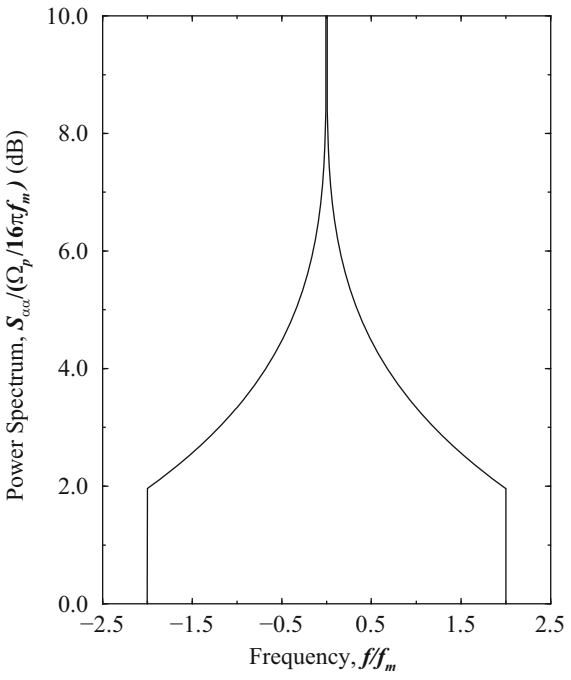

Fig. 2.14 Continuous portion of the normalized envelope psd against the normalized frequency f/f_m for a 2-D isotropic scattering channel with an isotropic receiver antenna

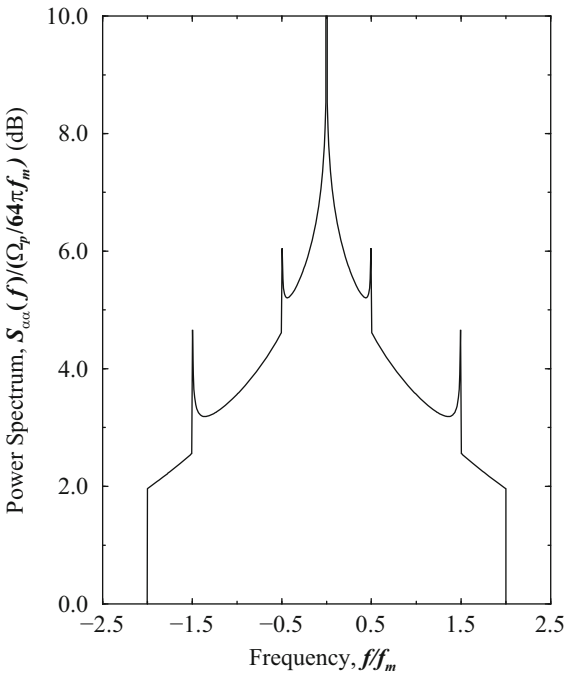

Fig. 2.15 Continuous portion of the normalized envelope psd against the normalized frequency f/f_m for the scattering environment shown in Fig. 2.7; $K = 10$ and $\theta_0 = \pi/3$

$$S^c_{\alpha\alpha}(f) = \left(\frac{1}{K+1}\right)^2 \frac{\Omega_p}{16\pi f_m} \left\{ K\left(\sqrt{1-\left(\frac{f}{2f_m}\right)^2} \right) + \frac{K\pi}{\sqrt{1-(f/f_m+\cos(\theta_0))^2}} + \frac{K\pi}{\sqrt{1-(f/f_m-\cos(\theta_0))^2}} + K^2\pi^2 f_m \delta(f) \right\}. \tag{2.79}$$

Figure 2.15 shows a plot of the continuous portion of the normalized envelope psd $S_{\alpha\alpha}(f)/(\Omega_p/(K+1)^2 16\pi f_m)$ against the normalized frequency f/f_m for $K = 10$ and $\theta_0 = \pi/3$.

2.1.4.1 Squared-Envelope Correlation and Spectrum

The autocorrelation of the squared-envelope is

$$\phi_{\alpha^2\alpha^2}(\tau) = \mathrm{E}[\alpha^2(t)\alpha^2(t+\tau)]. \tag{2.80}$$

Since $\alpha^2(t) = g_I^2(t) + g_Q^2(t)$, it follows that

$$\phi_{\alpha^2\alpha^2}(\tau) = \mathrm{E}[g_I^2(t)g_I^2(t+\tau)] + \mathrm{E}[g_Q^2(t)g_Q^2(t+\tau)] + \mathrm{E}[g_I^2(t)g_Q^2(t+\tau)] + \mathrm{E}[g_Q^2(t)g_I^2(t+\tau)]. \tag{2.81}$$

First consider the case where the propagation environment is such that $g_I(t)$ and $g_Q(t)$ have zero mean. Then the squared-envelope autocorrelation is (see Problem 2.14)

$$\begin{aligned} \phi_{\alpha^2\alpha^2}(\tau) &= 4\phi^2_{g_Ig_I}(0) + 4\phi^2_{g_Ig_I}(\tau) + 4\phi^2_{g_Ig_Q}(\tau) \\ &= 4\phi^2_{g_Ig_I}(0) + 4\left|\phi_{gg}(\tau)\right|^2. \end{aligned} \tag{2.82}$$

Finally, the squared-envelope autocovariance is

$$\begin{aligned} \lambda_{\alpha^2\alpha^2}(\tau) &= \phi_{\alpha^2\alpha^2}(\tau) - \mathrm{E}^2[\alpha^2(t)] \\ &= 4\left|\phi_{gg}(\tau)\right|^2. \end{aligned} \tag{2.83}$$

With 2-D isotropic scattering and an isotropic receiver antenna, the above expression reduces to

$$\lambda_{\alpha^2\alpha^2}(\tau) = \Omega_p^2 J_0^2(2\pi f_m \tau). \tag{2.84}$$

By comparing (2.74) and (2.83), observe that the *approximate* autocorrelation function of the envelope and the *exact* autocorrelation function of the squared-envelope are identical, except for a multiplicative constant. If the propagation environment is characterized by a specular or LoS component (e.g., Ricean fading), then $g_I(t)$ and $g_Q(t)$ have non-zero means and the autocovariance of the squared-envelope has a more complicated form. Let

$$g_I(t) = \hat{g}_I(t) + m_I(t) \tag{2.85}$$

$$g_Q(t) = \hat{g}_Q(t) + m_Q(t), \tag{2.86}$$

where $m_I(t)$ and $m_Q(t)$ are the means of $g_I(t)$ and $g_Q(t)$, respectively. From Problem 2.15,

$$\begin{aligned}\phi_{\alpha^2\alpha^2}(\tau) = 4|\phi_{\hat{g}\hat{g}}|^2(\tau) + 4\phi^2_{\hat{g}_I\hat{g}_I}(0) + 4\mathrm{Re}\left\{m(t)m^*(t+\tau)\phi_{\hat{g}\hat{g}}(\tau)\right\} \\ +2\left(|m(t)|^2 + |m(t+\tau)|^2\right)\phi_{\hat{g}_I\hat{g}_I}(0) + |m(t)|^2|m(t+\tau)|^2,\end{aligned} \tag{2.87}$$

where

$$m(t) = m_I(t) + jm_Q(t) \tag{2.88}$$

$$m(t+\tau) = m_I(t+\tau) + jm_Q(t+\tau). \tag{2.89}$$

The squared-envelope autocovariance is

$$\lambda_{\alpha^2\alpha^2}(\tau) = 4\left|\phi_{\hat{g}\hat{g}}(\tau)\right|^2 + 4\mathrm{Re}\left\{m(t)m^*(t+\tau)\phi_{\hat{g}\hat{g}}(\tau)\right\}. \tag{2.90}$$

Consider the scattering environment shown in Fig. 2.7. The corresponding correlation functions $\phi_{g_Ig_I}(\tau)$ and $\phi_{g_Ig_Q}(\tau)$ are given by (2.46) and (2.47), respectively, and the means $m_I(t)$ and $m_Q(t)$ are defined in (2.59) and (2.60). It can be shown that

$$\phi_{\hat{g}_I\hat{g}_I}(\tau) = \frac{1}{K+1}\frac{\Omega_p}{2}J_0(2\pi f_m\tau) \tag{2.91}$$

$$\phi_{\hat{g}_I\hat{g}_Q}(\tau) = 0 \tag{2.92}$$

and

$$\begin{aligned}m(t)m^*(t+\tau) &= s^2\Big(\cos(2\pi f_m\tau\cos(\theta_0)) - j\sin(2\pi f_m\tau\cos(\theta_0))\Big) \\ &= \frac{K\Omega_p}{K+1}\Big(\cos(2\pi f_m\tau\cos(\theta_0)) - j\sin(2\pi f_m\tau\cos(\theta_0))\Big),\end{aligned} \tag{2.93}$$

where K is the Rice factor and θ_0 is the angle that the specular component makes with the MS direction of motion. Using these results in (2.90) gives

$$\lambda_{\alpha^2\alpha^2}(\tau) = \left(\frac{\Omega_p}{K+1}\right)^2 J_0(2\pi f_m\tau)\Big(J_0(2\pi f_m\tau) + 2K\cos(2\pi f_m\tau\cos(\theta_0))\Big). \tag{2.94}$$

The normalized squared-envelope autocovariance is plotted in Fig. 2.16 as a function of the normalized time delay $f_m\tau$ for various values of K and θ_0.

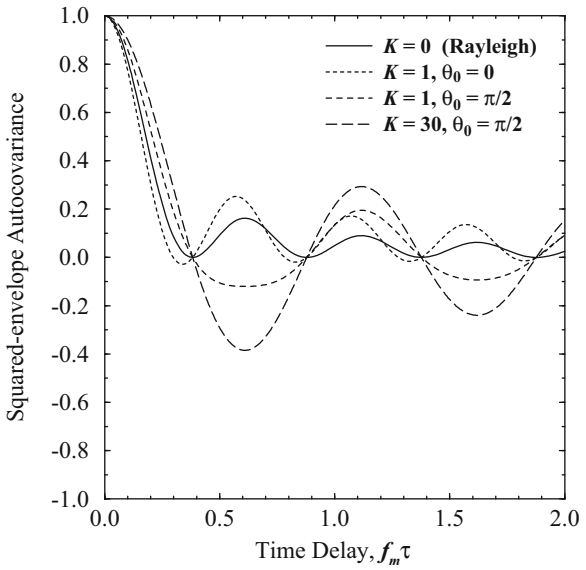

Fig. 2.16 Squared-envelope autocovariance against the normalized time delay $f_m\tau$ for the scattering environment shown in Fig. 2.7

2.1.5 Level Crossing Rate and Fade Duration

Two important second order statistics associated with envelope fading are the level crossing rate (how often the envelope crosses a specified level) and the average fade duration (how long the envelope remains on average below a specified level). Also of interest is the zero crossing rate of the real and imaginary components of the complex faded envelope. These quantities are affected not only by the scattering environment but also by the velocity of the MS.

2.1.5.1 Envelope Level Crossing Rate

The envelope level crossing rate at a specified envelope level R, L_R, is defined as the rate (in crossings per second) at which the envelope α crosses the level R in the positive (or negative) going direction. Obtaining the level crossing rate requires the joint pdf, $p(\alpha, \dot{\alpha})$, of the envelope level $\alpha = |g(t_1)|$ and the envelope slope $\dot{\alpha} = \mathrm{d}|g(t_1)|/\mathrm{d}t$ at any time instant t_1.[1] In terms of the joint pdf $p(\alpha, \dot{\alpha})$, the expected amount of time the envelope lies in the interval $(R, R + \mathrm{d}\alpha)$ for a given envelope slope $\dot{\alpha}$ and time increment $\mathrm{d}t$ is

$$p(R, \dot{\alpha})\mathrm{d}\alpha d\mathrm{d}\dot{\alpha}\mathrm{d}t. \tag{2.95}$$

The time required for the envelope α to traverse the interval $(R, R + \mathrm{d}\alpha)$ *once* for a given envelope slope $\dot{\alpha}$ is

$$\mathrm{d}\alpha/\dot{\alpha}. \tag{2.96}$$

The ratio of these two quantities is the expected number of crossings of the envelope α within the interval $(R, R + \mathrm{d}\alpha)$ for a given envelope slope $\dot{\alpha}$ and time increment $\mathrm{d}t$, viz.

$$\dot{\alpha}p(R, \dot{\alpha})\mathrm{d}\dot{\alpha}\mathrm{d}t. \tag{2.97}$$

The expected number of crossings of the envelope level R for a given envelope slope $\dot{\alpha}$ in a time interval of duration T is

$$\int_0^T \dot{\alpha}p(R, \dot{\alpha})\mathrm{d}\dot{\alpha}\mathrm{d}t = \dot{\alpha}p(R, \dot{\alpha})\mathrm{d}\dot{\alpha}T. \tag{2.98}$$

[1] For simplicity of notation, the time variable is suppressed as $\alpha \equiv \alpha(t_1)$ and $\dot{\alpha} \equiv \dot{\alpha}(t_1)$.

The expected number of crossings of the envelope level R with a positive slope in the time interval T is

$$N_R = T\int_0^\infty \dot{\alpha} p(R,\dot{\alpha})\mathrm{d}\dot{\alpha}. \tag{2.99}$$

Finally, the expected number of crossings per second of the envelope level R, or the level crossing rate, is

$$L_R = \int_0^\infty \dot{\alpha} p(R,\dot{\alpha})\mathrm{d}\dot{\alpha}. \tag{2.100}$$

This is actually a general result that applies to any random process characterized by the joint pdf $p(\alpha,\dot{\alpha})$.

Rice has derived the joint pdf $p(\alpha,\dot{\alpha})$ for a sine wave in bandpass Gaussian noise [283]. A Ricean fading channel similarly consists of LoS or specular (sine wave) component plus a scatter (Gaussian noise) component. For the case of a Ricean fading channel,

$$p(\alpha,\dot{\alpha}) = \frac{\alpha(2\pi)^{-3/2}}{\sqrt{Bb_0}}\int_{-\pi}^{\pi}\exp\left\{-\frac{1}{2Bb_0}\left[B\left(\alpha^2 - 2\alpha s\cos(\theta)+s^2\right)+\left(b_0\dot{\alpha}+b_1 s\sin(\theta)\right)^2\right]\right\}\mathrm{d}\theta \tag{2.101}$$

where s is the non-centrality parameter in the Rice distribution, and $B = b_0b_2 - b_1^2$, and where b_0, b_1, and b_2 are constants that are derived from the power spectrum of the scatter component. For the scattering environment described by (2.45) and Fig. 2.7, the sine wave corresponds to the specular component arriving at angle θ_0, while the Gaussian noise is due to the scatter component with azimuth distribution $\hat{p}(\theta) = 1/(2\pi), -\pi \le \theta \le \pi$. Note that the joint pdf derived by Rice in (2.101) is general enough to apply to scattering environments described by other $\hat{p}(\theta)$ as well.

Suppose that the specular or LoS component of the complex envelope $g(t)$ has a Doppler frequency equal $f_q = f_m\cos(\theta_0)$, where $0 \le |f_q| \le f_m$. In this case [283]

$$b_n = (2\pi)^n\int_{-f_m}^{f_m} S_{gg}^c(f)(f-f_q)^n\mathrm{d}f \tag{2.102}$$

$$= (2\pi)^n b_0\int_0^{2\pi}\hat{p}(\theta)G(\theta)\left(f_m\cos(\theta)-f_q\right)^n\mathrm{d}\theta, \tag{2.103}$$

where $\hat{p}(\theta)$ is the azimuth distribution of the *scatter* component, $G(\theta)$ is the antenna gain pattern, and $S_{gg}^c(f)$ is the corresponding continuous portion of the Doppler power spectrum. Equivalence between (2.102) and (2.103) can be established by using (2.42). Note that $S_{gg}^c(f)$ is given by the Fourier transform of

$$\phi_{gg}^c(\tau) = \phi_{g_Ig_I}^c(\tau) - j\phi_{g_Ig_Q}^c(\tau), \tag{2.104}$$

where

$$\phi_{g_Ig_I}^c(\tau) = \frac{\Omega_p}{2}\int_0^{2\pi}\cos(2\pi f_m\tau\cos(\theta))\hat{p}(\theta)G(\theta)\mathrm{d}\theta \tag{2.105}$$

$$\phi_{g_Ig_Q}^c(\tau) = \frac{\Omega_p}{2}\int_0^{2\pi}\sin(2\pi f_m\tau\cos(\theta))\hat{p}(\theta)G(\theta)\mathrm{d}\theta. \tag{2.106}$$

In some special cases, the psd $S_{gg}^c(f)$ is symmetrical about the frequency $f_q = f_m\cos(\theta_0)$. This condition occurs, for example, when $f_q = 0$ ($\theta_0 = 90°$), $\hat{p}(\theta) = 1/(2\pi), -\pi \le \theta \le \pi$, and $G(\theta) = 1$. In this case, $b_n = 0$ for all odd values of n (and in particular $b_1 = 0$) so that (2.101) reduces to the convenient product form

$$p(\alpha,\dot{\alpha}) = \sqrt{\frac{1}{2\pi b_2}}\exp\left\{-\frac{\dot{\alpha}^2}{2b_2}\right\}\cdot\frac{\alpha}{b_0}\exp\left\{-\frac{(\alpha^2+s^2)}{2b_0}\right\}I_0\left(\frac{\alpha s}{b_0}\right)$$

$$= p(\dot{\alpha})\cdot p(\alpha). \tag{2.107}$$

Since $p(\alpha, \dot{\alpha}) = p(\dot{\alpha}) \cdot p(\alpha)$ in (2.107), it follows that α and $\dot{\alpha}$ are statistically independent. When $f_q = 0$ and $\hat{p}(\theta) = 1/(2\pi)$, a closed form expression can be obtained for the envelope level crossing rate. Substituting (2.44) into (2.102) gives

$$b_n = \begin{cases} b_0 (2\pi f_m)^n \frac{1 \cdot 3 \cdot 5 \cdots (n-1)}{2 \cdot 4 \cdot 6 \cdots n} & n \text{ even} \\ 0 & n \text{ odd} \end{cases}. \tag{2.108}$$

Therefore, $b_1 = 0$ and $b_2 = b_0 (2\pi f_m)^2/2$. By substituting the joint density in (2.107) into (2.100) and using the expression for b_0 in (2.61), the envelope level crossing rate is obtained as

$$L_R = \sqrt{2\pi(K+1)} f_m \rho \mathrm{e}^{-K-(K+1)\rho^2} I_0 \left(2\rho \sqrt{K(K+1)} \right), \tag{2.109}$$

where

$$\rho = \frac{R}{\sqrt{\Omega_p}} = \frac{R}{R_{\text{rms}}} \tag{2.110}$$

and $R_{\text{rms}} \triangleq \sqrt{\mathrm{E}[\alpha^2]}$ is the rms envelope level. Under the further condition that $K = 0$ (Rayleigh fading), the above expression simplifies to

$$L_R = \sqrt{2\pi} f_m \rho \mathrm{e}^{-\rho^2}. \tag{2.111}$$

Notice that the level crossing rate is directly proportional to the maximum Doppler frequency f_m and, hence, the MS speed $v = f_m \lambda_c$. The normalized level crossing rate L_R/f_m in (2.109) is plotted in Fig. 2.17 as a function of ρ and K.

2.1.5.2 Zero Crossing Rate

Recall that received complex envelope $g(t) = g_I(t) + g_Q(t)$ is a complex Gaussian random process. If the channel is characterized by a specular or LoS component, then $g_I(t)$ and $g_Q(t)$ have mean values $m_I(t)$ and $m_Q(t)$, respectively. Of interest, is the zero crossing rate of the zero-mean Gaussian random processes $\hat{g}_I(t) = g_I(t) - m_I(t)$ and $\hat{g}_Q(t) = g_Q(t) - m_Q(t)$. Rice [283] has derived this zero crossing rate as

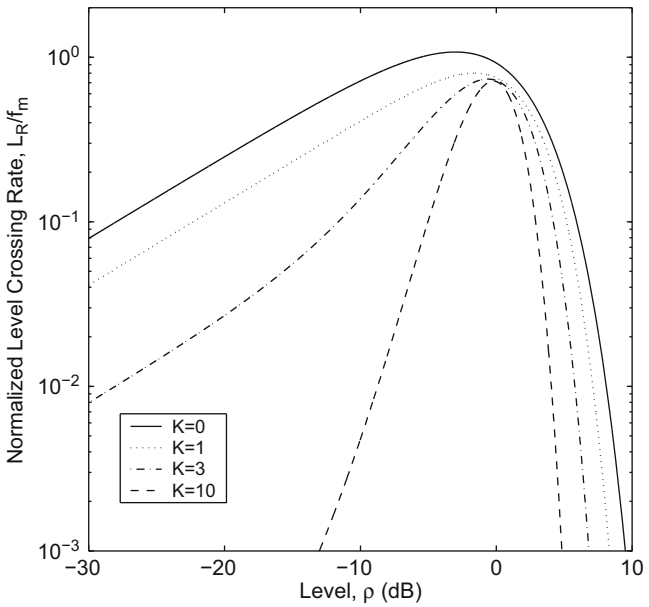

Fig. 2.17 Normalized level crossing rate for the scattering environment shown in Fig. 2.7 with $\theta_0 = 90°$

$$L_Z = \frac{1}{\pi}\sqrt{\frac{b_2}{b_0}}. \tag{2.112}$$

When the scatter component has the azimuth distribution $\hat{p}(\theta) = 1/(2\pi), -\pi \le \theta \le \pi$, the zero crossing rate is

$$L_Z = \sqrt{2} f_m. \tag{2.113}$$

Similar to the level crossing rate, the zero crossing rate is directly proportional to the maximum Doppler frequency f_m.

2.1.5.3 Average Fade Duration

Another quantity of interest is the average duration that the envelope remains below a specified level R. Although the pdf of the envelope fade duration is unknown, the average fade duration can be calculated. Consider a very long time interval of length T and let t_i be the duration of the ith fade below the level R. The probability that the received envelope is less than R is

$$\mathrm{P}[\alpha \le R] = \frac{1}{T}\sum_i t_i. \tag{2.114}$$

The average fade duration is equal to

$$\bar{t} = \frac{\sum_i t_i}{TL_R} = \frac{\mathrm{P}[\alpha \le R]}{L_R}. \tag{2.115}$$

If the envelope is Ricean distributed as in (2.62), then

$$\mathrm{P}(\alpha \le R) = \int_0^R p(\alpha)\mathrm{d}\alpha \;=\; 1 - Q\left(\sqrt{2K}, \sqrt{2(K+1)\rho^2}\right), \tag{2.116}$$

where $Q(a, b)$ is the Marcum Q function. Moreover, if it is again assumed that $f_q = 0$ and $\hat{p}(\theta) = 1/(2\pi)$, then

$$\bar{t} \;=\; \frac{1 - Q\left(\sqrt{2K}, \sqrt{2(K+1)\rho^2}\right)}{\sqrt{2\pi(K+1)} f_m \rho \mathrm{e}^{-K-(K+1)\rho^2} I_0\left(2\rho\sqrt{K(K+1)}\right)}. \tag{2.117}$$

If $K = 0$ (Rayleigh fading), then

$$\mathrm{P}[\alpha \le R] = \int_0^R p(\alpha)\mathrm{d}\alpha \;=\; 1 - \mathrm{e}^{-\rho^2} \tag{2.118}$$

and

$$\bar{t} \;=\; \frac{\mathrm{e}^{\rho^2} - 1}{\rho f_m \sqrt{2\pi}}. \tag{2.119}$$

The normalized average fade duration $\bar{t} f_m$ in (2.117) is plotted in Fig. 2.18 as a function of ρ.

The level crossing rate, zero crossing rate, and average fade duration all depend on the velocity of the MS, since $f_m = v/\lambda_c$. Very deep fades tend to occur infrequently and do not last very long. For example, at 60 mi/hr and 900 MHz, the maximum Doppler frequency is $f_m = 80$ Hz. Therefore, with 2-D isotropic scattering and Rayleigh fading ($K = 0$) there are $L_R = 74$ fades/s at $\rho = 0$ dB with an average fade duration of 8.5 ms. However, at $\rho = -20$ dB there are only 20 fades/s with an average fade duration of 0.5 ms. Note that since ρ represents a normalized envelope (magnitude) level, $\rho_{(\mathrm{dB})} = 20\log_{10}\rho$. Also observe from Fig. 2.17 that for small $\rho_{(\mathrm{dB})}$, the level crossing rate decreases with an increasing Rice factor K. Furthermore, from Fig. 2.18, for small $\rho_{(\mathrm{dB})}$ the average fade duration increases with increasing K. Hence, as K increases the fades occur less frequently, but last longer when they do occur.

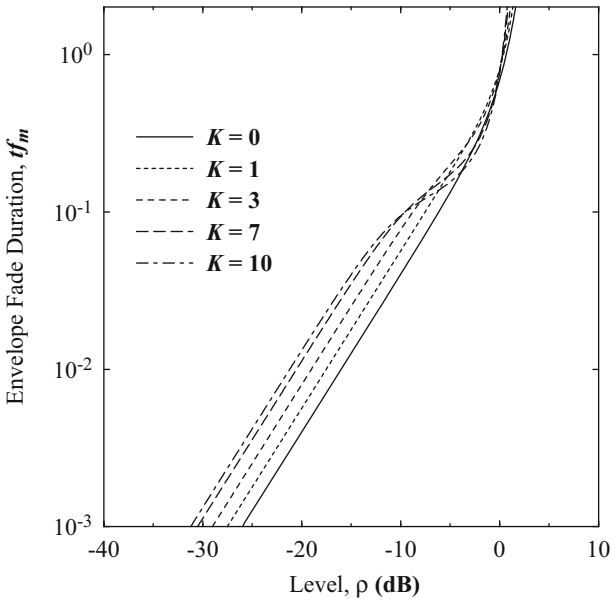

Fig. 2.18 Normalized average fade duration for the scattering environment shown in Fig. 2.7 with $\theta_0 = 90°$

2.1.6 Space-Time Correlation

Many mobile radio systems employ receiver antenna diversity, where spatially separated receiver antennas are used to provide multiple faded replicas of the same information bearing signal. In order for such diversity systems to provide the maximum diversity gain, it is desirable that the multiple faded replicas experience uncorrelated fading. The spatial correlation characteristics are needed for determining the required spatial separation between antenna elements so that they are sufficiently decorrelated. Moreover, it is sometimes desirable to simultaneously characterize both the spatial and temporal channel correlation characteristics. For this purpose, the space-time correlation function is useful. To obtain the space-time correlation functions, it is necessary to specify the scattering geometry. One possibility for NLoS conditions is the single-ring model shown in Fig. 2.19, where the BS and MS are located at O_B and O_M, respectively, and separated by distance D, and the scatterers are assumed to be located on a ring of radius R centered around the MS. Very often, a local scattering assumption is made such that $D \gg R$, in order to simplify and obtain closed for expressions for the various space-time correlation functions. For short distances between the transmitter and receiver, or large scattering radii, the local scattering assumption is not applicable.

2.1.6.1 Space-Time Correlation at the Mobile Station

Consider two MS antennas, $A_M^{(q)}, q = 1, 2$, separated by distance δ_M. The MS antenna array is oriented with angle θ_M with respect to the x-axis, and the MS moves with velocity v and angle γ_M with respect to the x-axis. For the environment shown in Fig. 2.19, the channel from O_B to $A_M^{(q)}$ has the complex envelope

$$g_q(t) = \sum_{n=1}^{N} C_n e^{j\phi_n - j2\pi(\epsilon_n + \epsilon_{nq})/\lambda_c} e^{j2\pi f_m t \cos(\alpha_M^{(n)} - \gamma_M)}, \quad q = 1, 2, \tag{2.120}$$

where ϵ_n and ϵ_{nq} denote the distances $O_B - S_n$ and $S_M^{(n)} - A_M^{(q)}$, $q = 1, 2$, respectively. From the law of cosines, the distances ϵ_n and ϵ_{nq} can be expressed as a function of the angle-of-arrival $\alpha_M^{(n)}$ as follows:

$$\epsilon_n^2 = D^2 + R^2 + 2DR\cos(\alpha_M^{(n)}) \tag{2.121}$$

$$\epsilon_{nq}^2 = ((1.5 - q)\delta_M)^2 + R^2 - 2(1.5 - q)\delta_M R\cos(\alpha_M^{(n)} - \theta_M), \quad q = 1, 2. \tag{2.122}$$

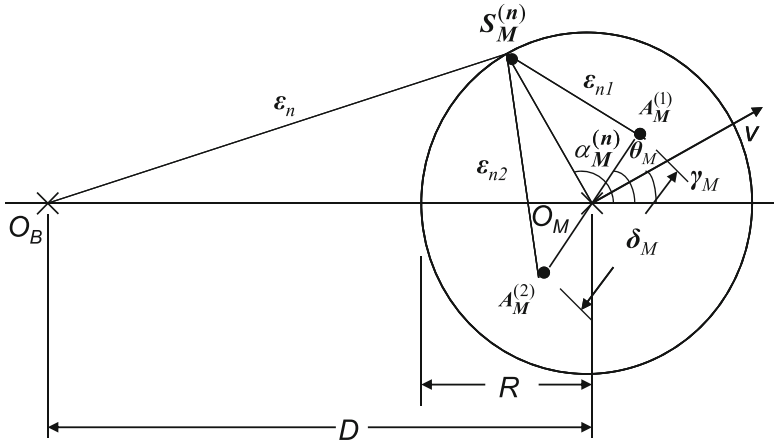

Fig. 2.19 Single-ring scattering model for NLoS propagation on the forward link of a cellular system. The MS is surrounded by a scattering ring of radius R and is at distance D from the BS, where $R \ll D$

Assuming that $R/D \ll 1$, $\delta_M \ll R$ and using the approximation $\sqrt{1 \pm x} \approx 1 \pm x/2$ for small x, gives

$$\epsilon_n \approx D + R\cos(\alpha_M^{(n)}) \tag{2.123}$$

$$\epsilon_{nq} \approx R - (1.5 - q)\delta_M \cos(\alpha_M^{(n)} - \theta_M)\ ,\ q = 1, 2. \tag{2.124}$$

Substituting (2.123) and (2.124) into (2.120) gives

$$g_q(t) = \sum_{n=1}^{N} C_n e^{j\phi_n - j2\pi\left(D + R\cos\alpha_M^{(n)} + R - (1.5-q)\delta_M\cos(\alpha_M^{(n)} - \theta_M)\right)/\lambda_c + j2\pi f_m t\cos(\alpha_M^{(n)} - \gamma_M)}\ ,\ q = 1, 2. \tag{2.125}$$

The space-time correlation function between the two complex faded envelopes $g_1(t)$ and $g_2(t)$ is

$$\phi_{g_1,g_2}(\delta_M, \tau) = \frac{1}{2}\mathrm{E}\left[g_1^*(t)g_2(t+\tau)\right]. \tag{2.126}$$

Using (2.125) and (2.126), the space-time correlation function between $g_1(t)$ and $g_2(t)$ can be written as

$$\phi_{g_1,g_2}(\delta_M, \tau) = \frac{\Omega_p}{2N}\sum_{n=1}^{N}\mathrm{E}\left[e^{-j2\pi(\delta_M/\lambda_c)\cos(\alpha_M^{(n)} - \theta_M) + j2\pi f_m \tau\cos(\alpha_M^{(n)} - \gamma_M)}\right]. \tag{2.127}$$

Since the number of scatters is infinite, the discrete angles-of-arrival $\alpha_M^{(n)}$ can be replaced with a continuous random variable α_M with probability density function $p(\alpha_M)$. Hence, the space-time correlation function becomes

$$\phi_{g_1,g_2}(\delta_M, \tau) = \frac{\Omega_p}{2}\int_0^{2\pi} e^{-jb\cos(\alpha_M - \theta_M)}e^{ja\cos(\alpha_M - \gamma_M)}p(\alpha_M)\mathrm{d}\alpha_M, \tag{2.128}$$

where $a = 2\pi f_m\tau$ and $b = 2\pi\delta_M/\lambda_c$.

For the case of 2-D isotropic scattering with isotropic MS antenna, $p(\alpha_M) = 1/(2\pi)$, $-\pi \le \alpha_M \le \pi$, and the space-time correlation function becomes

$$\phi_{g_1,g_2}(\delta_M, \tau) = \frac{\Omega_p}{2}J_0\left(\sqrt{a^2 + b^2 - 2ab\cos(\theta_M - \gamma_M)}\right). \tag{2.129}$$

The spatial and temporal correlation functions can be obtained by setting $\tau = 0$ and and $\delta_M = 0$, respectively. This gives $\phi_{g_1,g_2}(\delta_M) = \phi_{g_1,g_2}(\delta_M, 0) = \frac{\Omega_p}{2}J_0(2\pi\delta_M/\lambda_c)$ and $\phi_{gg}(\tau) = \phi_{g_1,g_2}(0, \tau) = \frac{\Omega_p}{2}J_0(2\pi f_m\tau)$, which matches our earlier result

in (2.29) as expected. For the case of 2-D isotropic scattering and an isotropic MS antenna, it follows that Fig. 2.13 also plots the normalized envelope spatial autocovariance function $\lambda_{\alpha\alpha}(\ell)/(\pi\Omega_p/16)$ against the normalized spatial separation $f_m\tau = \delta_M/\lambda_c$. The spatial autocovariance function is zero at $\delta_M/\lambda_c = 0.38$ and is less than 0.3 for $\delta_M/\lambda_c > 0.38$. The implication is that, under conditions of 2-D isotropic scattering and isotropic MS antennas, sufficient spatial decorrelation can be obtained by spacing the MS antenna elements roughly a half-wavelength apart.

2.1.6.2 Space-Time Correlation at the Base Station

Radio channels are reciprocal in the sense that if a propagation path exists, it will carry energy equally well in either the uplink or downlink directions. That is, the plane waves in either direction will propagate by exactly the same set of scatterers. Therefore, the temporal autocorrelation functions and Doppler spectra are expected to be the same for both the uplink and downlink directions. However, for cellular land mobile radio applications, most of the scatters are in the vicinity of the MS, while the BS antennas are elevated and free of local scatters. Consequently, the plane waves will arrive at the BS antennas with a narrow angle-of-arrival spread, whereas they arrive with a large angle-of-arrival spread at the MS. This will cause significant differences in the spatial correlation properties of the uplink and downlink. It will be shown that a much larger spatial distance is required to obtain a given degree of spatial decorrelation at the BS as compared to the MS.

To obtain the space-time correlation functions, it is once again necessary to specify the scattering geometry. One possibility for NLoS conditions is the single-ring model shown in Fig. 2.20, where the MS and BS are located at O_M and O_B, respectively, and separated by distance D, and the scatterers are assumed to be located on a ring of radius R centered around the MS. Once again, a local scattering assumption is often made such that $D \gg R$.

Consider two BS antennas, $A_B^{(q)}, q = 1, 2$, separated by distance δ_B. The BS antenna array is oriented with angle θ_B with respect to the x-axis, and the MS moves with velocity v and angle γ_M with respect to the x-axis. For the environment shown in Fig. 2.20, the channel from O_M to $A_B^{(q)}$ has the complex envelope

$$g_q(t) = \sum_{m=1}^{N} C_m e^{j\phi_m - j2\pi(R+\epsilon_{mq})/\lambda_c} e^{j2\pi f_m t\cos(\alpha_M^{(m)} - \gamma_M)},\ q = 1, 2, \tag{2.130}$$

where ϵ_{mq} denotes the distance $S_M^{(m)} - A_B^{(q)}, q = 1, 2$. To proceed further, ϵ_{mq} needs to be expressed as a function of $\alpha_M^{(m)}$.

Applying the cosine law to the triangle $\triangle S_M^{(m)} O_B A_B^{(q)}$, the distance ϵ_{mq} can be expressed as a function of the angle $\theta_B^{(m)} - \theta_B$ as follows:

$$\epsilon_{mq}^2 = ((1.5 - q)\delta_B)^2 + \epsilon_m^2 - 2(1.5 - q)\delta_B\epsilon_m\cos(\theta_B^{(m)} - \theta_B)\ , q = 1, 2, \tag{2.131}$$

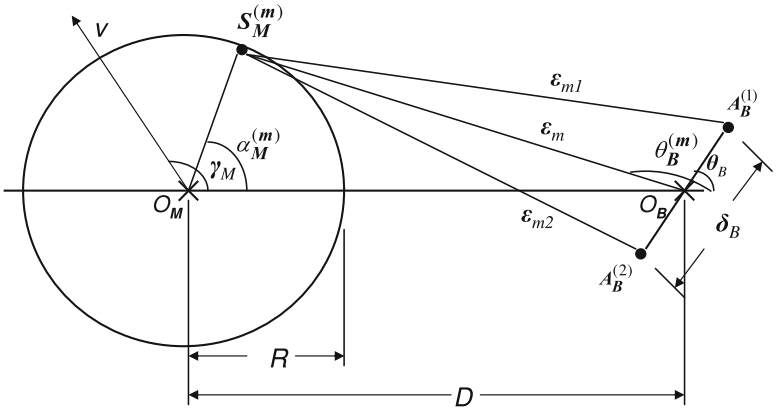

Fig. 2.20 Single-ring scattering model for NLoS propagation on the reverse link of a cellular system. The MS is surrounded by a scattering ring of radius R and is at distance D from the BS, where $R \ll D$

where ϵ_m is the distance $S_M^{(m)} - O_B$. By applying the sine law to the triangle $\triangle O_M S_M^{(m)} O_B$, the following identity is obtained

$$\frac{\epsilon_m}{\sin(\alpha_M^{(m)})} = \frac{R}{\sin\left(\pi - \theta_B^{(m)}\right)} = \frac{D}{\sin\left(\pi - \alpha_M^{(m)} - \left(\pi - \theta_B^{(m)}\right)\right)}. \tag{2.132}$$

Since the angle $\pi - \theta_B^{(m)}$ is small, the small angle approximations $\sin x \approx x$ and $\cos x \approx 1$ for small x can be applied to the second equality in the above identity. This gives

$$\frac{R}{(\pi - \theta_B^{(m)})} \approx \frac{D}{\sin\left(\pi - \alpha_M^{(m)}\right)} \tag{2.133}$$

or

$$(\pi - \theta_B^{(m)}) \approx (R/D)\sin(\pi - \alpha_M^{(m)}). \tag{2.134}$$

It follows that the cosine term in (2.131) becomes

$$\begin{aligned}
\cos(\theta_B^{(m)} - \theta_B) &= \cos(\pi - \theta_B - (\pi - \theta_B^{(m)})) \\
&= \cos(\pi - \theta_B)\cos(\pi - \theta_B^{(m)}) + \sin(\pi - \theta_B)\sin(\pi - \theta_B^{(m)}) \\
&\approx \cos(\pi - \theta_B) + \sin(\pi - \theta_B)(R/D)\sin(\pi - \alpha_M^{(m)}) \\
&= -\cos(\theta_B) + (R/D)\sin(\theta_B)\sin(\alpha_M^{(m)}).
\end{aligned} \tag{2.135}$$

Substituting the approximation in (2.135) into (2.131), along with $\delta_B/\epsilon_m \ll 1$, gives

$$\epsilon_{mq}^2 \approx \epsilon_m^2 \left(1 - 2(1.5 - q)\frac{\delta_B}{\epsilon_m}\left((R/D)\sin(\theta_B)\sin(\alpha_M^{(m)}) - \cos(\theta_B)\right)\right). \tag{2.136}$$

Applying the approximation $\sqrt{1 \pm x} \approx 1 \pm x/2$ for small x gives

$$\epsilon_{mq} \approx \epsilon_m - (1.5 - q)\delta_B\left((R/D)\sin(\theta_B)\sin(\alpha_M^{(m)}) - \cos(\theta_B)\right). \tag{2.137}$$

Applying the cosine law to the triangle $\triangle O_M S_M^{(m)} O_B$ gives

$$\begin{aligned}
\epsilon_m^2 &= D^2 + R^2 - 2DR\cos(\alpha_M^{(m)}) \\
&\approx D^2\left(1 - 2(R/D)\cos(\alpha_M^{(m)})\right),
\end{aligned} \tag{2.138}$$

and again using the approximation $\sqrt{1 \pm x} \approx 1 \pm x/2$ for small x gives

$$\epsilon_m \approx D - R\cos(\alpha_M^{(m)}). \tag{2.139}$$

Finally, using (2.139) in (2.131) gives

$$\epsilon_{mq} \approx D - R\cos(\alpha_M^{(m)}) - (1.5 - q)\delta_B\left((R/D)\sin(\theta_B)\sin(\alpha_M^{(m)}) - \cos(\theta_B)\right). \tag{2.140}$$

Substituting (2.140) into (2.130) gives the result

$$g_q(t) = \sum_{m=1}^{N} C_m e^{j\phi_m + j2\pi f_m t\cos(\alpha_M^{(m)} - \gamma_M) - j2\pi\left(R + D - R\cos(\alpha_M^{(m)}) - (1.5-q)\delta_B\left((R/D)\sin(\theta_B)\sin(\alpha_M^{(m)}) - \cos(\theta_B)\right)\right)/\lambda_c}, \tag{2.141}$$

which is a function of the azimuth angle of departure $\alpha_M^{(m)}$.

The space-time correlation function between the two complex faded envelopes $g_1(t)$ and $g_2(t)$ at the BS is once again given by (2.126). Using (2.141) and (2.126), the space-time correlation function between $g_1(t)$ and $g_2(t)$ can be written as

$$\phi_{g_1,g_2}(\delta_B,\tau) = \frac{\Omega_p}{2N}\sum_{m=1}^{N} \mathrm{E}\left[\mathrm{e}^{-j2\pi(\delta_B/\lambda_c)\left((R/D)\sin(\theta_B)\sin(\alpha_M^{(m)})-\cos(\theta_B)\right)+j2\pi f_m\tau\cos(\alpha_M^{(m)}-\gamma_M)}\right]. \tag{2.142}$$

Since the number of scatters around the MS is infinite, the discrete angles-of-arrival $\alpha_M^{(m)}$ can be replaced with a continuous random variable α_M with probability density function $p(\alpha_M)$. Hence, the space-time correlation function becomes

$$\phi_{g_1,g_2}(\delta_B,\tau) = \frac{\Omega_p}{2}\int_{-\pi}^{\pi} \mathrm{e}^{ja\cos(\alpha_M-\gamma_M)}\mathrm{e}^{-jb((R/D)\sin(\theta_B)\sin(\alpha_M)-\cos(\theta_B))}p(\alpha_M)d\alpha_M, \tag{2.143}$$

where $a = 2\pi f_m\tau$ and $b = 2\pi\delta_B/\lambda_c$.

For the case of 2-D isotropic scattering with an isotropic MS transmit antenna, $p(\alpha_M) = 1/(2\pi), -\pi \le \alpha_M \le \pi$, and the space-time correlation function becomes

$$\phi_{g_1,g_2}(\delta_B,\tau) = \frac{\Omega_p}{2}\mathrm{e}^{jb\cos(\theta_B)}J_0\left(\sqrt{a^2+b^2(R/D)^2\sin^2(\theta_B)-2ab(R/D)\sin(\theta_B)\sin(\gamma_M)}\right). \tag{2.144}$$

The spatial and temporal correlation functions can be obtained by setting $\tau = 0$ and and $\delta_B = 0$, respectively. For the temporal correlation function $\phi_{gg}(\tau) = \phi_{g_1,g_2}(0,\tau) = \frac{\Omega_p}{2}J_0(2\pi f_m\tau)$ which matches our earlier result in (2.29) as expected. The spatial correlation function is

$$\phi_{g_1,g_2}(\delta_B) = \phi_{g_1,g_2}(\delta_B,0) = \frac{\Omega_p}{2}\mathrm{e}^{jb\cos(\theta_B)}J_0\Big(b(R/D)\sin(\theta_B)\Big). \tag{2.145}$$

Figure 2.21 plots the magnitude of the normalized spatial envelope crosscovariance function, $|\phi_{g_1,g_2}(\delta_B)|/(\Omega_p/2)$, for $R = 60\,\mathrm{m}$ and various BS array orientation angles θ_B. Likewise, Fig. 2.22 plots $|\phi_{g_1,g_2}(\delta_B)|/(\Omega_p/2)$ for $\theta_B = \pi/3$ and various scattering radii, R. In general, a much greater spatial separation is required to achieve a given degree of envelope decorrelation at the BS as compared to the MS. This can be readily seen by the term $R/D \ll 1$ in the argument of the Bessel function in (2.145). Also, the spatial correlation increases as the angle θ_B and scattering radii R decrease. BS antenna arrays that are broadside with the MS direction will experience the lowest correlation, while those that are in-line with the MS direction will experience the highest correlation. In fact, for in-line BS antennas $|\phi_{g_1,g_2}(\delta_B)| = 1$ and, therefore, the faded envelopes on the different BS antennas are perfectly correlated.

2.2 Mobile-to-Mobile Channels

Mobile-to-mobile (M-to-M) communication channels arise when both the transmitter and receiver are in motion and are equipped with low elevation antennas that are surrounded by local scatterers. The statistical properties of M-to-M channels differ significantly from those of conventional fixed-to-mobile (F-to-M) cellular land mobile radio channels, where the mobile station is surrounded by local scatterers and the base station is stationary, elevated, and relatively free of local scattering. Akki and Haber [13, 14] were the first to propose a mathematical reference model for M-to-M flat fading channels under NLoS propagation conditions. The Akki and Haber model was extended by Vatalaro and Forcella [329] to account for 3-D scattering, and by Linnartz and Fiesta [209] to include LoS propagation conditions. Channel measurements for outdoor-to-outdoor, narrow-band outdoor-to-indoor, and wide-band mobile-to-mobile communications have been reported in [9, 182, 188, 222], and methods for simulating M-to-M channels have been proposed in [259, 345, 371].

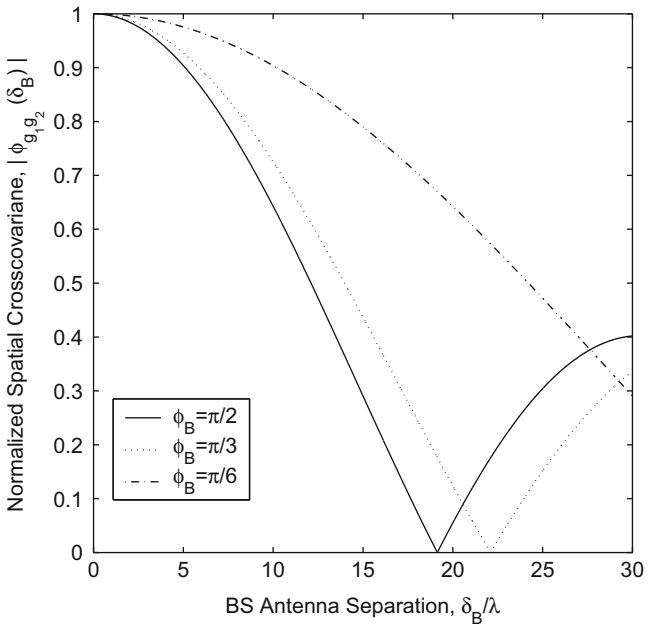

Fig. 2.21 Envelope cross-correlation magnitude at the base station for $R = 60$ m and various arrival angles, θ_B; $D = 3000$ m

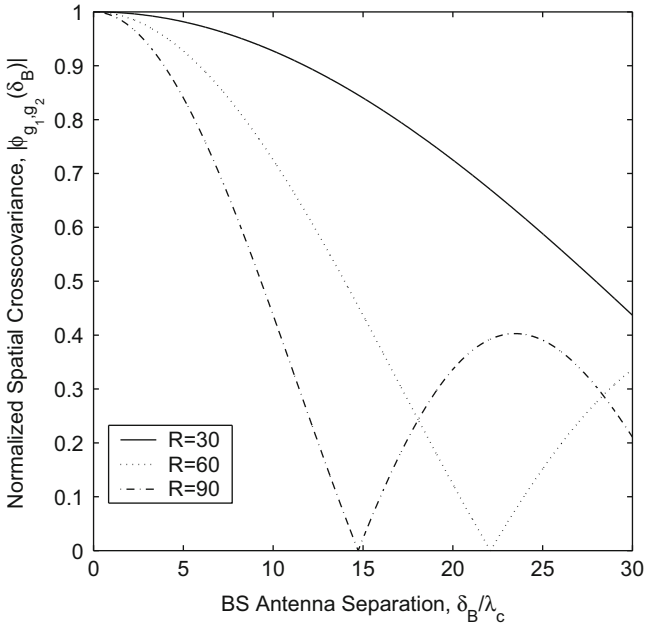

Fig. 2.22 Envelope cross-correlation magnitude at the base station for $\theta_B = \pi/3$ and various scattering radii, R; $D = 3000$ m

2.2.1 Mobile-to-Mobile Reference Model

Akki and Haber's mathematical reference model for M-to-M flat fading channels gives the complex faded envelope as [14]

$$g(t) = \sqrt{\frac{1}{N}} \sum_{n=1}^{N} e^{j2\pi \left(f_m^T \cos(\alpha_T^{(n)}) + f_m^R \cos(\alpha_R^{(n)}) \right) t + j\phi_n}, \tag{2.146}$$

where N is the number of propagation paths; f_m^T and f_m^R are the maximum Doppler frequencies due to the motion of the transmitter and receiver, respectively; $\alpha_T^{(n)}$ is the random angle of departure and $\alpha_R^{(n)}$ is the random angle of arrival of the nth propagation path measured with respect to the transmitter and receiver velocity vectors, respectively; ϕ_n is a random phase uniformly distributed on $[-\pi, \pi)$ independent of $\alpha_T^{(n)}$ and $\alpha_R^{(n)}$ for all n.

In the above model, the Doppler frequency experienced by each propagation path is the sum of the individual Doppler frequencies induced by the motion of the transmitter and receiver. Once again, for sufficiently large N, the central limit theorem can be invoked with the result that $g_I(t)$ and $g_Q(t)$ can be treated as zero-mean Gaussian random processes. If isotropic transmitter and receiver antennas and 2-D isotropic scattering around both the transmitter and receiver are assumed, then the envelope $|g(t)|$ is Rayleigh distributed at any time t. This is similar to the case of conventional F-to-M cellular land mobile radio channels with 2-D isotropic scattering and an isotropic antenna at the MS. However, the ensemble averaged temporal correlation function of the faded envelope of M-to-M channels is quite different from that of F-to-M channels, and can be derived as follows [13, 14]:

$$\begin{aligned}
\phi_{g_I g_I}(\tau) &= \frac{1}{2} J_0(2\pi f_m^T \tau) J_0(2\pi a f_m^T \tau) \\
\phi_{g_Q g_Q}(\tau) &= \frac{1}{2} J_0(2\pi f_m^T \tau) J_0(2\pi a f_m^T \tau) \\
\phi_{g_I g_Q}(\tau) &= \phi_{g_Q g_I}(\tau) = 0 \\
\phi_{gg}(\tau) &= \frac{1}{2} J_0(2\pi f_m^T \tau) J_0(2\pi a f_m^T \tau),
\end{aligned} \tag{2.147}$$

where $a = f_m^R / f_m^T$ is the ratio of the two maximum Doppler frequencies (or speeds) of the receiver and transmitter, and $0 \le a \le 1$ assuming $f_m^R \le f_m^T$. Observe that the temporal correlation functions of M-to-M channels involve a product of two Bessel functions in contrast to the single Bessel function found in F-to-M channels. Also, $a = 0$ yields the temporal correlation functions for F-to-M channels as expected. The corresponding Doppler spectrum, obtained by taking the Fourier transform of (2.147) is

$$S_{gg}(f) = \frac{1}{\pi^2 f_m^T \sqrt{a}} K\left(\frac{1+a}{2\sqrt{a}} \sqrt{1 - \left(\frac{f}{(1+a) f_m^T} \right)^2} \right), \tag{2.148}$$

where $K(\cdot)$ is the complete elliptic integral of the first kind. The Doppler spectrum of M-to-M channels in (2.148) differs from the classical spectrum of F-to-M cellular land mobile radio channels, as illustrated in Fig. 2.23, which shows the Doppler spectrum for different values of a.

2.3 Statistical Characterization of Multipath-Fading Channels

Multipath-fading channels can be modeled as randomly time-variant linear filters, whose inputs and outputs can be described in both the time and frequency domains. This leads to four possible transmission functions [35]; the time-variant impulse response $g(\tau, t)$, the output Doppler-spread function $H(f, \nu)$, the time-variant transfer function $T(f, t)$, and the delay Doppler-spread function $S(\tau, \nu)$. The time-variant impulse response relates the complex low-pass input and output time waveforms, $\tilde{s}(t)$ and $\tilde{r}(t)$, respectively, through the convolution integral

$$\tilde{r}(t) = \int_0^t g(t, \tau) \tilde{s}(t - \tau) \mathrm{d}\tau. \tag{2.149}$$

In physical terms, $g(t, \tau)$ can be interpreted as the channel response at time t due to an impulse applied at time $t - \tau$. Since a physical channel is causal, $g(t, \tau) = 0$ for $\tau < 0$ and, therefore, the lower limit of integration in (2.149) is zero. If the convolution in (2.149) is approximated as a discrete sum, then

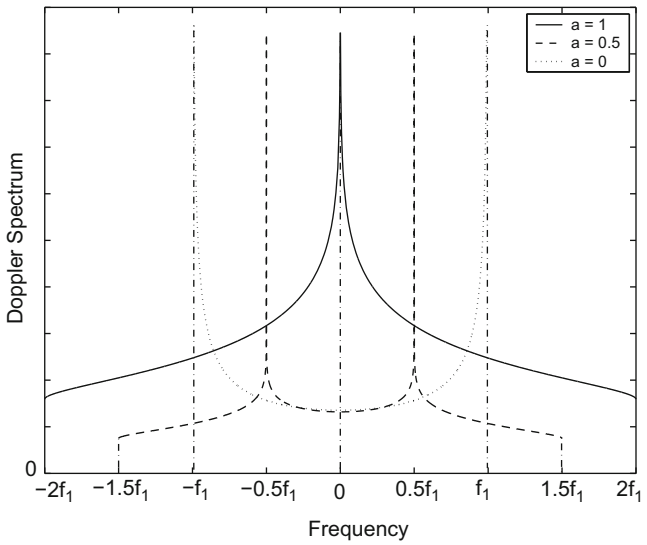

Fig. 2.23 Doppler spectrum for M-to-M and F-to-M channels

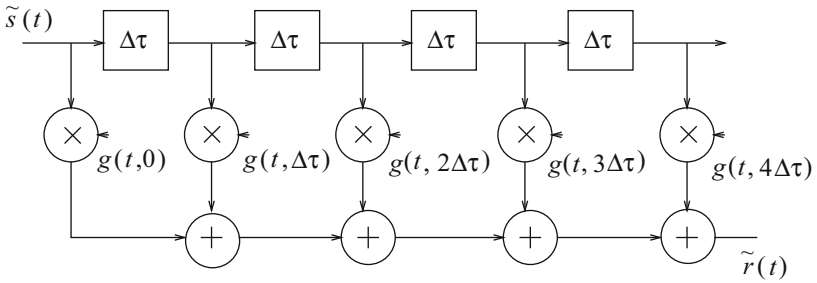

Fig. 2.24 Discrete-time tapped delay line model for a multipath-fading channel

$$\tilde{r}(t) = \sum_{m=0}^{n} g(t, m\Delta\tau)\tilde{s}(t - m\Delta\tau)\Delta\tau. \tag{2.150}$$

This representation allows us to visualize the channel as a transversal filter with tap spacing $\Delta\tau$ and time-varying tap gains $g(t, m\Delta\tau)$ as shown in Fig. 2.24.

The second transmission function relates the input and output spectra, $\tilde{S}(f)$ and $\tilde{R}(f)$, respectively, through the integral equation

$$\tilde{R}(f) = \int_{-\infty}^{\infty} H(f - \nu, \nu)\tilde{S}(f - \nu)\mathrm{d}\nu. \tag{2.151}$$

Bello called the function $H(f, \nu)$ the output Doppler-spread function [35]. This function explicitly shows the effect of Doppler shift or spectral broadening on the output spectrum. In physical terms, the frequency-shift variable ν can be interpreted as the Doppler shift that is introduced by the channel. Once again, the integral in (2.151) can be approximated by the discrete sum

$$\tilde{R}(f) = \sum_{m=1}^{n} H(f - m\Delta\nu, m\Delta\nu)\tilde{S}(f - m\Delta\nu)\Delta\nu. \tag{2.152}$$

This allows the channel to be represented by a bank of filters with transfer functions $H(f, m\Delta\nu)\Delta\nu$ followed by a dense frequency conversion chain with tap spacing $\Delta\nu$ that produces the Doppler shifts as shown in Fig. 2.25.

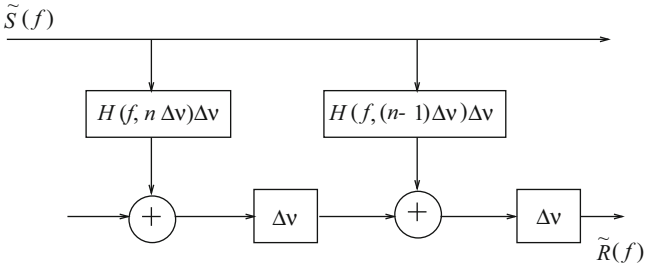

Fig. 2.25 Frequency conversion model for a multipath-fading channel

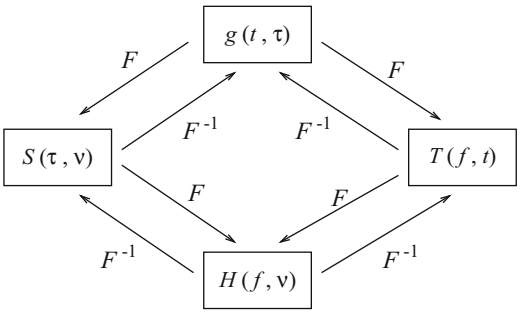

Fig. 2.26 Fourier transform relations between the transmission functions

The third transmission function $T(f, t)$ is the time-variant transfer function, which relates the output time waveform to the input spectrum as follows:

$$\tilde{r}(t) = \int_{-\infty}^{\infty} \tilde{S}(f) T(f, t) e^{j2\pi ft} df. \tag{2.153}$$

The final description relates the input and output time waveforms through the double integral

$$\tilde{r}(t) = \int_{-\infty}^{\infty} \int_{-\infty}^{\infty} S(\tau, \nu) \tilde{s}(t - \tau) e^{j2\pi f\tau} d\nu d\tau. \tag{2.154}$$

The function $S(\tau, \nu)$ is called the delay Doppler-spread function [35], and provides a measure of the scattering amplitude of the channel in terms of the time delay τ and Doppler frequency ν.

The four transmission functions are related to each other through Fourier transform pairs as shown in Fig. 2.26. In each Fourier transform pair there is always a fixed variable, so that the transform involves the other two variables.

2.3.1 Statistical Channel Correlation Functions

Similar to flat fading channels, the channel impulse response $g(t, \tau) = g_I(t, \tau) + jg_Q(t, \tau)$ of a frequency-selective fading channel can be modeled as a complex Gaussian random process, where the quadrature components $g_I(t, \tau)$ and $g_Q(t, \tau)$ are real Gaussian random processes. Hence, all of the transmission functions defined in the last section are themselves random processes. Since the underlying process is Gaussian, a complete statistical description of these transmission functions is provided by their means and autocorrelation functions. In the following discussion, zero-mean Gaussian random processes are assumed for simplicity so that only the autocorrelation functions are of interest. Since there are four transmission functions, four autocorrelation functions can be defined as follows [255, 272]:

$$\phi_g(t, s; \tau, \eta) = \mathrm{E}[g^*(t, \tau) g(s, \eta)] \tag{2.155}$$

$$\phi_T(f, m; t, s) = \mathrm{E}[T^*(f, t) T(m, s)] \tag{2.156}$$

$$\phi_H(f, m; \nu, \mu) = \mathrm{E}[H^*(f, \nu) H(m, \mu)] \tag{2.157}$$

$$\phi_S(\tau, \eta; \nu, \mu) = \mathrm{E}[S^*(\tau, \nu) S(\eta, \mu)]. \tag{2.158}$$

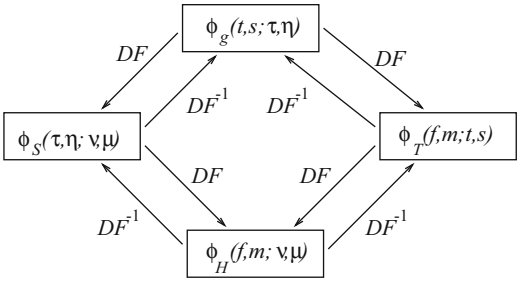

Fig. 2.27 Double Fourier transform relations between the channel autocorrelation functions

These autocorrelation functions are related to each other through double Fourier transform pairs. For example,

$$\phi_S(\tau,\eta;\nu,\mu) = \int_{-\infty}^{\infty}\int_{-\infty}^{\infty} \phi_g(t,s;\tau,\eta)\mathrm{e}^{-j2\pi(\nu t-\mu s)}\mathrm{d}t\mathrm{d}s \tag{2.159}$$

$$\phi_g(t,s;\tau,\eta) = \int_{-\infty}^{\infty}\int_{-\infty}^{\infty} \phi_S(\tau,\eta;\nu,\mu)\mathrm{e}^{j2\pi(\nu t-\mu s)}\mathrm{d}\nu\mathrm{d}\mu. \tag{2.160}$$

The complete set of such relationships is summarized in Fig. 2.27.

2.3.2 *Classification of Channels*

Wide-sense stationary (WSS) channels have fading statistics that remain constant over small periods of time or short spatial distances. This implies that the channel correlation functions depend on the time variables t and s only through the time difference $\Delta_t = s - t$. It can be demonstrated (see Problem 2.23) that WSS channels give rise to scattering with uncorrelated Doppler shifts. This behavior suggests that the attenuations and phase shifts associated with multipath components having different Doppler shifts are uncorrelated. This makes sense, because multipath components with different Doppler shifts arrive from different directions and, hence, propagate via different sets of scatterers. For WSS channels the correlation functions become

$$\phi_g(t,t+\Delta_t;\tau,\eta) = \phi_g(\Delta_t;\tau,\eta) \tag{2.161}$$

$$\phi_T(f,m;t,t+\Delta_t) = \phi_T(f,m;\Delta_t) \tag{2.162}$$

$$\phi_H(f,m;\nu,\mu) = \psi_H(f,m;\nu)\delta(\nu-\mu) \tag{2.163}$$

$$\phi_S(\tau,\eta;\nu,\mu) = \psi_S(\tau,\eta;\nu)\delta(\nu-\mu), \tag{2.164}$$

where

$$\psi_H(f,m;\nu) = \int_{-\infty}^{\infty} \phi_T(f,m;\Delta_t)\mathrm{e}^{-j2\pi\nu\Delta_t}\mathrm{d}\Delta_t \tag{2.165}$$

$$\psi_S(\tau,\eta;\nu) = \int_{-\infty}^{\infty} \phi_g(\Delta_t;\tau,\eta)\mathrm{e}^{-j2\pi\nu\Delta_t}\mathrm{d}\Delta_t \tag{2.166}$$

are Fourier transform pairs.

Uncorrelated scattering (US) channels are characterized by paths of different delays having uncorrelated complex gains. Bello showed that US channels are wide-sense stationary in the frequency variable so that the correlation functions depend on the frequency variables f and m only through the frequency difference $\Delta f = m - f$ [35]. Analogous to (2.163) and (2.164), the channel correlation functions are singular in the time-delay variable (see Problem 2.24). Again, this makes sense because multipath components arriving with different delays propagate via different sets of scatterers. For US channels, the channel correlation functions become

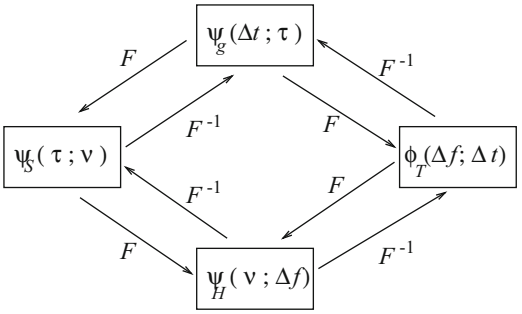

Fig. 2.28 Fourier transform relations between the channel correlation functions for WSSUS channels

$$\phi_g(t,s;\tau,\eta) = \psi_g(t,s;\tau)\delta(\eta-\tau) \tag{2.167}$$

$$\phi_T(f,f+\Delta_f;t,s) = \phi_T(\Delta_f;t,s) \tag{2.168}$$

$$\phi_H(f,f+\Delta_f;\nu,\mu) = \phi_H(\Delta_f;\nu,\mu) \tag{2.169}$$

$$\phi_S(\tau,\eta;\nu,\mu) = \psi_S(\tau;\nu,\mu)\delta(\eta-\tau), \tag{2.170}$$

where

$$\psi_g(t,s;\tau) = \int_{-\infty}^{\infty} \phi_T(\Delta_f;t,s)\mathrm{e}^{j2\pi\Delta_f\tau}\mathrm{d}\Delta_f \tag{2.171}$$

$$\psi_S(\tau;\nu,\mu) = \int_{-\infty}^{\infty} \phi_H(\Delta_f;\nu,\mu)\mathrm{e}^{j2\pi\Delta_f\tau}\mathrm{d}\Delta_f \tag{2.172}$$

are Fourier transform pairs.

Wide-sense stationary uncorrelated scattering (WSSUS) channels exhibit uncorrelated scattering in both the time-delay and Doppler shift domains. Fortunately, many radio channels can be effectively modeled as WSSUS channels. For WSSUS channels, the correlation functions have singular behavior in both the time delay and Doppler shift variables, and reduce to the following simple forms:

$$\phi_g(t,t+\Delta_t;\tau,\eta) = \psi_g(\Delta_t;\tau)\delta(\eta-\tau) \tag{2.173}$$

$$\phi_T(f,f+\Delta_f;t,t+\Delta_t) = \phi_T(\Delta_f;\Delta_t) \tag{2.174}$$

$$\phi_H(f,f+\Delta_f;\nu,\mu) = \psi_H(\Delta_f;\nu)\delta(\nu-\mu) \tag{2.175}$$

$$\phi_S(\tau,\eta;\nu,\mu) = \psi_S(\tau,\nu)\delta(\eta-\tau)\delta(\nu-\mu). \tag{2.176}$$

The correlation functions for WSSUS channels are related through the Fourier transform pairs shown in Fig. 2.28.

2.3.3 *Power-Delay Profile and Coherence Bandwidth*

The function $\psi_g(0;\tau) \equiv \psi_g(\tau)$ is called the power-delay profile and gives the average power at the channel output as a function of the time delay τ. A typical power-delay profile is shown in Fig. 2.29. One quantity of interest is the average delay, defined as

$$\mu_\tau = \frac{\int_0^\infty \tau\psi_g(\tau)\mathrm{d}\tau}{\int_0^\infty \psi_g(\tau)\mathrm{d}\tau}. \tag{2.177}$$

Note that the normalization $\int_0^\infty \psi_g(\tau)\mathrm{d}\tau$ is applied because $\psi_g(\tau)$ does not necessarily integrate to unity like a probability density function. Another quantity of interest is the rms delay spread, defined as

$$\sigma_\tau = \sqrt{\frac{\int_0^\infty (\tau-\mu_\tau)^2\psi_g(\tau)\mathrm{d}\tau}{\int_0^\infty \psi_g(\tau)\mathrm{d}\tau}}. \tag{2.178}$$

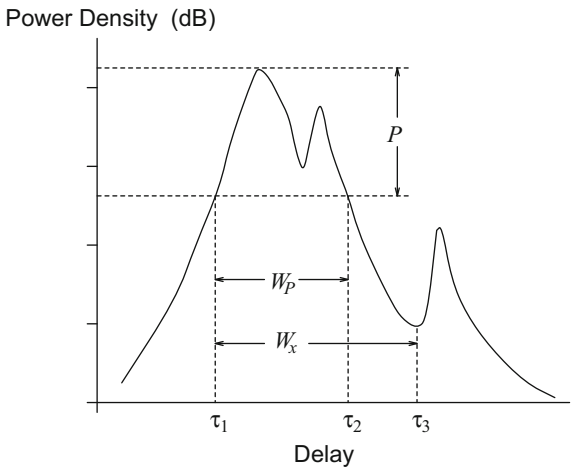

Fig. 2.29 A typical power-delay profile

There are other quantities that can also be used to describe the power-delay profile. One is the width, W_x, of the middle portion of the power-delay profile that contains a fraction x of the total power in the profile. Referring to Fig. 2.29

$$W_x = \tau_3 - \tau_1 \tag{2.179}$$

where τ_1 and τ_3 are chosen so that

$$\int_0^{\tau_1} \psi_g(\tau)\mathrm{d}\tau = \int_{\tau_3}^{\infty} \psi_g(\tau)\mathrm{d}\tau \tag{2.180}$$

and

$$\int_{\tau_1}^{\tau_3} \psi_g(\tau)\mathrm{d}\tau = x\int_0^{\infty} \psi_g(\tau)\mathrm{d}\tau. \tag{2.181}$$

Another quantity is the difference in delays where the power-delay profile rises to a value P dB below its maximum value for the first time and where the power-delay profile drops to a value P dB below its maximum value for the last time. This quantity is denoted by W_P and is also illustrated in Fig. 2.29, where $W_P = \tau_2 - \tau_1$. In general, the average delay and delay spread of the channel will diminish with decreasing cell size, the reason being that the radio path lengths are shorter. While the delay spread in a typical macrocellular application may be on the order of 1–10 μs, the delay spreads in a typical microcellular applications are much less. Delay spreads for indoor channels can range anywhere from 30 to 60 ns in buildings with interior walls and little metal, to 300 ns in buildings with open plans and a significant amount of metal.

The function $\phi_T(\Delta_t; \Delta_f)$ is called the spaced-time spaced-frequency correlation function. The function $\phi_T(0; \Delta_f) \equiv \phi_T(\Delta_f)$ measures the frequency correlation of the channel. The coherence bandwidth, B_c, of the channel is defined as the smallest value of Δ_f for which $\phi_T(\Delta_f) = x\phi_T(0)$ for some suitably small value of $x, 0 < x < 1$. As a result of the Fourier transform relation between $\phi_g(\tau)$ and $\phi_T(\Delta_f)$, the reciprocal of either the average delay or the delay spread is a measure of the coherence bandwidth of the channel i.e.,

$$B_c \propto \frac{1}{\mu_\tau} \quad \text{or} \quad B_c \propto \frac{1}{\sigma_\tau}. \tag{2.182}$$

Wideband fading channels can be classified according to the relationship between the transmitted signal bandwidth W_s and the coherence bandwidth B_c. If $B_c < W_s$, the channel is said to exhibit frequency-selective fading which introduces intersymbol interference (ISI) into the received signal. If $B_c \gg W_s$, the channel is said to exhibit flat fading, and very little ISI is introduced into the received signal.

The function $\psi_H(\nu; 0) \equiv \psi_H(\nu)$ is identical to the Doppler spectrum $S_{gg}(f)$ in (2.30), i.e., $\psi_H(\nu) \equiv S_{gg}(f)$, and gives the average power at the channel output as a function of the Doppler frequency ν. The range of values over which $\psi_H(\nu)$ is significant is called the Doppler spread and is denoted by B_d. Since $\psi_H(\nu)$ and $\phi_T(\Delta_t)$ are a Fourier transform pair, it follows that the inverse of the Doppler spread gives a measure of the channel coherence time, T_c, i.e.,

$$T_c \approx \frac{1}{B_d}. \tag{2.183}$$

Wideband fading channels can also be classified according to the relationship between the transmitted symbol duration, T, and the coherence time T_c. If $T_c < T$, the channel is said to exhibit fast fading which introduces severe frequency dispersion into the received signal. If $T_c \gg T$, the channel is said to exhibit slow fading which introduces very little frequency dispersion into the received signal.

Finally, the function $\psi_S(\tau, \nu)$ is called the scattering function and gives the average power output of the channel as a function of the time delay τ and the Doppler shift ν. Plots of the scattering function are often used to provide a concise statistical description of a multipath-fading channel from measurement data.

2.3.4 System Correlation Functions

The astute reader may wonder why the factor of 1/2 does not appear in the definition of the channel correlation functions in (2.158). The multipath-fading channel can be treated as a time-variant linear filter, such that the complex envelopes of the channel input and output are related through the convolution integral in (2.149). By using (2.149), the autocorrelation functions of the output waveform $\tilde{r}(t)$ and of the input waveform $\tilde{s}(t)$ can be related. Assuming that the channel is WSSUS, the time autocorrelation function of the channel output $\tilde{r}(t)$ is

$$\begin{aligned}
\phi_{\tilde{r}\tilde{r}}(t, t+\Delta_t) &= \frac{1}{2}\mathrm{E}\left[\tilde{r}^*(t)\tilde{r}(t+\Delta_t)\right] \\
&= \frac{1}{2}\mathrm{E}\left[\int_0^t g^*(t,\alpha)\tilde{s}^*(t-\alpha)\mathrm{d}\alpha \times \int_0^{t+\Delta_t} g(t+\Delta_t,\beta)\tilde{s}(t+\Delta_t-\beta)\mathrm{d}\beta\right] \\
&= \int_0^t \int_0^{t+\Delta_t} \mathrm{E}\left[g^*(t,\alpha)g(t+\Delta_t,\beta)\right]\frac{1}{2}\mathrm{E}\left[\tilde{s}^*(t-\alpha)\tilde{s}(t+\Delta_t-\beta)\right]\mathrm{d}\alpha\mathrm{d}\beta \\
&= \int_0^t \int_0^{t+\Delta_t} \psi_g(\Delta_t;\alpha)\delta(\beta-\alpha)\frac{1}{2}\mathrm{E}\left[\tilde{s}^*(t-\alpha)\tilde{s}(t+\Delta_t-\beta)\right]\mathrm{d}\alpha\mathrm{d}\beta \\
&= \int_0^t \psi_g(\Delta_t;\alpha)\frac{1}{2}\mathrm{E}\left[\tilde{s}^*(t-\alpha)\tilde{s}(t+\Delta_t-\alpha)\right]\mathrm{d}\alpha \\
&= \int_0^t \psi_g(\Delta_t;\alpha)\phi_{\tilde{s}\tilde{s}}(t-\alpha, t-\alpha+\Delta_t)\mathrm{d}\alpha \\
&= \psi_g(\Delta_t;t) * \phi_{\tilde{s}\tilde{s}}(t, t+\Delta_t)
\end{aligned} \tag{2.184}$$

where

$$\phi_{\tilde{s}\tilde{s}}(t, t+\Delta_t) = \frac{1}{2}\mathrm{E}\left[\tilde{s}^*(t)\tilde{s}(t+\Delta_t)\right].$$

Thus, the output autocorrelation function is the convolution of the channel correlation function $\psi_g(\Delta_t; t)$ and the correlation function of the input waveform. Note that the factor of 1/2 in the definition of $\phi_{\tilde{r}\tilde{r}}(t, t+\Delta_t)$ is absorbed into the similar definition of $\phi_{\tilde{s}\tilde{s}}(t, t+\Delta_t)$. Consequently, a factor of 1/2 does not appear in the definition of the channel (or system) correlation functions in (2.158). For digital modulation, the input waveform $\tilde{s}(t)$ is a cyclostationary random process as described in Sect. 4.9.1 and, hence, the channel output waveform will be cyclostationary as well.

2.4 Polarized Channel Modeling

Multi-polarized antennas have attracted considerable attention as a means for increasing channel capacity and reducing the required antenna spacing through the principle of polarization diversity [19, 184, 191, 198, 245, 299, 330]. Such antennas exploit channel depolarization and have the potential to double or even triple the channel capacity that is achievable with single-polarized antennas [19, 110, 111, 245, 299, 306]. In practice, cellular land mobile radio systems have employed slant polarized array antennas at the base stations to good benefit.

Depolarization can occur as a result of two factors. One factor arises from the transmit and receive antennas themselves. Any practical antenna gain pattern can be described in terms of two orthogonal antenna polarization functions. For a vertically polarized antenna these polarization functions are f^a_{VV} and f^a_{HV}, while for a horizontally polarized antenna they are f^a_{HH} and f^a_{VH}, where H and V refer to horizontal and vertical polarization, respectively. For an ideal linear vertically or horizontally polarized antenna only f^a_{VV} or f^a_{HH} is non-zero, respectively. However, for practical antennas, the cross-polarization functions f^a_{VH} and f^a_{HV} will be non-zero as well due to antenna depolarization.

The other factor causing depolarization is the radio channel propagation environment. Similar to antenna depolarization, the radio channel can be characterized in terms of four orthogonal channel polarization functions identified as f_{VV}, f_{HV}, f_{VH}, and f_{HH}, where again H and V refer to horizontal and vertical polarization, respectively. The antenna and channel depolarization can be decoupled, and in order to isolate the effects of channel depolarization, ideal linear polarized antennas are assumed.

The degree of depolarization is often measured in terms of the cross polarization discrimination (XPD), defined as the ratio of the co-polarized average received power to the cross-polarized average received power. For a vertically polarized transmit antenna the XPD can be defined as

$$\text{XPD} = \frac{\text{E}[f^2_{VV}]}{\text{E}[f^2_{HV}]}. \tag{2.185}$$

In conventional XPD modeling, it is assumed that $\text{E}[f^2_{VV}] = \text{E}[f^2_{HH}] = 1 - \zeta$, and $\text{E}[f^2_{HV}] = \text{E}[f^2_{VH}] = \zeta$, resulting in

$$\text{XPD} = \frac{1-\zeta}{\zeta}, \tag{2.186}$$

where ζ is a parameter that having the range $0 \leq \zeta \leq 1$. Such a model ensures a conservation of power or energy, where the total received power is split between the co-polarized and cross-polarized components. When $\zeta = 0$, only the co-polarized component exists and $\text{XPD} = \infty$, and when $\zeta = 1$, only the cross-polarized component exists and $\text{XPD} = 0$. The polarized channel is conventionally treated as a 2×2 MIMO channel, such that

$$\mathbf{G} = \mathbf{Z} \otimes \mathbf{G}_{\text{iid}} \tag{2.187}$$

where $\mathbf{G}_{\text{iid}}$ is a 2×2 matrix of zero-mean complex i.i.d. Gaussian random variables,

$$\mathbf{Z} = \begin{bmatrix} \sqrt{1-\zeta} & \sqrt{\zeta} \\ \sqrt{\zeta} & \sqrt{1-\zeta} \end{bmatrix}, \tag{2.188}$$

and $\otimes$ denotes the Hamadard product or Schur product (element-by-element matrix multiplication).

Despite its simplicity, the conventional model for XPD provides little insight into the mechanisms of channel depolarization and how the parameter ζ behaves. Typically, a value or ranges of values for ζ are merely assumed. The remainder of this section considers a geometrical theoretical model for channel depolarization in wireless fixed-to-mobile channels, characterized by isotropic or non-isotropic azimuthal scattering and with either non-line-of-sight (NLoS) or line-of-sight (LoS) conditions between the transmitter and receiver. Predictions from the model are compared with previously reported measurement data [110, 191, 306] and shown to have close agreement. Finally, the theoretical geometry-based XPD model is used to explain the origin of some phenomena observed in these empirical results.

2.4.1 Geometric Model for Channel Depolarization

Consider the 3-D cylindrical model shown in Fig. 2.30, where scatterers are distributed on a cylindrical surface in the vicinity of the mobile station.[2] These scatterers result in single-bounced propagation between a BS and a MS. The high-elevation BS antenna is assumed to be free of local scattering, which is typical of cellular land mobile radio systems. A LoS component may or may not exist between the BS and MS. The cylindrical scattering surface is characterized by its radius R_r, and the

[2]Here the term "scatterer" refers to a plane boundary that is typically much larger than a wavelength.

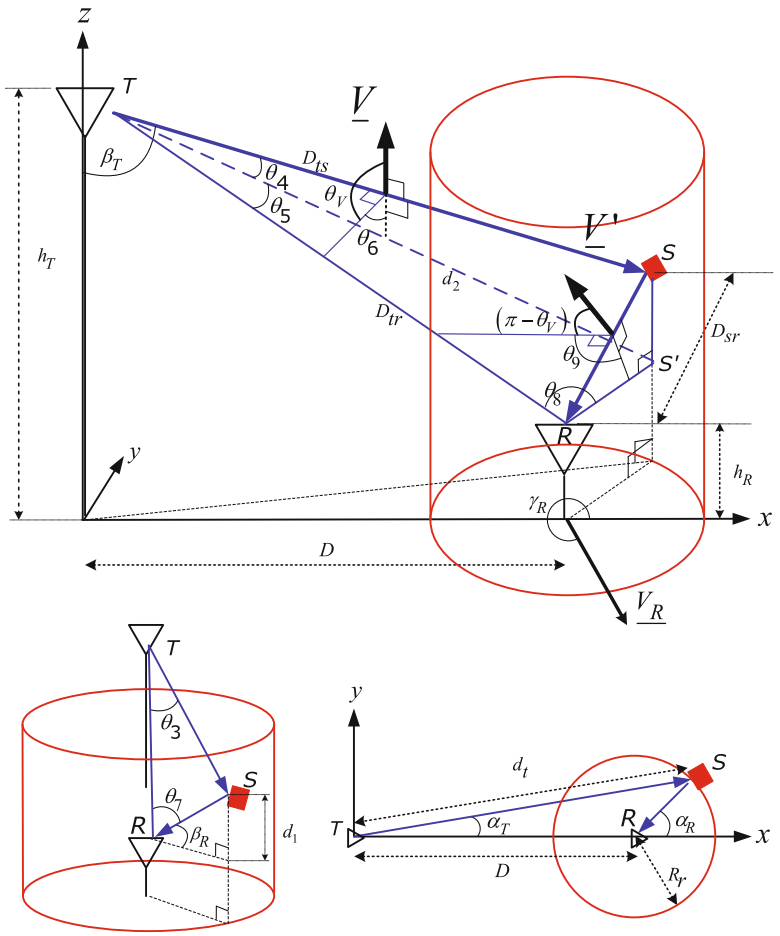

Fig. 2.30 3-D cylindrical scattering model for fixed-to-mobile channels

ray incident on the MS antenna from each scatterer on the cylinder has an associated azimuth angle of arrival (AAoA), α_R, and elevation angle of arrival (EAoA), β_R. As will be explained later, a 3-D scattering model is necessary to explain the mechanism of channel depolarization.

The phenomenon of channel depolarization between a MS and MS can be explained by the NLoS plane waves that arrive at the MS via scattering objects. Figure 2.30 presents a scenario where a vertically polarized plane wave emitted from the BS can result in a horizontally polarized plane wave component being received at the MS. The vector $\underline{V}$ in Fig. 2.30 is the vertical polarization vector of a plane wave from the BS, and $\underline{V}$' is the corresponding polarization vector of the plane wave after reflection from a scatterer. By convention the vertical and horizontal polarization vectors are parallel to $\underline{e}_\theta$ and $\underline{e}_\phi$, respectively, when describing the plane wave's direction of propagation at the BS or MS in a spherical coordinate system. It is clear that $\underline{V}$' is not entirely vertically polarized at the MS, but has a cross-polarization component as well.

Channel depolarization is affected by the scattering geometry as illustrated in Fig. 2.30. For the plane wave that is emitted from the BS and received at the MS via a scatterer, the plane that is defined by the BS, MS, and the scatterer must be taken into account. The left side of Fig. 2.31 depicts one such plane (corresponding to the page in this book). The circled dot and arrow represent the vectors of the perpendicular and parallel polarization components associated with the plane, whose directions are from the backside to the front side of the figure and the arrow's direction, respectively [59]. If each scatterer is modeled as a planar boundary, then the directions of the vectors of the perpendicular and parallel polarization components as viewed from the BS and MS will be the same within the plane. Since any polarization vector can be expressed as a linear combination of the perpendicular and parallel polarization component vectors, as shown in the right side of Fig. 2.31, the polarization angle viewed at the BS will be same as that observed at the MS [59]. For this reason, each BS-scatterer-MS plane in Figs. 2.30 and 2.31 is called a *conservation-of-polarization plane* (CoP-plane).

The polarization angle associated with a CoP-plane, denoted by θ_V in Fig. 2.30, is defined as the angle between $\underline{V}$ and the line that includes the projection of $\underline{V}$ onto the CoP plane. Due to the conservation of polarization principle, the angle between

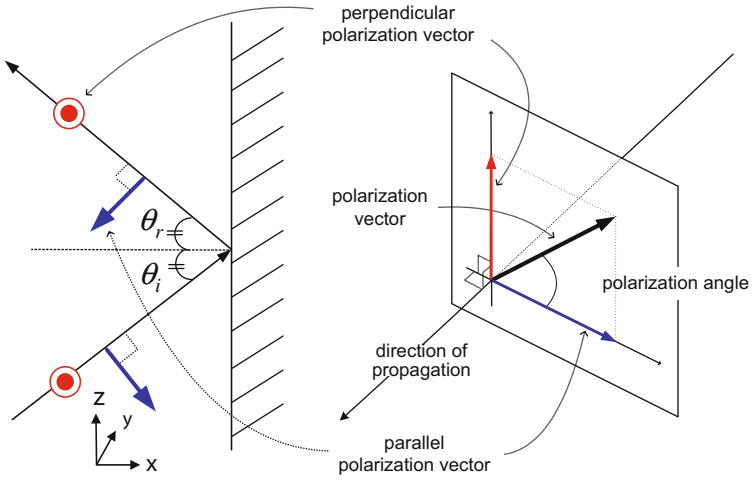

Fig. 2.31 Conservation of polarization (CoP) plane and polarization angle

$\underline{V}$' and the line that includes the projection of $\underline{V}$' onto the same CoP plane in Fig. 2.30 is equal to $\pi - \theta_V$ [59]. Thus, by using the polarization angle with respect to the CoP-plane, the polarization vector, $\underline{V}$' or $\underline{H}$' on its CoP-plane can be decomposed into vertical and horizontal polarization components with respect to the plane wave's direction of propagation at the MS.

Consider a vertically polarized plane wave from the BS, and let A_{VV} (A_{HV}) be the amplitude of the received plane wave at a vertically (horizontally) polarized MS antenna via a single scatterer. The geometry in Fig. 2.30 implies that A_{VV} and A_{HV} can be expressed as a function of D, D_{ts}, D_{sr}, R_r, α_R, and β_R as follows:

$$\begin{bmatrix} A_{\mathrm{VV}} \\ A_{\mathrm{HV}} \end{bmatrix} = A_V \begin{bmatrix} f_{\mathrm{VV}}(D, D_{ts}, D_{sr}, R_r, \alpha_R, \beta_R) \\ f_{\mathrm{HV}}(D, D_{ts}, D_{sr}, R_r, \alpha_R, \beta_R) \end{bmatrix}, \tag{2.189}$$

where A_V is the amplitude of $\underline{V}$' at the MS. The azimuth and elevation angles of departure (AAoDs and EAoDs) from the BS are dependent upon and are fixed by the azimuth and elevation angles of arrival (AAoAs and EAoAs) at the MS and, thus, the channel polarization functions f_{VV} and f_{HV} in (2.189) do not depend on α_T and β_T. Similarly, for the case of a horizontally polarized plane wave from the BS:

$$\begin{bmatrix} A_{\mathrm{VH}} \\ A_{\mathrm{HH}} \end{bmatrix} = A_H \begin{bmatrix} f_{\mathrm{VH}}(D, D_{ts}, D_{sr}, R_r, \alpha_R, \beta_R) \\ f_{\mathrm{HH}}(D, D_{ts}, D_{sr}, R_r, \alpha_R, \beta_R) \end{bmatrix}, \tag{2.190}$$

where A_H is the amplitude of $\underline{H}$' at the MS. From the geometry in Fig. 2.30, the distances are

$$d_t = \sqrt{(D + R_r \cos\alpha_R)^2 + (R_r \sin\alpha_R)^2}, \tag{2.191}$$

$$D_{ts} = \sqrt{d_t^2 + (\Delta_h - R_r \tan\beta_R)^2}, \tag{2.192}$$

$$D_{sr} = R_r/\cos\beta_R, d_1 = R_r \tan\beta_R, \tag{2.193}$$

$$D_{tr} = \sqrt{D^2 + \Delta_h{}^2}, d_2 = \sqrt{d_t^2 + \Delta_h{}^2}, \tag{2.194}$$

where $\Delta_h = (h_T - h_R)$. Based on (2.191)–(2.194) and the law of cosines, the angles in Fig. 2.30 can be written as

$$\cos\theta_3 = \frac{D_{ts}{}^2 + D_{tr}{}^2 - D_{sr}{}^2}{2D_{ts}D_{tr}} \frac{a_2 - a_3 + a_4}{\sqrt{(a_1{}^2 + 2a_2 - 2a_3 + a_4)\, a_4}}, \tag{2.195}$$

$$\cos\theta_4 = \frac{D_{ts}{}^2 + d_2{}^2 - d_1{}^2}{2D_{ts}d_2} \frac{(R_r/D)^2 + 2a_2 - a_3 + a_4}{\sqrt{(a_1{}^2 + 2a_2 - 2a_3 + a_4)\,(2a_2 + a_4 + a_5{}^2)}}, \tag{2.196}$$

$$\cos\theta_5 = \frac{{d_2}^2 + {D_{tr}}^2 - {R_r}^2}{2d_2 D_{tr}} = \frac{a_2 + a_4}{\sqrt{(2a_2 + a_4 + {a_5}^2)\, a_4}}, \tag{2.197}$$

$$\cos\theta_6 = \frac{\cos\theta_5 - \cos\theta_3 \cos\theta_4}{\sqrt{(1-\cos^2\theta_3)\,(1-\cos^2\theta_4)}}, \tag{2.198}$$

$$\cos\theta_7 = \frac{{D_{sr}}^2 + {D_{tr}}^2 - {D_{ts}}^2}{2D_{sr}D_{tr}} = \frac{(-a_2 + a_3)\cos\beta_R}{a_5\sqrt{a_4}}, \tag{2.199}$$

$$\cos\theta_8 = \frac{{D_{tr}}^2 + {R_r}^2 - {d_2}^2}{2D_{tr}R_r} = -\frac{\cos\alpha_R}{\sqrt{a_4}}, \tag{2.200}$$

$$\cos\theta_9 = \frac{\cos\theta_8 - \cos\theta_7 \cos\beta_R}{\sqrt{(1-\cos^2\theta_7)\,(1-\cos^2\beta_R)}}, \tag{2.201}$$

$$\theta_V = \pi - \theta_6 \tag{2.202}$$

where

$$a_1 = \frac{R_r/D}{\cos\beta_R}, a_2 = \frac{R_r}{D}\cos\alpha_R, a_3 = \frac{R_r \Delta_h}{D^2}\tan\beta_R,$$
$$a_4 = 1 + \left(\frac{\Delta_h}{D}\right)^2, a_5 = \frac{R_r}{D}. \tag{2.203}$$

The angles $\cos\theta_6$ and $\cos\theta_9$ in (2.198) and (2.201), respectively, can be used to derive the channel polarization functions $f_{\mathrm{VV}}, f_{\mathrm{HV}}, f_{\mathrm{HH}}$, and f_{VH} in (2.189) and (2.190) as is now described.

From the geometry in Fig. 2.30, the amplitudes of the vertical and horizontal polarization components that are received from a vertically polarized transmitted plane wave are, respectively,

$$A_{\mathrm{VV}} = A_V\,|\cos(\theta_9 + (\pi - \theta_V) - \pi)| \tag{2.204}$$
$$= A_V \left|\cos\theta_6\cos\theta_9 - \sqrt{1-\cos^2\theta_6}\sqrt{1-\cos^2\theta_9}\right|,$$
$$A_{\mathrm{HV}} = A_V\,|\sin(\theta_9 + (\pi - \theta_V) - \pi)| \tag{2.205}$$
$$= A_V \left|\cos\theta_6\sqrt{1-\cos^2\theta_9} + \cos\theta_9\sqrt{1-\cos^2\theta_6}\right|,$$

where $\cos\theta_6$ and $\cos\theta_9$ in (2.204) and (2.205), respectively, are functions of $D, R_r, \alpha_R, \beta_R$ as is evident from (2.195)–(2.201). Comparing (2.204) and (2.205) with (2.189), the channel polarization functions f_{VV} and f_{HV} can be written as:

$$f_{\mathrm{VV}}(D, D_{ts}, D_{sr}, R_r, \alpha_R, \beta_R)$$
$$\equiv f_{\mathrm{VV}}(D, R_r, \alpha_R, \beta_R)$$
$$= \left|\cos\theta_6\cos\theta_9 - \sqrt{1-\cos^2\theta_6}\sqrt{1-\cos^2\theta_9}\right|, \tag{2.206}$$
$$f_{\mathrm{HV}}(D, D_{ts}, D_{sr}, R_r, \alpha_R, \beta_R)$$
$$\equiv f_{\mathrm{HV}}(D, R_r, \alpha_R, \beta_R)$$
$$= \left|\cos\theta_6\sqrt{1-\cos^2\theta_9} + \cos\theta_9\sqrt{1-\cos^2\theta_6}\right|. \tag{2.207}$$

In a similar fashion, the channel polarization functions f_{HH} and f_{VH} can be written as:

$$f_{\mathrm{VH}}(D, D_{ts}, D_{sr}, R_r, \alpha_R, \beta_R)$$
$$\equiv f_{\mathrm{VH}}(D, R_r, \alpha_R, \beta_R)$$

$$= \left| \cos\theta_6 \sqrt{1-\cos^2\theta_9} + \cos\theta_9 \sqrt{1-\cos^2\theta_6} \right|, \tag{2.208}$$

$$f_{\mathrm{HH}}(D, D_{ts}, D_{sr}, R_r, \alpha_R, \beta_R)$$
$$\equiv f_{\mathrm{HH}}(D, R_r, \alpha_R, \beta_R)$$
$$= \left| \cos\theta_6 \cos\theta_9 - \sqrt{1-\cos^2\theta_6} \sqrt{1-\cos^2\theta_9} \right|. \tag{2.209}$$

Note that a symmetry exists in the co- and cross-polarization functions such that

$$f_{\mathrm{VV}} = f_{\mathrm{HH}}, f_{\mathrm{HV}} = f_{\mathrm{VH}}. \tag{2.210}$$

This model may be enhanced so as to include reflection coefficients following the methodology in [189].

2.4.2 XPD in Polarized Multipath-Fading Channels

The polarized channels in Fig. 2.30 can be modeled by combining the channel polarization functions with the conventional co-polarized channel impulse response functions derived for the exact same 3-D single cylinder scattering geometry shown in Fig. 2.30. First consider the case of vertically polarized BS and MS antennas (VV-channel). The complex low-pass channel impulse response for the VV-channel can be expressed as

$$g_{\mathrm{VV}}(t) = g_{\mathrm{VV}}^{\mathrm{SBR}}(t) + g_{\mathrm{VV}}^{\mathrm{LoS}}(t), \tag{2.211}$$

where

$$g_{\mathrm{VV}}^{\mathrm{SBR}}(t) = \sum_{n=1}^{N} A_{V,n} f_{\mathrm{VV},n}\, \mathrm{e}^{j\phi_n(t)},$$
$$g_{\mathrm{VV}}^{\mathrm{LoS}}(t) = A_V^{\mathrm{LoS}}\, \mathrm{e}^{j\phi^{\mathrm{LoS}}(t)}, \tag{2.212}$$

are the diffuse single-bounce receive-side (SBR) and LoS components, respectively, and

$$A_{V,n} = A_V(\alpha_{R,n}, \beta_{R,n}), \tag{2.213}$$

$$f_{\mathrm{VV},n} = f_{\mathrm{VV}}(D, R_r, \alpha_{R,n}, \beta_{R,n}), \tag{2.214}$$

$$\phi_n(t) = 2\pi(f_c + f_{D,n}) \left(t - (D_{ts,n} + D_{sr,n})/c_0 \right) + \phi_n, \tag{2.215}$$

$$\phi^{\mathrm{LoS}}(t) = 2\pi(f_c + f_D^{\mathrm{LoS}}) \left(t - D_{tr}/c_0 \right), \tag{2.216}$$

$$f_c = \frac{c_0}{\lambda}, \; f_{D,n} = \left(\frac{v_R}{\lambda} \right) \cos\beta_{R,n} \cos\left(\gamma_R - \alpha_{R,n}\right), \tag{2.217}$$

$$f_D^{\mathrm{LoS}} = \frac{D}{\sqrt{D^2 + \Delta_h^{\,2}}} \left(\frac{v_R}{\lambda} \right) \cos\left(\gamma_R - \pi\right), \tag{2.218}$$

where c_0, λ, v_R, and γ_R are the velocity of light, the carrier wavelength, the velocity of the MS, and the angle of the MS's moving direction with respect to the positive x-axis, respectively. Further, f_c and $f_{D,n}$ are the carrier and Doppler frequency associated with the nth arriving plane wave, respectively. Note that the MS is considered to be in the center of the scattering cylinder regardless of the physical location and velocity of the MS, which is a typical assumption for geometrical channel modeling. Of course the exact location of the scatterers on the cylinder will change with the physical location of the MS, due to site specific propagation conditions. In this case, the channel is modeled as being locally wide-sense stationary, i.e., the locations of the scatterers with respect to the MS will stay the same if the MS moves over small distances.

It is assumed at this stage that the phases $\{\phi_n\}$ in (2.215) are independent and identically distributed (i.i.d.) uniform random variables on the interval $[-\pi, \pi)$, and the $\{\phi_n\}$ are independent of the AAoAs $\{\alpha_{R,n}\}$, EAoAs $\{\beta_{R,n}\}$ and the radius of the scattering cylinder. For large N, the central limit theorem can be invoked and $g_{\mathrm{VV}}(t)$ can be treated as a complex Gaussian random process. By using the complex low-pass channel impulse response and the aforementioned properties, it is straightforward to obtain the received power through the VV-channel at the Rx as follows:

$$\Omega_{\mathrm{VV}} = \Omega_{\mathrm{VV}}^{\mathrm{SBR}} + \Omega_{\mathrm{VV}}^{\mathrm{LoS}} = (1+K)\,\Omega_{\mathrm{VV}}^{\mathrm{SBR}}, \tag{2.219}$$

$$\begin{aligned}\Omega_{\mathrm{VV}}^{\mathrm{SBR}} &= \mathrm{E}\left[\left|g_{\mathrm{VV}}^{\mathrm{SBR}}(t)\right|^2\right] \\ &= \mathrm{E}\left[\left(\sum_{n=1}^{N} A_{V,n} f_{\mathrm{VV},n}\, e^{j\phi_n(t)}\right)\left(\sum_{m=1}^{N} A_{V,n} f_{\mathrm{VV},n}\, e^{-j\phi_m(t)}\right)\right] \\ &= \mathrm{E}\left[\sum_{n=1}^{N} A_{V,n}^2 f_{\mathrm{VV},n}^2\right],\end{aligned} \tag{2.220}$$

$$\Omega_{\mathrm{VV}}^{\mathrm{LoS}} = \left|A_V^{\mathrm{LoS}}\right|^2 = K\Omega_{\mathrm{VV}}^{\mathrm{SBR}}, \tag{2.221}$$

where K denotes the Ricean K-factor, and the third equality in (2.220) is due to the fact that the phases $\{\phi_n\}$ in (2.215) are independent and identically distributed (i.i.d.) uniform random variables on the interval $[-\pi, \pi)$. Further, as $N \to \infty$, the discrete AAoAs, $\alpha_{R,n}$, and discrete EAoAs, $\beta_{R,n}$, can be replaced with continuous random variables α_R and β_R having the joint probability density function (pdf), $f(\alpha_R, \beta_R)$. Here, the azimuth and elevation angles of arrival are assumed independent of each other and, thus, the joint pdf $f(\alpha_R, \beta_R)$ can be decomposed as $f(\alpha_R)f(\beta_R)$. It follows that

$$\Omega_{\mathrm{VV}}^{\mathrm{SBR}} = A_V^2 \int_{-\pi}^{\pi} \int_{-\beta_{R,\mathrm{Max}}}^{\beta_{R,\mathrm{Max}}} f_{\mathrm{VV}}^2(D, R_r, \alpha_R, \beta_R) p_r(\beta_R)\, p_r(\alpha_R)\; d\beta_R d\alpha_R, \tag{2.222}$$

where $\beta_{R,\mathrm{Max}}$ is the absolute value of the maximum EAoA.

Several different distributions have been suggested in the literature to characterize the AAoA distribution, such as uniform, Gaussian, and Laplacian. Later, the von Mises distribution in (2.51) will be used such that

$$p_r(\alpha_R) = \frac{\exp[k_R \cos(\alpha_R - \mu_R)]}{2\pi I_0(k_R)},\ k_R \geq 0, \tag{2.223}$$

where $\alpha_R \in [-\pi, \pi)$, $I_0(\cdot)$ is the zero-order modified Bessel function of the first kind, $\mu_R \in [-\pi, \pi)$ is the mean AAoA of the scatterers in the x - y plane with respect to the positive x axis, and k_R controls the spread of the scatterers around the mean AAoA μ_R. Prior work has also used several different distributions to characterize the EAoA distribution. Later, the cosine pdf in (2.52) will be used such that

$$p_r(\beta_R) = \frac{\pi}{4\beta_{R,\mathrm{Max}}} \cos\left(\frac{\pi}{2}\frac{\beta_R}{\beta_{R,\mathrm{Max}}}\right), \quad |\beta_R| \leq \beta_{R,\mathrm{Max}} \leq \pi/2, \tag{2.224}$$

where $\beta_{R,\mathrm{Max}}$ typically lies in the range $20° < \beta_{R,\mathrm{Max}} < 45°$ for fixed-to-mobile land mobile radio channels [185, 191, 257]. Of course, other suitable distributions for $p_r(\alpha_R)$ and $p_r(\beta_R)$ can be used as well at this stage.

Similar to (2.222), the SBR power at the MS with a horizontally polarized MS antenna and a vertically polarized BS antenna (HV-channel), a vertically polarized MS antenna and a horizontally polarized BS antenna (VH-channel), and horizontally polarized MS and BS antennas (HH-channel), denoted by P_{HV}, P_{VH}, and P_{HH}, respectively, can be expressed as

$$\Omega_{\mathrm{HV}}^{\mathrm{SBR}} = A_V^2 \int_{-\pi}^{\pi} \int_{-\beta_{R,\mathrm{Max}}}^{\beta_{R,\mathrm{Max}}} \left(f_{\mathrm{HV}}(D, R_r, \alpha_R, \beta_R)\right)^2 p_r(\beta_R)\, p_r(\alpha_R)\; d\beta_R d\alpha_R, \tag{2.225}$$

$$\Omega_{\mathrm{VH}}^{\mathrm{SBR}} = A_H^2 \int_{-\pi}^{\pi} \int_{-\beta_{R,\mathrm{Max}}}^{\beta_{R,\mathrm{Max}}} \left(f_{\mathrm{VH}}(D, R_r, \alpha_R, \beta_R) \right)^2 p_r(\beta_R)\, p_r(\alpha_R)\; d\beta_R d\alpha_R, \tag{2.226}$$

$$\Omega_{\mathrm{HH}}^{\mathrm{SBR}} = A_H^2 \int_{-\pi}^{\pi} \int_{-\beta_{R,\mathrm{Max}}}^{\beta_{R,\mathrm{Max}}} \left(f_{\mathrm{HH}}(D, R_r, \alpha_R, \beta_R) \right)^2 p_r(\beta_R)\, p_r(\alpha_R)\; d\beta_R d\alpha_R. \tag{2.227}$$

Notice that by taking into account the statistical distribution of scatterers, the total power of the vertical and horizontal polarization components can be derived via the superposition of the CoP-plane components by averaging over the pdfs of the AAoA and EAoA, $p(\alpha_R)$ and $p(\beta_R)$, respectively. Finally, the average XPD values are obtained from (2.222) and (2.225)–(2.227) as

$$\mathrm{XPD}_{\mathrm{VV/HV}} = \frac{\Omega_{\mathrm{VV}}}{\Omega_{\mathrm{HV}}}, \mathrm{XPD}_{\mathrm{HH/VH}} = \frac{\Omega_{\mathrm{HH}}}{\Omega_{\mathrm{VH}}}. \tag{2.228}$$

2.4.3 *Polarized Channel Model Application*

This section compares the analytical XPD predicted from the geometrical depolarization model developed in Sects. 2.4.1 and 2.4.2 with some previously reported XPD results obtained from empirical data [110, 306]. The empirical XPD data reported in [110, 306] were based on narrow-band fixed-to-mobile channel measurements taken in a suburban area at 2.48 GHz, where the corresponding h_T and h_R in Fig. 2.30 were 20 m and 3 m, respectively.

The parameters in (2.223)–(2.224) are set as $\mu_R = 180°$ and $\beta_{R,\mathrm{Max}} = 40°$, unless otherwise stated, particularly when comparing our analytical XPD results with the XPD measurement data in [110, 306]. It is stated in [110, 306] that the direction of the strongest signal was the Tx–Rx bore sight path in most cases, corresponding to $\mu_R = 180°$ in the model described in Sects. 2.4.1 and 2.4.2. The spread constant of the AAoA distribution, k_R, in (2.223) can exhibit substantial variation from one location to the next due to variations in the local scattering environment around the Rx. Finally, R_r in Fig. 2.30 is set to 30 m.

2.4.3.1 Suburban Area in San Jose

Figures 2.32 and 2.33 portray the analytical mean XPD curves of F2M fading channels as k_R varies from 0 to 9 and from 10 to 700, respectively. The same antenna configuration as that in [110, 306] is utilized in the analysis to allow for comparison with the measurement data illustrated in Fig. 2.32, which is a $\pm 45°$ dual-polarization antenna at both the BS and MS. Note that a directional MS antenna with the azimuthal beamwidth of 90° and a gain of 12 dBi was used in the measurements in [110, 306]. Figure 2.32 shows that the XPD curve tends to decrease from roughly 6.5–0 dB as k_R increases from 0 to 9. On the other hand, the XPD curve increases from 0 dB to roughly 7.5 dB as k_R increases from 10 to 700 in Fig. 2.33. The XPD curve for $0 \leq k_R \leq 700$ at a fixed BS–MS distance, $D = 1$ km, is also illustrated in the insert of Fig. 2.33 to further illustrate the effect of k_R on the XPD shown in Figs. 2.32 and 2.33. The reason for the strong dependency of the mean XPD on k_R will be explained later when discussing Fig. 2.34.

When k_R is in the range 7–10, the XPD stays at around 0 dB regardless of the distance between the BS and MS, and it can be shown that the AAoA spread in (2.223) is roughly 90° when k_R is 7–10 [3]. As the distance between the BS and MS, D, increases it is expected that k_R will tend to decrease since the plane waves at the MS for large distances and NLoS conditions will come from many angles due to local scattering and, hence, the azimuthal scattering will become more isotropic; $k_R = 0$ corresponds to the case of isotropic azimuthal scattering. However, in the case of isotropic scattering the observed AAoA spread will be determined by the beam pattern of the 90° directional Rx antenna that was used to make the measurements. Thus, while the actual scattering environment may be near isotropic, i.e., $k_R \approx 0$, the observed value of k_R will lay in the range 7–10. For this reason, the empirical XPD tends to converge toward 0 dB as D increases, and it is in close agreement with the analytical XPD results with k_R in the range 7–10, as previously stated.

The AAoA spread factor, k_R, is expected to increase as the horizontal BS–MS distance, D, decreases. As the MS moves closer to the BS most of the scatters will tend to be in the direction of the Tx so that k_R will tend to increase and the scattering will be non-isotropic. If the AAoA distribution is modeled using the von Mises pdf in (2.223) with $\mu_R = 180°$,

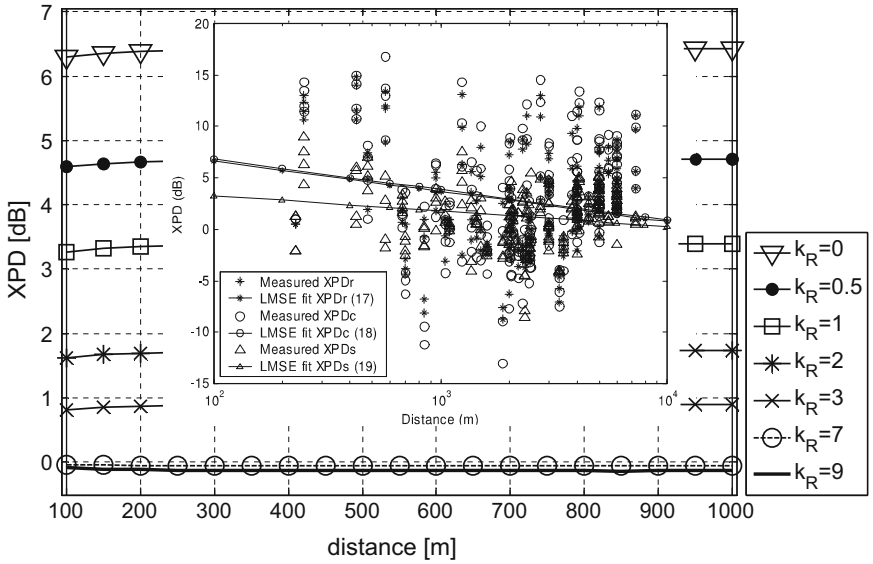

Fig. 2.32 $\overline{\text{XPD}}^{F2M}$ curves for a variety of k_R (0–9) with BS–MS distance in the range 100 m to 1 km, and the measurement data in [306]

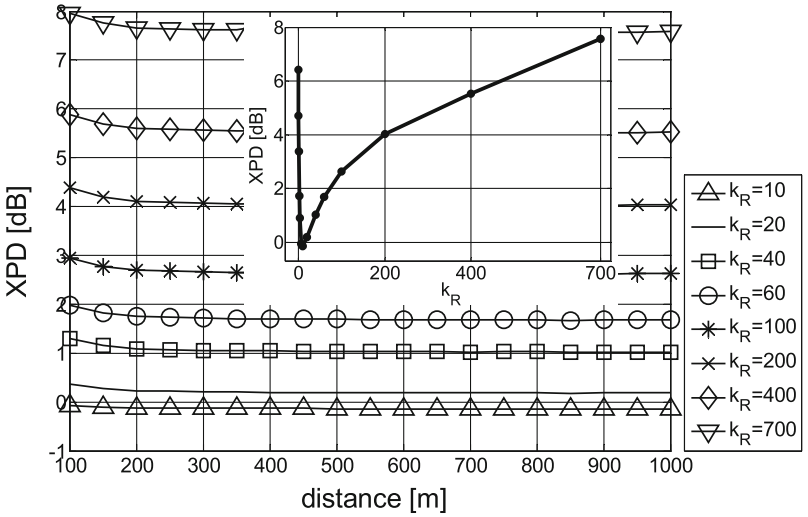

Fig. 2.33 $\overline{\text{XPD}}^{F2M}$ curves for a variety of k_R (10–700) with BS–MS distance in the range 100 m to 1 km

then the effective value of k_R will be greater than 7, since a directional antenna with an azimuthal beamwidth of 90° was used in the measurements. Notice that as k_R increases, the azimuthal angular spread becomes narrower. When the actual AAoA spread factor, k_R, is equal to 3 for example, $p_r(\alpha_R = 180°)|_{k_R=3} \simeq 0.66$, and the effective value of k_R due to the directional Rx antenna gain of 12 dBi (15.8 in linear scale) in the direction of BS–MS boresight ($\alpha_R = 180°$) is roughly $0.66 \times 15.8 \simeq 10.43$, which is close to $p_r(\alpha_R = 180°)|_{k_R=700} \simeq 10.55$. Thus, while the actual value of the AAoA spread factor may be in the neighborhood of $k_R = 3$, the observed value may be considerably higher and in the range of $k_R = 700$ due to the gain of the directional MS measurement antenna.

The empirical XPD data from [110, 306] are illustrated in Fig. 2.32, where XPD_r, XPD_c, and XPD_s represent the XPD of the total received signal, the XPD of the time-invariant portion of the received signal, and the XPD of the time-varying portion of the received signal. The empirical data in [110, 306] shows that the LMSE curve fit for the XPD of total received signal is almost same as the XPD for only the time-invariant portion of the received signal. This is expected, since the measurements in [110, 306] were made with a stationary MS. Most of the surrounding scatterers will be stationary and contribute to XPD_c, while only the moving scatterers such as nearby moving vehicles (which are not included in the model) will contribute to XPD_s. It is also shown that the LMSE curve fit of XPD_r tends to decrease from 6.5 to 0 dB as D increases from 100 m to 10 km. This phenomenon can be explained by the XPD curve for varying k_R inserted in Fig. 2.33, such that a

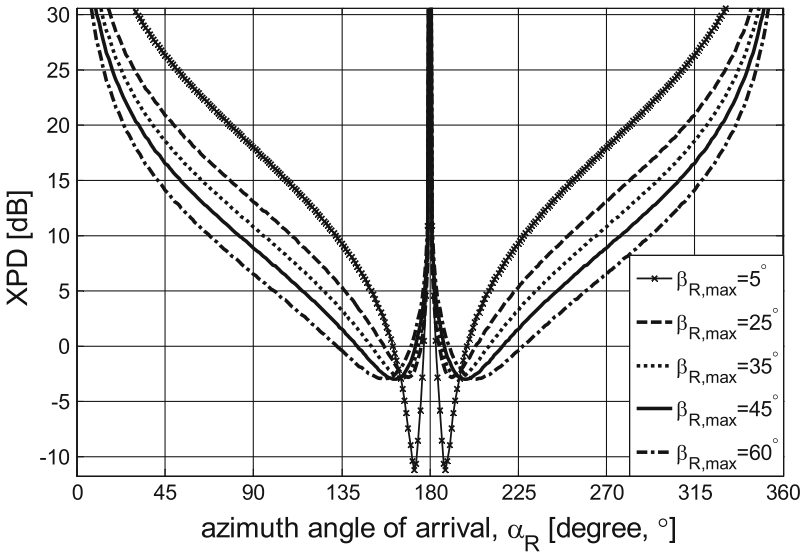

Fig. 2.34 $\overline{\text{XPD}}^{F2M}$ curves for varying α_R and $\beta_{\text{Max},R}$

decrease in the effective value of k_R from 550 to 7 corresponds to a decrease in the XPD from 6.5 to 0, as D increases from 100 m to 10 km. Even though an LMSE curve fit can be obtained from the measurement data, the measured XPD values show substantial variation even at the same D as portrayed in Figs. 2.32 and 2.33. The reason is that the AAoA spread factor k_R varies depending on the site specific local scattering environment, even at the same D. The XPD is not directly dependent on D, but k_R is expected to have a tendency to decrease with increasing D as mentioned earlier, which is reflected on the LMSE curve in the illustrated empirical results. Finally, the analytical XPD curves in the range 1–10 km are omitted from Figs. 2.32 and 2.33, since the XPD remains constant after 1 km.

The AAoA α_R has a significant impact on the XPD as shown in Fig. 2.34, and computing the XPD as a function of the AAoA α_R provides insight for the mean XPD that is obtained when averaging over the AAoA and EAoA distributions. Figure 2.34 also shows the XPD averaged over the EAoA distribution only at each AAoA, α_R. For AAoAs equal to 180°, 0° and 360°, which represent vertical CoP planes, the XPD goes infinity, meaning that there are no cross-polarization components at those angles. This makes sense given the geometry in Fig. 2.30. Remarkably, each XPD curve has a minimum point when the AAoA α_R lays in the range 155–170°. The XPD at this minimum point is below 0 dB, meaning that the power of the cross-polarization component is stronger than that of the co-polarization component. Figure 2.34 also shows that a larger maximum EAoA will result in a smaller mean XPD, since the XPD is below 0 dB over a larger AAoA range. Considering the XPD averaged over AAoA distribution with $\mu_R = 180°$ and k_R varying from 0 to 9, it can be recognized that as k_R increases the mean XPD decreases, since the impact of the small XPDs for AAoAs around the minimum point will dominate the high XPDs for AAoAs that are far from the minimum point. Furthermore, small changes in the AAoA distribution near 180° (bore sight) due to site specific local scattering will cause significant changes in the mean XPD which explains the high variance of the empirical XPD values observed in [110, 306].

2.5 Simulation of Multipath-Fading Channels

A channel simulator is an essential component for the development and testing of wireless systems. Simulation of mobile radio channels is commonly used as opposed to field trials, because it allows for less expensive and more reproducible system tests and evaluations. For this purpose it is desirable to generate complex faded envelopes that match the statistical characteristics of a reference model while at the same time having low complexity. For example, the reference model might be a 2-D isotropic scattering channel with an isotropic receiving antenna.

Two fundamentally different approaches to channel simulation models are the filtered white Gaussian noise models and the sum-of-sinusoids models. The basic idea of the filtered white noise approach is to shape the power spectrum of a white Gaussian noise process by using a filter whose magnitude response is the square root of the desired Doppler spectrum. The sum of sinusoids approach, on the other hand, approximates the complex fading envelope by the superposition of a finite number of sinusoids with properly chosen amplitudes, frequencies, and phases to yield the desired Doppler spectrum.

2.5.1 Filtered White Gaussian Noise Models

Recall that the faded envelope $g(t) = g_I(t) + jg_Q(t)$ is a complex Gaussian random process. A straightforward method for constructing a fading simulator is to low-pass filter two independent white Gaussian noise processes, as shown in Fig. 2.35. Since the input processes to the low-pass filters are independent, the random processes $g_I(t)$ and $g_Q(t)$ are also independent and have power spectral densities that are shaped by the squared magnitude response of the low-pass filters. If the white Gaussian noise sources have power spectral densities equal to $\Omega_p/2$ watts/Hz and the low-pass filters have transfer function $H(f)$, then

$$S_{g_I g_I}(f) = S_{g_Q g_Q}(f) = \frac{\Omega_p}{2}|H(f)|^2$$
$$S_{g_I g_Q}(f) = 0, \tag{2.229}$$

where the normalization $\int_{-\infty}^{\infty}|H(f)|^2 df = 1$ is assumed so that the envelope power is equal to Ω_p. The processes $g_I(t)$ and $g_Q(t)$ are independent zero-mean Gaussian random process, such that the envelope $\alpha \equiv |g(t_1)|$ is Rayleigh distributed at any time t_1. The problem is to construct the low-pass filter $H(f)$ to give the desired Doppler spectrum.

2.5.1.1 IDFT Method

One approach for generating the faded envelope using the filtering method has been suggested by Young and Beaulieu [369] and is based on an inverse discrete Fourier transform (IDFT) as shown in Fig. 2.36. The input sequences $\{A[k]\}$ and $\{B[k]\}$ are first generated, each consisting of N i.i.d. real zero-mean Gaussian random variables with variance $N\Omega_p/2$. These samples are then applied to a filter with frequency response $H[k], k = 0, \ldots, N-1$, followed by an N-point IDFT to generate the time-domain samples of the complex faded envelope as

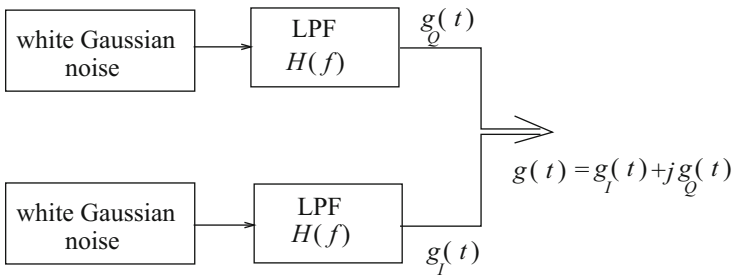

Fig. 2.35 Fading simulator that uses low-pass filtered white Gaussian noise

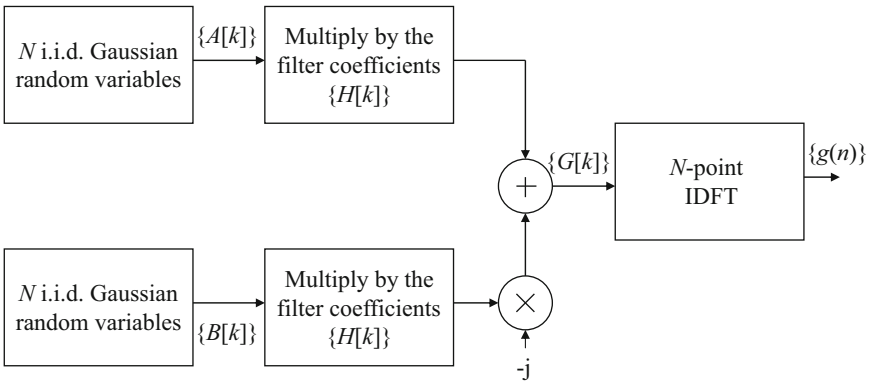

Fig. 2.36 IDFT-based fading simulator

$$g[n] = \text{IDFT}\left\{A[k]H[k] - jB[k]H[k]\right\}_{n=0}^{N-1}$$
$$= \frac{1}{N}\sum_{k=0}^{N-1}\left(A[k]H[k] - jB[k]H[k]\right)\mathrm{e}^{j2\pi kn/N},\ n = 0,\ldots,N-1. \tag{2.230}$$

Due to linearity of the IDFT operation, the discrete-time autocorrelation function of the output sample sequence $\{g[n]\} = \{g_I[n]\} + j\{g_Q[n]\}$ is [369]

$$\phi_{gg}[n] = \phi_{g_Ig_I}[n] + j\phi_{g_Ig_Q}[n]$$
$$= \frac{\Omega_p}{2}\left(a_I[n] + ja_Q[n]\right), \tag{2.231}$$

where $\{a[n]\} = \{a_I[n]\} + j\{a_Q[n]\}$ is given by the IDFT of the sequence $\{(H[k])^2\}$, i.e.,

$$a[n] = \frac{1}{N}\sum_{k=0}^{N-1}(H[k])^2\mathrm{e}^{j2\pi kn/N},\ n = 0,\ldots,N-1. \tag{2.232}$$

The only problem remaining is to design the filter, $H[k]$. To do so, the argument by Young and Beaulieu [369] is followed.

A sequence $\{A_{\text{CS}}[k]\}$ that satisfies the property $A_{\text{CS}}[k] = A^*_{\text{CS}}[N-k]$ is called a conjugate-symmetric sequence, while a sequence $\{A_{\text{CAS}}[k]\}$ that satisfies the property $A_{\text{CAS}}[k] = -A^*_{\text{CAS}}[N-k]$ is called a conjugate-antisymmetric sequence. The IDFT of a conjugate-symmetric sequence is real-valued, while the IDFT of a conjugate-antisymmetric sequence is imaginary-valued. If the sequence $\{a[n]\}$ has discrete Fourier transform (DFT) $\{A[k]\}$, then

$$a[n] = a_I[n] + ja_Q[n] = \text{IDFT}\{A[k]\}$$
$$= \text{IDFT}\{A_{\text{CS}}[k]\} + \text{IDFT}\{A_{\text{CAS}}[k]\}. \tag{2.233}$$

Also, note that

$$A_{\text{CS}}[k] = \frac{1}{2}A[k] + \frac{1}{2}A^*[N-k] \tag{2.234}$$

and

$$A_{\text{CAS}}[k] = \frac{1}{2}A[k] - \frac{1}{2}A^*[N-k] \tag{2.235}$$

for any sequence $\{A[k]\}$, where $A[k] = A_{\text{CS}}[k] + A_{\text{CAS}}[k]$. Thus, the sequence $\{A[k]\}$ can always be decomposed into the sum of conjugate-symmetric and conjugate-antisymmetric components. To ensure that the quadrature components of the faded envelope, $\{g_I[n]\}$ and $\{g_Q[n]\}$, are uncorrelated, which is the case for 2-D isotropic scattering environment and an isotropic receive antenna, it is required that $A_{\text{CAS}}[k] = 0$ for all k. Using (2.234), the filter should have the following structure:

$$H[k] = \begin{cases} \sqrt{H_s[0]} & ,\ k = 0 \\ \sqrt{\frac{H_s[k]}{2}} & ,\ k = 1,2,\ldots,\left(\frac{N}{2}-1\right) \\ \sqrt{H_s[k]} & ,\ k = \frac{N}{2} \\ \sqrt{\frac{H_s[N-k]}{2}} & ,\ k = \left(\frac{N}{2}+1\right),\ldots,(N-1) \end{cases}, \tag{2.236}$$

where the filter $H_s[k]$ can be obtained from the sampled Doppler spectrum.

To obtain the required filter $H[k]$, assume 2-D isotropic scattering with an isotropic receiver antenna. The required normalized autocorrelation function and normalized Doppler spectrum are, respectively,

$$\phi_{gg}(\tau) = J_0(2\pi f_m\tau) \tag{2.237}$$

and

$$S_{gg}(f) = \begin{cases} \frac{1}{\pi f_m} \frac{1}{\sqrt{1-(f/f_m)^2}} & |f| \le f_m \\ 0 & \text{otherwise} \end{cases}. \tag{2.238}$$

Ideally, the generated sequence $g[n]$ should have the normalized autocorrelation function

$$\phi_{gg}[n] = J_0(2\pi \hat{f}_m |n|), \tag{2.239}$$

where $\hat{f}_m = f_m T_s$ is the maximum normalized Doppler frequency and T_s is the sampling period. However, an exact realization of this autocorrelation function is not possible, because the time-domain sequence is truncated to N samples. Looked at another way, while the theoretical Doppler spectrum is bandlimited, the truncation to N samples in the time-domain means that the realized Doppler spectrum is not bandlimited.

To obtain the required filter, the continuous spectrum in (2.238) is sampled at frequencies $f_k = k/(NT_s), k = 0, \ldots, N-1$. Special treatment is given to the frequency domain coefficients at two points. The first is at zero frequency, where $H_s[0] = 0$ to ensure that the generated time-domain sequence always has zero mean regardless of the particular values assumed by the length-N input sequences $\{A[k]\}$ and $\{B[k]\}$. The second is at the index k_m that is at, or just below, the maximum Doppler frequency, i.e.,

$$k_m = \lfloor f_m N T_s \rfloor = \lfloor \hat{f}_m N \rfloor, \tag{2.240}$$

where $\lfloor x \rfloor$ is the largest integer contained in x. The realized maximum Doppler frequency is $k_m/(NT_s)$ Hz. The area under the Doppler spectrum curve in (2.238) from zero to frequency f is [147, 2.271.4]

$$C(f) = \frac{k_m}{NT_s} \arcsin(fNT_s/k_m), \quad 0 \le f \le k_m/(NT_s). \tag{2.241}$$

The area under the Doppler spectrum between the frequencies represented by the samples $(k_m - 1)$ and k_m is equal to $C(k_m/(NT_s)) - C([k_m - 1]/(NT_s)$. Approximating this area by a rectangle of height $(H_s[k_m])^2$ and width $1/(NT_s)$ gives

$$H_s[k_m] = \sqrt{k_m \left[\frac{\pi}{2} - \arctan\left(\frac{k_m - 1}{\sqrt{2k_m - 1}} \right) \right]}. \tag{2.242}$$

The complete filter $H[k]$ can now be specified as follows:

$$H[k] = \begin{cases} 0 & , \ k = 0 \\ \sqrt{\frac{1}{2\pi f_m \sqrt{1-(k/(N\hat{f}_m))^2}}} & , \ k = 1, 2, \ldots, k_m - 1 \\ \sqrt{k_m \left[\frac{\pi}{2} - \arctan\left(\frac{k_m - 1}{\sqrt{2k_m - 1}} \right) \right]} & , \ k = k_m \\ 0 & , \ k = k_m + 1, \ldots, N - k_m - 1 \\ \sqrt{k_m \left[\frac{\pi}{2} - \arctan\left(\frac{k_m - 1}{\sqrt{2k_m - 1}} \right) \right]} & , \ k = N - k_m \\ \sqrt{\frac{1}{2\pi f_m \sqrt{1-(N-k/(N\hat{f}_m))^2}}} & , \ N - k_m + 1, \ldots, N - 1 \end{cases} \tag{2.243}$$

The IDFT method will generate a Rayleigh faded envelope with an autocorrelation function that closes matches the reference model for large N. However, the main limitation of the IDFT approach arises from the block-oriented structure which precludes continuous transmission in that there is a discontinuity in the time series (i.e., the faded envelope) from one block of N samples to the next.

2.5.1.2 IIR Filtering Method

Another approach implements the filters in the time domain as finite impulse response (FIR) or infinite impulse response (IIR) filters. There are two main challenges with this approach. The first challenge arises from the fact that the sampled channel waveform is bandlimited to a discrete frequency $\hat{f}_m = f_m T_s$, where T_s is the sample period. Consider, for example, a cellular system operating at a carrier frequency of $f_c = 1800$ MHz with a maximum MS speed of 300 km/h. In this case, the maximum Doppler frequency is $f_m = f_c(v/\lambda_c) = 500$ Hz, where c is the speed of light. If the signal is sampled at rate $R_s = 1/T_s = 1$ MHz, then the normalized Doppler frequency is $\hat{f}_m = f_m T_s = 0.0005$. If implemented as a finite impulse response (FIR) filter, such an extremely narrowband filter would require an impractically high filter order. Fortunately, this can be satisfied by using a filter designed at a lower sampling frequency followed by an interpolator to increase the sampling frequency. For example, the filter could be designed at a sampling frequency of 2 kHz, which is 2 times the Nyquist frequency. Afterwards interpolate by a factor of $I = 500$ to obtain the desired sampling frequency of 1 MHz.

The second main challenge is that the square-root of the target Doppler spectrum for 2-D isotropic scattering and an isotropic receive antenna in (2.238) is irrational and, therefore, none of the straightforward filter design methods can be applied. However, an approach developed by Steiglitz [307] allows the design of an IIR filter with an arbitrary magnitude response. Another possibility is to use the MATLAB function `iirlpnorm` [221].

Consider an IIR filter of order $2K$ that is synthesized as the cascade of K Direct-Form II second-order (two poles and two zeroes) sections (biquads) having the form

$$H(z) = A \prod_{k=1}^{K} \frac{1 + a_k z^{-1} + b_k z^{-2}}{1 + c_k z^{-1} + d_k z^{-2}}. \tag{2.244}$$

For example, for $f_m T_s = 0.4$, $K = 5$, and an ellipsoidal accuracy of 0.01, the filter design procedure described by Komninakis [181] results in the coefficients tabulated in Table 2.1. Figure 2.37 plots the magnitude response of the designed filter, which is shown to closely match that of the theoretical ideal filter.

2.5.2 *Sum of Sinusoids Methods*

Sum-of-sinusoids (SoS) channel models attempt to simulate the channel as a stationary complex Gaussian random process, formed by the sum of multiple sinusoids having appropriately selected frequencies, amplitudes, and phases. The objective is to generate a faded envelope having statistical properties that are as close as possible to a specified reference model, while at the same time minimizing the number of sinusoids that are required to achieve a given degree of modeling accuracy. SoS models are broadly categorized as either *deterministic* or *statistical*. Deterministic SoS models use fixed frequencies, amplitudes, and phases for the sinusoidal components. Therefore, the statistical properties of the faded envelope are deterministic for all simulation trials. Such models are useful for simulations that require continuous transmission over

Table 2.1 Coefficients for $K = 5$ biquad stage elliptical filter

Stage	Filter coefficients			
k	a_k	b_k	c_k	d_k
1	1.5806655278853	0.99720549234156	−0.64808639835819	0.88900798545419
2	0.19859624284546	0.99283177405702	−0.62521063559242	0.97280125737779
3	−0.60387555371625	0.9999939585621	−0.62031415619505	0.99996628706514
4	−0.56105447536557	0.9997677910713	−0.79222029531477	0.2514924845181
5	−0.39828788982331	0.99957862369507	−0.71405064745976	0.64701702807931
A	0.020939537466725			

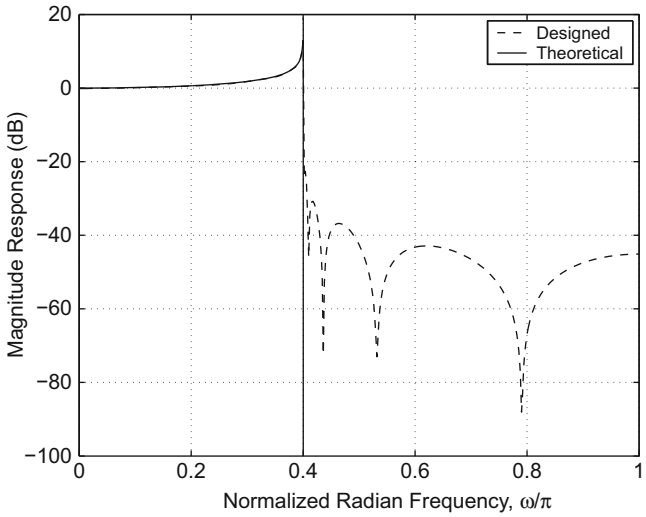

Fig. 2.37 Magnitude response of the designed shaping filter with $K = 5$ biquad sections

a long time interval, such as a real-time hardware channel simulator. In contrast, the statistical SoS models require multiple simulation trials, where one or more of the parameter sets (frequencies, amplitudes, or phases) are randomly selected for each simulation trial. As a result, the simulated channels have statistical properties that vary for each simulation trial, but they converge to the desired statistical properties when averaged over a sufficiently large number of simulation trials. Since a statistical model requires multiple simulation trials, it cannot be used in cases where continuous transmission is required. An ergodic statistical SoS model is one whose statistical properties converge to the desired properties in a single simulation trial. For this reason an ergodic statistical model is essentially a deterministic model, but differs in the sense that one of the parameter sets, usually the phases, is randomly generated when the simulator is initialized.

2.5.2.1 Clarke's Model

Clarke derived a statistical SoS simulation model that begins with (2.10) and (2.6) and assumes equal strength multipath components ($C_n = \sqrt{1/N}$). The received complex envelope has the form

$$g(t) = \sqrt{\frac{1}{N}} \sum_{n=1}^{N} \mathrm{e}^{j(2\pi f_m t \cos(\theta_n) + \hat{\phi}_n)} , \tag{2.245}$$

where N is the number of sinusoids and the phases $\hat{\phi}_n$ are independent identically distributed (i.i.d.) uniform random variables on $[-\pi, \pi)$.

If a reference model having 2-D isotropic scattering and an isotropic antenna is assumed, then the θ_n are also i.i.d. uniform random variables on $[-\pi, \pi)$, and are independent of the $\hat{\phi}_n$. Based on the above assumptions concerning the C_n, $\hat{\phi}_n$, and θ_n, the ensemble averaged correlation functions of Clarke's model in (2.245) for a *finite* N are[3]

$$\phi_{g_I g_I}(\tau) = \phi_{g_Q g_Q}(\tau) = \frac{1}{2} J_0(2\pi f_m \tau) \tag{2.246}$$

$$\phi_{g_I g_Q}(\tau) = \phi_{g_Q g_I}(\tau) = 0 \tag{2.247}$$

$$\phi_{gg}(\tau) = \frac{1}{2} J_0(2\pi f_m \tau) \tag{2.248}$$

$$\phi_{\alpha^2\alpha^2}(\tau) = 1 + \frac{N-1}{N} J_0^2(2\pi f_m \tau). \tag{2.249}$$

[3]Note that $\Omega_p = \sum_{n=1}^{N} C_n^2 = 1$ in this case; other values of Ω_p can be obtained by straightforward scaling.

Note that for finite N, the auto- and cross-correlation functions of $g_I(t)$ and $g_Q(t)$ match those of the reference model in (2.29) and (2.31), while the squared-envelope autocorrelation function reaches the desired form $1 + J_0^2(2\pi f_m \tau)$ in (2.82) asymptotically as $N \to \infty$.

2.5.2.2 Jakes' Model

Jakes [171] derived a deterministic SoS simulation model that is perhaps the most widely cited fading model in literature. Jakes' model begins by choosing the N sinusoidal components to be uniformly distributed in angle, i.e.,

$$\theta_n = \frac{2\pi n}{N}, \quad n = 1,\ 2, \ldots,\ N. \tag{2.250}$$

By choosing $N/2$ to be an odd integer, the sum in (2.245) can be rearranged into the form

$$g(t) = \sqrt{\frac{1}{N}} \left\{ \sum_{n=1}^{N/2-1} \left[\mathrm{e}^{-j(2\pi f_m t \cos(\theta_n) + \hat{\phi}_{-n})} + \mathrm{e}^{j(2\pi f_m t \cos(\theta_n) + \hat{\phi}_n)} \right] + \mathrm{e}^{-j(2\pi f_m t + \hat{\phi}_{-N})} + \mathrm{e}^{j(2\pi f_m t + \hat{\phi}_N)} \right\}, \tag{2.251}$$

where the phase indices have been relabeled. Note that the Doppler shifts progress from $-2\pi f_m \cos(2\pi/N)$ to $+2\pi f_m \cos(2\pi/N)$ as n progresses from 1 to $N/2 - 1$ in the first sum, while they progress from $+2\pi f_m \cos(2\pi/N)$ to $-2\pi f_m \cos(2\pi/N)$ in the second sum. Therefore, the frequencies in these terms overlap. To reduce the number of sinusoidal components used in the model, Jakes uses non-overlapping frequencies to write $g(t)$ as

$$g(t) = \sqrt{\frac{1}{N}} \left\{ \sqrt{2} \sum_{n=1}^{M} \left[\mathrm{e}^{-j(2\pi f_m t \cos(\theta_n)) + \hat{\phi}_{-n}} + \mathrm{e}^{j(2\pi f_m t \cos(\theta_n) + \hat{\phi}_n)} \right] + \mathrm{e}^{-j(2\pi f_m t + \hat{\phi}_{-N})} + \mathrm{e}^{j(2\pi f_m t + \hat{\phi}_N)} \right\} \tag{2.252}$$

where

$$M = \frac{1}{2}\left(\frac{N}{2} - 1\right) \tag{2.253}$$

and the factor $\sqrt{2}$ is included so that the total power remains unchanged. Note that (2.251) and (2.252) are not equal. In (2.251) all phases are independent. However, (2.252) implies that $\hat{\phi}_n = -\hat{\phi}_{-N/2+n}$ and $\hat{\phi}_{-n} = -\hat{\phi}_{N/2-n}$ for $n = 1, \ldots, M$. If the phases are further constrained such that $\hat{\phi}_n = -\hat{\phi}_{-n}, n = 1, \ldots, M$ and $\hat{\phi}_N = -\hat{\phi}_{-N}$, then (2.252) can be rewritten in the form $g(t) = g_I(t) + j g_Q(t)$, where

$$g_I(t) = \sqrt{\frac{2}{N}} \left(2 \sum_{n=1}^{M} \cos(\beta_n) \cos(2\pi f_n t) + \sqrt{2} \cos(\alpha) \cos(2\pi f_m t) \right) \tag{2.254}$$

$$g_Q(t) = \sqrt{\frac{2}{N}} \left(2 \sum_{n=1}^{M} \sin(\beta_n) \cos(2\pi f_n t) + \sqrt{2} \sin(\alpha) \cos(2\pi f_m t) \right), \tag{2.255}$$

with $\alpha = \hat{\phi}_N$ and $\beta_n = \hat{\phi}_n$.

Jakes chooses the phases α and β_n with the objective of making $\langle g_I^2(t) \rangle = \langle g_Q^2(t) \rangle$ and $\langle g_I(t) g_Q(t) \rangle = 0$, where $\langle \cdot \rangle$ denotes time averaging. From (2.254) and (2.255),

$$\begin{aligned} \langle g_I^2(t) \rangle &= \frac{2}{N} \left[2 \sum_{n=1}^{M} \cos^2(\beta_n) + \cos^2(\alpha) \right] \\ &= \frac{2}{N} \left[M + \cos^2(\alpha) + \sum_{n=1}^{M} \cos(2\beta_n) \right], \end{aligned} \tag{2.256}$$

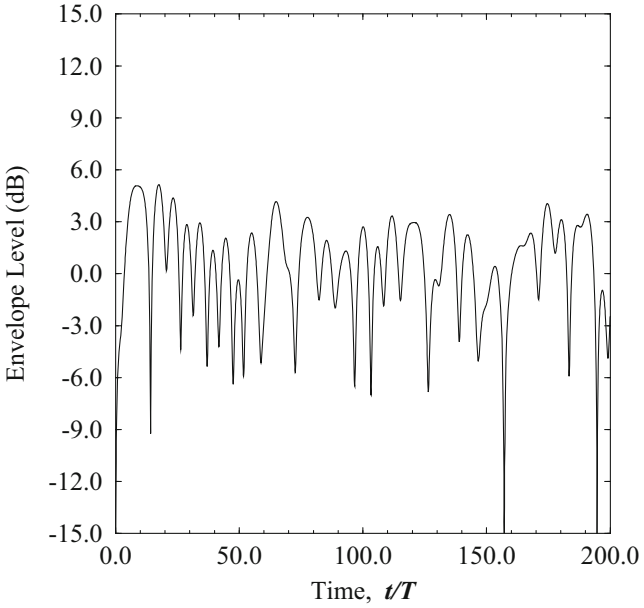

Fig. 2.38 Faded envelope generated by using Jakes' method with $M = 8$ oscillators; $f_m T = 0.1$

$$\langle g_Q^2(t)\rangle = \frac{2}{N}\left[2\sum_{n=1}^{M}\sin^2(\beta_n) + \sin^2(\alpha)\right]$$
$$= \frac{2}{N}\left[M + \sin^2(\alpha) - \sum_{n=1}^{M}\cos(2\beta_n)\right], \tag{2.257}$$

and

$$\langle g_I(t)g_Q(t)\rangle = \frac{2}{N}\left[2\sum_{n=1}^{M}\sin(\beta_n)\cos(\beta_n) + \sin(\alpha)\cos(\alpha)\right]. \tag{2.258}$$

Choosing $\alpha = 0$ and $\beta_n = \pi n/M$ gives $\langle g_Q^2(t)\rangle = M/(2M+1)$, $\langle g_I^2(t)\rangle = (M+1)/(2M+1)$ and $\langle g_I(t)g_Q(t)\rangle = 0$. Note that there is a small imbalance in the values of $\langle g_Q^2(t)\rangle$ and $\langle g_I^2(t)\rangle$. Finally, $\langle g_I^2(t)\rangle + \langle g_Q^2(t)\rangle = \Omega_p = 1$. The envelope power $\langle g_I^2(t)\rangle + \langle g_Q^2(t)\rangle$ can be easily scaled to any other desired value. A typical faded envelope, obtained by using Jakes' method with $N = 34$ ($M = 8$) is shown in Fig. 2.38.

The accuracy of Jakes' simulator can be evaluated by comparing the autocorrelation functions of the complex envelope with those of the 2-D isotropic scattering reference model. Suppose Clarke's method is modified by imposing the additional restrictions of even N and $\theta_n = 2\pi n/N$. The resulting simulation model is a statistical model, because the phases $\hat{\phi}_n$ are i.i.d. uniform random variable on $[-\pi, \pi)$. A faded envelope is obtained having the ensemble averaged autocorrelation function

$$\phi_{gg}(\tau) = \frac{1}{2N}\sum_{n=1}^{N}\cos\left(2\pi f_m \tau\cos\left(\frac{2\pi n}{N}\right)\right), \tag{2.259}$$

where ensemble averaging is performed over the random phases $\hat{\phi}_n$. Note that this autocorrelation tends to a Bessel function as $N \to \infty$. The normalized autocorrelation functions in (2.248) and (2.259) with $N = 8$ are plotted against the normalized time delay $f_m\tau$ in Fig. 2.39. Observe that Clark's model with $\theta_n = 2\pi n/N$ yields an autocorrelation function that deviates from the desired values at large lags. This can be improved upon by increasing the number of oscillators that are used in the simulator. For example, Fig. 2.40 shows the autocorrelation function when the number of oscillators is doubled from $N = 8$ to $N = 16$.

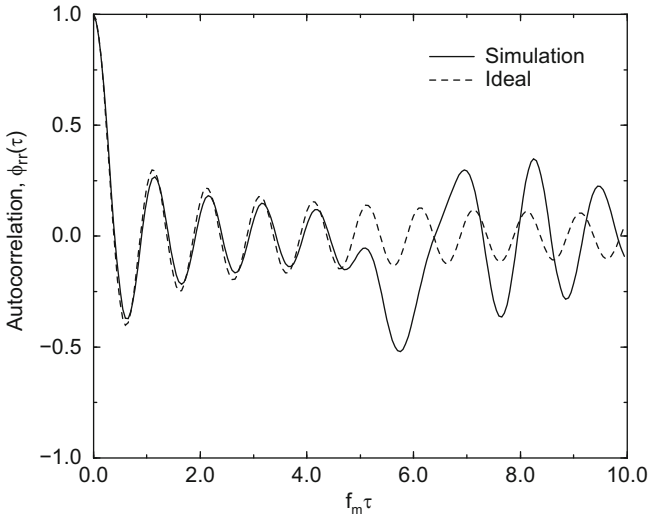

Fig. 2.39 Autocorrelation of in-phase and quadrature components obtained by using Clarke's method with $\theta_n = 2\pi n/N$ and $N = 8$ oscillators

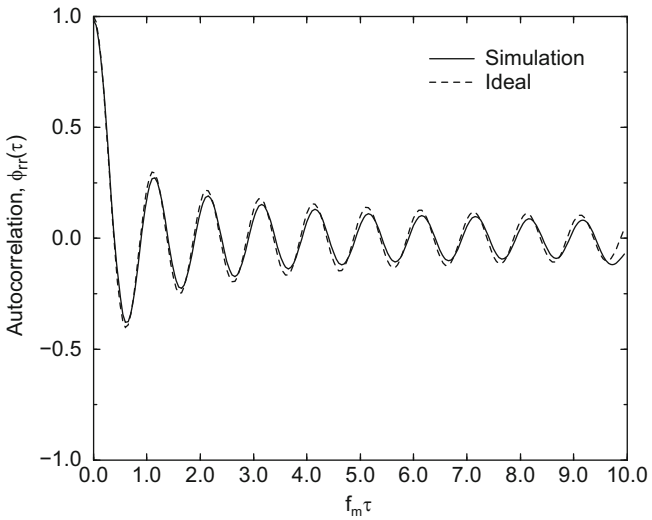

Fig. 2.40 Autocorrelation of in-phase and quadrature components obtained by using Clarke's method with $\theta_n = 2\pi n/N$ and $N = 16$ oscillators

The autocorrelation function in (2.259) was originally reported in Jakes' book [171] and it may be confused with the autocorrelation function of the faded envelope generated by (2.254) and (2.255). However, Jakes' method as described in (2.254) and (2.255) is a deterministic simulation model with no random parameters and, therefore, only the time averaged autocorrelation function exists. This time averaged autocorrelation function has been derived by Pop and Beaulieu as [264]

$$\hat{\phi}_{gg}(t, t+\tau) = \frac{1}{2N}\left(\cos(2\pi f_m \tau) + \cos(2\pi f_m(2t+\tau))\right) + \frac{1}{N}\sum_{n=1}^{M}\left(\cos(2\pi f_n \tau) + \cos(2\pi f_n(2t+\tau))\right). \quad (2.260)$$

From (2.260), it is apparent that the time averaged autocorrelation function obtained with the Jakes' method, $\hat{\phi}_{gg}(t, t+\tau)$, depends on the time variable t. Hence, Jakes' method yields a faded envelope that is not a stationary or even a wide-sense stationary random process. The root cause of this non-stationary behavior is the correlation that is introduced into the phases when using Jakes' method, i.e., the restrictions that $\hat{\phi}_n = -\hat{\phi}_{-N/2+n}$, $\hat{\phi}_{-n} = -\hat{\phi}_{N/2-n}$, $\hat{\phi}_n = -\hat{\phi}_{-n}, n = 1, \ldots, M$, and $\hat{\phi}_N = -\hat{\phi}_{-N}$. Due to the non-stationary behavior of the original Jakes simulator, and also due to the fact that the Jakes' method yields only a single faded envelope, a number of subsequent sum-of-sinusoids models have been proposed in the literature.

2.5.2.3 Method of Exact Doppler Spreads

Pätzold et al. [261] proposed a deterministic simulation model, called the method of exact Doppler spreads (MEDS). The method is derived by starting with an integral representation for the zero-order Bessel function of the first kind:

$$J_0(x) = \frac{2}{\pi}\int_0^{\pi/2} \cos(x\sin\theta)\mathrm{d}\theta \tag{2.261}$$

and replacing the integral by a series expansion as follows:

$$J_0(x) = \lim_{N_I\to\infty} \frac{2}{\pi}\sum_{n=1}^{N_I} \cos(x\sin\alpha_n)\Delta_\alpha, \tag{2.262}$$

where $\alpha_n \triangleq \pi(2n-1)/(4N_I)$ and $\Delta_\alpha \triangleq \pi/(2N_I)$. Hence,

$$\phi_{g_I g_I}(\tau) = \frac{1}{2}J_0(2\pi f_m\tau) = \lim_{N_I\to\infty}\frac{1}{2N_I}\sum_{n=1}^{N_I}\cos(2\pi f_{n,I}\tau) \tag{2.263}$$

where

$$f_{n,I} = f_m \sin\left[\frac{\pi}{2N_I}\left(n-\frac{1}{2}\right)\right]. \tag{2.264}$$

With finite N_I, the autocorrelation is

$$\phi_{g_I g_I}(\tau) = \frac{1}{2N_I}\sum_{n=1}^{N_I}\cos(2\pi f_{n,I}\tau). \tag{2.265}$$

Using the above result, the complex fading envelope, $g(t) = g_I(t) + jg_Q(t)$, is generated as

$$g_{I/Q}(t) = \sqrt{\frac{1}{N_{I/Q}}}\sum_{n=1}^{N_{I/Q}}\cos(2\pi f_{I/Q,n}t + \phi_{I/Q,n}). \tag{2.266}$$

where the phases $\phi_{I/Q,n}$ are chosen as arbitrary realizations of uniform random variables on the interval $[-\pi, \pi)$. Since the phases only need to be generated once, the MEDS model is an ergodic statistical (deterministic) model.

With the MEDS model, the autocorrelation functions of $g_I(t)$ and $g_Q(t)$ for infinite $N_{I/Q}$ match those of the 2-D isotropic scattering reference model. The quadrature components $g_I(t)$ and $g_Q(t)$ will also be uncorrelated if they do not share common frequencies. This condition can be achieved by choosing $N_Q = N_I + 1$.

2.5.2.4 Zheng & Xiao Statistical Model

Zheng and Xiao proposed a number of statistical simulation models [359, 360, 376, 377]. These models differ from one another in terms of the model parameters and, consequently, their statistical properties. Patel et al. [259] have shown that the model in [376] has the best overall performance, so the discussion here is limited to that model. The complex fading envelope, $g(t) = g_I(t) + jg_Q(t)$, is generated as

$$g_I(t) = \sqrt{\frac{1}{N}}\sum_{n=1}^{N}\cos[2\pi f_m t\cos(\theta_n) + \phi_{I,n}] \tag{2.267}$$

$$g_Q(t) = \sqrt{\frac{1}{N}}\sum_{n=1}^{N}\cos[2\pi f_m t\sin(\theta_n) + \phi_{Q,n}], \tag{2.268}$$

where the angles θ_n are

$$\theta_n = \frac{2\pi n - \pi + \theta}{4N}, \qquad n = 1, 2, \ldots, N, \tag{2.269}$$

and where θ, $\phi_{I,n}$, and $\phi_{Q,n}$ are all mutually independent uniform random variables on the interval $[-\pi, \pi)$.

The statistical correlation functions of the quadrature components have been computed by Zheng and Xiao [376] and match the desired functions in (2.246)–(2.248). The autocorrelation function of the squared-envelope is [259]

$$\phi_{\alpha^2\alpha^2}(\tau) = 1 + \frac{J_0(4\pi f_m \tau)}{4N} + \frac{1}{N^2} \sum_{n=1}^{N} \sum_{\substack{m=1 \\ n \neq m}}^{N} \mathrm{E}\{\cos[2\pi f_m \tau \cos\theta_n] \cos[2\pi f_m \tau \cos\theta_m]\}. \tag{2.270}$$

Unfortunately, there is no closed form expressions for the squared-envelope autocorrelation function due to the presence of the double summation in (2.270). The 2-D isotropic scattering reference model requires that

$$\phi_{\alpha^2\alpha^2}(\tau) = 1 + J_o^2(2\pi f_m \tau) \tag{2.271}$$

Clearly, as N increases the second term in (2.270) diminishes with $1/N$, while the third term should approach $J_o^2(2\pi f_m \tau)$.

2.5.2.5 Modified Hoeher Model

The modified Hoeher model is a statistical simulation model. The complex faded envelope, $g(t) = g_I(t) + jg_Q(t)$, is generated as [260]

$$g_I(t) = \sqrt{\frac{1}{N}} \sum_{n=1}^{N_I} \cos(2\pi f_{I,n} t + \phi_{I,n}) \tag{2.272}$$

$$g_Q(t) = \sqrt{\frac{1}{N}} \sum_{m=1}^{N_Q} \cos(2\pi f_{Q,m} t + \phi_{Q,m}), \tag{2.273}$$

where

$$f_{I/Q,n/m} = f_m \sin\left(\frac{\pi}{2} u_{I/Q,n/m}\right). \tag{2.274}$$

The Doppler frequencies $f_{I/Q,n/m}$ for the I and Q components are determined by the random variables $u_{I/Q,n/m}$, where the $u_{I/Q,n/m}$ are uniform on $(0, 1]$ and are mutually independent for all n and m. The random phases $\phi_{I/Q,n/m}$ are uniform on $[-\pi, \pi)$, are mutually independent for all n and m, and are also independent of the $u_{I/Q,n/m}$. For convenience, the number of sinusoids in the quadrature components are usually set equal, i.e., $N_I = N_Q = N$. This model is based on Hoeher's model in [165], but differs by considering only the positive Doppler frequencies. Hence, it is referred to here as the modified Hoeher model.

Observe that the MEDS and modified Hoeher models are the same except for the arguments of the sine function in (2.264) and (2.274), respectively. The set of numbers $\{(n - 1/2)/N_i, i = 1, \ldots, N_i\}$ are uniformly spaced on the interval $(0, 1]$ in the MEDS model, while the $u_{I/Q,n/m}$ are uniformly distributed on the interval $(0, 1]$ in the modified Hoeher model.

The statistical correlation functions for the modified Hoeher model match those of the 2-D isotropic scattering reference model. The squared-envelope autocorrelation function for the modified Hoeher model is [259]

$$\phi_{\alpha^2\alpha^2}(\tau) = 1 + \frac{1}{4N} J_0(4\pi f_m \tau) + \frac{N-1}{N} J_0^2(2\pi f_m \tau) \tag{2.275}$$

which differs from the reference model in (2.82) for finite N.

The time-averaged correlation functions of the modified Hoeher model can be derived as follows [259]:

$$\hat{\phi}_{g_I g_I}(\tau) = \lim_{T\to\infty} \frac{1}{2T} \int_{-T}^{T} g_I(t) g_I(t+\tau) \mathrm{d}t$$
$$= \frac{1}{2N} \sum_{n=1}^{N} \cos(2\pi f_{I,n}\tau) \tag{2.276}$$

$$\hat{\phi}_{g_Q g_Q}(\tau) = \frac{1}{2N} \sum_{n=1}^{N} \cos(2\pi f_{Q,n}\tau) \tag{2.277}$$

$$\hat{\phi}_{g_I g_Q}(\tau) = \hat{\phi}_{g_Q g_I}(\tau) = 0 \tag{2.278}$$

$$\hat{\phi}_{gg}(\tau) = \frac{1}{2} \lim_{T\to\infty} \frac{1}{2T} \int_{-T}^{T} g^*(t) g(t+\tau) \mathrm{d}t$$
$$= \frac{1}{4N} \sum_{n=1}^{N} \cos(2\pi f_{I,n}\tau) + \cos(2\pi f_{Q,n}\tau). \tag{2.279}$$

The variances of the time-averaged autocorrelation and cross-correlation of the quadrature components, and the variance of the autocorrelation of the complex envelope $g(t)$ are [259]

$$\mathrm{Var}[\hat{\phi}_{g_I g_I}(\tau)] = \mathrm{Var}[\hat{\phi}_{g_Q g_Q}(\tau)] = \frac{1 + J_0(4\pi f_m \tau) - 2J_0^2(2\pi f_m \tau)}{8N} \tag{2.280}$$

$$\mathrm{Var}[\hat{\phi}_{g_I g_Q}(\tau)] = \mathrm{Var}[\hat{\phi}_{g_Q g_I}(\tau)] = 0 \tag{2.281}$$

$$\mathrm{Var}\hat{\phi}_{gg}(\tau) = \frac{1 + J_0(4\pi f_m \tau) - 2J_0^2(2\pi \tau)}{16N}. \tag{2.282}$$

2.5.3 *Multiple Uncorrelated Faded Envelopes*

In many cases it is necessary to generate multiple uncorrelated faded envelopes. Jakes [171] suggested a method to modify the method in Sect. 2.5.2.2 to generate up to M fading envelopes. However, the method yields faded envelopes that exhibit very large cross-correlations at some non-zero lags and, therefore, the method is not recommended. Dent et al. [93] suggested a modification to Jakes' approach that uses orthogonal Walsh-Hadamard codewords to decorrelate the multiple faded envelopes. However, the approach generates multiple faded envelopes that still have significant cross-correlation functions at large lags. Several simulation models to generate multiple faded envelopes are now discussed that have low cross-correlations.

2.5.3.1 Zheng and Xiao Statistical Model

The Zheng and Xiao statistical method can be easily extended to generate multiple faded envelopes. The kth complex faded envelope, $g_k(t) = g_{I,k}(t) + jg_{Q,k}(t)$, is generated as

$$g_{I,k}(t) = \sqrt{\frac{1}{N}} \sum_{n=1}^{N} \cos[2\pi f_m t \cos(\theta_{n,k}) + \phi_{I,n,k}] \tag{2.283}$$

$$g_{Q,k}(t) = \sqrt{\frac{1}{N}} \sum_{n=1}^{N} \cos[2\pi f_m t \sin(\theta_{n,k}) + \phi_{Q,n,k}], \tag{2.284}$$

where

$$\theta_{n,k} = \frac{2\pi n - \pi + \theta_k}{4N}, \qquad n = 1, 2, \ldots, N \tag{2.285}$$

and where θ_k, $\phi_{I,n,k}$, and $\phi_{Q,n,k}$ are all uniform on $[-\pi, \pi)$, and all values are mutually independent. The $g_k(t)$ are all uncorrelated.

2.5.3.2 Li & Huang Model

Li and Huang proposed a deterministic fading model that can generate multiple uncorrelated faded envelopes. They assume that P uncorrelated fading envelopes are required, each of which is composed of N sinusoids. The kth complex faded envelope, $g_k(t) = g_{I,k}(t) + jg_{Q,k}(t)$, is generated as [202]

$$g_{I,k}(t) = \sqrt{\frac{1}{N}} \sum_{n=0}^{N-1} \cos(2\pi f_m \cos\theta_{n,k} t + \phi_{I,n,k}) \tag{2.286}$$

$$g_{Q,k}(t) = \sqrt{\frac{1}{N}} \sum_{n=0}^{N-1} \sin(2\pi f_m \sin\theta_{n,k} t + \phi_{Q,n,k}). \tag{2.287}$$

The phases $\phi_{I,n,k}$ and $\phi_{Q,n,k}$ arbitrary realizations of independent random variables uniform on $[-\pi, \pi)$, and

$$\theta_{n,k} = \frac{2\pi n}{N} + \frac{2\pi k}{PN} + \theta_{00}, \quad n = 0, \ldots, N, k = 0, \ldots, P-1, \tag{2.288}$$

where θ_{00} is an initial arrival angle chosen to satisfy $0 < \theta_{00} < 2\pi/PN$ and $\theta_{00} \neq \pi/PN$. Although the Li & Huang model generates uncorrelated faded envelopes, it fails to satisfy Eqs. (2.29) and (2.82) of the reference model [371].

2.5.3.3 Zajić & Stüber Deterministic Model

With the Zajić & Stüber deterministic model the kth faded envelope, $g_k(t) = g_{I,k}(t) + jg_{Q,k}(t)$, is generated as [372]

$$g_{I,k}(t) = \sqrt{\frac{2}{N}} \sum_{n=0}^{M} a_n \cos(2\pi f_m t \cos(\theta_{n,k}) + \phi_{n,k}) \tag{2.289}$$

$$g_{Q,k}(t) = \sqrt{\frac{2}{N}} \sum_{n=0}^{M} b_n \sin(2\pi f_m t \cos(\theta_{n,k}) + \phi_{n,k}), \tag{2.290}$$

where

$$M = \frac{1}{2}\left(\frac{N}{2} - 1\right), \tag{2.291}$$

and

$$a_n = \begin{cases} 2\cos(\beta_n), & n = 1, \ldots, M \\ \sqrt{2}\cos(\beta_n), & n = 0 \end{cases} \tag{2.292}$$

$$b_n = \begin{cases} 2\sin(\beta_n), & n = 1, \ldots, M \\ \sqrt{2}\sin(\beta_n), & n = 0 \end{cases} \tag{2.293}$$

$$\beta_n = \frac{\pi n}{M}, \quad n = 0, \ldots, M \tag{2.294}$$

$$\theta_{n,k} = \frac{2\pi n}{N} + \frac{2\pi k}{PN} + \theta_{0,0}\ ,\ \ n = 0, \ldots, M\ ,\ \ k = 0, \ldots, P-1. \tag{2.295}$$

This method will generate P faded envelopes, where $1 \leq P \leq M$.

The angle $\theta_{n,k}$ is chosen so that the arrival angles associated with the kth faded envelope are obtained by rotating the arrival angles of the $(k-1)$th faded envelope by $2\pi/PN$. This ensures an asymmetrical arrangement of arrival angles, which minimizes the correlation between the multiple faded envelopes. The initial arrival angle, $\theta_{0,0}$, can be optimized to minimize the correlation between the quadrature components of each faded envelope. This results in the choice $\theta_{0,0} = 0.2\pi/PN$, a value optimized by experimentation. Finally, the phases $\phi_{n,k}$ are chosen as arbitrary realizations of uniform random variables on the interval $[0, 2\pi)$.

For the Zajić & Stüber deterministic model, the auto- and cross-correlation functions of the quadrature components, the auto- and cross-correlation functions of the multiple faded envelopes, and the squared-envelope autocorrelation are, respectively, [372]

$$\begin{aligned}
\lim_{N\to\infty} \phi_{g_{I,k}g_{I,k}}(\tau) &= \lim_{N\to\infty} \frac{2}{N} \sum_{n=0}^{M} \frac{a_n^2}{2} \cos(2\pi f_m \tau \cos(\theta_{n,k})) \\
&= \frac{1}{2} J_0(2\pi f_m \tau) + \frac{1}{2} J_4(2\pi f_m \tau),
\end{aligned} \tag{2.296}$$

$$\begin{aligned}
\lim_{N\to\infty} \phi_{g_{Q,k}g_{Q,k}}(\tau) &= \lim_{N\to\infty} \frac{2}{N} \sum_{n=0}^{M} \frac{b_n^2}{2} \cos(2\pi f_m \tau \sin(\theta_{n,k})) \\
&= \frac{1}{2} J_0(2\pi f_m \tau) - \frac{1}{2} J_4(2\pi f_m \tau),
\end{aligned} \tag{2.297}$$

$$\phi_{g_{I,k}g_{Q,k}}(\tau) = \phi_{g_{Q,k}g_{I,k}}(\tau) = \phi_{g_k g_{l\neq k}}(\tau) = 0, \tag{2.298}$$

$$\begin{aligned}
\lim_{N\to\infty} \phi_{g_k g_k}(\tau) &= \lim_{N\to\infty} \frac{2}{N} \sum_{n=0}^{M} \frac{a_n^2}{2} \cos(2\pi f_m \tau \cos(\theta_{n,k})) \\
&\quad + \lim_{N\to\infty} \frac{2}{N} \sum_{n=0}^{M} \frac{b_n^2}{2} \cos(2\pi f_m \tau \sin(\theta_{n,k})) \\
&= \frac{1}{2} J_0(2\pi f_m \tau),
\end{aligned} \tag{2.299}$$

$$\begin{aligned}
\phi_{\alpha_k^2\alpha_k^2}(\tau) = &\ \frac{2}{N^2} \sum_{n=0}^{M} a_n^4 + \frac{2}{N^2} \sum_{n=0}^{M} b_n^4 + \frac{1}{2} \phi_{g_{I,k}g_{I,k}}^2(\tau) \\
&+ \frac{1}{2} \phi_{g_{Q,k}g_{Q,k}}^2(\tau) + \phi_{g_{I,k}g_{Q,k}}^2(\tau) \\
= &\ \frac{1}{4} J_0^2(\omega_m \tau),
\end{aligned} \tag{2.300}$$

where $J_0(\cdot)$ is the zero-order Bessel function of the first kind and $J_4(\cdot)$ is the fourth-order Bessel function of the first kind.

Figures 2.41 and 2.42 confirm that, for $M = 8$, the auto- and cross-correlations of the quadrature components and the auto- and cross-correlation of the multiple faded envelopes approach values given by (2.296)–(2.299), respectively. The model satisfies (2.247) and (2.248) of the reference model. However, the auto-correlations of the quadrature components and the auto-correlation of the squared-envelope are close to, but do not perfectly match, (2.246) and (2.249).

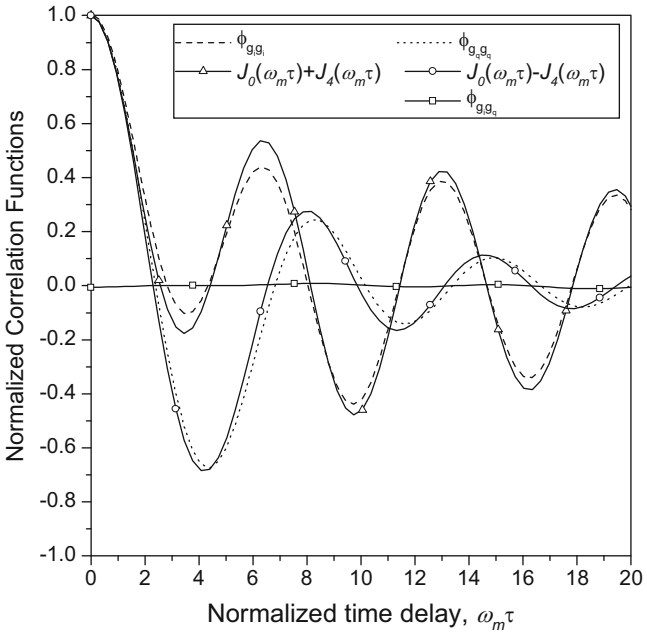

Fig. 2.41 Theoretical and simulated auto-correlation functions and the cross-correlation function of the in-phase and quadrature components of the Zajić and Stüber deterministic model

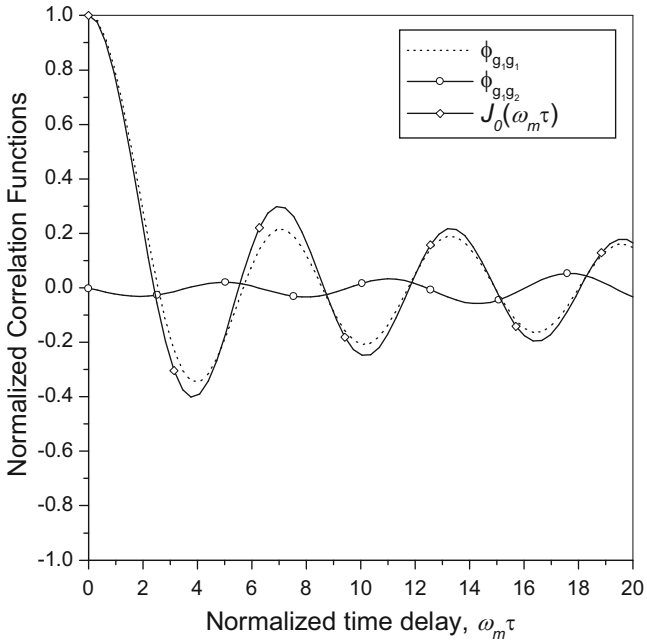

Fig. 2.42 Theoretical and simulated auto-correlation functions and the cross-correlation function of the first and the second complex envelope of the Zajić and Stüber deterministic model

2.5.3.4 Zajić & Stüber Statistical Model

The Zajić & Stüber deterministic model can be modified to better match the statistical properties of the reference model by introducing randomness into the model. To do so, the kth faded envelope, $g_k(t) = g_{I,k}(t) + jg_{Q,k}(t)$, is generated as

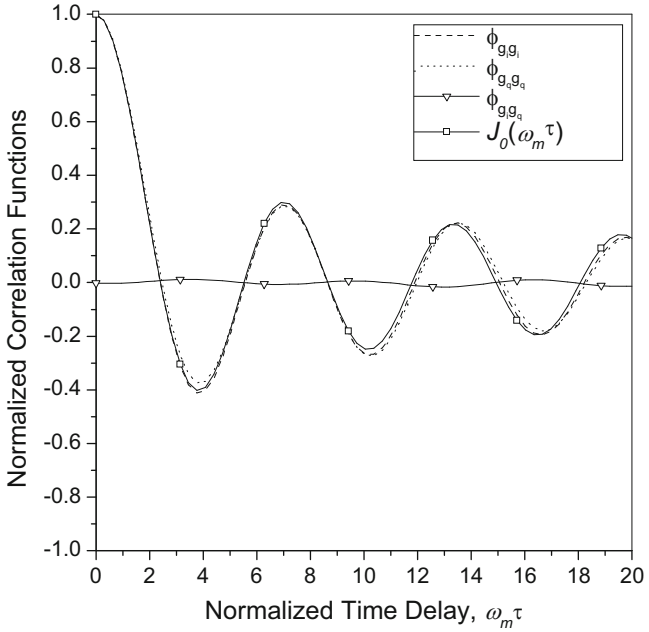

Fig. 2.43 Theoretical and simulated autocorrelation functions and the cross-correlation function of the quadrature components of the Zajić and Stüber statistical model

$$g_{I,k}(t) = \sqrt{\frac{2}{N}} \sum_{n=0}^{M} \cos(\beta_{n,k}) \cos(2\pi f_m t \cos(\theta_{n,k}) + \phi_{n,k}) \tag{2.301}$$

$$g_{Q,k}(t) = \sqrt{\frac{2}{N}} \sum_{n=0}^{M} \sin(\beta_{n,k}) \sin(2\pi f_m t \cos(\theta_{n,k}) + \phi_{n,k}), \tag{2.302}$$

where $M = N/4$,

$$\theta_{n,k} = \frac{2\pi n}{N} + \frac{2\pi k}{PN} + \frac{\alpha - \pi}{N}, \quad n = 1, \ldots, M, \; k = 0, \ldots, P-1, \tag{2.303}$$

and $\phi_{n,k}$, $\beta_{n,k}$, and α are independent uniform random variables on the interval $[-\pi, \pi)$. The parameter $\theta_{n,k}$ is chosen in the following manner: the arrival angles of the kth faded envelope are obtained by rotating the arrival angles of the $(k-1)$th faded envelope by $\pi/2MN$. Randomness in the Doppler frequencies is introduced by random variable α. Again, this method will generate P faded envelopes, where $1 \leq P \leq M$.

Figures 2.43 and 2.44 show that, for $M = P = 8$ and $N_{\text{stat}} = 30$ simulation trials, the auto- and cross-correlations of the quadrature components, and the auto- and cross-correlations of the complex faded envelopes approach those of the reference model in (2.246) and (2.248). Although not shown, the squared-envelope autocorrelation also approaches that of the reference model in (2.249).

2.5.3.5 SoS Simulation Model Comparisons

This section compares the various sum-of-sinusoids simulation models for fixed-to-mobile channels. A more detailed comparison is available in [259, 371]. In all simulations, a normalized sampling period $f_m T_s = 0.05$ and $M = P = 8$ is used. However, for the MEDS model $N_I = 8$ and $N_Q = 9$ are used to obtain uncorrelated quadrature components in the faded envelope. Note that in the Li & Huang, MEDS and Zajić & Stüber deterministic models, the random phases associated with the sinusoidal components are computed before the actual simulation starts, because an ergodic statistical ("deterministic")

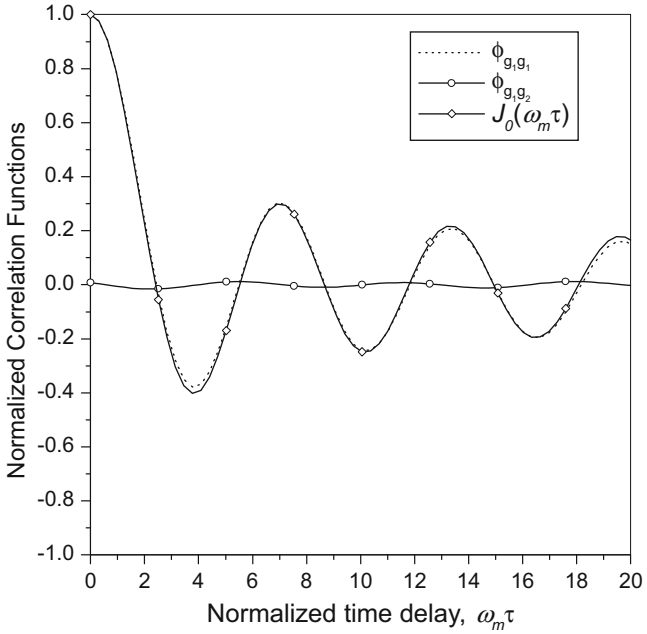

Fig. 2.44 Theoretical and simulated autocorrelation functions and the cross-correlation function of the first and the second complex envelopes of the Zajić and Stüber statistical model

simulator needs only one simulation trial. During the simulations, all parameters are kept constant to provide simulation results that are always the same, i.e., deterministic.

In the Zajić & Stüber deterministic model, the following set of uniformly distributed random phases (in radians) are used: $\phi_{n,0}$ =[4.0387, 1.7624, 2.7844, 1.5590, 0.9523, 1.2972, 5.7420, 3.6592, 4.3548] and $\phi_{n,1}$ =[5.3798, 3.0556, 2.1528, 2.6296, 0.7457, 3.2572, 6.1027, 2.0670, 2.1304]. The same set of phases is used in MEDS model, for $g_Q(t)$, while for $g_I(t)$ the following set is used $\phi_{I,n,0}$ =[2.2107, 5.3033, 2.4634, 1.0679, 2.2818, 4.6113, 0.7513, 0.7383] and $\phi_{I,n,1}$ =[3.2627, 4.7036, 0.5824, 2.1097, 4.6264, 5.4790, 0.9391, 0.2017]. Li & Huang's model uses the same set of phases as the MEDS model for $g_I(t)$, while for $g_Q(t)$ the following set is used: $\phi_{Q,n,0}$ =[2.6372, 4.7339, 4.9865, 5.7784, 5.3059, 2.3099, 3.8994, 4.5933], and $\phi_{Q,n,1}$ =[4.1175, 2.4616, 3.9403, 4.3911, 2.4948, 2.5981, 4.115, 5.2610].

Figure 2.45 compares the cross-correlation functions of the quadrature components obtained with the various simulation models. Since the Zheng & Xiao model is a statistical model, the plotted correlation functions have been averaged over $N_{\text{stat}} = 50$ trials. Figure 2.45 shows that the Zajić & Stüber deterministic model yields a lower cross-correlation between the I and Q components of the faded envelope. Figure 2.46 compares the cross-correlation functions of two faded envelopes. Again, since the Zheng & Xiao model is a statistical model, the plotted cross-correlation function has been averaged over $N_{\text{stat}} = 50$ trials. The Li & Huang, Zheng & Xiao, and Zajić & Stüber deterministic models all yield a low cross-correlation between different faded envelopes.

Figures 2.47 and 2.48 compare the cross-correlation functions of the quadrature components and the cross-correlation functions of two faded envelopes, respectively, for the various statistical models. For the Zheng & Xiao model averaging is done over $N_{\text{stat}} = 100$ trials, while for the Zajić & Stüber statistical model averaging is done over $N_{\text{stat}} = 30$ and $N_{\text{stat}} = 50$ trials. From Fig. 2.47, the Zajić & Stüber statistical model with $N_{\text{stat}} = 30$ performs similar when compared to the Zheng & Xiao model with $N_{\text{stat}} = 100$. Increasing the number of trials in the Zajić & Stüber statistical model to $N_{\text{stat}} = 50$ yields a significantly lower cross-correlation between the quadrature components of the complex faded envelope. Furthermore, with $N_{\text{stat}} = 50$ trials, the Zajić & Stüber statistical model achieves a larger de-correlation between different complex envelopes than the Zheng & Xiao model with $N_{\text{stat}} = 100$ trials. Figures 2.47, 2.48, and 2.49 show that with the Zajić & Stüber statistical model, adequate statistics can be achieved with $N_{\text{stat}} = 30$ trials.

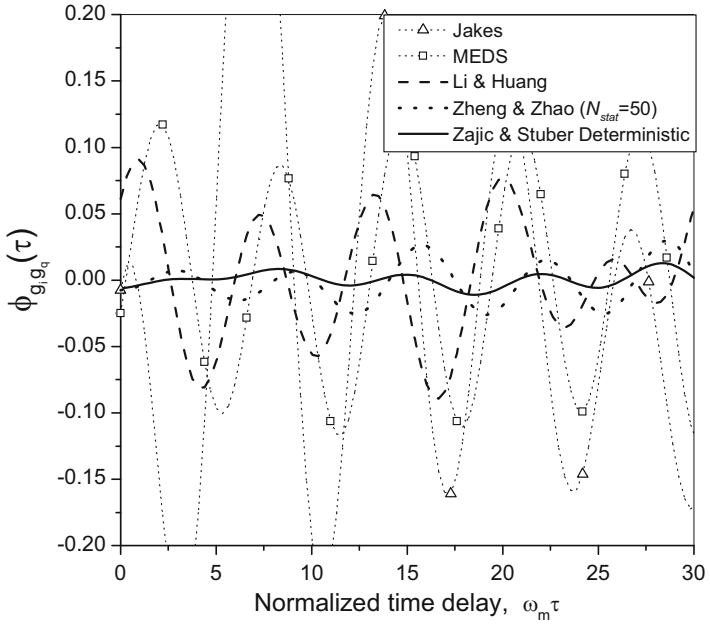

Fig. 2.45 Normalized cross-correlation function between the quadrature components of the faded envelope for various simulation models

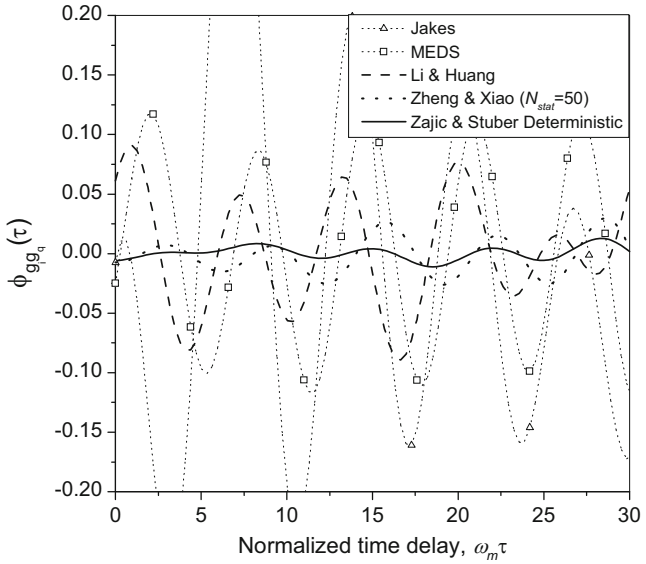

Fig. 2.46 Normalized cross-correlation function between the first and second faded envelopes for various simulation models

2.5.4 Wide-Band Simulation Models

Wide-band channels can be modeled by a tapped delay line with irregularly spaced tap delays. Each channel tap is the superposition of a large number of scattered plane waves that arrive with approximately the same delay and, therefore, the channel taps will undergo fading. The wide-band channel has the time-variant impulse response

$$g(t,\tau) = \sum_{i=1}^{\ell} g_i(t)\delta(\tau - \tau_i), \tag{2.304}$$

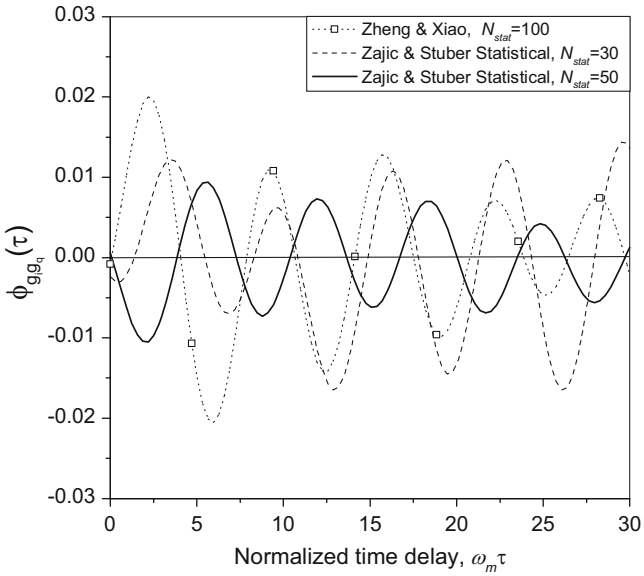

Fig. 2.47 Normalized cross-correlation function of the in-phase and quadrature components for various statistical simulation models

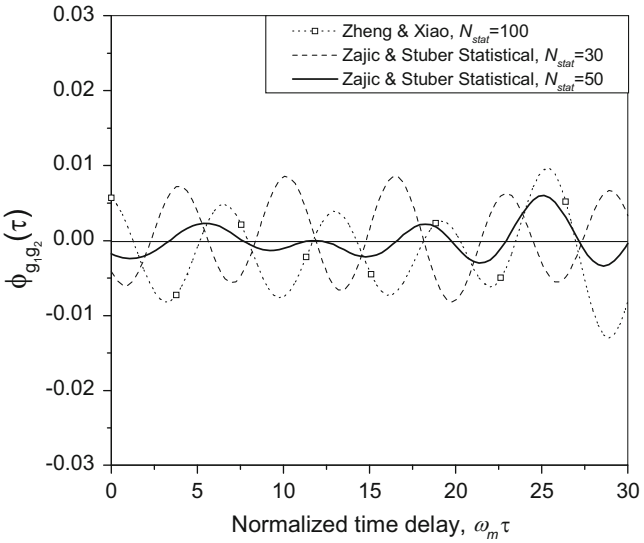

Fig. 2.48 Normalized cross-correlation function of the first and the second complex envelope for various statistical simulation models

where ℓ is the number of channel taps, and the $\{g_i(t)\}$ and $\{\tau_i\}$ are the complex gains and path delays associated with the channel taps. The corresponding time-variant transfer function is

$$T(f,t) = \sum_{i=1}^{\ell} g_i(t) e^{j2\pi f \tau_i}. \tag{2.305}$$

Usually, the tap delays are multiples of some very small delay τ, such that $\tau_i = K_i\tau\ ,\ \ i = 1,\ldots,\ell$, which yields the sparse tapped delay line channel model shown in Fig. 2.50, sometimes called the "τ-spaced" model. Many of the tap coefficients in the tapped delay line are zero, reflecting the fact that no energy is received at these delays. Also, the K_i should be chosen to be relatively prime so as to prevent any periodicity in the channel. Assuming a WSSUS channel, the autocorrelation function of the time-variant channel impulse response in (2.304) is

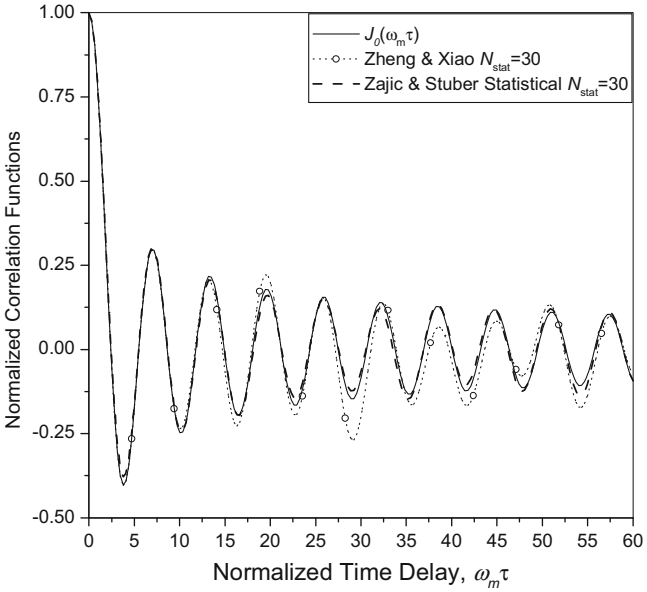

Fig. 2.49 Theoretical and simulated normalized auto-correlation functions for the various statistical simulation models

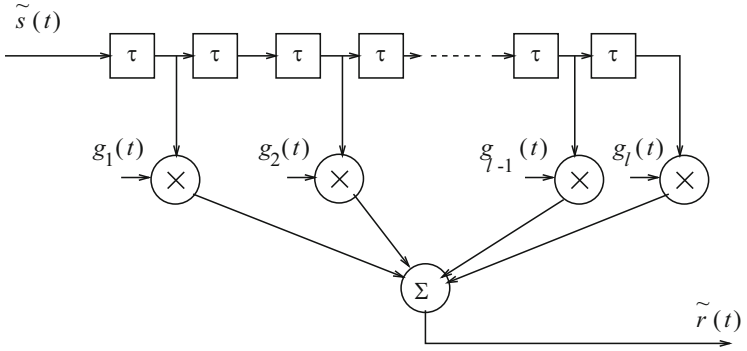

Fig. 2.50 Sparse tapped delay line model for wide-band multipath-fading channels

$$\phi_g(t, s; \tau, \eta) = \mathrm{E}[g(t, \tau)g^*(s, \eta)] \tag{2.306}$$

$$= \sum_{i=1}^{\ell} \phi_{g_i g_i}(\Delta t)\delta(\tau - \tau_i)\delta(\eta - \tau) \tag{2.307}$$

It follows that the channel correlation function is

$$\psi_g(\Delta t; \tau) = \sum_{i=1}^{\ell} \phi_{g_i g_i}(\Delta t)\delta(\tau - \tau_i) \tag{2.308}$$

and the power-delay profile is

$$\psi_g(\tau) = \psi_g(0; \tau) = \sum_{i=1}^{\ell} \Omega_i \delta(\tau - \tau_i), \tag{2.309}$$

where $\Omega_i = \phi_{g_i g_i}(0)$ is the envelope power of the ith channel tap, and the total envelope power is

$$\Omega_p = \sum_{k=1}^{\ell} \Omega_k. \tag{2.310}$$

Hence, the channel can be described by the power profile

$$\mathbf{\Omega} = (\Omega_0,\ \Omega_1, \ldots, \Omega_\ell). \tag{2.311}$$

and the delay profile

$$\boldsymbol{\tau} = (\tau_1,\ \tau_2, \ldots, \tau_\ell). \tag{2.312}$$

Taking the Fourier transform of (2.308) with respect to the τ variable yields the spaced-time spaced-frequency correlation function

$$\phi_T(\Delta f; \Delta t) = \sum_{i=1}^{\ell} \phi_{g_i g_i}(\Delta t) \mathrm{e}^{-j2\pi \Delta f \tau_i} \tag{2.313}$$

Sometimes the channel taps are assumed to have the same time correlation function, such that

$$\phi_{g_i g_i}(\Delta t) = \Omega_i \phi_t(\Delta t)\ ,\ \ i = 1, \ldots, \ell. \tag{2.314}$$

For example, if each tap is characterized by 2-D isotropic scattering, then $\phi_t(\Delta t) = \frac{1}{2} J_0(2\pi f_m \Delta t)$. In this case the spaced-time spaced-frequency correlation function has the separable form

$$\phi_T(\Delta f; \Delta t) = \phi_t(\Delta t)\phi_f(\Delta f), \tag{2.315}$$

where

$$\phi_f(\Delta f) = \sum_{i=1}^{\ell} \Omega_i \mathrm{e}^{-j2\pi \Delta f \tau_i}. \tag{2.316}$$

2.5.4.1 COST 207 Models

The COST 207 models were developed for the GSM cellular system. Four different Doppler spectra, $S_{gg}(f)$ are specified in the COST 207 models [79]. First define the function

$$G(A, f_1, f_2) = A \exp\left\{ -\frac{(f - f_1)^2}{2 f_2^2} \right\} \tag{2.317}$$

which has the shape of a Gaussian probability density function with mean f_1 and variance f_2^2. COST 207 specifies the following Doppler spectra:

a) CLASS is the classical Doppler spectrum, and is used for excess path delays not exceeding 500 ns ($\tau_i \leq 500$ ns);

$$\text{(CLASS)} \qquad S_{gg}(f) = \frac{A}{\sqrt{1 - (f/f_m)^2}}\ , \qquad |f| \leq f_m \tag{2.318}$$

Multipath components arriving with short path delays are those that experience local scattering around the MS. In the COST 207 models, the local scattering is modeled as 2-D isotropic scattering and the MS is assumed to have an isotropic antenna.

b) GAUS1 is the sum of two Gaussian functions, and is used for excess path delays ranging from 500 ns to 2 μs; (500 ns $\leq$ $\tau_i \leq 2$ μs)

$$\text{(GAUS1)} \qquad S_{gg}(f) = G(A, -0.8 f_m, 0.05 f_m) + G(A_1, 0.4 f_m, 0.1 f_m), \tag{2.319}$$

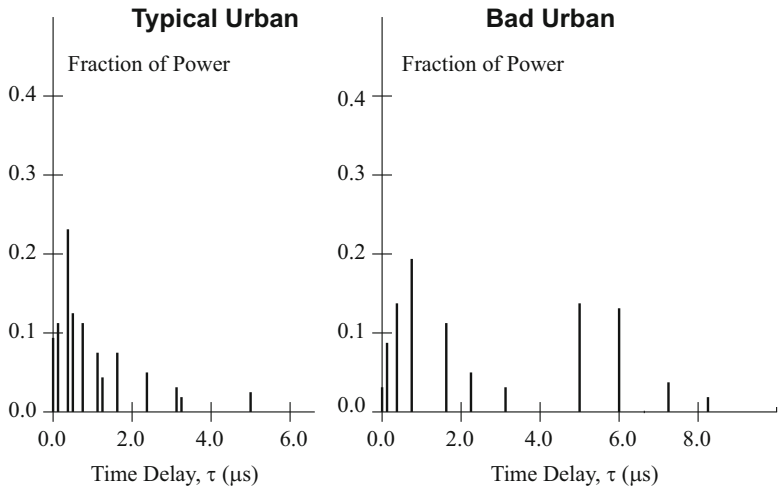

Fig. 2.51 COST 207 typical urban (TU) and bad urban (BU) power-delay profiles

where A_1 is 10 dB below A. The GAUS1 Doppler spectra implies two clusters of scattering objects. The larger cluster is located behind the MS such that the mean angle-of-arrival is $\theta = \cos^{-1}(-0.8) = \pm 143°$. A smaller cluster is located in front of the MS such that the mean angle-of-arrival is $\theta = \cos^{-1}(0.4) = \pm 66°$.

c) GAUS2 is the sum of two Gaussian functions, used for excess path delays exceeding 2 μs; ($\tau_i > 500$ ns)

$$\text{(GAUS2)} \qquad S_{gg}(f) = G(B, 0.7f_m, 0.1f_m) + G(B_1, -0.4f_m, 0.15f_m), \tag{2.320}$$

where B_1 is 15 dB below B. Like GAUS1, GAUS2 implies two clusters of scattering objects such that the mean angles-of-arrival are $\theta = \cos^{-1}(0.7) = \pm 45°$ and $\theta = \cos^{-1}(-0.4) = \pm 113°$.

d) RICE is a combination of 2-D isotropic scattering and a line-of-sight component;

$$\text{(RICE)} \qquad S_{gg}(f) = \frac{0.41}{2\pi f_m \sqrt{1-(f/f_m)^2}} + 0.91\delta(f - 0.7f_m)\,, \qquad |f| \le f_m \tag{2.321}$$

The RICE scattering environment is depicted in Fig. 2.7, where $\theta_0 = \cos^{-1}(0.7) = 45°$.

Several power-delay profiles have been defined in the COST 207 study for different propagation environments [79]. Typical urban (TU) (non-hilly) and bad urban (BU) (hilly) discrete power-delay profiles are shown in Fig. 2.51 and Table 2.7 of Appendix 2A. In these figures and tables, the fractional power sums to unity, i.e., the total envelope power Ω_p is normalized to unity. Also notice that the discrete tap delays in Table 2.7 are chosen to avoid a regular spacing between taps so as to avoid any periodicities in the time-variant transfer function. Sometimes it is desirable to use a smaller number of taps to reduce the computational requirements of computer simulations. Figure 2.52 and Table 2.8 of Appendix 2A show the 6-ray reduced typical urban and reduced bad urban channel. Also provided in Appendix 2A are discrete power-delay profiles for rural (non-hilly) areas (RA) in Table 2.9, typical hilly terrain (HT) in Table 2.10, and reduced hilly terrain (HT) in Table 2.11.

2.5.4.2 COST 259 Models

The COST 207 models were developed for the GSM system having a channel bandwidth of 200 kHz. However, the COST 207 models are not be appropriate for wideband CDMA (WCDMA) systems having 5, 10, and 20 MHz channel bandwidths. Similar to the COST 207 models, typical realizations have been developed by 3GPP for the COST 259 models [113]. These are tabulated in Tables 2.12, 2.13, and 2.14 of Appendix 2B for typical urban (TU), rural area (RA), and hilly terrain (HT). Notice that the tap delays in the 3GPP realizations of the COST 259 models have a resolution of 0.001 μs as compared to the 0.1 μs resolution used in the COST 207 models. Moreover, a large number of paths (20) are included to ensure that the frequency domain correlation properties are realistic, which is important for wide-band systems.

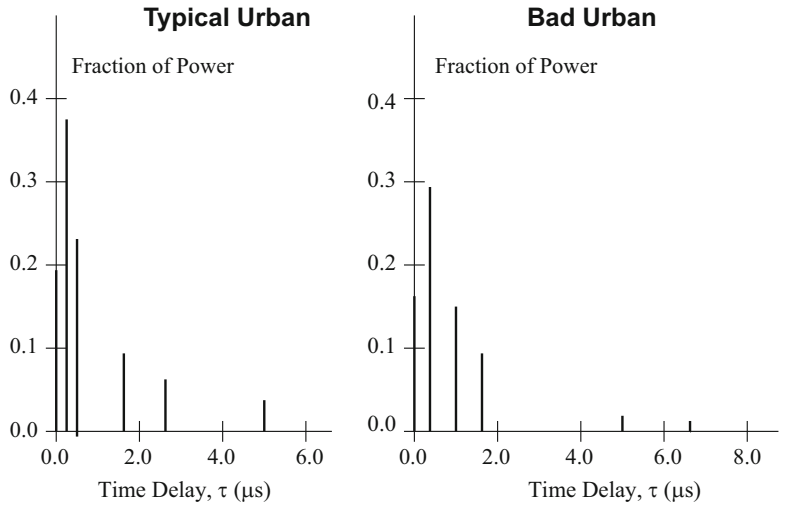

Fig. 2.52 COST 207 reduced typical urban (TU) and bad urban (BU) power-delay profiles

2.5.4.3 ITU Models

Several models have been developed by the International Telecommunications Union (ITU) for indoor office, outdoor to indoor and pedestrian, and vehicular—high antenna [276]. These models are summarized in Tables 2.15 and 2.16 of Appendix 2C.

2.5.5 Mobile-to-Mobile Simulation Models

An important distinction between F-to-M cellular land mobile radio channels and M-to-M channels arises due to the scattering and mobility at both ends of the link. In contrast to cellular F-to-M channels, it is natural for both the transmitter and the receiver to have low elevation antennas in M-to-M applications. This results in local scattering around both the transmitter and receiver antennas which led to the 2-D isotropic scattering assumption in the Akki and Haber reference model [14].

2.5.5.1 Akki & Haber Model

An obvious M-to-M channel simulation model follows from (2.146), where N sinusoidal components are used with randomly generated angles of departure and arrival, and random phases. This model is called the Akki & Haber (A & H) model, since they originally proposed the model in (2.146). Although the ensemble averaged statistical correlations of this model, given in (2.147), do not depend on N, the time averaged correlations functions [denoted by $\hat{\phi}(\cdot)$] do depend on N [259]. For example, the time average auto-correlation of the complex envelope is

$$\begin{aligned}\hat{\phi}_{gg}(\tau) &= \lim_{T\to\infty}\frac{1}{2T}\int_{-T}^{T}\frac{1}{2}g^*(t)g(t+\tau)\mathrm{d}t \\ &= \frac{1}{2N}\sum_{n=1}^{N} e^{j(2\pi f_m^T\cos(\alpha_n^T)\tau + 2\pi f_m^R\cos(\alpha_n^R)\tau)}.\end{aligned} \tag{2.322}$$

The time average correlations are random due to the random angles of departure and arrival and, hence, they will vary with each simulation trial. The variance $\mathrm{Var}[\hat{\phi}(\cdot)] = \mathrm{E}[|\hat{\phi}(\cdot) - \lim_{N\to\infty}\phi(\cdot)|^2]$ provides a measure of the usefulness of the model with finite N. A lower variance means that a smaller number of simulation trials are needed to achieve the desired statistical properties to a given degree of accuracy and, hence, the corresponding simulation model is better. The variance of

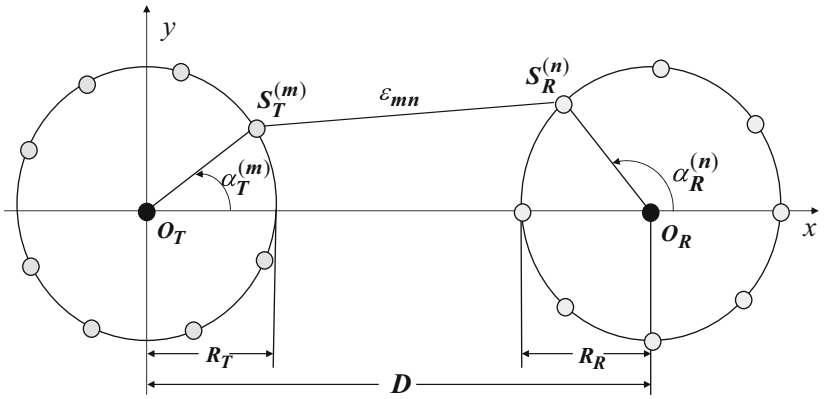

Fig. 2.53 Double-ring model for M-to-M radio propagation with isotropic scattering at the transmitter and receiver

the time averaged auto-correlation and the cross-correlation of the quadrature components of the complex envelope are as follows [259]:

$$\begin{aligned}\mathrm{Var}[\hat{\phi}_{g_I g_I}(\tau)] &= \mathrm{Var}[\hat{\phi}_{g_Q g_Q}(\tau)] \\ &= \frac{1 + J_0(4\pi f_m^T \tau) J_0(4\pi a f_m^T \tau) - 2J_0^2(2\pi f_m^T \tau) J_0^2(2\pi a f_m^T \tau)}{8N}\end{aligned} \tag{2.323}$$

$$\mathrm{Var}[\hat{\phi}_{g_I g_Q}(\tau)] = \mathrm{Var}[\hat{\phi}_{g_Q g_I}(\tau)] = \frac{1 - J_0(4\pi f_m^T \tau) J_0(4\pi a f_m^T \tau)}{8N} \tag{2.324}$$

$$\mathrm{Var}[\hat{\phi}_{gg}(\tau)] = \frac{1 - J_0^2(2\pi f_m^T \tau) J_0^2(2\pi a f_m^T \tau)}{4N}. \tag{2.325}$$

2.5.5.2 Double Ring Simulation Models

To develop other M-to-M channel simulation models, a double-ring concept is applied that defines two rings of isotropic scatterers, one placed around the transmitter and another placed around the receiver as shown in Fig. 2.53. Assuming omnidirectional antennas at both ends, the waves from the transmitter antenna first arrive at the scatterers located on the transmitter ring. Considering these fixed scatterers as "virtual base stations (VBS)," the communication link from each VBS to the receiver is treated like an F-to-M link. The signals from each VBS arrive at the receiver antenna uniformly from all directions in the horizontal plane due to isotropic scatterers located on the receiver end ring. It should be noted here that the double-ring model has been often used in various forms, for example in [50] and the references therein for the study and simulation of the spatial correlations and capacity in multiple-input multiple-output (MIMO) systems, where multiple antennas are used at both the transmitter and receiver. Here the double-ring model is applied to M-to-M channel modeling. The use of a double-ring model has a strong rationale. First and foremost, it is a mathematically convenient reference model. Second, considering the lack of detailed and standardized M-to-M channel models, the model provides a generic scenario with isotropic scattering at both ends of the communication link. Finally, empirical Doppler spectrum measurements for vehicle-to-vehicle communication links [9, 222] more or less match those predicted by the double-ring model.

Using the double-ring model in Fig. 2.53, the complex faded envelope can be written as

$$g(t) = \sqrt{\frac{2}{NM}} \sum_{m=1}^{N} \sum_{n=1}^{M} \mathrm{e}^{-j2\pi \varepsilon_{mn}/\lambda_c} \mathrm{e}^{j2\pi t\{f_m^T \cos(\alpha_T^{(m)}) + f_m^R \cos(\alpha_R^{(n)})\} + j\phi_{n,m}}, \tag{2.326}$$

where the index "m" refers to the paths traveling from the transmitter to the N scatterers located on the transmitter end ring, the index "n" refers to the paths traveling from the M scatterers on the receiver end ring to the receiver. The angle $\alpha_T^{(m)}$ is the random angle of departure and $\alpha_R^{(n)}$ is the random angle of arrival of the $\{m, n\}$th propagation path measured with respect to the x-axis, respectively. The phases $\phi_{n,m}$ are uniformly distributed on $[-\pi, \pi)$ and are independent for all pairs $\{n, m\}$. Note that the single summation in (2.146) is replaced with a double summation, because each plane wave on its way from the transmitter to the receiver is double bounced. The temporal correlation characteristics remain the same as those of the model

in (2.146), because each path will undergo a Doppler shift due to the motion of both the transmitter and receiver. Finally, the temporal correlation properties do not depend on the distance ϵ_{mn} in Fig. 2.53. Although not discussed here, the spatial correlation properties will depend on ϵ_{mn} and, through ϵ_{mn}, on the scattering radii R_T and R_R, and the distance D.

2.5.5.3 Patel & Stüber Deterministic (P & S Det.) Model

An ergodic statistical (deterministic) simulation model is now suggested. By choosing only the phases to be random variables, the statistical correlation properties of this model will converge to those of the reference model in a single simulation trial. The complex faded envelope, $g(t) = g_I(t) + jg_Q(t)$, is generated as

$$g_I(t) = \sqrt{\frac{1}{N_I M_I}} \sum_{m=1}^{M_I} \sum_{n=1}^{N_I} \cos\left(2\pi f_m^T \cos(\alpha_{I,n}^T)t + 2\pi f_m^R \cos(\alpha_{I,m}^R)t + \phi_{I,n,m}\right), \tag{2.327}$$

$$g_Q(t) = \sqrt{\frac{1}{N_Q M_Q}} \sum_{m=1}^{M_Q} \sum_{n=1}^{N_Q} \cos\left(2\pi f_m^T \cos(\alpha_{Q,n}^T)t + 2\pi f_m^R \cos(\alpha_{Q,m}^R)t + \phi_{Q,n,m}\right), \tag{2.328}$$

where $\phi_{I,n,m}$ and $\phi_{Q,n,m}$ are all independent random phases uniformly distributed on $[-\pi, \pi)$. The nth angle of departure is equal to $\alpha_{I/Q,n}^T = \pi(n-0.5)/(2N_{I/Q})$, for $n = 1, 2, \ldots, N_{I/Q}$. The mth angle of arrival is equal to $\alpha_{I/Q,m}^R = \pi(m-0.5)/(M_{I/Q})$, for $m = 1, 2, \ldots, M_{I/Q}$.

There are two remarks about this model. First, the angles $\alpha_{I/Q,n}^T$ are essentially the same as those in the MEDS (method of exact Doppler spreads) model [260], while the angles $\alpha_{I/Q,m}^R$ are chosen to reproduce desired statistical properties for M-to-M channels. Second, to make the time average correlation functions deterministic and independent of the random phases $\phi_{I/Q,n,m}$, the frequencies $f_m^T \cos(\alpha_{I,n}^T) + f_m^R \cos(\alpha_{I,m}^R)$ in $g_I(t)$ and $f_m^T \cos(\alpha_{Q,n}^T) + f_m^R \cos(\alpha_{Q,m}^R)$ in $g_Q(t)$ must all be distinct and, moreover, they must also be distinct among themselves for all pairs (n, m) and (k, l). Although it is difficult to establish a general rule to meet this criterion, choosing $N_I = M_I$ and $N_Q = M_Q = N_I + 1$ yields distinct Doppler frequencies for practical ranges of N_I varying from 5 to 60 and for different Doppler frequency ratios, i.e., different values of $a = f_m^R/f_m^T$. This rule is similar to the one used in the MEDS model [260]. Under these assumptions, it can be shown that the time average correlation functions are

$$\hat{\phi}_{g_I g_I}(\tau) = \frac{1}{2N_I^2} \sum_{n,m=1}^{N_I,N_I} \cos\left(2\pi f_m^T \tau \cos(\alpha_{I,n}^T) + 2\pi f_m^R \tau \cos(\alpha_{I,m}^R)\right) \tag{2.329}$$

$$\hat{\phi}_{g_Q g_Q}(\tau) = \frac{1}{2(N_I+1)^2} \sum_{n,m=1}^{(N_I+1),(N_I+1)} \cos(2\pi f_m^T \tau \cos(\alpha_{Q,n}^T) + 2\pi f_m^R \tau \cos(\alpha_{Q,m}^R)) \tag{2.330}$$

$$\hat{\phi}_{g_I g_Q}(\tau) = \hat{\phi}_{g_Q g_I}(\tau) = 0. \tag{2.331}$$

The P & S Det. model has the disadvantage that the time averaged correlation functions match those of the reference model only for a small range of normalized time delays ($0 \le f_m^T \tau \le 5$). To improve upon the statistical properties, two alternative statistical SoS models are suggested. By allowing all three parameter sets (amplitudes, phases, and Doppler frequencies) to be random variables for each simulation trial, the statistical properties of these models will vary for each simulation trial, but they will converge to those of the reference model when averaged over a sufficient number of simulation trials.

2.5.5.4 Patel & Stüber Statistical (P & S Stat.) Model

The P & S Stat. model modifies the model proposed by Zheng et al. [376] for F-to-M cellular land mobile radio channels. The complex faded envelope, $g(t) = g_I(t) + jg_Q(t)$, is generated as

$$g_I(t) = \sqrt{\frac{1}{N_0 M}} \sum_{n=1}^{N_0} \sum_{m=1}^{M} \cos\left(2\pi f_m^T \cos(\alpha_n^T)t + 2\pi f_m^R \cos(\alpha_m^R)t + \phi_{I,n,m}\right) \tag{2.332}$$

$$g_Q(t) = \sqrt{\frac{1}{N_0 M}} \sum_{n=1}^{N_0} \sum_{m=1}^{M} \cos\left(2\pi f_m^T \sin(\alpha_n^T)t + 2\pi f_m^R \cos(\alpha_m^R)t + \phi_{Q,n,m}\right), \tag{2.333}$$

where $\phi_{I,n,m}$ and $\phi_{Q,n,m}$ are all independent random phases uniformly distributed on $[-\pi, \pi)$. The P & S Stat. model assumes N_0 scatterers located on the transmitter ring and M scatterers located on the receiver ring. The nth angle of departure is $\alpha_n^T = (2\pi n - \pi + \theta)/(4N_0)$, where θ is an independent uniform random variable on $[-\pi, \pi)$. The mth angle of arrival is equal to $\alpha_m^R = (2\pi m - \pi + \psi)/(2M)$, where ψ is an independent uniform random variable on $[-\pi, \pi)$.

The ensemble averaged statistical properties of the P & S Stat. model match those of the reference model in (2.147) [259]. The time averaged correlation functions can be derived as:

$$\hat{\phi}_{g_I g_I}(\tau) = \frac{1}{2NM} \sum_{n,m=1}^{N,M} \cos(2\pi f_m^T \cos(\alpha_n^T)\tau + 2\pi f_m^R \cos(\alpha_m^R)\tau) \tag{2.334}$$

$$\hat{\phi}_{g_Q g_Q}(\tau) = \frac{1}{2NM} \sum_{n,m=1}^{N,M} \cos(2\pi f_m^T \sin(\alpha_n^T)\tau + 2\pi f_m^R \cos(\alpha_m^R)\tau) \tag{2.335}$$

$$\hat{\phi}_{g_I g_Q}(\tau) = \hat{\phi}_{g_Q g_{iI}}(\tau) = 0 \tag{2.336}$$

$$\hat{\phi}_{gg}(\tau) = \frac{1}{2NM} \sum_{n,m=1}^{N,M} \left[\cos(2\pi f_m^T \cos(\alpha_n^T)\tau + 2\pi f_m^R \cos(\alpha_m^R)\tau) + \cos(2\pi f_m^T \sin(\alpha_n^T)\tau + 2\pi f_m^R \cos(\alpha_m^R)\tau)\right]. \tag{2.337}$$

The P & S Stat. model requires a fairly large number of simulation trials (at least 50) to obtain adequate statistical properties. Being a statistical model, its time average correlations are random and depend on the random Doppler frequencies. However, for the same complexity, the model performs better than the A & H Model in terms of the variance of these correlation functions [259]. These variances are not given here, since they do not exist in closed form.

2.5.5.5 Zajić & Stüber Statistical (Z & S Stat.) Model

The P & S models have difficulty in producing time averaged auto- and cross-correlation functions that match those of the reference model. Here another statistical model is suggested where orthogonal functions are chosen for the quadrature components of the complex faded envelope. This model is also able to generate multiple uncorrelated complex envelopes, something that the other models cannot do.

The following function is considered as the kth complex faded envelope:

$$g_k(t) = \sqrt{\frac{1}{NM}} \sum_{n=1}^{N} \sum_{m=1}^{M} e^{j(2\pi f_m^T \cos(\alpha_{k,n}^T)t + 2\pi f_m^R \cos(\alpha_{k,m}^R)t + \phi_{k,n,m})}, \tag{2.338}$$

where f_m^T, f_m^R, $\alpha_{k,n}^T$, $\alpha_{k,m}^R$, and $\phi_{k,n,m}$ are the maximum Doppler frequencies, the random angle of departure, the random angle of arrival, and the random phase, respectively. It is assumed that P independent complex faded envelopes are required ($k = 0, \ldots, P-1$) each consisting of NM sinusoidal components.

The number of sinusoidal components needed for simulation can be reduced by choosing $N_0 = N/4$ to be an integer, by taking into account shifts of the angles $\alpha_{k,n}^T$ and $\alpha_{k,m}^R$, and by splitting the sum in (2.338) into four terms, viz.,

$$\begin{aligned} g_k(t) = {} & \sqrt{\frac{1}{NM}} \sum_{m=1}^{M} e^{j2\pi f_m^R t \cos(\alpha_{k,m}^R)} \left[\sum_{n=1}^{N_0} \left\{e^{j(2\pi f_m^T t \cos(\alpha_{k,n}^T) + \phi_{k,n,m})} + e^{j(2\pi f_m^T t \cos(\alpha_{k,n}^T + \pi/2) + \phi_{k,n,m} + \pi/2)}\right\}\right] \\ & + \sqrt{\frac{1}{NM}} \sum_{m=1}^{M} e^{j2\pi f_m^R t \cos(\alpha_{k,m}^R)} \left[\sum_{n=1}^{N_0} \left\{e^{j(2\pi f_m^T t \cos(\alpha_{k,n}^T + \pi) + \phi_{k,n,m} + \pi)} + e^{j(2\pi f_m^T t \cos(\alpha_{k,n}^T + 3\pi/2) + \phi_{k,n,m} + 3\pi/2)}\right\}\right]. \end{aligned} \tag{2.339}$$

Equation (2.339) simplifies as

$$g_k(t) = \sqrt{\frac{1}{N_0 M}} \sum_{n=1}^{N_0} \sum_{m=1}^{M} \cos\left(2\pi f_m^R t \cos(\alpha_{k,m}^R)\right) \cos\left(2\pi f_m^T t \cos(\alpha_{k,n}^T) + \phi_{k,n,m}\right)$$
$$+ j\sqrt{\frac{1}{N_0 M}} \sum_{n=1}^{N_0} \sum_{m=1}^{M} \sin\left(2\pi f_m^R t \cos(\alpha_{k,m}^R)\right) \sin\left(2\pi f_m^T t \sin(\alpha_{k,n}^T) + \phi_{k,n,m}\right). \tag{2.340}$$

Based on $g_k(t)$ in (2.340), the Z & S statistical simulation model can be defined. The kth complex faded envelope, $g_k(t) = g_{I,k}(t) + jg_{Q,k}(t)$, is generated as

$$g_{I,k}(t) = \frac{1}{\sqrt{N_0 M}} \sum_{n=1}^{N_0} \sum_{m=1}^{M} \cos\left(2\pi f_m^R \cos(\alpha_{k,m}^R)t\right) \cos\left(2\pi f_m^T \cos(\alpha_{k,n}^T)t + \phi_{k,n,m}\right) \tag{2.341}$$

$$g_{Q,k}(t) = \frac{1}{\sqrt{N_0 M}} \sum_{n=1}^{N_0} \sum_{m=1}^{M} \sin\left(2\pi f_m^R \cos(\alpha_{k,m}^R)t\right) \sin\left(2\pi f_m^T \sin(\alpha_{k,n}^T)t + \phi_{k,n,m}\right). \tag{2.342}$$

It is assumed that P independent complex envelopes are desired ($k = 0, \ldots, P-1$), each having MN_0 sinusoidal terms in the I and Q components. The angles of departures and the angles of arrivals are chosen as follows:

$$\alpha_{k,n}^T = \frac{2\pi n}{4N_0} + \frac{2\pi k}{4PN_0} + \frac{\theta - \pi}{4N_0}, \tag{2.343}$$

$$\alpha_{k,m}^R = 0.5\left(\frac{2\pi m}{M} + \frac{2\pi k}{PM} + \frac{\psi - \pi}{M}\right), \tag{2.344}$$

for $n = 1, \ldots, N_0$, $m = 1, \ldots, M$ $k = 0, \ldots, P-1$. The angles of departure and the angles of arrival in the kth complex faded envelope are obtained by rotating the angles of departure and the angles of arrival in the $(k-1)$th complex envelope by $(2\pi)/(4PN_0)$ and $(2\pi)/(2PM)$, respectively. The parameters $\phi_{k,n,m}$, θ, and ψ are independent uniform random variables on the interval $[-\pi, \pi)$.

The ensemble averaged statistical correlation functions of the Z & S Stat. model match those of the reference model [371]. For brevity, only the derivation of the auto-correlation function of the in-phase component is presented. Other properties can be derived in an analogous fashion. The auto-correlation function of the in-phase component of the kth complex faded envelope is

$$\phi_{g_{k,I}g_{k,I}}(\tau) = \mathrm{E}[g_{k,I}(t)g_{k,I}(t+\tau)] \tag{2.345}$$
$$= \frac{4}{N_0 M} \sum_{n,m=1}^{N_0,M} \sum_{p,r=1}^{N_0,M} \mathrm{E}\left[\cos(2\pi f_m^R(t+\tau)\cos(\alpha_{k,m}^R))\right.$$
$$\times \cos(2\pi f_m^R t \cos(\alpha_{k,p}^R)) \cos(2\pi f_m^T(t+\tau)\cos(\alpha_{k,n}^T) + \phi_{k,n,m})$$
$$\left.\times \cos(2\pi f_m^T t \cos(\alpha_{k,r}^T) + \phi_{k,p,r})\right]$$
$$= \frac{1}{N_0 M} \sum_{n=1}^{N_0} \sum_{m=1}^{M} \mathrm{E}\left[\cos(2\pi f_m^R \tau \cos(\alpha_{k,m}^R)) \cos(2\pi f_m^T \tau \cos(\alpha_{k,n}^T))\right]$$
$$= \frac{1}{M} \sum_{m=1}^{M} \frac{1}{2\pi} \int_{-\pi}^{\pi} \cos\left(2\pi f_m^R \tau \cos\left(\frac{2\pi m}{2M} + \frac{2\pi k}{2PM} + \frac{\psi - \pi}{2M}\right)\right) \mathrm{d}\psi$$
$$\times \frac{1}{N_0} \sum_{n=1}^{N_0} \frac{1}{2\pi} \int_{-\pi}^{\pi} \cos\left(2\pi f_m^T \tau \cos\left(\frac{2\pi n}{4N_0} + \frac{2\pi k}{4PN_0} + \frac{\theta - \pi}{4N_0}\right)\right) \mathrm{d}\theta \tag{2.346}$$

Table 2.2 Mean square error, maximum deviation and variations, for various mobile-to-mobile channel simulators

Simulator	P & S Det.	P & S Stat. $N_{\text{stat}} = 1$	P & S Stat. $N_{\text{stat}} = 50$	Z & S Stat. $N_{\text{stat}} = 1$	Z & S Stat. $N_{\text{stat}} = 30$	Z & S Stat. $N_{\text{stat}} = 50$
mse($\phi_{g_I g_Q}$)	$1.8 \cdot 10^{-3}$	$1.1 \cdot 10^{-3}$	$3.16 \cdot 10^{-5}$	$8.81 \cdot 10^{-4}$	$4.39 \cdot 10^{-5}$	$2.05 \cdot 10^{-5}$
Max($\phi_{g_I g_Q}$)	$9.61 \cdot 10^{-2}$	$5.91 \cdot 10^{-2}$	$1.27 \cdot 10^{-2}$	$6.84 \cdot 10^{-2}$	$1.28 \cdot 10^{-2}$	$7.0 \cdot 10^{-3}$
Var($\phi_{g_I g_Q}$)	$2.74 \cdot 10^{-6}$	$4.59 \cdot 10^{-6}$	$6.67 \cdot 10^{-9}$	$3.11 \cdot 10^{-6}$	$5.69 \cdot 10^{-9}$	$2.51 \cdot 10^{-9}$
mse($\phi_{g_1 g_2}$)	$5.8 \cdot 10^{-3}$	$1.1 \cdot 10^{-3}$	$1.31 \cdot 10^{-5}$	$7.02 \cdot 10^{-4}$	$3.59 \cdot 10^{-5}$	$1.26 \cdot 10^{-5}$
Max($\phi_{g_1 g_2}$)	$1.59 \cdot 10^{-1}$	$6.34 \cdot 10^{-2}$	$0.63 \cdot 10^{-2}$	$6.57 \cdot 10^{-2}$	$9.6 \cdot 10^{-3}$	$5.6 \cdot 10^{-3}$
Var($\phi_{g_1 g_2}$)	$1.24 \cdot 10^{-4}$	$1.77 \cdot 10^{-6}$	$7.38 \cdot 10^{-10}$	$1.22 \cdot 10^{-6}$	$3.0 \cdot 10^{-9}$	$4.39 \cdot 10^{-10}$

As in [360], the derivation can be completed by replacing the variables of integration, θ and ψ, with $\gamma_{k,n} = (2\pi n)/(4N_0) + (2\pi k)/(4PN_0) + (\theta - \pi)/(4N_0)$ and $\delta_{k,m} = (2\pi m)/(2M) + (2\pi k)/(2PM) + (\psi - \pi)/(2M)$, respectively. Finally,

$$\lim_{N_0, M \to \infty} \phi_{g_{k,I} g_{k,I}}(\tau) = J_0(2\pi f_m^T \tau) J_0(2\pi f_m^R \tau). \tag{2.347}$$

The performance of the various models is now compared. All simulations use a normalized sampling rate of $f_m T_s = .01$ ($f_m = f_m^T = f_m^R$ are the maximum Doppler frequencies) and $M = N_0 = P = 8$. For the P & S Det. model, $N_I = M_I = 8$ and $N_Q = M_Q = 9$ are used to obtain a complex envelope with uncorrelated quadrature components. Using these parameters, the mean square error (mse) and maximum deviations (Max) from the theoretical value (zero) have been calculated for the normalized cross-correlations of the I and Q components, and for the normalized cross-correlations of the first and the second faded envelopes. The results are shown in Table 2.2. Note that different simulation trials yield slightly different simulation results. To estimate these differences, the variances are computed by averaging over 1000 simulation trials. The variances of the normalized cross-correlations of the I and Q components, and the variances of the normalized cross-correlations of the first and the second faded envelopes are also shown in Table 2.2. From Table 2.2, the Z & S Stat. model with $N_{\text{stat}} = 1$ has cross-correlations similar to the P & S Det. model and the P & S Stat. model with $N_{\text{stat}} = 1$. The Z & S Stat. model with $N_{\text{stat}} = 30$ performs similar to the P & S Stat. model with $N_{\text{stat}} = 50$ and significantly better than the P & S Det. model. Increasing the number of simulation trials to $N_{\text{stat}} = 50$ yields a lower cross-correlation between the I and Q components of the complex faded envelope.

Figure 2.54 shows that, for $N_0 = M = P = 8$ and 30 simulation trials, the auto- and cross-correlations of the complex faded envelopes produced by the Z & S Stat. model approach those of the reference model.

Figures 2.55 and 2.56 compare the variance of the time averaged auto-correlation functions of the quadrature components averaged over 1000 simulation trials. For the statistical models, the variance is defined as $\text{Var}[\hat{\phi}(\cdot)] = E[|\hat{\phi}(\cdot) - \lim_{N \to \infty} \phi(\cdot)|^2]$, where $\hat{\phi}(\cdot)$ denotes the time averaged correlation functions and $\phi(\cdot)$ denotes the statistical correlation functions. For the P & S Det. model, the relevant quantity is the squared error $|\hat{\phi}(\cdot) - \phi(\cdot)|^2$. The variance for the A & H model is obtained using (2.323). The variance provides a measure of the usefulness of the model in simulating the desired channel with a finite N. A lower variance means that a smaller number of simulation trials are needed to achieve the desired statistical properties and, hence, the corresponding model is better. Since the A & H model does not exploit the symmetry of the double-ring model, as the other models do, for fair comparison $N = 4N_0 \times 2M = 512$ sinusoids are used when using the A & H model. From Fig. 2.55, it can be concluded that the Z & S Stat. model with one simulation trial has a variance similar to the P & S Det. model and a lower variance than the P & S Stat. model with one simulation trial. A single simulation trial is chosen for this comparison because the P & S Det. model is an ergodic statistical simulation model that requires only a single simulation trial. In any case, Fig. 2.55 shows that all three models do not perform as well as the A & H model for a single simulation trial. Figure 2.56 shows that increasing the number of simulation trials to 30 in the P & S and Z & S Stat. models yields a significantly lower variance of the auto-correlation function of the quadrature components. Figure 2.56 shows that the Z & S Stat. model with 30 simulation trials outperforms the P & S Stat. model with 30 simulation trials, and outperforms P & S Det. model and the A & H model each with one simulation trial.

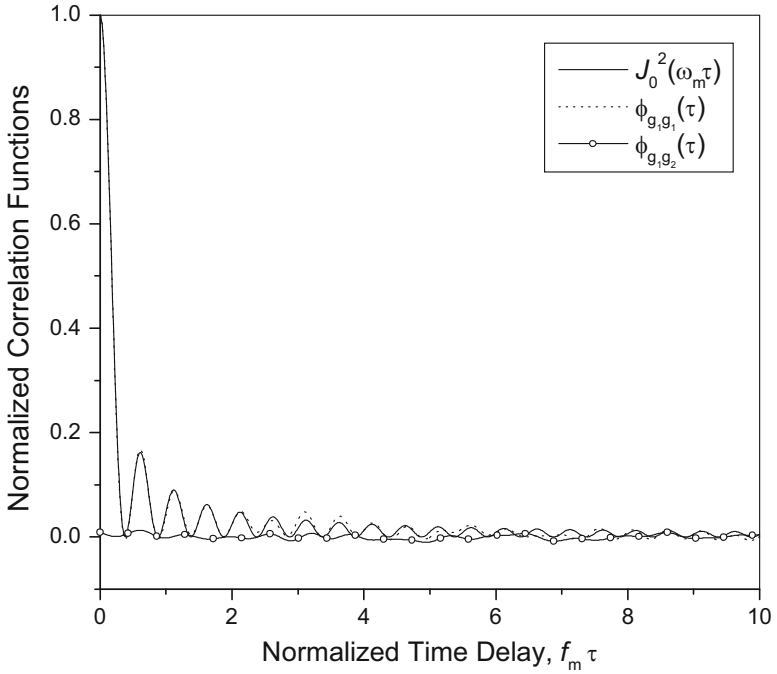

Fig. 2.54 Theoretical and simulated auto-correlation functions and cross-correlation function of the first and the second faded envelopes produced by the Z & S Stat. model with 30 simulation trials

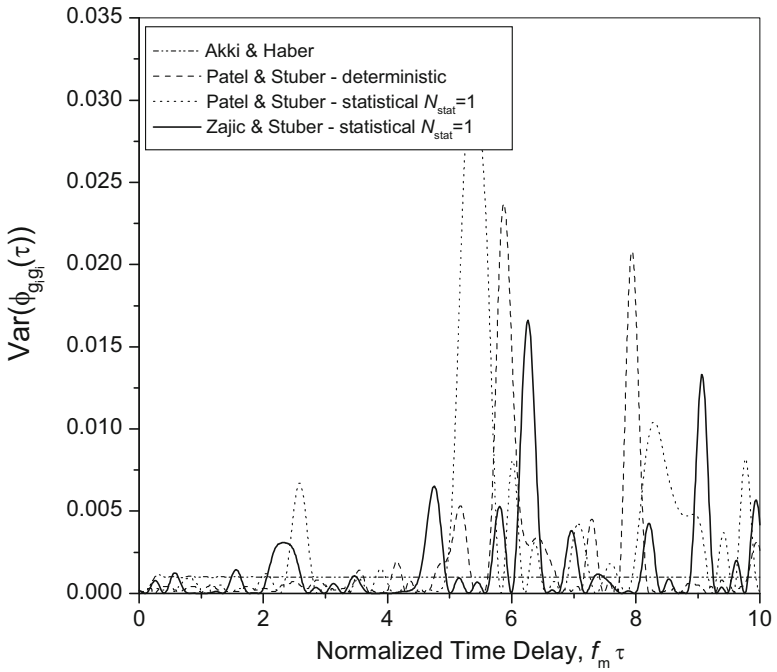

Fig. 2.55 Variance of the auto-correlation function of the quadrature components with a single simulation trial ($N_{\text{stat}} = 1$)

2.5.6 Symbol-Spaced Models

The baseband representation of a typical digital communication system consists of the concatenation of an up-sampler, a discrete-time transmit filter or pulse shaping filter, digital-to-analog converter (DAC), waveform channel, analog-to-digital converter (ADC), and discrete-time receiver filter or matched filter, and down-sampler as shown in Fig. 2.57. The channel

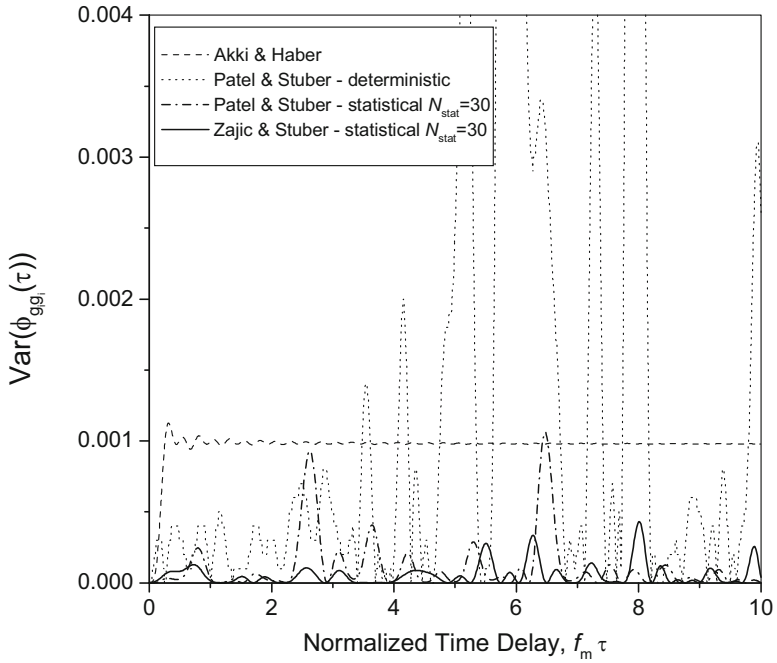

Fig. 2.56 Variance of the auto-correlation function of the quadrature components with 30 simulation trials ($N_{stat} = 30$)

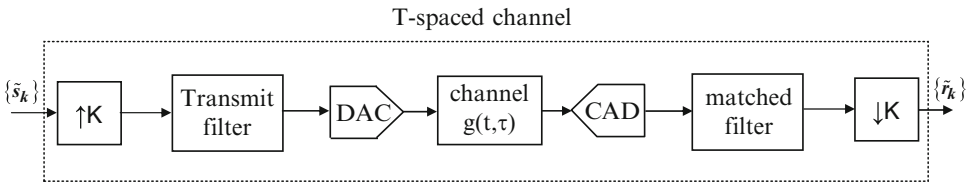

Fig. 2.57 Baseband model for a typical digital communication system

$g(t, \tau)$ is assumed to have the structure in (2.304) or Fig. 2.50. Data symbols are input to the up-sampler, one every T seconds, where T is the baud period. Usually, the bandwidth of the transmitted signal W will exceed the Nyquist frequency $1/2T$; for example, when root-raised cosine pulse shaping is used. Therefore, up-sampling is required at the transmitter so that the DAC operates with sample period T/K, where K is the up-sampling factor. At the receiver, the ADC also operates with a sampling period T/K. The up-sampling factor K must be chosen to at least satisfy the sampling theorem at the transmit side, i.e., $K/T \geq 2W$, but often K is made larger to facilitate timing synchronization in the receiver and to accommodate the Doppler spreading that is introduced by the channel. Once the correct sample timing phase is determined, the sample sequence at the output of the receiver filter can be down-sampled for further processing. For the purpose of illustration, down-sampling by factor of K is assumed, so that symbol-spaced samples are taken at the output of the receiver filter.[4]

Form the above discussion, it is apparent that the overall channel from the input to the transmitter filter to the output of the receiver filter can be modeled as a finite impulse response (FIR) filter as shown in Fig. 2.58, where the $\{g_n^T[k]\}$ are the tap gains. While it is true that the channel taps, $\{g_i(t)\}$ in the underlying waveform channel in Fig. 2.50 are uncorrelated for WSSUS channels, the same cannot be said of the taps $\{g_n^T[k]\}$ in the FIR filter of Fig. 2.58. The tap correlations in the symbol-spaced model often leads to analytical intractability when evaluating the theoretical performance of digital communication systems that operate on these channels. This difficulty is often overcome by assuming that the taps $\{g_n^T[k]\}$ are uncorrelated [90, 107, 140, 192, 206, 301, 320], when in fact they are not. However, when the same systems are evaluated by software simulation, such modeling simplifications are unnecessary and in fact undesirable. A method is now described for generating the tap coefficients $\{g_n^T[k]\}$ with the proper cross-correlations in the case where linear modulation schemes are used. The procedure can be readily extended to generate the required tap coefficients when fractional sampling is used, i.e., if $K > 1$.

[4] In practice, $T/2$-spaced samples at the output of the receiver filter are often used for further processing, such as equalization.

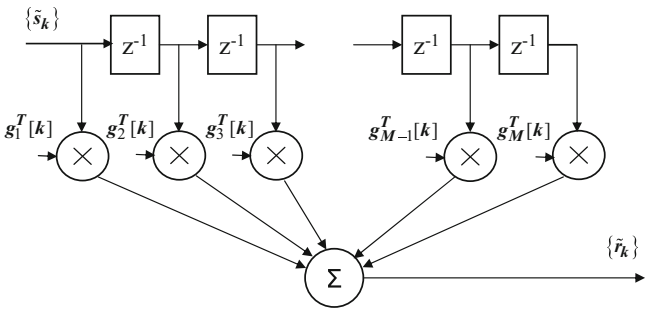

Fig. 2.58 Symbol-spaced tapped delay line model for wide-band multipath-fading channels

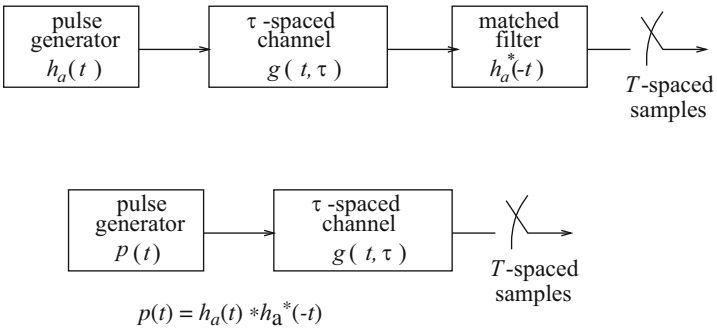

Fig. 2.59 Method for generating correlated tap coefficients in a T-spaced channel model

Consider the arrangement shown in Fig. 2.59, where the equivalent analog representation of the transmit filter, $h_a(t)$, and receiver matched filter $h_a^*(-t)$ are assumed. Pulses that are shaped by the transmit filter $h_a(t)$ are transmitted through the channel $g(t,\tau)$ and the receiver matched filter $h_a^*(-t)$. The output of the receiver matched filter is sampled at symbol-spaced intervals. Since the filters $h_a(t)$, $g(t,\tau)$ and $h_a^*(-t)$ are linear, their order may be exchanged as shown in Fig. 2.59, where the overall pulse is equal to $p(t) = h_a(t) * h_a^*(-t)$. The overall pulse $p(t)$ is usually chosen to be a Nyquist pulse. For example, $p(t)$ might be a raised cosine pulse, such that $h_a(t)$ and $h_a^*(-t)$ are root-raised cosine pulses. To obtain the symbol-spaced channel tap coefficients, the pulse $p(t)$ is passed through the channel $g(t,\tau)$ and symbol-spaced samples are extracted at the output. Assuming that the channel has the form in (2.304), the symbol-spaced samples are now shown to be a linear combination of the elements of the tap gain vector

$$\mathbf{g}(t) = (g_1(t),\ g_2(t),\ \ldots,\ g_\ell(t))^T. \tag{2.348}$$

Suppose that a vector of M, symbol-spaced, tap coefficients

$$\mathbf{g}^T(t) = (g_1^T(t),\ g_2^T(t),\ \ldots,\ g_M^T(t))^T \tag{2.349}$$

is to be generated. Then $\mathbf{g}^T(t) = \mathbf{A}\mathbf{g}(t)$, where $\mathbf{g}(t)$ is defined in (2.348), and $\mathbf{A}$ is an $M \times \ell$ real matrix. As shown in Example 2.1 below, the entries of the matrix $\mathbf{A}$ are determined by the overall pulse $p(t)$, the delay profile $\boldsymbol{\tau}$ in (2.312), and the timing phase of the sampler that extracts the symbol-spaced samples. The matrix $\mathbf{A}$ must be generated each time the delay profile and/or the sampler timing phase changes. For systems where timing information is derived from a training sequence or synchronization word that is inserted into every transmitted slot or burst, the sampler timing phase is usually adjusted on a burst-by-burst basis and, consequently, the matrix $\mathbf{A}$ must be computed on a burst-by-burst basis as well.

The autocovariance matrix of the symbol-spaced tap gain vector $\mathbf{g}^T(t)$ is

$$\begin{aligned}\Phi_{\mathbf{g}^T}(\tau) &= \frac{1}{2}\mathrm{E}\left[\mathbf{g}^T(t)\mathbf{g}^{T\,H}(t+\tau)\right] \\ &= \frac{1}{2}\mathrm{E}\left[\mathbf{A}\mathbf{g}(t)\mathbf{g}^H(t+\tau)\mathbf{A}^T\right] \\ &= \mathbf{A}\frac{1}{2}\mathrm{E}\left[\mathbf{g}(t)\mathbf{g}^H(t+\tau)\right]\mathbf{A}^T \\ &= \mathbf{A}\Phi_{\mathbf{g}}(\tau)\mathbf{A}^T.\end{aligned}$$

For a WSSUS channel and 2-D isotropic scattering on each of the channel taps $g_i(t)$,

$$\Phi_{\mathbf{g}}(\tau) = \frac{1}{2}\mathrm{diag}[\Omega_1, \Omega_2, \ldots, \Omega_\ell]J_0(2\pi f_m\tau). \tag{2.350}$$

Example 2.1. Suppose that the channel $g(t,\tau)$ consists of two taps having the spacing $\tau_s = |\tau_1(t) - \tau_0(t)|$. In this example, the two main taps in the symbol-spaced channel model, $g_0^T(t)$ and $g_1^T(t)$, are generated. Let

$$\begin{aligned}\mathbf{g}(t) &= (g_0(t), g_1(t))^T \\ \mathbf{g}^T(t) &= (g_0^T(t), g_1^T(t))^T\end{aligned}$$

and

$$\mathbf{g}^T(t) = \mathbf{A}\mathbf{g}(t).$$

The entries of matrix $\mathbf{A}$ depend on the timing phase of the T-spaced samples taken at the output of the pulse generator. In a practical system, the sampler timing phase is determined by the synchronization process in the receiver. Suppose that the taps just happen to have equal strength, $|g_0(t)|^2 = |g_1(t)|^2$, when the sampler timing is being determined, i.e., during the training sequence or synchronization word. Furthermore, for the purpose of illustration, suppose that the result of the sampler timing phase adjustment is such that the symbol-spaced taps have equal strength as well, i.e., $|g_0^T(t)|^2 = |g_1^T(t)|^2$. Figure 2.60 illustrates this situation. The entries of matrix $\mathbf{A}$ can be obtained by writing

$$\begin{aligned}g_0^T(t) &= p(\tau_s/2 - T/2)g_0(t) + p(-\tau_s/2 - T/2)g_1(t) \\ g_1^T(t) &= p(\tau_s/2 + T/2)g_0(t) + p(-\tau_s/2 + T/2)g_1(t).\end{aligned}$$

Hence,

$$\mathbf{A} = \begin{bmatrix} p(\tau_s/2 - T/2) & p(-\tau_s/2 - T/2) \\ p(\tau_s/2 + T/2) & p(-\tau_s/2 + T/2) \end{bmatrix}.$$

Now suppose that the combination of the transmitter and receiver filter is a raised cosine pulse[5]

$$p(t) = \mathrm{sinc}(t/T) \cdot \frac{\cos(\pi\beta t/T)}{1 - 4\beta^2 t^2/T^2}, \tag{2.351}$$

(continued)

[5] See Chap. 4 for a discussion of raised cosine pulse shaping.

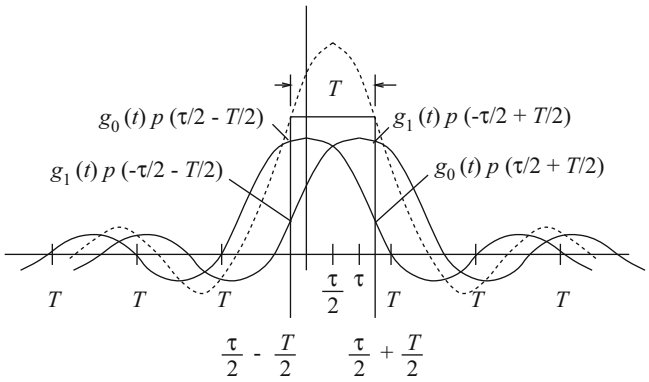

Fig. 2.60 Generation symbol-spaced channel taps

Example 2.1 (continued)
with roll-off factor $\beta = 0.35$, and $\tau_s = T/4$. Then

$$\mathbf{A} = \begin{bmatrix} p(-3T/8) & p(-5T/8) \\ p(5T/8) & p(3T/8) \end{bmatrix} = \begin{bmatrix} 0.7717 & 0.4498 \\ 0.4498 & 0.7717 \end{bmatrix}$$

2.6 Shadowing

It was shown earlier in (2.26) that the received envelope power is

$$\Omega_p = \mathrm{E}[|g(t)|^2] = \sum_{n=1}^{N} C_n^2, \tag{2.352}$$

where C_n depends on the cross sectional area of the nth local scatterer. In practice, the local mean is calculated by computing the time average

$$\hat{\Omega}_p = \frac{1}{T}\int_T |g(t)|^2 \mathrm{d}t, \tag{2.353}$$

where the time interval T is chosen to correspond to a spatial averaging interval that is large enough to average over the envelope fades. In practice, this corresponds to a spatial averaging distance of about 20 wavelengths. Note that the required averaging interval T will depend on velocity. The averaging interval must be small enough so that the $\{C_n\}$ do not change over the averaging interval. The location area is defined as the largest volume of space where this condition will hold true. Sometimes Ω_p is called the local mean because it is computed within a location area. If the receiver moves outside the location area, the $\{C_n\}$ will change due to the presence of large terrain features like hills, valley, and buildings. Therefore, the local mean Ω_p (or $\hat{\Omega}_p$) changes with location in a process known as shadowing. The same statements can also be made for the mean envelope $\Omega_v = \mathrm{E}[|g(t)|]$ and its time average

$$\hat{\Omega}_v = \frac{1}{T}\int_T |g(t)|\mathrm{d}t. \tag{2.354}$$

Empirical studies have shown that Ω_p has the log-normal distribution

$$p_{\Omega_p}(x) = \frac{1}{x\sigma_\Omega \xi \sqrt{2\pi}} \exp\left\{ -\frac{\left(10\log_{10}\{x\} - \mu_{\Omega_p\ (\text{dBm})}\right)^2}{2\sigma_\Omega^2} \right\}, \tag{2.355}$$

where

$$\mu_{\Omega_p\ (\text{dBm})} = 10\text{E}[\log_{10}\{\Omega_p\}], \tag{2.356}$$

σ_Ω is the shadow standard deviation in decibel units, and $\xi = \ln(10)/10$. Note that since the local mean is in units of dBm (decibels with respect to 1 mW), the units of Ω_p in (2.355) are milliwatts (mW).

The mean value $\mu_{\Omega_p\ (\text{dBm})}$ is sometimes called the area mean because it corresponds to an extended location area defined as the largest volume of space where the $\{C_n\}$ can be characterized as stationary random variables and N is a constant. Within an extended location area, the mean envelope power $\mu_{\Omega_p} = \text{E}[\Omega_p]$ is constant. The mean envelope power depends on the propagation path loss between the transmitter and receiver, such that the path loss is constant within the extended location area.

By using a transformation of random variables, it can be shown that $\Omega_{p\ (\text{dBm})} = 10\log_{10}\{\Omega_p\}$ has the Gaussian density

$$p_{\Omega_p\ (\text{dBm})}(x) = \frac{1}{\sqrt{2\pi}\sigma_\Omega} \exp\left\{ -\frac{(x - \mu_{\Omega_p\ (\text{dBm})})^2}{2\sigma_\Omega^2} \right\}. \tag{2.357}$$

Note that the logarithm of the log-normal random variable yields a normal random variable.

Some confusion may arise in the literature because some authors [127, 128, 232] treat the mean envelope Ω_v as being log-normally distributed with shadow standard deviation σ_Ω, while other authors [208, 227, 267] treat the mean square-envelope Ω_p as being log-normally distributed with the same value of σ_Ω. Clearly, the mean envelope and mean square-envelope are not the same, and one may wonder if the same shadow standard deviation should be used in each case. It is shown in Appendix 2D that the shadow standard deviation σ_Ω is indeed the same in each case. However, with Ricean fading the means differ by

$$\mu_{\Omega_p\ (\text{dBm})} = \mu_{\Omega_v\ (\text{dBm})} + 10\log_{10}\{C(K)\}, \tag{2.358}$$

where

$$C(K) = \frac{4\text{e}^{2K}(K+1)}{\pi\, {}_1F_1^2(3/2, 1; K)} \tag{2.359}$$

and ${}_1F_1(\cdot, \cdot; \cdot)$ denotes the confluent hypergeometric function.

The shadow standard deviation σ_Ω ranges from 5 to 12 dB with 8 dB being a typical value for macrocellular applications. The shadow standard deviation increases slightly with frequency (0.8 dB higher at 1800 MHz than at 900 MHz), but has been observed to be nearly independent radio path length, even for distances that are very close to the transmitter [227]. The shadow standard deviation that is observed in microcells varies between 4 and 13 dB [40, 142, 143, 216, 228, 280]. Mogensen [228] has reported $\sigma_\Omega = 6.5$–8.2 dB at 900 MHz in urban areas, while Mockford et al. [227] report a value of 4.5 dB for urban areas. Berg [40] and Goldsmith and Greenstein [142] report that σ_Ω is around 4 dB for a spatial averaging window of 20 wavelengths and BS antenna heights of about 10 m. Several studies suggest that σ_Ω decreases with an increase in the degree of urbanization or density of scatters. For example, the results presented by Mockford et al. [227] suggest that σ_Ω is 1.3–1.8 dB higher in a suburban environment than in an urban environment.

2.6.1 Shadow Simulation

One of the challenges when constructing a shadow simulator is to account for the spatial correlation of the shadows. Several studies have investigated the spatial correlation of shadows [151, 152, 161, 170, 216]. One simple model has been suggested by Gudmundson [152], where log-normal shadowing is modeled as a Gaussian white noise process that is filtered by a first-order low-pass filter. With this model

$$\Omega_{k+1\ (\text{dBm})} = \zeta\Omega_{k\ (\text{dBm})} + (1 - \zeta)v_k, \tag{2.360}$$

where $\Omega_{k\ (\mathrm{dBm})}$ is the mean envelope or mean squared-envelope, expressed in decibels, that is experienced at index k, ζ is a parameter that controls the spatial correlation of the shadows, and v_k is a zero-mean Gaussian random variable with $\phi_{\mathrm{vv}}(n) = \tilde{\sigma}^2\delta(n)$. It can be shown that the spatial autocorrelation function of $\Omega_{k\ (\mathrm{dBm})}$ as generated by (2.360) is

$$\phi_{\Omega_{(\mathrm{dBm})}\Omega_{(\mathrm{dBm})}}(k) = \frac{1-\zeta}{1+\zeta}\tilde{\sigma}^2\zeta^{|k|}. \tag{2.361}$$

Since the shadow variance is

$$\sigma_\Omega^2 = \phi_{\Omega_{(\mathrm{dBm})}\Omega_{(\mathrm{dBm})}}(0) = \frac{1-\zeta}{1+\zeta}\tilde{\sigma}^2 \tag{2.362}$$

the autocorrelation of Ω_k can be expressed as

$$\phi_{\Omega_{(\mathrm{dBm})}\Omega_{(\mathrm{dBm})}}(k) = \sigma_\Omega^2\zeta^{|k|}. \tag{2.363}$$

This approach generates shadows that decorrelate exponentially with distance. Mandayam et al. [214] have shown through an extreme value analysis that log-normal shadows cannot decorrelate exponentially with distance. Nevertheless, in the absence of anything better, Gudmundson's model in (2.360) is still useful and effective.

While shadows decorrelate spatially, simulations are usually conducted in discrete-time. Therefore, to use the simulator in (2.360), the spatial decorrelation parameter ζ must be related to the simulation index k. Suppose the shadows that are experienced by a MS that is traveling with velocity v are to be modeled. The envelope (or squared-envelope) is sampled every T seconds. In kT seconds the MS moves a distance vkT. Let ζ_D be the shadow correlation between two points separated by a distance of D m. Then the time autocorrelation of shadowing is

$$\phi_{\Omega_{(\mathrm{dBm})}\Omega_{(\mathrm{dBm})}}(k) \equiv \phi_{\Omega_{(\mathrm{dBm})}\Omega_{(\mathrm{dBm})}}(kT) = \sigma_\Omega^2\zeta_D^{(vT/D)|k|}. \tag{2.364}$$

Comparing (2.363) and (2.364), observe that $\zeta = \zeta_D^{(vT/D)}$. For typical suburban propagation at 900 MHz, it has been experimentally verified by Gudmundson [150] that $\sigma_\Omega \approx 7.5$ dB and $\zeta_{100} = 0.82$. For typical microcellular propagation at 1700 MHz, Gudmundson has also reported $\sigma_\Omega = 4.3$ dB and $\zeta_{10} = 0.3$.

2.6.2 Composite Shadowing–Fading Distributions

Sometimes it is desirable to obtain the composite envelope distribution due to shadowing and multipath-fading. Such a composite distribution is relevant in cases where the MSs are slowly moving or stationary. In this case, the fading rate may be so slow that entire codewords are either faded completely or not at all regardless of the interleaving depth that is used, and the code fails. In this case, the composite shadow-fading distribution is useful for evaluating system coverage, i.e., the fraction of the service area having an acceptable quality of service.

Two different approaches have been suggested in the literature for obtaining the composite shadow-fading distribution. The first approach is to express the squared-envelope as a conditional density, conditioned on Ω_p, and then integrate over the density of Ω_p to obtain the composite distribution. This results in the composite shadow-fading distribution

$$p_{\alpha_c^2}(x) = \int_0^\infty p_{\alpha^2|\ \Omega_p}(x|w)p_{\Omega_p}(w)\mathrm{d}w. \tag{2.365}$$

For the case of Rayleigh fading, at any time instant t_1

$$\Omega_p = \mathrm{E}[\alpha^2(t_1)] = 2b_0 \tag{2.366}$$

and, hence,

$$p_{\alpha^2|\ \Omega_p}(x|w) = \frac{x}{w}e^{-x/w}. \tag{2.367}$$

The composite squared-envelope distribution with Rayleigh fading and log-normal shadowing is

$$p_{\alpha_c^2}(x) = \int_0^\infty \frac{1}{w} e^{-x/w} \frac{1}{w\sigma_\Omega \xi \sqrt{2\pi}} \exp\left\{ -\frac{\left(10\log_{10}\{w\} - \mu_{\Omega_p\ (\mathrm{dBm})}\right)^2}{2\sigma_\Omega^2} \right\} \mathrm{d}w. \tag{2.368}$$

where $\xi = \ln(10)/10$. Unfortunately, this distribution does not exist in closed form, but can be efficiently evaluated using Gauss–Hermite quadrature integration.

The second approach, originally suggested by Lee and Yeh [199], expresses the composite squared-envelope as the product of the squared-envelope due to multipath-fading and shadow fading. Using this approach,

$$\hat{\alpha}_c^2(t) = \alpha^2(t) \cdot \Omega_p(t). \tag{2.369}$$

Under the assumption that the fading and shadowing are independent random processes, both approaches lead to identical results as is now shown. The composite squared-envelope in (2.369) is the product of two random variables at any time instant t_1. Hence, the corresponding density function of the squared-envelope can be obtained by using a bivariate transformation of random variables and then integrating to obtain the marginal density. This leads to the composite density function

$$p_{\hat{\alpha}_c^2}(x) = \int_0^\infty \frac{1}{w} p_{\alpha^2}\left(\frac{x}{w}\right) p_{\Omega_p}(w) \mathrm{d}w. \tag{2.370}$$

Again, consider the case of log-normal shadowing and Rayleigh fading. Using (2.54) and (2.355) gives

$$p_{\hat{\alpha}_c^2}(x) = \int_0^\infty \frac{1}{\Omega_p w} \exp\left\{ -\frac{x}{\Omega_p w} \right\} \frac{1}{w\sigma_\Omega \xi \sqrt{2\pi}} \exp\left\{ -\frac{\left(10\log_{10}\{w\} - \mu_{\Omega_p\ (\mathrm{dBm})}\right)^2}{2\sigma_\Omega^2} \right\} \mathrm{d}w. \tag{2.371}$$

Observe that (2.368) and (2.371) are related by

$$p_{\alpha_c}(x) = \Omega_p p_{\hat{\alpha}_c}\left(\Omega_p x\right). \tag{2.372}$$

Hence, if the faded envelope $\alpha(t)$ in the second approach is assumed to have $\mathrm{E}[\alpha(t)^2] = \Omega_p = 1$, then α_c^2 and $\hat{\alpha}_c^2$ will have the exact same composite distribution. Although the above result may not matter much for analysis, it does have implications for software simulation. When simulating the combined effects of fading and shadowing, the composite squared-envelope can be obtained by generating the fading and shadowing processes separately and multiplying them together as shown in (2.369). To do so, the faded envelope should be generated such that $\Omega_p = 1$.

2.6.2.1 Composite Gamma-Log-Normal Distribution

It is sometimes very useful to model the radio propagation environment as a shadowed Nakagami fading channel, because the Nakagami distribution is mathematically convenient and can closely approximate a Rice distribution. The composite distribution of the squared-envelope due to Nakagami fading and log-normal shadowing has the Gamma-log-normal density function

$$p_{\alpha_c^2}(x) = \int_0^\infty \left(\frac{m}{w}\right)^m \frac{x^{m-1}}{\Gamma(m)} \exp\left\{ -\frac{mx}{w} \right\} \frac{1}{\sqrt{2\pi}\xi\sigma_\Omega w} \exp\left\{ -\frac{(10\log_{10}\{w\} - \mu_{\Omega_p\ (\mathrm{dBm})})^2}{2\sigma_\Omega^2} \right\} \mathrm{d}w. \tag{2.373}$$

where $\xi = \ln(10)/10$. As shown in Appendix 2E, the composite Gamma-log-normal distribution in (2.373) can be closely approximated by a log-normal distribution with parameters

$$\begin{aligned} \mu_{(\mathrm{dBm})} &= \xi^{-1}\left(\psi(m) - \ln(m)\right) + \mu_{\Omega_p\ (\mathrm{dBm})} \\ \sigma^2 &= \xi^{-2}\zeta(2, m) + \sigma_\Omega^2 \end{aligned} \tag{2.374}$$

where $\psi(\cdot)$ is the Euler psi function and $\zeta(\cdot,\cdot)$ is Riemann's zeta function as defined in Appendix 2E. When $m = 1$ the approximation is valid for $\sigma_\Omega > 6\,\text{dB}$; when $m = 2$, $\sigma_\Omega > 6$ must be greater than or equal to 4 dB; when $m \geq 4$, the approximation is good for all σ_Ω [164].

The effect of Nakagami fading in (2.374) is to decrease the mean and increase the variance of the composite squared-envelope. However, this affect decreases as the shape factor m increases (corresponding to less severe fading). For example, with $m = 1$ (Rayleigh fading), $\mu_{(\text{dBm})} = \mu_{\Omega_p\,(\text{dBm})} - 2.50675$ and $\sigma^2 = \sigma_\Omega^2 + 31.0215$ while, with $m = 8$, $\mu_{(\text{dBm})} = \mu_{\Omega_p\,(\text{dBm})} - 0.277$ and $\sigma^2 = \sigma_\Omega^2 + 2.50972$.

2.7 Path Loss Models

Path loss is the largest and most variable quantity in a communication link budget. It depends on frequency, antenna heights, and distance and topography. A variety of theoretical and empirical path loss models exist in the literature. Our discussion starts with a discussion of theoretical models, followed by empirical models.

2.7.1 Free Space Path Loss

Free-space path loss (FSPL) is proportional to the square of the distance between the transmitter and receiver, and also proportional to the square of the frequency f_c of the radio signal. The FSPL equation is

$$L_{\text{FS}} = \left(\frac{4\pi d}{\lambda_c}\right)^2 = \left(\frac{4\pi d f_c}{c}\right)^2. \tag{2.375}$$

FSPL is a combination of two effects: First, the intensity of an electromagnetic wave in free space decays with the square of the radio path length, d, such that the received power per unit area or power spatial density (in watts per meter-squared) at distance d is

$$\Omega_r(d) = \Omega_t \frac{1}{4\pi d^2}, \tag{2.376}$$

where Ω_t is the total transmit power in watts. Note that this term is not frequency dependent.

The second effect is due to aperture, which determines how well an antenna picks up power from an incoming electromagnetic wave. For an isotropic antenna,

$$\Omega_p(d) = \Omega_r(d) \frac{\lambda_c^2}{4\pi}, \tag{2.377}$$

where $\Omega_p(d)$ is the received power. Note that this is entirely dependent on wavelength, λ_c, which is how the frequency-dependent behavior arises.

Using (2.376) and (2.377) gives the free space propagation path loss as

$$\begin{aligned} L_{\text{FS (dB)}} = 10\log_{10}\left\{\frac{\Omega_t}{\Omega_p(d)}\right\} &= 10\log_{10}\left\{\left(\frac{4\pi d}{\lambda_c}\right)^2\right\} \\ &= 10\log_{10}\left\{\left(\frac{4\pi d f_c}{c}\right)^2\right\} \\ &= 20\log_{10}\{f_c\} + 20\log_{10}\{d\} - 147.55\ \text{dB}. \end{aligned} \tag{2.378}$$

2.7.2 Flat Earth Path Loss

The signals in land mobile radio environments do not experience free space propagation. A more appropriate theoretical path loss model is one that assumes propagation over a flat reflecting surface, the Earth, as shown in Fig. 2.61. The length of the direct path is

$$d_1 = \sqrt{d^2 + (h_b - h_m)^2} \tag{2.379}$$

and the length of the reflected path is

$$d_2 = \sqrt{d^2 + (h_b + h_m)^2} \tag{2.380}$$

Given that $d \gg h_b h_m$, it follows that $d_1 \approx d$ and $d_2 \approx d$. However, since the wavelength is small, the direct and reflected paths may add constructively or destructively over small distances. The carrier phase difference between the direct and reflected paths is

$$\phi_2 - \phi_1 = \frac{2\pi}{\lambda_c}(d_2 - d_1) \tag{2.381}$$

Taking into account the phase difference, the received envelope power is

$$\mu_{\Omega_p} = \Omega_t \left(\frac{\lambda_c}{4\pi d}\right)^2 \left|1 + a\mathrm{e}^{-jb}\mathrm{e}^{j(\phi_2 - \phi_1)}\right|^2, \tag{2.382}$$

where a and b are the amplitude attenuation and phase change introduced by the flat reflecting surface. If a perfect specular reflection is assumed, then $a = 1$ and $b = \pi$ for small θ and

$$\begin{aligned}\mu_{\Omega_p} &= \Omega_t \left(\frac{\lambda_c}{4\pi d}\right)^2 \left|1 - \mathrm{e}^{j\left(\frac{2\pi}{\lambda_c}\Delta_d\right)}\right|^2 \\ &= 4\Omega_t \left(\frac{\lambda_c}{4\pi d}\right)^2 \sin^2\left(\frac{\pi}{\lambda_c}\Delta_d\right),\end{aligned} \tag{2.383}$$

where $\Delta_d = (d_2 - d_1)$. Given that $d \gg h_b$ and $d \gg h_m$, and applying the approximation $\sqrt{1+x} \approx 1 + x/2$ for small x to (2.379) and (2.380),

$$\Delta_d \approx \frac{2h_b h_m}{d}. \tag{2.384}$$

Finally, the received envelope power is

$$\mu_{\Omega_p} \approx 4\Omega_t \left(\frac{\lambda_c}{4\pi d}\right)^2 \sin^2\left(\frac{2\pi h_b h_m}{\lambda_c d}\right), \tag{2.385}$$

where h_b and h_m are the heights of the BS and MS antennas, respectively. Under the condition that $d \gg h_b h_m$, (2.385) reduces to

$$\mu_{\Omega_p} \approx \Omega_t \left(\frac{h_b h_m}{d^2}\right)^2, \tag{2.386}$$

where the small angle approximation $\sin x \approx x$ for small x has been invoked. Observe that when $d \gg h_b h_m$, the propagation over a flat reflecting surface differs from free space propagation in two ways. First, the path loss is not frequency dependent and, second, the envelope power is inversely proportional to the fourth power of the distance rather than the square of the distance. Finally, the model in (2.386) shows that the received signal power is proportional to the product of the square of the BS and MS antenna heights.

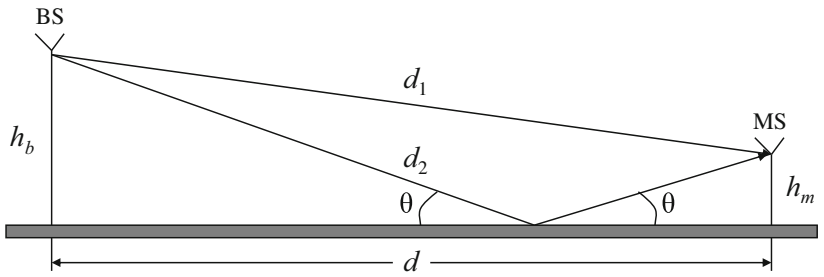

Fig. 2.61 Radio propagation over a flat reflecting surface

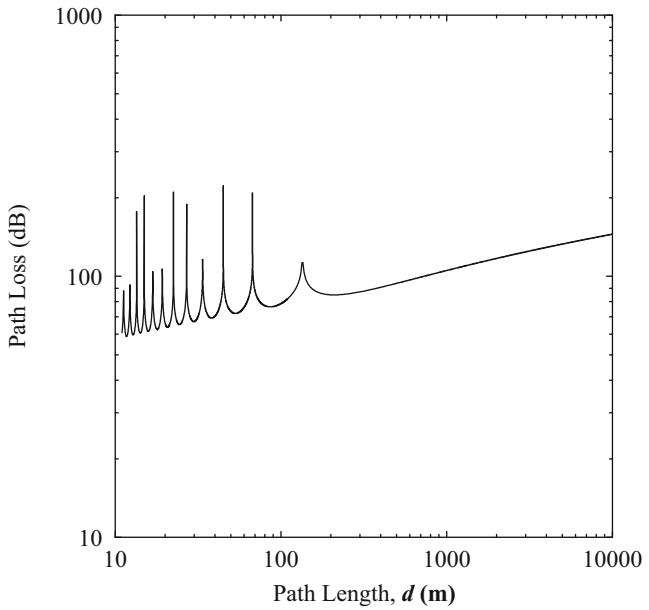

Fig. 2.62 Propagation path loss with distance over a flat reflecting surface; $h_b = 7.5\,\text{m}$, $h_m = 1.5\,\text{m}$, $f_c = 1800\,\text{MHz}$

Figure 2.62 plots the flat Earth path loss (FEPL)

$$\begin{aligned} L_{\text{FE (dB)}} &= 10\log_{10}\left\{\frac{\Omega_t}{\mu_{\Omega_p}}\right\} \\ &= -10\log_{10}\left\{4\left(\frac{\lambda_c}{4\pi d}\right)^2 \sin^2\left(\frac{2\pi h_b h_m}{\lambda_c d}\right)\right\} \quad \text{dB} \end{aligned} \tag{2.387}$$

against the distance d. Notice that the path loss and, hence, the received envelope power has alternate minima and maxima when the path length is small. This propagation property has been noted in experiments by Milstein et al. [225]. The last local maxima in the path loss occurs when

$$\frac{2\pi h_b h_m}{\lambda_c d} = \frac{\pi}{2},$$

giving the break-point distance

$$d_{BP} = \frac{4h_b h_m}{\lambda_c d}. \tag{2.388}$$

2.7.3 Empirical Path Loss Models

Several highly useful empirical models for macrocellular systems have been obtained by curve fitting experimental data. Two of the more useful models for 900 MHz cellular systems are Hata's model [250] based on Okumura's prediction method [161] and Lee's model [196].

2.7.3.1 Okumura–Hata and CCIR Models

Hata's empirical model [161] is simple to use, and distinguishes between various degrees of urbanization. The empirical data for this model was collected by Okumura [250] in the city of Tokyo. The Okumura–Hata model is expressed in terms of the carrier frequency $150 \leq f_c \leq 1000$ (MHz), BS antenna height $30 \leq h_b \leq 200$ (m), the MS antenna height $1 \leq h_m \leq 10$ (m), and the distance $1 \leq d \leq 20$ (km) between the BS and MS. Note the units of the parameters that are used in the model. The model is known to match the experimental data from which is formed to within 1 dB for distances ranging from 1 to 20 km. With the Okumura–Hata model, the path loss between two isotropic BS and MS antennas is:

$$L_{p\ (\mathrm{dB})} = \begin{cases} A + B\log_{10}\{d\} & \text{for urban area} \\ A + B\log_{10}\{d\} - C & \text{for suburban area} \\ A + B\log_{10}\{d\} - D & \text{for open area} \end{cases} \tag{2.389}$$

where

$$\begin{aligned} A &= 69.55 + 26.16\log_{10}\{f_c\} - 13.82\log_{10}\{h_b\} - a(h_m) \\ B &= 44.9 - 6.55\log_{10}\{h_b\} \\ C &= 5.4 + 2\left(\log_{10}\{f_c/28\}\right)^2 \\ D &= 40.94 + 4.78\left(\log_{10}\{f_c\}\right)^2 - 18.33\log_{10}\{f_c\} \end{aligned} \tag{2.390}$$

and

$$a(h_m) = \begin{cases} \left(1.1\log_{10}\{f_c\} - 0.7\right)h_m - \left(1.56\log_{10}\{f_c\} - 0.8\right) & \\ & \text{for medium or small city} \\ \begin{cases} 8.28\left(\log_{10}\{1.54h_m\}\right)^2 - 1.1 & \text{for } f_c \leq 200 \text{ MHz} \\ 3.2\left(\log_{10}\{11.75h_m\}\right)^2 - 4.97 & \text{for } f_c \geq 400 \text{ MHz} \end{cases} & \\ & \text{for large city} \end{cases} \tag{2.391}$$

Typical values from the Okumura–Hata "large city" model are plotted in Fig. 2.63, for a BS height of 70 m, a MS antenna height of 1.5 m, and a carrier frequency of 900 MHz. The reader is cautioned that, due to a lesser degree of urbanization, the path losses for Japanese suburban areas do not match North American suburban areas very well. The latter are more like the quasi-open areas in Japan. Also, the North American urban areas have path losses more like the Japanese suburban areas.

To account for varying degrees of urbanization, the CCIR (Comité International des Radio-Communication, now ITU-R) developed an empirical model for the path loss as:

$$L_{p\ (\mathrm{dB})} = A + B\log_{10}\{d\} - E, \tag{2.392}$$

where A and B are defined in (2.390) with $a(h_m)$ being the medium or small city value in (2.391). The parameter E accounts for the degree of urbanization and is given by

$$E = 30 - 25\log_{10}\{\%\text{ of area covered by buildings}\}, \tag{2.393}$$

where $E = 0$ when the area is covered by approximately 16% buildings.

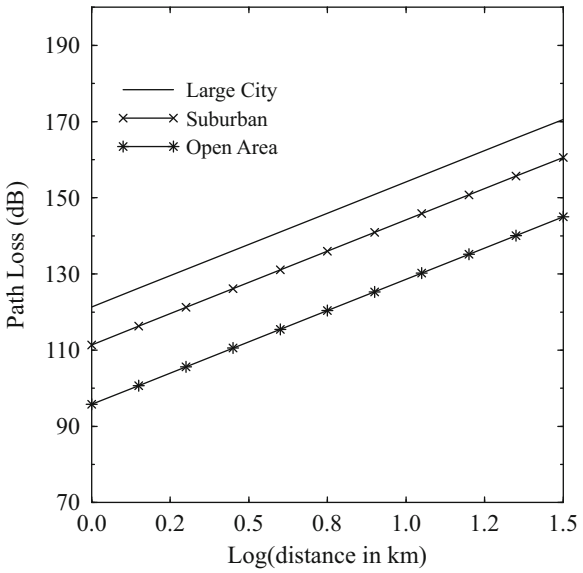

Fig. 2.63 Path loss obtained from the Okumura–Hata model; $h_b = 70\,\text{m}$, $h_m = 1.5\,\text{m}$, $f_c = 900\,\text{Mhz}$

2.7.3.2 Lee's Area-to-Area Model

William C. Y. Lee's area-to-area model [196] can be used to predict a path loss over flat terrain. If the actual terrain is not flat, e.g., hilly, there will be large prediction errors, and other prediction models can be used [196]. Two parameters are required for Lee's area-to-area model; the received power at a 1 mile (1.6 km) point of interception, $\mu_{\Omega_p}(d_o)$, and the path-loss exponent, β. The received signal power at distance d can be expressed as

$$\mu_{\Omega_p}(d) = \mu_{\Omega_p}(d_o)\left(\frac{d}{d_o}\right)^{-\beta}\left(\frac{f}{f_o}\right)^{-n}\alpha_0 \tag{2.394}$$

or in decibel units

$$\mu_{\Omega_p\ (\text{dBm})}(d) = \mu_{\Omega_p\ (\text{dBm})}(d_o) - 10\beta\log_{10}\left\{\frac{d}{d_o}\right\} - 10n\log_{10}\left\{\frac{f}{f_o}\right\} + 10\log_{10}\{\alpha_0\}, \tag{2.395}$$

where d is in units of kilometers and $d_o = 1.6\,\text{km}$. The parameter α_0 is a correction factor used to account for different BS and MS antenna heights, transmit powers, and antenna gains. The following set of *nominal* conditions are assumed in Lee's area-to-area model:

- frequency $f_o = 900\,\text{MHz}$
- BS antenna height $= 30.48\,\text{m}$
- BS transmit power $= 10$ watts
- BS antenna gain $= 6\,\text{dB}$ above dipole gain
- MS antenna height $= 3\,\text{m}$
- MS antenna gain $= 0\,\text{dB}$ above dipole gain

If the actual conditions are different from those listed above, then the following parameters are computed:

$$\alpha_1 = \left(\frac{\text{BS antenna height (m)}}{30.48\ \text{m}}\right)^2$$

$$\alpha_2 = \left(\frac{\text{MS antenna height (m)}}{3\ \text{m}}\right)^{\kappa}$$

$$\alpha_3 = \frac{\text{transmitter power}}{10\ \text{watts}}$$

Table 2.3 Parameters for Lee's area-to-area model in various propagation environments, from [196]

Terrain	$\mu_{\Omega_{p\ (\mathrm{dBm})}}(d_o)$	β
Free space	−45	2
Open area	−49	4.35
North American Suburban	−61.7	3.84
North American Urban (Philadelphia)	−70	3.68
North American Urban (Newark)	−64	4.31
Japanese Urban (Tokyo)	−84	3.05

$$\begin{aligned}\alpha_4 &= \frac{\text{BS antenna gain with respect to } \lambda_c/2 \text{ dipole}}{4}\\ \alpha_5 &= \text{different antenna-gain correction factor at the MS}\end{aligned} \tag{2.396}$$

From these parameters, the correction factor α_0 is

$$\alpha_0 = \alpha_1 \cdot \alpha_2 \cdot \alpha_3 \cdot \alpha_4 \cdot \alpha_5. \tag{2.397}$$

The parameters β and $\mu_{\Omega_p}(d_o)$ have been found from empirical measurements, and are listed in Table 2.3.

Experimental data suggest that n in (2.395) ranges between 2 and 3 with the exact value depending upon the carrier frequency and the geographic area. For $f_c < 450$ MHz in a suburban or open area, $n = 2$ is recommended. In an urban area with $f_c > 450$ MHz, $n = 3$ is recommended. The value of κ in (2.396), also determined from empirical data, is

$$\kappa = \begin{cases} 2 \text{ for a MS antenna height } > \ 10 \text{ m} \\ 3 \text{ for a MS antenna height } < \ 3 \text{ m} \end{cases}. \tag{2.398}$$

The path loss $L_{p\ (\mathrm{dB})}$ is the difference between the transmitted and received envelope power, $L_{p\ (\mathrm{dB})} = \mu_{\Omega_{p\ (\mathrm{dBm})}}(d) - \mu_{\Omega_{t\ (\mathrm{dBm})}}$. To compare directly with the Okumura–Hata model in Fig. 2.63, we assume an isotropic BS antenna with 0 dB gain, such that $\alpha_4 = -6$ dB. Then by using the same parameters as in Fig. 2.63, $h_b = 70$ m, $h_m = 1.5$ m, $f_c = 900$ MHz, a nominal BS transmitter power of 40 dBm (10 watts), and the parameters in Table 2.3 for $\mu_{\Omega_{p\ (\mathrm{dBm})}}(d_o)$ and β, the following path losses are obtained:

$$L_{p\ (\mathrm{dB})} = \begin{cases} 85.74 + 20.0\log_{10}\{d\} & \text{Free Space} \\ 84.94 + 43.5\log_{10}\{d\} & \text{Open Area} \\ 98.68 + 38.4\log_{10}\{d\} & \text{Suburban} \\ 107.31 + 36.8\log_{10}\{d\} & \text{Philadelphia} \\ 100.02 + 43.1\log_{10}\{d\} & \text{Newark} \\ 122.59 + 30.5\log_{10}\{d\} & \text{Tokyo} \end{cases} \tag{2.399}$$

These typical values from Lee's area-to-area model are plotted in Fig. 2.64.

2.7.3.3 COST231-Hata Model

The COST231-Hata model is based on the proposal by Mogensen et al. [228] to extend the Okumura–Hata model for use in the 1500–2000 MHz frequency range, where it is known that the Okumura–Hata model underestimates the path loss. The COST231-Hata model is expressed in terms of the carrier frequency $1500 \le f_c \le 2000$ (MHz), BS antenna height $30 \le h_b \le 200$ (m), MS antenna height $1 \le h_m \le 10$ (m), and distance $1 \le d \le 20$ (km). Note again that the parameters must be used in the model with their specified units. The path loss as predicted by the COST231-Hata model is [80]

$$L_{p\ (\mathrm{dB})} = A + B\log_{10}\{d\} + C, \tag{2.400}$$

where

$$A = 46.3 + 33.9\log_{10}\{f_c\} - 13.82\log_{10}\{h_b\} - a(h_m)$$

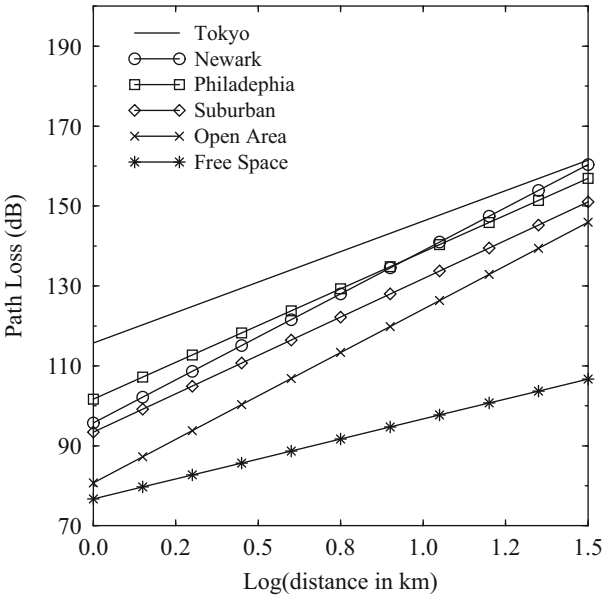

Fig. 2.64 Path loss obtained by using Lee's method; $h_b = 70\,\text{m}$, $h_m = 1.5\,\text{m}$, $f_c = 900\,\text{MHz}$, and an isotropic BS antenna

$$B = 44.9 - 6.55\log_{10}\{h_b\}$$

$$C = \begin{cases} 0 & \text{medium city and suburban areas} \\ & \quad \text{with moderate tree density} \\ 3 & \text{for metropolitan centers} \end{cases}$$

Although both the Okumura and Hata and the COST231-Hata models are limited to BS antenna heights greater than 30 m, they can be used for lower BS antenna heights provided that the surrounding buildings are well below the BS antennas. They should not be used to predict path loss in urban canyons. They should not be used for smaller ranges, where path loss becomes highly dependent upon the local topography. The COST231-Hata model is good down to a path length of 1 km.

2.7.3.4 COST231-Walfish–Ikegami Model

The COST231-Walfish–Ikegami model was developed for microcellular systems and distinguishes between LoS and NLoS propagation. The model is accurate for carrier frequencies in the range $800 \le f_c \le 2000\,(\text{MHz})$, and path distances in the range $0.02 \le d \le 5\,(\text{km})$.

LoS Propagation:

For LoS propagation in a street canyon, the path loss is

$$L_{p\ (\text{dB})} = 42.6 + 26\log_{10}\{d\} + 20\log_{10}\{f_c\}\,,\quad d \ge 20\,\text{m}, \tag{2.401}$$

where the first constant is chosen so that L_p is equal to the FSPL at a distance of 20 m. The model parameters are the distance d (km) and carrier frequency f_c (MHz).

NLoS Propagation:

As defined in Fig. 2.65, the path loss for non-line-of-sight (NLoS) propagation is expressed in terms of the following parameters:

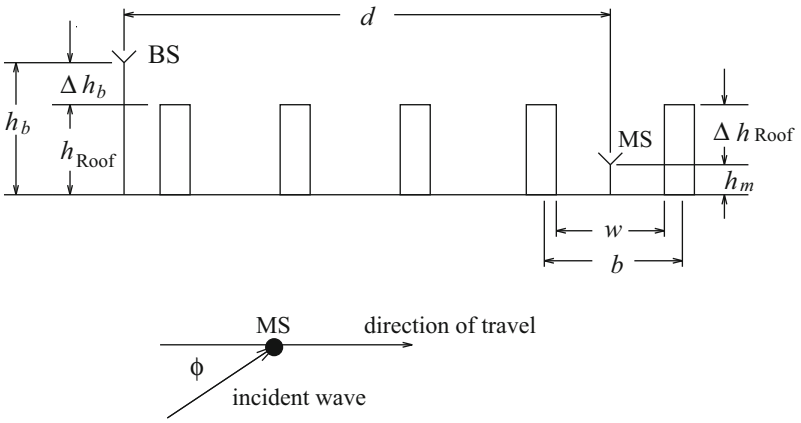

Fig. 2.65 Definition of parameters used in the COST231-Walfish–Ikegami model

$$
\begin{aligned}
d &= \text{distance (m)} \\
h_b &= \text{BS antenna height over street level, } 4 \le h_b \le 50 \text{ (m)} \\
h_m &= \text{MS antenna height over street level, } 1 \le h_m \le 3 \text{ (m)} \\
h_{\text{Roof}} &= \text{nominal roof height of buildings (m)} \\
\Delta h_b &= h_b - h_{\text{Roof}} = \text{height of BS relative to rooftops (m)} \\
\Delta h_m &= h_{\text{Roof}} - h_m = \text{height of MS relative to rooftops (m)} \\
w &= \text{width of streets (m)} \\
b &= \text{building separation (m)} \\
\phi &= \text{angle of incident wave with respect to street (degrees)}
\end{aligned}
$$

If no data on the structure of the buildings and roads are available, the following default values are recommended, $b = 20 \ldots 50$ (m), $w = b/2$ (m), $\phi = 90°$, and $h_{\text{Roof}} = 3 \times$ number of floors + roof (m), where roof = 3 (m) pitched and 0 (m) flat.

The NLoS path loss is composed of three terms, viz.,

$$
L_{p\ (\text{dB})} = \begin{cases} L_o + L_{\text{rts}} + L_{\text{msd}} & \text{, for } L_{\text{rts}} + L_{\text{msd}} \ge 0 \\ L_o & \text{, for } L_{\text{rts}} + L_{\text{msd}} < 0 \end{cases}, \tag{2.402}
$$

where

$$
\begin{aligned}
L_o &= \text{free-space loss} = 32.4 + 20\log_{10}\{d\} + 20\log_{10}\{f_c\} \\
L_{\text{rts}} &= \text{roof-top-to-street diffraction and scatter loss} \\
L_{\text{msd}} &= \text{multi-screen diffraction loss.}
\end{aligned}
$$

Note that the expression for free-space loss differs from (2.378) because here the units of d are in kilometers and the units of f_c are in megahertz. The roof-top-to-street diffraction and scatter loss represents the coupling of the wave propagation along the multi-screen path into the street where the MS is located, and is given by

$$
L_{\text{rts}} = -16.9 - 10\log_{10}\{w\} + 10\log_{10}\{f_c\} + 20\log_{10}\{\Delta h_m\} + L_{\text{ori}}, \tag{2.403}
$$

where

$$L_{\text{ori}} = \begin{cases} -10 + 0.354(\phi) & , \ 0 \le \phi \le 35° \\ 2.5 + 0.075(\phi - 35°) & , \ 35° \le \phi \le 55° \\ 4.0 - 0.114(\phi - 55°) & , \ 55° \le \phi \le 90° \end{cases} . \tag{2.404}$$

is a street orientation loss.

The multi-screen diffraction loss is

$$L_{\text{msd}} = L_{\text{bsh}} + k_a + k_d \log_{10}\{d\} + k_f \log_{10}\{f_c\} - 9\log_{10}\{b\}, \tag{2.405}$$

where

$$L_{\text{bsh}} = \begin{cases} -18\log_{10}\{1 + \Delta h_b\} & , \ h_b > h_{\text{Roof}} \\ 0 & , \ h_b \le h_{\text{Roof}} \end{cases} \tag{2.406}$$

is the shadowing gain (negative loss) for cases when the BS antenna is above the rooftops. The parameters k_a and k_d depend on the path length, d, and base station elevation with respect to the rooftops, Δh_b. The term k_a accounts for the increase in path loss when the BS antennas are situated below the roof tops of adjacent buildings, and is given by

$$k_a = \begin{cases} 54 , & h_b > h_{\text{Roof}} \\ 54 - 0.8\Delta h_b , & d \ge 0.5 \text{ km and } h_b \le h_{\text{Roof}} \\ 54 - 0.8\Delta h_b d/0.5 , & d < 0.5 \text{ km and } h_b \le h_{\text{Roof}} \end{cases} . \tag{2.407}$$

The terms k_d and k_f control the dependency of the multi-screen diffraction loss on the distance and frequency, respectively, and are given by

$$k_d = \begin{cases} 18 , & h_b > h_{\text{Roof}} \\ 18 - 15\Delta h_b / h_{\text{Roof}} , & h_b \le h_{\text{Roof}} \end{cases} \tag{2.408}$$

$$k_f = -4 + \begin{cases} 0.7(f_c/925 - 1) , & \text{medium city and suburban} \\ 1.5(f_c/925 - 1) , & \text{metropolitan area} \end{cases} . \tag{2.409}$$

The COST231-Walfish–Ikegami model works best for $h_b \gg h_{\text{Roof}}$. Large prediction errors can be expected for $h_b \approx h_{\text{Roof}}$. The model is poor for $h_b \ll h_{\text{Roof}}$ because the terms in (2.407) do not consider wave guiding in street canyons and diffraction at street corners.

2.7.3.5 Street Microcells

For ranges less than 500 m and antenna heights less than 20 m, some empirical measurements have shown that the received signal strength for LoS propagation along city streets can be described by the two-slope model [149, 160, 173, 267, 338, 351]

$$\mu_{\Omega_p} = \frac{k\Omega_t}{d^a(1 + d/g)^b}, \tag{2.410}$$

where Ω_t is the transmitted power, k is a constant of proportionality, and d (m) is the distance. For small path length distances, free space propagation will prevail so that $a = 2$. The parameter g is called the break-point and ranges from 150 to 300 m [149, 160, 173, 351]. At larger distances, an inverse-fourth to -eighth power law is experienced so that b ranges from 2 to 6 [160]. The model parameters that were obtained by Harley are listed in Table 2.4. Xia [358] has demonstrated that the break-point occurs where the Fresnel zone between the transmit and receive antennas just touches the ground assuming a flat surface. This distance is

$$g = \frac{1}{\lambda_c}\sqrt{(\Sigma^2 - \Delta^2)^2 - 2(\Sigma^2 + \Delta^2)\left(\frac{\lambda_c}{2}\right)^2 + \left(\frac{\lambda_c}{2}\right)^4}, \tag{2.411}$$

Table 2.4 Two-slope path loss parameters obtained by Harley, from [160]

Base antenna height (m)	a	b	Break-point g (m)
5	2.30	−0.28	148.6
9	1.48	0.54	151.8
15	0.40	2.10	143.9
19	−0.96	4.72	158.3

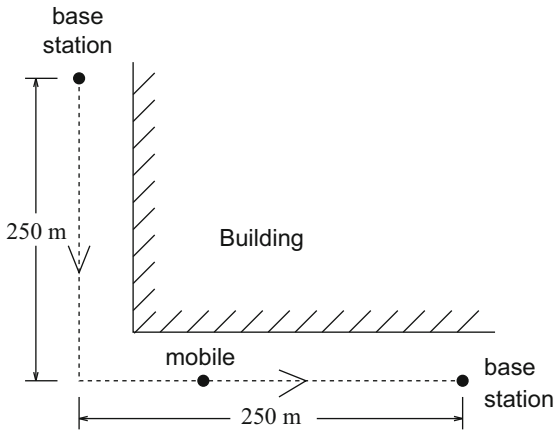

Fig. 2.66 The corner effect in a street microcell environment

where $\Sigma = h_b + h_m$ and $\Delta = h_b - h_m$. For high frequencies this distance can be approximated as $g = 4h_b h_m/\lambda_c$, which is the same distance as the last local maxima in the flat reflecting surface model in Sect. 2.7.2. Notice that the break-point is dependent on frequency, with the break-point at 1.9 GHz being about twice that for 900 MHz.

Street microcells may also exhibit NLoS propagation when a MS rounds a street corner as shown in Fig. 2.66. In this case, the average received signal strength can drop by as much as 25–30 dB over distances as small as 10 m for low antenna heights in an area with multi-story buildings [61, 210, 233, 286, 324], and by 25–30 dB over distances of 45–50 m for low antenna heights in a region with only one- or two-story buildings [286]. This phenomenon is known as the corner effect.

Grimlund and Gudmundson [149] have proposed an empirical street corner path loss model. Their model assumes LoS propagation until the MS reaches a street corner. The NLoS propagation after rounding a street corner is modeled by assuming LoS propagation from a virtual transmitter that is located at the street corner having a transmit power equal to the received power at the street corner from the serving BS. That is, the received is given by

$$\mu_{\Omega_p} = \begin{cases} \frac{k\Omega_t}{d^a(1+d/g)^b} & d \le d_c \\ \frac{k\Omega_t}{d_c^a(1+d_c/g)^b} \cdot \frac{1}{(d-d_c)^a(1+(d-d_c)/g)^b} & d > d_c \end{cases}, \tag{2.412}$$

where d_c (m) is the distance between the serving BS and the corner. For the scenario depicted in Fig. 2.66, the received signal strength with this model is shown in Fig. 2.67. The heavy curves show the average received signal strength from the two BSs as the MS traverses the dashed path shown in Fig. 2.66. These curves were obtained by using $a = 2$, $b = 2$, $g = 150$ m, and $d_c = 250$ m in (2.412), and assuming that $\mu_{\Omega_p} = 1$ dBm at $d = 1$ m. The dotted curves superimposed on the heavy lines in Fig. 2.67 show the received signal strength with the combined effects of path loss, log-normal shadowing, and multipath-fading. The latter two were obtained by using the simulators described in Sects. 2.6.1 and 2.5.2.2.

2.7.3.6 3GPP 3-D Path Loss Models

The 3GPP path loss models as described in [1] are valid from 2 to 6 GHz for different BS and MS antenna heights. The distance definitions are defined in Fig. 2.68 for outdoor scenarios and Fig. 2.69 for outdoor–indoor scenarios. The 3GPP path loss models are categorized into urban macrocell (UMa) and urban microcell (UMi) cases, corresponding to BS antenna heights of 25 m or less and 25 m or more, respectively. The UMa and UMi cases are further categorized into LoS, NLoS, and outdoor-to-indoor scenarios.

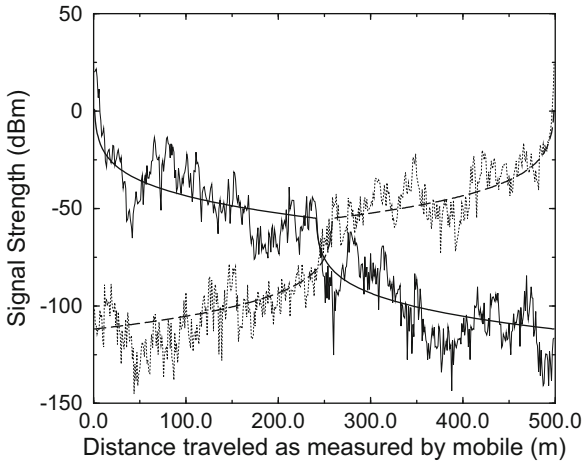

Fig. 2.67 Received signal strength for the street microcell environment in Fig. 2.66. Solid lines show the area mean signal strength, while the dashed lines account for shadowing and fading as well. For this latter case, $\sigma_\Omega = 6\,\text{dB}$ and $\phi_{\Omega_p\,(\text{dBm})\Omega_p\,(\text{dBm})}(d) = 0.1\sigma_\Omega^2$ at $d = 30\,\text{m}$. For each BS, the received signal strength is shown when the MS is connected to that particular BS and the MS moves along the route in Fig. 2.66

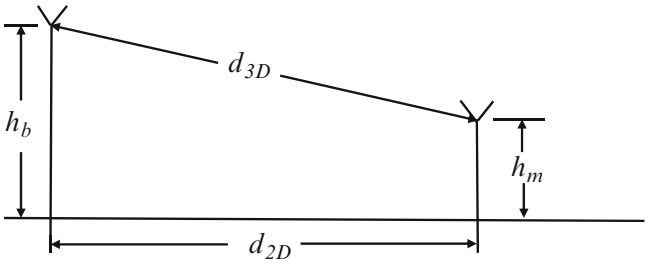

Fig. 2.68 Definition of d_{2D}, and d_{3D} for outdoor mobile stations, from [1]

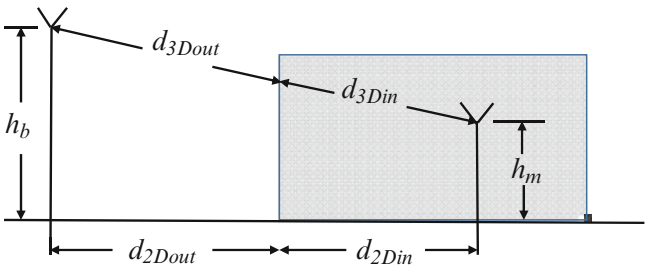

Fig. 2.69 Definition of $d_{2\text{Dout}}$, $d_{2\text{Din}}$, $d_{3\text{Dout}}$ and $d_{3\text{Din}}$ for indoor mobile stations, from [1]

LoS Probability

The various 3GPP path loss models make use of the probability of LoS condition. For microcells and outdoor MSs, the probability of LoS is [1]

$$\text{P}_{\text{LoS}} = \min(18/d_{2D}, 1)(1 - \text{e}^{-d_{2D}/36}) + \text{e}^{-d_{2D}/36} \tag{2.413}$$

For microcells and indoor MSs, the above formula is used with d_{2D} replaced by $d_{2\text{Dout}}$. For macrocells and outdoor MSs, the probability of LoS is [1]

$$\text{P}_{\text{LoS}} = \left(\min(18/d_{2D}, 1)(1 - \text{e}^{-d_{2D}/63}) + \text{e}^{-d_{2D}/63}\right)(1 + C(d_{2D}, h_m)) \tag{2.414}$$

where

$$C(d_{2D}, h_m) = \begin{cases} 0 & , \quad h_m < 13\,\text{m} \\ \left(\frac{h_m - 13}{10}\right)^{1.5} g(d_{2D}) & , \quad 13\,\text{m} \le h_m \le 23\,\text{m} \end{cases} \tag{2.415}$$

and

$$g(d_{2D}) = \begin{cases} (1.25\mathrm{e}^{-6}) d_{2D}^2 \mathrm{e}^{d_{2D}/150} & , \ d_{2D} > 18\,\mathrm{m} \\ 0 & , \ \text{otherwise} \end{cases} \tag{2.416}$$

For macrocells and indoor MSs, the above formulas are used with d_{2D} replaced by $d_{2\mathrm{Dout}}$. For frequencies above 6 GHz, including mm-wave frequencies, the study in [158] recommends to use the above 3GPP LoS models.

Using the above LoS probability models, the 3GPP 3-D path loss models are defined below for various topographic scenarios, as described in [1].

3D-UMa LoS

For macrocells with LoS conditions

$$L_{\mathrm{UMaLoS\ (dB)}} = 22.0 \log_{10}(d_{3D}) + 28.0 + 20 \log_{10}(f_c)\ , \quad 10\,\mathrm{m} < d_{2D} < d_{BP} \tag{2.417}$$

$$\begin{aligned} L_{\mathrm{UMaLoS\ (dB)}} &= 40 \log_{10}(d_{3D}) + 28.0 + 20 \log_{10}(f_c) - 9 \log_{10}\left(d_{BP}^2 + (h_b - h_m)^2\right)\ , \quad d_{BP} < d_{2D} < 5000\,\mathrm{m} \\ h_b &= 25\,\mathrm{m};\ 1.5\,\mathrm{m} \le h_m \le 22.5\,\mathrm{m} \end{aligned} \tag{2.418}$$

The break-point distance is given by $d_{BP} = 4 h_b h_m f_c / c$ corresponding to the last local maxima in the flat earth model (2.388). In the 3D-UMa scenario the effective antenna heights h_b and h_m are computed as follows: $h_b = \hat{h}_b - h_E$, $h_m = \hat{h}_m - h_E$, where $\hat{h}_b$ and $\hat{h}_m$ are the actual antenna heights, and the effective environment height h_E depends on the link between a BS and a MS. For LoS links, $h_E = 1$ m with probability $1/(1 + C(d_{2D}, h_m))$, where the function $C(d_{2D}, h_m)$ is defined in (2.415). Otherwise, h_E is chosen from a discrete uniform distribution on the set $\{12, 15, \ldots, (h_m - 1.5)\}$.

The shadow standard deviation is $\sigma_\Omega = 4$ dB.

3D-UMa NLoS

For macrocells with NLoS conditions

$$L_{\mathrm{UMaNLOS\ (dB)}} = \max\left\{L_{\mathrm{UMaNLoS\ (dB)}},\ L_{\mathrm{UMaLoS\ (dB)}}\right\}, \tag{2.419}$$

where

$$\begin{aligned} L_{\mathrm{UMaNLoS\ (dB)}} = {} & 161.04 - 7.1 \log_{10}(W) + 7.5 \log_{10}(h_{\mathrm{build}}) \\ & - \left(24.37 - 3.7 (h_{\mathrm{build}}/h_b)^2\right) \log_{10}(h_b) \\ & + (43.42 - 3.1 \log_{10}(h_b)) \left(\log_{10}(d_{3D}) - 3\right) \\ & + 20 \log_{10}(f_c) - \left(3.2 (\log_{10}(17.625))^2 - 4.97\right) - 0.6 (h_m - 1.5) \end{aligned} \tag{2.420}$$

and

$10\,\mathrm{m} < d_{2D} < 5000\,\mathrm{m}$

h_{build} = average building height

W = street width

$h_b = 25\,\mathrm{m},\ 1.5\,\mathrm{m} \le h_m \le 22.5\,\mathrm{m},\ W = 20\,\mathrm{m},\ h_{\mathrm{build}} = 20\,\mathrm{m}$

Applicable ranges:

$5\,\mathrm{m} < h_{\mathrm{build}} < 50\,\mathrm{m}$

$5\,\mathrm{m} < W < 50\,\mathrm{m}$

$$10\,\text{m} < h_b < 150\,\text{m}$$
$$1.5\,\text{m} \leq h_m \leq 22.5\,\text{m}$$

The shadow standard deviation is $\sigma_\Omega = 6\,\text{dB}$.

3D-UMa O-to-I

For macrocells with outdoor-to-indoor conditions

$$L_{\text{UMaO-to-I (dB)}} = L_{\text{b (dB)}} + L_{\text{tw (dB)}} + L_{\text{in (dB)}} \tag{2.421}$$

For a hexagonal cell layout:

$$L_{\text{b (dB)}} = L_{\text{UMa (dB)}}(d_{3D-\text{out}} + d_{3D-\text{in}})$$
$$L_{\text{tw (dB)}} = 20 \ \text{(loss through wall)}$$
$$L_{\text{in (dB)}} = 0.5 d_{2D-\text{in}} \ \text{(inside loss)}$$

where

$$10\,\text{m} < d_{2D-\text{out}} + d_{2D-\text{in}} < 1000\,\text{m}$$
$$0\,\text{m} < d_{2D-\text{in}} < 25\,\text{m}$$
$$h_b = 25\,\text{m}, h_m = 3(n_{fl} - 1) + 1.5\,, \ \ n_{fl} = 1, 2, 3, 4, 5, 6, 7, 8$$
$$d_{2D-\text{in}} \text{ is assumed uniformly distributed between 0 and 25.}$$

The shadow standard deviation is $\sigma_\Omega = 7\,\text{dB}$.

The building penetration loss (BPL) or "loss through wall" in the 3GPP 3D-UMa O-to-I model is 20 dB. However, this will vary greatly depending on the building. Moreover, the building penetration loss increases with frequency. An empirical BPL model was suggested in [158] as

$$\text{BPL}_{\text{(dB)}} = 10\log_{10}\left(A + Bf_c^2\right), \tag{2.422}$$

where f_c is the frequency in GHz, $A = 5$ and $B = 0.03$ for low loss buildings and $A = 10$ and $B = 5$ for high loss buildings.

3D-UMi LoS

The microcell LoS path loss is the same as the macrocell LoS path loss $L_{\text{UMaLOS (dB)}}$, except that $h_E = 1\,\text{m}$ with probability one and the shadow standard deviation is $\sigma_\Omega = 3\,\text{dB}$.

3D-UMi NLoS

For a hexagonal cell layout

$$L_{\text{UMiNLoS (dB)}} = \max\left\{L_{\text{UMiNLoS (dB)}},\ L_{\text{UMiLoS (dB)}}\right\}, \tag{2.423}$$

where

$$L_{\text{UMiNLoS (dB)}} = 36.7\log_{10}(d_{3D}) + 22.7 + 26\log_{10}(fc) - 0.3(h_m - 1.5) \tag{2.424}$$

$$10\,\text{m} < d_{2D} < 2000\,\text{m}$$
$$h_b = 10\,\text{m}$$
$$1.5\,\text{m} \leq h_m \leq 22.5\,\text{m}$$

The shadow standard deviation is $\sigma_\Omega = 4\,\text{dB}$.

3D-UMi O-to-I

The microcell outdoor-to-indoor path loss is the same as the macrocell outdoor-to-indoor path loss $L_{\text{UMaO-to-I (dB)}}$, except that $h_b = 10\,\text{m}$ instead of $h_b = 25\,\text{m}$. The shadow standard deviation remains at $\sigma_\Omega = 7\,\text{dB}$.

2.7.3.7 mm-Wave Path Loss Models

Next generation or 5G wireless systems will use frequencies from 600 MHz up to 100 GHz. Existing path loss models were developed for frequencies up to 6 GHz. For frequencies above 6 GHz, new path loss models are required for both LoS and NLoS environments.

Several models have been proposed for mm-wave path loss including the close-in (CI) path loss with a free-space reference distance, the close-in path loss model with a frequency dependent path loss exponent (CIF), and the Alpha-Beta-Gamma (ABG) path loss model, as described in [158].

The CI path loss model is defined by

$$L_{\text{CI (dB)}} = L_{\text{FS (dB)}}(f_c, 1\,\text{m}) + 10\beta\log_{10}\left(\frac{d}{1\,\text{m}}\right) \tag{2.425}$$

where $L_{\text{FS (dB)}}(f_c, 1\,\text{m})$ represents the FSPL at a distance of 1 m, and f_c is the frequency in Hz. From (2.378), the FSPL at 1 m at frequency f_c is given by

$$L_{\text{FS (dB)}}(f_c, 1\,\text{m}) = 10\log_{10}\left\{\left(\frac{4\pi f_c}{c}\right)^2\right\} \tag{2.426}$$

The CI path loss model requires only the path loss exponent β, and ties the path loss to the FSPL at a distance of 1 m and frequency f_c.

The CIF model is an extension of the CI LoS path loss model that captures the frequency dependency of the path loss across a range of operating frequencies. This is particularly important for wideband mm-wave systems, where the operating bandwidth may be tens of Gigahertz.

$$L_{\text{CIF (dB)}} = L_{\text{FS (dB)}}(f_c, 1\,\text{m}) + 10\beta\left(1 + b\left(\frac{f_c - f_o}{f_o}\right)\right)\log_{10}\left(\frac{d}{1\,\text{m}}\right) \tag{2.427}$$

where β is again the path loss exponent, while b is an optimization parameter that captures the frequency dependency of the path loss that balances at centroid frequency f_o. The path loss increases with frequency when b is a positive value. When $b = 0$ or $f_c = f_o$, the CIF path loss model reduces to the CI path loss model. The centroid frequency is determined according to a weighted average of empirical data as

$$f_o = \frac{\sum_{k=1}^{K} f_k N_k}{\sum_{k=1}^{K} N_k} \tag{2.428}$$

where N_k is the number of path loss measurements at frequency f_k.

The ABG path loss model is similar to Lee's Area-to-Area path loss model in Sect. 2.7.3.2. The ABG path loss is given by

$$L_{\text{ABG (dB)}} = \alpha_{\text{(dB)}} + 10\beta\log_{10}(d) + 10\gamma\log_{10}(f_c) \tag{2.429}$$

Table 2.5 Parameters for CI and ABG mm-wave path loss models, where SC stands for street canyon and OS stands for open square, from [158]

Scenario	CI model parameters	ABG model parameters
UMa-LoS	$\beta = 2.00$, $\sigma_\Omega = 4.1$ dB	N/A
UMa-NLoS	$\beta = 3.00$, $\sigma_\Omega = 6.8$ dB	$\alpha = 19.20$, $\beta = 3.40$, $\gamma = 2.30$, $\sigma_\Omega = 6.5$ dB
UMi-SC-LoS	$\beta = 1.98$, $\sigma_\Omega = 3.1$ dB	N/A
UMi-SC-NLoS	$\beta = 3.19$, $\sigma_\Omega = 8.2$ dB	$\alpha = 21.02$, $\beta = 3.48$, $\gamma = 2.34$, $\sigma_\Omega = 7.8$ dB
UMi-OS-LoS	$\beta = 1.85$, $\sigma_\Omega = 4.2$ dB	N/A
UMI-OS-NLos	$\beta = 2.89$, $\sigma_\Omega = 7.1$ dB	$\alpha = 3.66$, $\beta = 4.14$, $\gamma = 2.43$, $\sigma_\Omega = 7.0$ dB

Table 2.6 Path loss exponents and shadow standard deviations for several different types of buildings, from [18]

Building	Frequency (MHz)	β	σ_Ω (dB)
Retail stores	914	2.2	8.7
Grocery stores	914	1.8	5.2
Office, hard partition	1500	3.0	7.0
Office, soft partition	900	2.4	9.6
Office, soft partition	1900	2.6	14.1

where $\alpha_{(\text{dB})}$ is a floating offset value in dB units, and γ captures the frequency dependency of the model.

The usage of each path loss model will depend on the particular scenario. For outdoor mm-wave systems, two 3GPP models have been proposed [158]. The first applies to BS antenna heights of 25 m or less, and is called the urban microcell (UMi) model. The second applies to BS antenna heights of 25 m or more, and is called the urban macrocell (UMa) model. In each case, there are LoS and NLoS scenarios. Table 2.5 shows the parameters of the CI and ABG mm-wave path loss models for different environments.

2.7.3.8 Path Loss in Indoor Microcells

The path loss and shadowing characteristics for indoor microcells vary greatly from one building to the next. Typical path loss exponents and shadow standard deviations are provided in Table 2.6 for several different types of buildings.

For multistory buildings, the signal attenuation between floors is important. Measurements have shown that the greatest floor loss occurs when the transmitter and receiver are separated by a single floor. Typically, the floor loss is 15–20 dB for one floor and an additional 6–10 dB per floor up to a separation of 4 floors. For 5 or more floors of separation, the overall floor loss will increase only a few decibels for each additional floor. This effect is thought to be caused by signals diffracting up the sides of the building and signals scattering off the neighboring buildings. Also important for the deployment of indoor wireless systems is the building penetration loss. This loss depends on the frequency and height of the building. Turkmani et al. [323] have shown that the building penetration losses decrease with increasing frequency, in particular they are 16.4, 11.6, and 7.6 dB at 441, 896.5, and 1400 MHz, respectively. In general, the building penetration loss for signals propagating into a building tends to decrease with height, the reason being that a LoS path is more likely to exist at increased height. The building penetration loss decreases by about 2 dB per floor from ground level up to about 9–15 floors and then increases again [339]. Windows also have a significant effect on penetration loss. Plate glass provides an attenuation of about 6 dB, while lead lined glass provides an attenuation anywhere from 3 to 30 dB.

Appendix 2A: COST 207 Channel Models

The COST 207 study has specified typical realizations for the power-delay profile in the following environments; Typical Urban (TU), Bad Urban (BA), Reduced TU, Reduced BU, Rural Area (RA), and Hilly Terrain (HT) [79]. The models below are identical to the COST 207 models, except that fractional powers have been normalized so as to sum to unity, i.e., the envelope power is normalized to unity.

Table 2.7 COST 207 Typical Urban (TU) ($\sigma_\tau = 1.0\,\mu s$) and Bad Urban (BU) ($\sigma_\tau = 2.5\,\mu s$) power-delay profiles, from [79]

Typical Urban (TU)			Bad Urban (BU)		
Delay μs	Fractional power	Doppler category	Delay μs	Fractional power	Doppler category
0.0	0.092	CLASS	0.0	0.033	CLASS
0.1	0.115	CLASS	0.1	0.089	CLASS
0.3	0.231	CLASS	0.3	0.141	CLASS
0.5	0.127	CLASS	0.7	0.194	GAUS1
0.8	0.115	GAUS1	1.6	0.114	GAUS1
1.1	0.074	GAUS1	2.2	0.052	GAUS2
1.3	0.046	GAUS1	3.1	0.035	GAUS2
1.7	0.074	GAUS1	5.0	0.140	GAUS2
2.3	0.051	GAUS2	6.0	0.136	GAUS2
3.1	0.032	GAUS2	7.2	0.041	GAUS2
3.2	0.018	GAUS2	8.1	0.019	GAUS2
5.0	0.025	GAUS2	10.0	0.006	GAUS2

Table 2.8 COST 207 Reduced Typical Urban (TU) ($\sigma_\tau = 1.0\,\mu s$) and Reduced Bad Urban (BU) ($\sigma_\tau = 2.5\,\mu s$) power-delay profiles, from [79]

Typical Urban (TU)			Bad Urban (BU)		
Delay μs	Fractional power	Doppler category	Delay μs	Fractional power	Doppler category
0.0	0.189	CLASS	0.0	0.164	CLASS
0.2	0.379	CLASS	0.3	0.293	CLASS
0.5	0.239	CLASS	1.0	0.147	GAUS1
1.6	0.095	GAUS1	1.6	0.094	GAUS1
2.3	0.061	GAUS2	5.0	0.185	GAUS2
5.0	0.037	GAUS2	6.6	0.117	GAUS2

Table 2.9 COST 207 Typical Rural (non-hilly) Area (RA) power-delay profile ($\sigma_\tau = 0.1\,\mu s$), from [79]

Delay μs	Fractional power	Doppler category
0.0	0.602	RICE
0.1	0.241	CLASS
0.2	0.096	CLASS
0.3	0.036	CLASS
0.4	0.018	CLASS
0.5	0.006	CLASS

Table 2.10 COST 207 Typical Hilly Terrain (HT) power-delay profile ($\sigma_\tau = 5.0\,\mu s$), from [79]

Delay μs	Fractional power	Doppler category
0.0	0.026	CLASS
0.1	0.042	CLASS
0.3	0.066	CLASS
0.5	0.105	CLASS
0.7	0.263	GAUS1
1.0	0.263	GAUS1
1.3	0.105	GAUS1
15.0	0.042	GAUS2
15.2	0.034	GAUS2
15.7	0.026	GAUS2
17.2	0.016	GAUS2
20.0	0.011	GAUS2

Table 2.11 COST 207 Reduced Hilly Terrain (HT) power-delay profile ($\sigma_\tau = 5.0\,\mu s$), from [79]

Delay μs	Fractional power	Doppler category
0.0	0.413	CLASS
0.1	0.293	CLASS
0.3	0.145	CLASS
0.5	0.074	CLASS
15.0	0.066	GAUS2
17.2	0.008	GAUS2

Appendix 2B: COST 259 Channel Models

The 3GPP standards group has defined three typical realizations for the COST 259 models; Typical Urban (TUx), Rural Area (RAx), and Hilly Terrain (HTx), where x is the MS speed in km/h, [113]. Default speeds are 3, 50, and 120 km/h for the TUx model, 120 and 250 km/h for the RAx model, and 120 km/h for the HTx model.

Table 2.12 COST 259 Typical Urban (TUx) channel model, from [113]

Delay μs	Fractional power	Doppler category
0.000	0.26915	CLASS
0.217	0.17378	CLASS
0.512	0.09772	CLASS
0.514	0.09550	CLASS
0.517	0.09550	CLASS
0.674	0.07079	CLASS
0.882	0.04571	CLASS
1.230	0.02344	CLASS
1.287	0.02042	CLASS
1.311	0.01950	CLASS
1.349	0.01820	CLASS
1.533	0.01259	CLASS
1.535	0.01259	CLASS
1.622	0.01047	CLASS
1.818	0.00708	CLASS
1.836	0.00692	CLASS
1.884	0.00617	CLASS
1.943	0.00550	CLASS
2.048	0.00447	CLASS
2.140	0.00372	CLASS

Table 2.13 COST 259 Rural Area (RAx) channel model, from [113]

Delay μs	Fractional power	Doppler category
0.000	0.30200	Direct path, $f_0 = 0.7 f_m$
0.042	0.22909	CLASS
0.101	0.14454	CLASS
0.129	0.11749	CLASS
0.149	0.10000	CLASS
0.245	0.04898	CLASS
0.312	0.02951	CLASS
0.410	0.01413	CLASS
0.469	0.00912	CLASS
0.528	0.00575	CLASS

Table 2.14 COST 259 Hilly Terrain (HTx) channel model, from [113]

Delay μs	Fractional power	Doppler category
0.000	0.43652	CLASS
0.356	0.12882	CLASS
0.441	0.09550	CLASS
0.528	0.07079	CLASS
0.546	0.06607	CLASS
0.609	0.05370	CLASS
0.625	0.05012	CLASS
0.842	0.02399	CLASS
0.916	0.01862	CLASS
0.941	0.01698	CLASS
15.000	0.01738	CLASS
16.172	0.00537	CLASS
16.492	0.00389	CLASS
16.876	0.00263	CLASS
16.882	0.00263	CLASS
16.978	0.00240	CLASS
17.615	0.00126	CLASS
17.827	0.00102	CLASS
17.849	0.00100	CLASS
18.016	0.00085	CLASS

Appendix 2C: ITU Channel Models

ITU models have been developed indoor office, outdoor to indoor and pedestrian, and vehicular-high antenna [276]. The models below are identical to the ITU models, except that fractional powers have been normalized so as to sum to unity, i.e., the envelope power is normalized to unity.

Table 2.15 ITU indoor office environment power-delay profiles, from [276]

Channel A			Channel B		
Delay ns	Fractional power	Doppler category	Delay ns	Fractional power	Doppler category
0	0.61722	FLAT	0	0.57833	FLAT
50	0.30934	FLAT	100	0.25245	FLAT
110	0.06172	FLAT	200	0.11020	FLAT
170	0.00978	FLAT	300	0.04811	FLAT
290	0.00155	FLAT	500	0.00917	FLAT
310	0.00039	FLAT	700	0.00175	FLAT

Table 2.16 ITU outdoor to indoor and pedestrian power-delay profiles, from [276]

Channel A			Channel B		
Delay ns	Fractional power	Doppler category	Delay ns	Fractional power	Doppler category
0	0.88935	CLASSIC	0	0.40569	CLASSIC
110	0.09529	CLASSIC	200	0.32976	CLASSIC
190	0.01069	CLASSIC	800	0.13128	CLASSIC
410	0.00467	CLASSIC	1200	0.06430	CLASSIC
			2300	0.06733	CLASSIC
			3700	0.00165	CLASSIC

Table 2.17 ITU vehicular power-delay profiles, from [276]

Channel A			Channel B		
Delay ns	Fractional power	Doppler category	Delay ns	Fractional power	Doppler category
0	0.48500	CLASSIC	0	0.34020	CLASSIC
310	0.38525	CLASSIC	300	0.60498	CLASSIC
710	0.06106	CLASSIC	8900	0.03175	CLASSIC
1090	0.04850	CLASSIC	12,900	0.00605	CLASSIC
1730	0.01534	CLASSIC	17,100	0.00183	CLASSIC
2510	0.00485	CLASSIC	20,000	0.01520	CLASSIC

Appendix 2D: Derivation of Eq. (2.358)

This Appendix derives an expression for the second moment of a Ricean random variable in terms of its first moment. A Ricean random variable X has probability density function, cf., (2.57)

$$p_X(x) = \frac{x}{b_0} \exp\left\{-\frac{x^2+s^2}{2b_0}\right\} I_0\left(\frac{xs}{b_0}\right) \quad x > 0 \tag{2D.1}$$

and moments [272]

$$\mathrm{E}[X^n] = (2b_0)^{\frac{n}{2}} \exp\left\{-\frac{s^2}{2b_0}\right\} \Gamma\left((2+n)/2\right) \, {}_1\mathrm{F}_1\left(\frac{n+2}{2}, 1; \frac{s^2}{2b_0}\right) \tag{2D.2}$$

where $\Gamma(\cdot)$ is the Gamma function, and ${}_1\mathrm{F}_1(a,\ b;\ x)$ is the confluent hypergeometric function. The first moment of X is

$$\mathrm{E}[X] \equiv \Omega_v = (2b_0)^{\frac{1}{2}} \mathrm{e}^{-K} \frac{\sqrt{\pi}}{2} \, {}_1\mathrm{F}_1(3/2, 1; K), \tag{2D.3}$$

where $K = s^2/2b_0$ is the Rice factor. The second moment of X is

$$\begin{aligned} \mathrm{E}[X^2] \equiv \Omega_p &= 2b_0 \mathrm{e}^{-K} \, {}_1\mathrm{F}_1(2, 1; K) \\ &= 2b_0(K+1). \end{aligned} \tag{2D.4}$$

Substituting $2b_0$ from (2D.3) into (2D.4) gives

$$\Omega_p = \frac{4\mathrm{e}^{2K}\ (K+1)}{\pi \ {}_1\mathrm{F}_1^2(3/2, 1; K)} \ \Omega_v^2 = C(K)\ \Omega_v^2. \tag{2D.5}$$

Note that $C(0) = 4/\pi$, $C(\infty) = 1$, and $4/\pi \le C(K) \le 1$ for $0 \le K \le \infty$.

Appendix 2E: Derivation of Eq. (2.374)

From (2.373), the composite distribution for the squared-envelope, α_c^2, is

$$p_{\alpha_c^2}(x) = \int_0^\infty \left(\frac{m}{w}\right)^m \frac{x^{m-1}}{\Gamma(m)} \exp\left\{-\frac{mx}{w}\right\} \frac{1}{\sqrt{2\pi}\xi\sigma_\Omega w} \exp\left\{-\frac{(10\log_{10}\{w\} - \mu_{\Omega_p\ (\mathrm{dB})})^2}{2\sigma_\Omega^2}\right\} \mathrm{d}w, \tag{2E.1}$$

where $\xi = \ln(10)/10$. The mean of the approximate log-normal distribution is

$$\begin{aligned}\mu_{(\mathrm{dBm})} &= \mathrm{E}[10\log_{10}\{\alpha_c^2\}] \\ &= \int_0^\infty \int_0^\infty 10\log_{10}\{x\} \left(\frac{m}{w}\right)^m \frac{x^{m-1}}{\Gamma(m)} \exp\left\{-\frac{mx}{w}\right\} \frac{1}{\sqrt{2\pi}\xi\sigma_\Omega w} \exp\left\{-\frac{(10\log_{10}\{w\} - \mu_{\Omega_p\,(\mathrm{dB})})^2}{2\sigma_\Omega^2}\right\} \mathrm{d}w\mathrm{d}x \\ &= \frac{10m^m}{\sqrt{2\pi}\xi\sigma_\Omega\Gamma(m)} \int_0^\infty \frac{1}{w^{m+1}} \exp\left\{-\frac{(10\log_{10}\{w\} - \mu_{\Omega_p\,(\mathrm{dB})})^2}{2\sigma_\Omega^2}\right\} \int_0^\infty \log_{10}\{x\}\, x^{m-1} \exp\left\{-\frac{mx}{w}\right\} \mathrm{d}x\mathrm{d}w. \end{aligned} \tag{2E.2}$$

Assuming that m is an integer, the inner integral becomes [147, 4.352.2]

$$\int_0^\infty \log_{10}\{x\} x^{m-1} \exp\left\{-\frac{mx}{w}\right\} \mathrm{d}x = \frac{\Gamma(m) w^m}{m^m \ln 10} \left(\psi(m) - \ln(m/w)\right). \tag{2E.3}$$

Then by using the change of variables $x = 10\log_{10}\{w\}$,

$$\mu_{(\mathrm{dBm})} = \xi^{-1} \left(\psi(m) - \ln(m)\right) + \mu_{\Omega_p\,(\mathrm{dB})}, \tag{2E.4}$$

where $\psi(\,\cdot\,)$ is the Euler psi function, and

$$\psi(m) = -C + \sum_{k=1}^{m-1} \frac{1}{k} \tag{2E.5}$$

and $C \simeq 0.5772$ is Euler's constant. Likewise, the second moment of the approximate log-normal distribution is

$$\begin{aligned}\mathrm{E}[(10\log_{10}(\alpha_c^2))^2] &= \int_0^\infty \int_0^\infty (10\log_{10}\{x\})^2 \left(\frac{m}{w}\right)^m \frac{x^{m-1}}{\Gamma(m)} \exp\left\{-\frac{mx}{w}\right\} \frac{1}{\sqrt{2\pi}\xi\sigma_\Omega w} \exp\left\{-\frac{(10\log_{10}\{w\} - \mu_{\Omega_{p(\mathrm{dB})}})^2}{2\sigma_\Omega^2}\right\} \mathrm{d}w\mathrm{d}x \\ &= \frac{m^m}{\sqrt{2\pi}\xi\Gamma(m)} \int_0^\infty \frac{1}{w^{m+1}} \exp\left\{-\frac{(10\log_{10}\{w\} - \mu_{\Omega_p\,(\mathrm{dB})})^2}{2\sigma_\Omega^2}\right\} \int_0^\infty (10\log_{10}\{x\})^2\, x^{m-1} \exp\left\{-\frac{mx}{w}\right\} \mathrm{d}x\mathrm{d}w. \end{aligned} \tag{2E.6}$$

Assuming again that m is an integer, the inner integral is [147, 4.358.2]

$$\int_0^\infty (10\log_{10}(x))^2\, x^{m-1} \exp\left\{-\frac{mx}{w}\right\} \mathrm{d}x = \frac{(m-1)! w^m}{m^m \ln 10} \left(\left(\psi(m) - \ln(m/w)\right)^2 + \zeta(2,m)\right)$$

leading to

$$\mathrm{E}[(10\log_{10}\{\alpha_c^2\})^2] = \zeta^2 \left(\left(\psi(m) - \ln(m)\right)^2 \mu_{\Omega_p\,(\mathrm{dB})}^2 + \zeta(2,m)\right) + 2\zeta \left(\psi(m) - \ln(m)\right) \mu_{\Omega_p\,(\mathrm{dB})} + \sigma^2 + \mu_{\Omega_p\,(\mathrm{dB})}^2, \tag{2E.7}$$

where

$$\zeta(2,m) = \sum_{k=0}^{\infty} \frac{1}{(m+k)^2} \tag{2E.8}$$

is Reimann's zeta function. Finally, the variance of the approximate log-normal distribution is

$$\begin{aligned}\sigma^2 &= \mathrm{E}[(10\log_{10}\{\alpha_c^2\})^2] - \mathrm{E}^2[10\log_{10}\{\alpha_c^2\}] \\ &= \xi^{-2}\zeta(2,m) + \sigma_\Omega^2. \end{aligned} \tag{2E.9}$$

Problems

2.1. Suppose that $r(t)$ is a wide-sense stationary (WSS) bandpass random process, such that

$$r(t) = g_I(t)\cos(2\pi f_c t) - g_Q(t)\sin(2\pi f_c t)$$

(a) Show that the auto- and cross-correlations of $g_I(t)$ and $g_Q(t)$ must satisfy the following conditions:

$$\phi_{g_I g_I}(\tau) = \phi_{g_Q g_Q}(\tau)$$
$$\phi_{g_I g_Q}(\tau) = -\phi_{g_Q g_I}(\tau)$$

(b) Under the conditions in part a) show that the autocorrelation of $r(t)$ is

$$\mathrm{E}[r(t)r(t+\tau)] = \phi_{g_I g_I}(\tau)\cos(2\pi f_c \tau) - \phi_{g_I g_Q}(\tau)\sin(2\pi f_c \tau).$$

2.2. What is the maximum Doppler shift for the GSM mobile cellular system on the "downlink" from the base station to the mobile unit (935–960 MHz RF band)? What is it on the "uplink" direction, or mobile to base (890–915 MHz RF band)? Assume a high-speed train traveling at a speed of $v = 250$ km/h.

2.3. This problem considers two ray channels exhibiting either frequency selective or time selective behavior.

(a) Consider the transmission of a bandpass signal having complex envelope $\tilde{s}(t)$ on a channel such that the received complex envelope is

$$\tilde{r}(t) = \alpha\tilde{s}(t) + \beta\tilde{s}(t-\tau_1),$$

where α and β are real valued.

i) Find the channel impulse response $g(t,\tau)$.
ii) Find the channel magnitude response $|G(t,f)|$.
iii) Find the channel phase response $\angle G(t,f)$.

(b) Consider the transmission of a bandpass signal having complex envelope $\tilde{s}(t)$ on a channel such that the received complex envelope is

$$\tilde{r}(t) = \alpha\tilde{s}(t) + \beta\tilde{s}(t)e^{j2\pi f_d t},$$

where α and β are real valued.

i) Find the channel impulse response $g(t,\tau)$.
ii) Find the channel magnitude response $|G(t,f)|$.
iii) Find the channel phase response $\angle G(t,f)$.

2.4. A wireless channel is characterized by the time-variant impulse response

$$g(t,\tau) = \left(1 - \frac{\tau}{T}\right)\cos(\Omega t + \phi_0), \quad 0 \le \tau \le T,$$

where $T = 0.05$ ms, $\Omega = 10\pi$, and $\phi_0 \in (-\pi, +\pi]$ is a constant.

(a) Determine the channel time-variant transfer function.
(b) Given an input signal having the complex envelope

$$\tilde{s}(t) = \begin{cases} 1, & 0 \le t \le T_s \\ 0, & \text{otherwise} \end{cases},$$

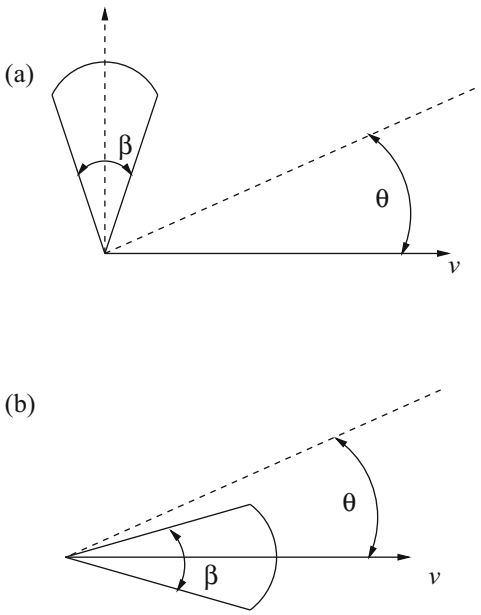

Fig. 2.70 Scenario for Problem 2.7 parts (**a**) and (**b**)

determine the complex envelope of the signal at the output of the channel, $\tilde{r}(t)$. Make sure to consider cases when $0 < T_s < T$ and $0 < T < T_s$, separately.

(c) Consider digital modulation scheme with a modulated symbol interval T_s. If the channel fading is frequency selective, specify the relation between T_s and T.

2.5. Suppose that an omnidirectional antenna is used and the azimuth angle-of-arrival distribution, $p(\theta)$, is given by (2.52). Find the Doppler power spectrum $S_{gg}(f)$.

2.6. A very useful model for a non-isotropic scattering environment assumes that the azimuth angle-of-arrival distribution is described by the von Mises pdf in (2.51).

(a) Assuming an isotropic receiver antenna, calculate the received Doppler power spectrum, $S_{gg}(f)$.
(b) Under what conditions are the quadrature components $g_I(t)$ and $g_Q(t)$ uncorrelated?

2.7. Determine and plot the (normalized) power spectral densities $S_{gg}(f)$ for the following cases. Assume 2-D isotropic scattering;

(a) A vertical loop antenna in the plane perpendicular to vehicle motion, $G(\theta) = \frac{3}{2}\sin^2(\theta)$.
(b) A vertical loop antenna in the plane of vehicle motion, $G(\theta) = \frac{3}{2}\cos^2(\theta)$.
(c) A directional antenna of beamwidth β directed perpendicular to vehicle motion with (see Fig. 2.70a)

$$G(\theta) = \begin{cases} G_0\,, & |\frac{\pi}{2} - \theta| < \beta/2 \\ 0\,, & \text{otherwise} \end{cases}.$$

(d) A directional antenna of beamwidth β directed along vehicle motion with (see Fig. 2.70b)

$$G(\theta) = \begin{cases} G_0\,, & |\theta| < \beta/2 \\ 0\,, & \text{otherwise} \end{cases}.$$

2.8. Consider a narrow-band channel with a 700 MHz carrier frequency. The complex channel gain at a mobile station is $g(t) = g_I(t) + jg_Q(t)$, such that

$$S_{g_I g_I}(f) = \begin{cases} \text{rect}\left(\frac{f}{200}\right), & |f| \le 100\,\text{Hz} \\ 0, & \text{elsewhere} \end{cases}$$

$$S_{g_I g_Q}(f) = 0.$$

(a) What is the speed of the mobile station?
(b) What is the cross-correlation function $\phi_{g_I g_Q}(\tau)$ of the I and Q components of the faded envelope?
(c) If antenna diversity is deployed at the mobile station, what are the possible spatial separations between the antenna elements such that the corresponding faded envelopes will be uncorrelated?
(d) Write down an expression for $\phi_{g_Q g_Q}(\tau)$.

2.9. Consider a Ricean fading channel with Rice factor K and average envelope power Ω_p. Assume that the means $m_I(t)$ and $m_Q(t)$ of the in-phase and quadrature components are given by (2.59) and (2.60), respectively. Derive an integral expression for the probability density function of the envelope phase in terms of K and Ω_p.

2.10. Consider a 2-D isotropic scattering channel. Show that the psd of the received envelope $\alpha(t) = |g(t)|$ is given by (2.77).

2.11. Suppose that the Doppler spectrum is given by

$$S_{gg}(f) = A\text{rect}\left(\frac{f+f_1}{W_d}\right) + A\text{rect}\left(\frac{f-f_1}{W_d}\right)$$

where

$$\text{rect}\left(\frac{f}{W_d}\right) = \begin{cases} 1 & , \quad |f| \leq W_d/2 \\ 0 & , \quad \text{elsewhere} \end{cases}$$

and A, f_1, and W_d are constants.

(a) Sketch the Doppler spectrum.
(b) Find the envelope correlation function

$$\phi_{gg}(\tau) = \phi_{g_I g_I}(\tau) + j\phi_{g_I g_Q}(\tau)$$

(c) For which values of τ are $g(t)$ and $g(t+\tau)$ uncorrelated?

2.12. Suppose that the Doppler power spectrum is given by the following function:

$$S_{gg}(f) = A\cos\left(\frac{\pi f}{2f_m}\right)\text{rect}\left(\frac{f}{2f_m}\right)$$

(a) Find the corresponding envelope autocorrelation function $\phi_{gg}(\tau)$.
(b) For what values of τ are $g_I(t)$ and $g_Q(t+\tau)$ uncorrelated?
(c) Given that

$$\Omega_p = \phi_{gg}(0) = \int_{-f_m}^{f_m} S_{gg}(f)df$$

find the value of A in terms of Ω_p.

2.13. Consider the non-isotropic scattering environment shown in Fig. 2.7. Show that the continuous portion of the psd of the received envelope $\alpha(t) = |g(t)|$ is given by (2.79).

2.14. Consider a wide-sense stationary zero-mean complex Gaussian random process $g(t)$ having the autocorrelation function $\phi_{gg}(\tau) = \phi_{g_I g_I}(\tau) + j\phi_{g_I g_Q}(\tau)$. Show that the autocorrelation and autocovariance functions of the squared-envelope $\alpha^2(t) = |g(t)|^2$ are given by (2.82) and (2.83), respectively.

2.15. Consider a wide-sense stationary non-zero-mean complex Gaussian random process $g(t) = g_I(t) + jg_Q(t)$, where

$$g_I(t) = \hat{g}_I(t) + m_I(t)$$
$$g_Q(t) = \hat{g}_Q(t) + m_Q(t)$$

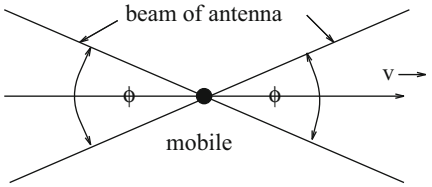

Fig. 2.71 Mobile with directional antenna for Problem 2.19

and $m_I(t)$ and $m_Q(t)$ are the means of $g_I(t)$ and $g_Q(t)$, respectively. Show that the autocorrelation and autocovariance functions of the squared-envelope $\alpha^2(t) = |g(t)|^2$ are given by (2.87) and (2.90), respectively.

2.16. Establish the equivalence between (2.102) and (2.103).

2.17. A flat Rayleigh fading signal at 6 GHz is received by a vehicle traveling at 80 km/hr.

(a) Determine the number of positive-slope zero crossings of the rms envelope level that occur over a 5 s interval.
(b) Determine the average duration of a fade below the rms envelope level.
(c) Determine the average duration of a fade at a level of 20 dB below the rms envelope level.

2.18. Consider a situation where the received envelope is Rayleigh faded ($K = 0$), but the Doppler power spectrum $S^c_{gg}(f)$ is not symmetrical about $f = 0$, i.e., a form of non-isotropic scattering. Show that the envelope level crossing rate is given by

$$L_R = \sqrt{\frac{b_2}{b_0} - \frac{b_1^2}{b_0^2}} \cdot \frac{\rho}{\sqrt{\pi}} \mathrm{e}^{-\rho^2},$$

where

$$\rho = \frac{R}{\sqrt{\Omega_p}} = \frac{R}{\sqrt{2b_0}}.$$

and the b_i are defined in (2.102) with $f_q = 0$.

2.19. Consider the situation in Fig. 2.71, where the mobile station employs a directional antenna with a beam width of $\phi°$. Assume a 2-D isotropic scattering environment.

(a) In receiving a radio transmission at 850 MHz, a Doppler frequency of 20–60 Hz is observed. What is the beam width of the mobile station antenna, and how fast is the mobile station traveling?
(b) Suppose that the mobile station antenna has a beam width of 13°. What is the level crossing rate with respect to the rms envelope level, assuming that the mobile station is traveling at a speed of 30 km/h?

2.20. Consider a cellular radio system with fixed base stations and moving mobile stations. The channel is characterized by flat Rayleigh fading channel with two-dimensional isotropic scattering. The mobile station employs omni-directional antennas and the system operates at an RF carrier frequency of 900 MHz.

(a) Determine the positive going level crossing rate at the normalized envelope level $\rho = 1$, when the maximum Doppler frequency is $f_m = 20$ Hz. Compute the velocity of the mobile station.
(b) Now suppose that the mobile station is travelling at a speed of 24 km/h. Calculate the average fade duration (AFD) and level crossing rate (LCR) at the normalized envelope level $\rho = 0.294$.

2.21. A vehicle experiences 2-D isotropic scattering and receives a Rayleigh faded 900 MHz signal while traveling at a constant velocity for 10 s. Assume that the local mean remains constant during travel, and the average duration of fades 10 dB below the rms envelope level is 1 ms.

(a) How far does the vehicle travel during the 10 s interval?
(b) How many fades is the envelope expected to undergo that are 10 dB below the rms envelope level during the 10 s interval?

2.22. A vehicle receives a Ricean faded signal where the specular component is at the frequency f_c and scatter component is due to 2-D isotropic scattering.

(a) Compute the average duration of fades that 10 dB below the rms envelope level for $K = 0, 7, 20$, and a maximum Doppler frequency of $f_m = 20$ Hz.

(b) Suppose that data is transmitted using binary modulation at a rate of 1 Mbps, and an envelope level that is 10 dB below the rms envelope level represents a threshold between "error-free" and "error-prone" conditions. During error-prone conditions, bits are in error with probability one-half. Assuming that the data is transmitted in 10,000-bit packets, how many bits errors (on the average) will each transmitted packet contain?

2.23. Show that for wide-sense stationary (WSS) channels

$$\phi_H(f, m; \nu, \mu) = \psi_H(f, m; \nu)\delta(\nu - \mu)$$
$$\phi_S(\tau, \eta; \nu, \mu) = \psi_S(\tau, \eta; \nu)\delta(\nu - \mu).$$

That is, the channel correlation functions $\phi_H(f, m; \nu, \mu)$ and $\phi_S(\tau, \eta; \nu, \mu)$ have a singular behavior with respect to the Doppler shift variable. What is the physical interpretation of this property?

2.24. Show that for uncorrelated scattering (US) channels

$$\phi_g(t, s; \tau, \eta) = \psi_g(t, s; \tau)\delta(\eta - \tau)$$
$$\phi_S(\tau, \eta; \nu, \mu) = \psi_S(\tau; \nu, \mu)\delta(\eta - \tau).$$

That is, the channel correlation functions $\phi_g(t, s; \tau, \eta)$ and $\phi_S(\tau, \eta; \nu, \mu)$ have a singular behavior with respect to the time delay variable. What is the physical interpretation of this property?

2.25. Given the channel input signal $\tilde{s}(t)$ and the channel delay-Doppler spread function $S(\tau, \nu)$, show that the channel output signal is

$$\tilde{r}(t) = \int_{-\infty}^{\infty}\int_{-\infty}^{\infty} \tilde{s}(t - \tau)S(\tau, \nu)\mathrm{e}^{-j2\pi f\tau}\mathrm{d}\nu\mathrm{d}\tau.$$

How do you interpret the channel function $S(\tau, \nu)$?

2.26. Suppose that the spaced-time spaced-frequency correlation function of a WSSUS channel has the following form

$$\phi_T(\Delta f; \Delta t) = \exp\{-b|\Delta t|\}\,\frac{1}{a + j2\pi\Delta f}.$$

(a) Find the corresponding channel correlation function $\psi_g(\Delta t; \tau)$.
(b) Find the corresponding scattering function $\psi_S(\nu; \tau)$.
(c) What is the average delay spread, μ_τ, and rms delay spread σ_τ?

2.27. The scattering function for a WSSUS scattering channel is given by

$$\psi_S(\tau, \nu) = \Omega_p \cdot \frac{2a}{a^2 + (2\pi\nu)^2} \cdot be^{-b\tau}u(\tau).$$

(a) What is the spaced-time spaced-frequency correlation function?
(b) What is the average delay?
(c) What is the rms delay spread?

2.28. The scattering function for a WSSUS channel is given by

$$\psi_S(\tau, \nu) = \begin{cases} \frac{\Omega_p}{100}b\mathrm{e}^{-b\tau}, & 0 \le |\nu| \le 50\,\mathrm{Hz}, 0 \le \tau \le \infty \\ 0, & \text{elsewhere} \end{cases}$$

(a) What is the speed of the mobile station?
(b) What is the channel correlation function $\psi_g(\Delta t; \tau)$?

(c) If the faded envelope is sampled, $g_k = g(kT_s)$, what sample spacings T_s will yield uncorrelated samples, g_k?
(d) What is the envelope level crossing rate, L_R?

2.29. The frequency correlation function of a channel is defined as

$$\phi_T(\Delta_f) \stackrel{\Delta}{=} \phi_T(\Delta_f, \Delta_t = 0)$$

where $\phi_T(\Delta_f, \Delta_t)$ is the spaced-time, spaced-frequency correlation function. Suppose that

$$\phi_T(\Delta_f) = \frac{A}{1 + j2\pi\Delta_f/f_o}$$

(a) Find the power-delay profile of the channel $\psi_g(\tau)$.
(b) Find the average delay μ_τ of the channel.

2.30. Consider a linear time-invariant channel consisting of two equal rays

$$g(t, \tau) = \delta(\tau) + \delta(\tau - \tau_1).$$

(a) Derive an expression for magnitude response of the channel $|T(f, t)|$ and sketch showing all important points.
(b) Repeat for the phase response of the channel $\angle T(f, t)$.

2.31. Consider a linear time-invariant channel having the impulse response

$$g(t, \tau) = \delta(\tau) + 2\delta(\tau - \tau_1) + \delta(\tau - 2\tau_1).$$

(a) Derive a closed-form expression for magnitude response of the channel $|T(f, t)|$ and sketch showing all important points.
(b) Repeat part a) for the phase response of the channel $\angle T(f, t)$.
(c) What is the mean delay and rms delay spread of the channel.

2.32. Consider a linear time-invariant channel having the impulse response

$$g(t, \tau) = \frac{1}{\sqrt{L}} \sum_{k=1}^{L} \delta(\tau - (k-1)\Delta_\tau)$$

(a) Find the magnitude response $|T(f)|$ and phase response $\angle T(f)$ of the channel, where $T(f)$ is the time-invariant transfer function of the channel. Simplify your expressions as much as possible. Plot $|T(f)|$ and $\angle T(f)$.
(b) What is the mean delay μ_τ and rms delay spread σ_τ of this channel? *The following may be useful:*

$$\sum_{k=1}^{n} k = \frac{n(n+1)}{2}$$

$$\sum_{k=1}^{n} k^2 = \frac{n(n+1)(2n+1)}{6}$$

$$\sum_{k=0}^{n} k^3 = \frac{n^2(n+1)^2}{4}$$

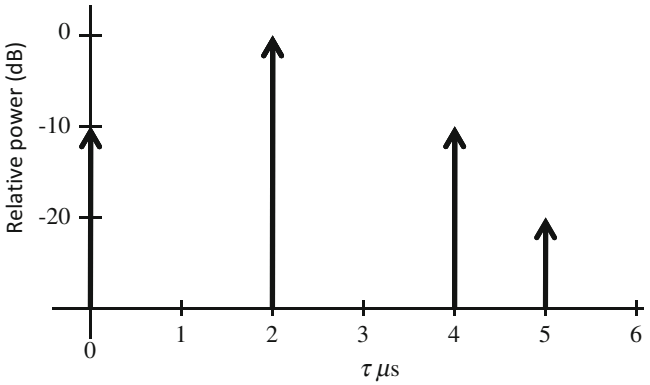

Fig. 2.72 Power-delay profile for Problem 2.35

2.33. The power-delay profile of a WSSUS channel is given by

$$\psi_g(\tau) = e^{-\tau/T}, \quad \tau \geq 0.$$

Assuming that $T = 10\,\mu$s, determine

(a) the average delay
(b) the rms delay spread
(c) the coherence bandwidth of the channel.

2.34. The power-delay profile of a WSSUS channel is given by

$$\psi_g(\tau) = \begin{cases} 0.5[1 + \cos(2\pi\tau/T)], & 0 \leq \tau \leq T/2 \\ 0, & \text{otherwise} \end{cases}.$$

(a) Find the channel frequency correlation function.
(b) Calculate the mean delay, rms delay spread, and the coherence bandwidth.
(c) If $T = 0.1$ ms, determine whether the channel exhibits frequency-selective fading to a GSM cellular system.

2.35. Consider the power-delay profile shown in Fig. 2.72. Calculate the following:

(a) mean delay
(b) rms delay spread
(c) If the modulated symbol duration is $40\,\mu$s, is the channel frequency selective? Why?

2.36. The power-delay profile in Fig. 2.73 is observed for a multipath-fading channel in hilly terrain.

(a) Compute the mean delay.
(b) Compute the rms delay spread.
(c) What is the frequency correlation function of the channel?

2.37. Consider a WSSUS channel with scattering function

$$\psi_S(\tau, \nu) = \psi_1(\tau) \cdot \psi_2(\nu)$$

where

$$\psi_1(\tau) = \begin{cases} 1, & 0 \leq \tau \leq 100\,\text{ms} \\ 0, & \text{otherwise} \end{cases}$$

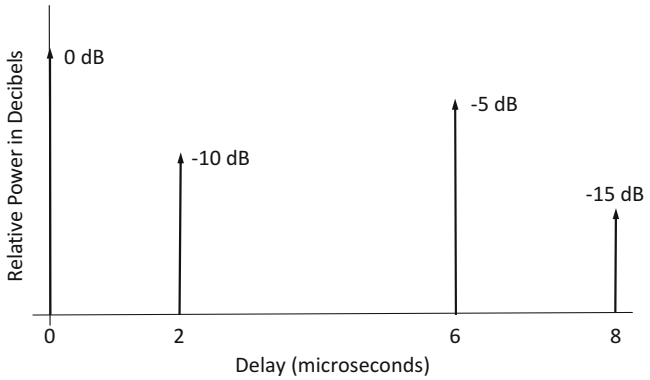

Fig. 2.73 Power-delay profile for Problem 2.36

$$\psi_2(\nu) = \begin{cases} \frac{1}{f_m}[1-(\nu/f_m)^2], & 0 \le |\nu| \le f_m \\ 0, & \text{otherwise} \end{cases}.$$

Assume $f_m = 10$ Hz. Find

(a) the power-delay profile.
(b) the Doppler power spectrum.
(c) the mean delay and the rms delay spread.
(d) the maximum Doppler frequency, the mean Doppler frequency, and the rms Doppler frequency.
(e) the coherence bandwidth and the coherence time of the channel.

2.38. Consider the COST-207 typical urban (TU) and bad urban (BU) power-delay profiles shown in Fig. 2.51 of the text with delays and fractional powers given in Table 2.7.

(a) Calculate the average delay, μ_τ.
(b) Calculate the rms delay spread, σ_τ.
(c) Calculate the approximate values of W_{50} and W_{90}.
(d) If the channel is to be used with a modulation scheme that requires an equalizer whenever the symbol duration $T < 10\sigma_\tau$, determine the maximum symbol rate that can be supported without requiring an equalizer.

2.39. The scattering function $\psi_S(\tau, \nu)$ for a multipath-fading channel is non-zero for the range of values $0 \le \tau \le 1\,\mu$s and $-40 \le \nu \le 40$ Hz. Furthermore, $\psi_S(\tau, \nu)$ is uniform in the two variables τ and ν.

(a) Find numerical values for the following parameters;

1. the average delay, μ_τ, and rms delay spread, σ_τ.
2. the rms Doppler spread, B_d
3. the approximate coherence time, T_c
4. the approximate coherence bandwidth, B_c

(b) Given the answers in part a), what does it mean when the channel is

1. frequency-nonselective
2. slowly fading
3. frequency-selective

2.40. The scattering function $\psi_S(\tau, \nu)$ for a multipath-fading channel is non-zero for the range of values $0 \le \tau \le 1\,\mu$s and $-40 \le \nu \le 40$ Hz. Assume that the scattering function is uniform in the two variables τ and ν with a value equal $A = 0.00125$.

(a) What is the average delay and *rms* delay spread of the channel?
(b) Find the spaced-time spaced-frequency correlation function $\psi_T(\Delta f, \Delta t)$ of the channel.
(c) What is the total envelope power? Express your answer in dBm units.

(d) If the scattering function describes a conventional fixed-to-mobile cellular land mobile radio channel, and a carrier frequency of 900 MHz is used with an isotropic receive antenna, how fast is the mobile station moving?

2.41. Suppose that the Doppler spectrum is given by

$$S_{gg}(f) = G(A, 0.5f_m, 0.1f_m)$$

where

$$G(A, f_1, f_2) = A \exp\left\{-\frac{(f-f_1)^2}{2f_2^2}\right\}$$

(a) Sketch the Doppler spectrum.
(b) Find the envelope correlation function

$$\phi_{gg}(\tau) = \phi_{g_I g_I}(\tau) + j\phi_{g_I g_Q}(\tau)$$

(c) For which values of τ are $g_I(t)$ and $g_Q(t+\tau)$ uncorrelated?

2.42. Suppose that a fading simulator is constructed by low-pass filtering white Gaussian noise as shown in Fig. 2.35. Assume that the white Gaussian noise generators that produce $g_I(t)$ and $g_Q(t)$ are uncorrelated, and have power density spectrum $\Omega_p/2$ watts/Hz. The low-pass filters that are employed have the transfer function

$$H(f) = \frac{A}{1 + j2\pi\beta f}.$$

(a) What is the Doppler power spectrum $S_{gg}(f)$ and autocorrelation function $\phi_{gg}(\tau)$?
(b) Find A such that the envelope power is equal to Ω_p.
(c) What is the joint probability density function of the output $g(t)$ and $g(t+\tau)$?

2.43. Suppose that a fading simulator is constructed using low-pass filtered white Gaussian noise as shown in Fig. 2.35. Assume that the white Gaussian noise generators used to produce $g_I(t)$ and $g_Q(t)$ are uncorrelated. The low-pass filters that are employed have the transfer function

$$H(f) = \frac{1}{\sqrt{B}}\text{rect}\left(\frac{f}{B}\right).$$

(a) What is the Doppler power spectrum $S_{gg}(f)$?
(b) For the $S_{gg}(f)$ in part (a), derive an expression for the envelope level crossing rate.

2.44. Consider Jakes' method in (2.254) and (2.255).

(a) With the choice that $\alpha = 0$ and $\beta_n = \pi n/(M+1)$ show that

$$< g_I(t)g_Q(t) > = 0$$
$$< g_Q^2(t) > = (M+1)/(2M+1)$$
$$< g_I^2(t) > = M/(2M+1)$$

(b) Rederive the time averages in part a) for the choice $\alpha = 0$ and $\beta_n = \pi n/M$.

2.45. (**Computer exercise**) You are to write a software fading simulator that uses Jakes' method and plot typical sample functions of the faded envelope. By scaling $g_I(t)$ and $g_Q(t)$ appropriately, generate a Rayleigh faded envelope having the mean-squared-envelope $\Omega_p = 1$. Plot a sample function of your faded envelope assuming a maximum Doppler frequency of $f_m T = 0.1$, where T is the simulation step size.

Note that Jakes' simulator is non-stationary as shown in (2.260). Therefore, you may not necessary get a plot that is identical to Fig. 2.38. In fact, it would be good if you could observe the non-stationary behavior of the simulator, i.e., the pdf of the envelope distribution changes with time.

2.46. (**Computer exercise**) In this problem you are to generate a Ricean faded envelope $\hat{g}(t) = \hat{g}_I(t) + j\hat{g}_Q(t)$ by making appropriate modifications to Jakes' method such that

$$\hat{g}_I(t) = m_I(t) + g_I(t)$$
$$\hat{g}_Q(t) = m_Q(t) + g_Q(t),$$

where $g_I(t)$ and $g_Q(t)$ are defined in (2.254) and (2.255), respectively. Assume that the means $m_I(t)$ and $m_Q(t)$ are generated according to Aulin's model in (2.59) and (2.60). For $f_m T = 0.1$, $\Omega_p = 1$ and $K = 0, 4, 7$, and 16, plot the following:

(a) The envelope $\hat{\alpha}(t) = \sqrt{\hat{g}_I^2(t) + \hat{g}_Q^2(t)}$.

(b) The wrapped phase $\phi(t) = \text{Tan}^{-1}\left(\hat{g}_Q(t)/\hat{g}_I(t)\right)$, mod 2π.

2.47. (**Computer exercise**) This problem uses the fading simulator developed in Problem 2.46. The objective is to compute an estimate of the mean-squared-envelope $\Omega_p = \text{E}[\hat{\alpha}^2(t)]$ from samples of $\hat{g}_I(kT)$ and $\hat{g}_Q(kT)$, where T is the sample spacing in seconds. The estimate is computed by forming the empirical average

$$\hat{\Omega}_p = \frac{1}{N}\sum_{i=1}^{N}\left(\hat{g}_I^2(iT) + \hat{g}_Q^2(iT)\right),$$

where NT is the window averaging length in seconds. Assuming a constant velocity, the distance the MS moves (in units of wavelengths) in a time of NT seconds is

$$\frac{d}{\lambda_c} = Nf_m T.$$

(a) For $K = 0, 4, 7$, and 16, generate 1000 estimates of the of Ω_p by using non-overlapping averaging windows of size $N = 50, 100, 150, 200, 250, 300$. Construct a graph that plots, for each K, the sample variance of the Ω_p estimate on the ordinate and the window size on the abscissa.

(b) Can you draw any qualitative conclusions from part a)?

Note that estimates of the local mean Ω_p are used in resource management algorithms such as handoff algorithms.

2.48. Suppose that two complex faded envelopes $g_i(t) = g_{I,i}(t) + jg_{Q,i}(t)$, $i = 1, 2$ are available, such that

$$\boldsymbol{\mu}_{\mathbf{g}} = \text{E}[\mathbf{g}(t)] = \mathbf{0}$$
$$\Phi_{\mathbf{g}}(\tau) = \frac{1}{2}\text{E}[\mathbf{g}(t)\mathbf{g}^H(t+\tau)] = \boldsymbol{\Omega} J_o(2\pi f_m \tau),$$

where

$$\mathbf{g}(t) = (g_1(t), g_2(t))$$
$$\boldsymbol{\Omega} = \begin{bmatrix} \Omega_1 & 0 \\ 0 & \Omega_2 \end{bmatrix}.$$

A third faded envelope $g_3(t)$ is now generated that is correlated with $g_1(t)$ and $g_2(t)$ according to

$$g_3(t) = \alpha g_1(t) + (1-\alpha)g_2(t), \qquad 0 \le \alpha \le 1.$$

(a) Compute the values of

$$\phi_{g_1 g_3}(\tau) = \frac{1}{2}\mathrm{E}[g_1^*(t)g_3(t+\tau)]$$
$$\phi_{g_2 g_3}(\tau) = \frac{1}{2}\mathrm{E}[g_2^*(t)g_3(t+\tau)]$$
$$\phi_{g_3 g_3}(\tau) = \frac{1}{2}\mathrm{E}[g_3^*(t)g_3(t+\tau)].$$

(b) What is the envelope distribution of $g_3(t)$?

2.49. Suppose that the two $\tau = T/4$ spaced taps in Example 2.1 do not have equal magnitude. In particular, suppose that $|g_0(t)|^2 = |g_1(t)|^2/2$. Once again, a T-spaced channel model is to be generated such that the two T-spaced taps capture the maximum possible total energy.

(a) Find the optimal sampler timing instant.
(b) Determine the corresponding matrix $\mathbf{A}$ for $\beta = 0.35$.

2.50. By starting with the Gaussian density for the local mean envelope power in (2.357) derive the log-normal density in (2.355).

2.51. One simple model for shadow simulation is to model log-normal shadowing as a Gaussian white noise process that is filtered by a first-order low-pass filter. With this model

$$\Omega_{k+1\ (\mathrm{dBm})} = \zeta\Omega_{k\ (\mathrm{dBm})} + (1-\zeta)v_k,$$

where $\Omega_{k\ (\mathrm{dBm})}$ is the mean envelope or mean squared-envelope, expressed in dBm units, that is experienced at *spatial* index k, ζ is a parameter that controls the spatial correlation of the shadows, and v_k is a zero-mean Gaussian random variable with $\phi_{vv}(n) = \tilde{\sigma}^2\delta(n)$.

(a) Show that the resulting spatial autocorrelation function of $\Omega_{k\ (\mathrm{dBm})}$ is

$$\phi_{\Omega_{(\mathrm{dBm})}\Omega_{(\mathrm{dBm})}}(n) = \frac{1-\zeta}{1+\zeta}\tilde{\sigma}^2\zeta^{|n|}.$$

(b) What is the mean and variance of $\Omega_{k\ (\mathrm{dBm})}$ at any spatial index k?

2.52. (**computer exercise**) The purpose of this problem is to generate variations in the local mean Ω_p due to shadowing. The shadows are generated according to the state equation in (2.360).

(a) Suppose that the simulation step size is $T = 0.1$ s and the mobile station velocity is $v = 30$ km/h. It is desired to have a shadow decorrelation of 0.1 at a distance of 30 m. Find ζ.
(b) Using the value of ζ obtained in part a) and a shadow standard deviation of $\sigma_\Omega = 8$ dB, plot a graph of $\Omega_{p\ (\mathrm{dB})}$ against the *distance* traveled. Scale your plot so the distance traveled goes from 0 to 100 m.

2.53. Plot and compare the path loss (dB) for the free-space and flat specular surface models at 800 MHz versus distance on a log-scale for distances from 1 m to 40 km. Assume that the antennas are isotropic and have a height of 10 m.

2.54. The measured path loss at a distance of 10 km in the city of Tokyo is 160 dB. The test parameters used in the experiment were the following:

- base station antenna height $h_b = 30$ m
- mobile station antenna height $h_m = 3$ m
- carrier frequency $f_c = 1000$ MHz
- isotropic base station and mobile station antennas.

Compare the measured path loss with the predicted path loss from Okumura and Hata's model and Lee's area-to-area model. *If any model parameters are undefined, then use the default values.*

2.55. Suppose that the received power from a transmitter at the input to a receiver is 1 mW at a distance of 1 km. Find the predicted power at the input to the same receiver (in dBm) at distances of 2, 3, and 5 km from the transmitter for the following path loss models:

(a) Free space.
(b) 2-ray ground reflection.
(c) Model described by

$$\mu_{\Omega_p\ (\text{dBm})}(d) = \mu_{\Omega_p\ (\text{dBm})}(d_o) - 10\beta \log_{10}(d/d_o) \ \ (\text{dBm})$$

where $d_o = 1$ km and $\beta = 3.5$.
(d) COST231-Hata model (medium city).

In all cases assume that $f_c = 1800$ MHz, $h_b = 40$ m, $h_m = 3$ m, $G_T = G_R = 0$ dB. Tabulate your results.

2.56. Consider Fig. 2.74 and the following data

- The symbol transmission rate is 24,300 symbols/s with 2 bits/symbol
- The channel bandwidth is 30 kHz
- The propagation environment is characterized by an rms delay spread of $\sigma_\tau = 1$ ns

A mobile station is moving from base station A (BSA) to base station B (BSB). Base station C (BSC) is a co-channel base station with BSA.

Explain how you would construct a computer simulator to model the received signal power at the mobile station from (BSA) and (BSC), as the mobile station moves from BSA to BSB. Clearly state your assumptions and explain the relationship between the propagation characteristics in your model.

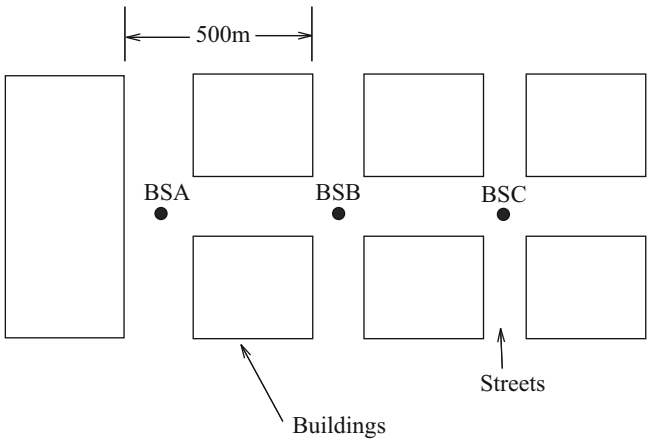

Fig. 2.74 Base station and street layout for Problem 2.56